



**A fundamental study of elemental sublimation during  
solution heat treatment of Ni-base alloys**

**Thesis submitted for the degree of  
Doctor of Philosophy  
at University of Leicester**

by

Zihui Dong

Department of Engineering

University of Leicester

2018

## **Abstract**

### **A fundamental study of elemental sublimation during solution heat treatment of Ni-base alloys**

Zihui Dong

Ni-base superalloys are currently the most important material for high-temperature applications used in gas turbines. High amount of refractory elements used in the latest generations superalloys requires heat treatment for dissolution of inter-dendritic phases. However, occurrence of surface defects during heat treatment significantly reduced high-temperature performance of superalloys. To understand the mechanism of defect formation, a fundamental study on discontinuous precipitation and elemental sublimation is carried out.

Discontinuous precipitation in single crystal superalloys during solution heat treatment has been examined. It is found that discontinuous precipitation is induced by local chemistry change near the casting surface and is dominated by the loss of Ni through sublimation. A phenomenological model is proposed to illustrate the phase evolution near the casting surface during solution heat treatment of single crystal alloys.

Model Ni-Cr-Al model alloys were designed and made for measuring partial vapour pressure and thermodynamic activities of major elements Ni, Al and Cr in Ni-base alloys. Partial vapour pressures of Ni, Cr and Al in the  $\gamma$  phase were measured over the temperature range of 1473-1650K using Knudsen Effusion Mass Spectrometry. The partial vapour pressure of Al is about two orders of magnitude lower than that of Ni, and five times lower than that of Cr, suggesting that the sublimation of Al is almost negligible compared with those of Ni and Cr at solutioning temperatures. The kinetics of Cr sublimation was measured in long-term isothermal experiments at 1573K and it is found that Cr partial vapour pressure reduces significantly during the first 20 hours. Equations for calculating partial vapour pressure and thermodynamic activity at high-temperature range have been obtained.

This fundamental study provides an enhanced understanding on microstructure instability of Ni-base alloys during heat treatment, and is useful for optimisation of heat treatment and alloy design of single crystal alloys.

## **Publications**

1. Z.H. Dong, D. Sergeev, N. D'Souza, S. Feng, D. Kobertz, M. Müller, H.B. Dong, Partial vapour pressures of Ni, Al and Cr in Ni-base alloys and their influence on elemental sublimation during solution heat treatment, submitted for Acta Materialia.
2. Z.H. Dong, N. D'Souza, G. Brewster, H.B. Dong, Formation of Surface Defects During Investment Casting of Ni-base Alloys, the 6th Decennial International Conference on Solidification Processing. Beaumont Estate, Old Windsor, UK, 2017, 482-485.
3. N. D'Souza, D. Welton, J. Kelleher, G.D. West, Z.H. Dong, G. Brewster, H.B. Dong, Microstructure Instability of Ni-Base Single Crystal Superalloys During Solution Heat Treatment, Superalloys 2016, John Wiley & Sons, Inc. 2016, 267-277.
4. D. Welton, N. D'Souza, J. Kelleher, S. Gardner, Z.H. Dong, G.D. West, H. Dong, Discontinuous Precipitation in Ni-Base Superalloys During Solution Heat Treatment, Metallurgical and Materials Transactions A 46(9) (2015) 4298-4315.

## Acknowledgement

I would like to sincerely express my gratitude to my academic supervisor Prof Hongbiao Dong for his tremendous contribution to my PhD study in past years. Without his supervision, it would never have overcome challenges in this work. In addition, he also provided opportunities for attending various conferences which helped inspire me with great improvement of critical thinking. It would be benefit to my PhD research as well as future career.

I also would like to thank industrial supervisor Dr Neil D'Souza from Rolls-Royce, plc for his guidance and suggestions of many specific problems in this project. My greatest appreciation also give to Dr Dmitry Sergeev and Dr Dietmar Kobertz at Forschungszentrum Jülich, Germany. Their organisation for KEMS experiments and discussion of data analysis are invaluable asset to my research. Dr Elena Yazhenskikh is also appreciated for her supports in FactSage calculations.

It is grateful to thank Prof Wei Liang at Taiyuan University of Technology, China for sample casting, Dr Fei Xue, Friedrich-Alexander-Universität Erlangen-Nürnberg, for supply of raw materials. Dr Joe Kelleher at ISIS is acknowledged for neutron diffraction experiment and relevant data analysis.

My friends and colleagues in engineering department are appreciated for their supports: Shuo Feng, Xingzhong Liang, Ruiyao Zhang, Andy Douglas and Mike Dodge. Sincere appreciation also delivers to Mrs Feng, Yun Jia who provided endless encouragement and support during my difficult time as well as Dr Jie Shen for his support and help in past years. My friends Weizheng Xu, Dr Jie Zhou are acknowledged for personal supports during my study.

At last, I would like to dedicate my deepest gratitude to my parents for their ultimate and overwhelming support during my ten-year study in the UK. I have to admit it was extremely time for them, and thank for them making sacrifice for my sake. It is my honour to dedicate this thesis to them.

# Contents

<b>1. Introduction .....</b>	<b>1</b>
<b>2. Literature review on processing of single crystal Ni-base superalloys.....</b>	<b>5</b>
2.1 Gas turbine engine and turbine blades.....	6
2.2 Nickel-base superalloys for turbine blade application.....	9
2.2.1 Alloying elements .....	9
2.2.2 Chemistry development in single crystal Ni-base superalloys .....	13
2.2.3 Phases and microstructures of single crystal Ni-base superalloys .....	14
2.2.4 Topologically close-packed phases in Ni-base superalloys .....	16
2.3 Processing of single crystal alloys .....	18
2.3.1 Investment casting process.....	18
2.3.2 Single crystal casting .....	21
2.3.3 Segregation during solidification of Nickel-base Superalloys .....	22
2.3.4 Solution heat treatment.....	24
2.3.5 Ageing heat treatment .....	28
<b>3. Literature review on oxidation and surface defect formation during casting and heat treatment of single crystal nickel-base superalloys.....</b>	<b>30</b>
3.1 Surface defects formation during casting and heat treatment .....	30
3.2 Formation of surface scale and its mechanism.....	32
3.3 Elemental losses in Ni-base superalloys during solution heat treatment.....	36
3.4 Sublimation induced microstructural instability in Ni-base superalloys during solution heat treatment .	38
3.4.1 Discontinues precipitation in SX Ni-base superalloys .....	38
3.4.2 KEMS studies of thermodynamic properties in Ni-base system .....	40
3.5 High temperature oxidation during processing of Ni-base alloys.....	43

3.5.1 High temperature oxidation.....	44
3.5.2 Thermodynamics of oxidation .....	44
3.5.3 The Ellingham diagram.....	45
3.5.4 Kinetics of oxidation.....	48
3.5.5 Oxidation mechanism of Ni-Cr-Al system .....	51
<b>4. Sublimation-induced discontinuous precipitation in CMSX-10N superalloys during solution heat treatment .....</b>	<b>54</b>
4.1 Surface stability and phase evolution in Ni-base superalloys during solution heat treatment .....	54
4.2 Experimental methods for investigation of discontinuous precipitation .....	55
4.2.1 Investment casting and heat treatment .....	55
4.2.2 Application of neutron diffraction method for determination of microstructural instability .....	56
4.2.3 Interrupted solutioning experiments to examine microstructures at the early stage of solution heat treatment .....	60
4.2.4 Electron microscopy.....	61
4.2.5 Differential Thermal Analyses to determine solvus temperature of CMSX-10N .....	62
4.3 Experimental observations of discontinuous precipitation at the surface of CMSX-10N superalloys during solution heat treatment.....	63
4.3.1 Microstructural evolution of discontinuous precipitation at the surface during solution heat treatment .....	63
4.3.2 Evolution of $\gamma'$ ahead of the discontinuous precipitation cell interface .....	74
4.4 Phenomenological model of discontinuous precipitation evolution in Ni-base superalloys.....	76
4.5 Conclusions .....	79
<b>5. Thermophysical properties of Ni-Cr-Al model alloys .....</b>	<b>80</b>
5.1 Materials and samples preparation .....	80

5.2 Chemical contents of as-cast Ni-Cr-Al model alloys.....	86
5.3 Microscopy characterisation.....	88
5.4 Measured liquidus and solidus temperatures of Ni-Cr-Al model alloys .....	92
5.4.1 DSC experiments for determination of liquidus and solidus temperature of model alloys.....	92
5.4.2 Results of DSC experiments .....	95
5.5 Thermodynamic data from CALPHAD calculations .....	98
5.6 Estimated activity data for preparation of KEMS experiments .....	100
5.6.1 Calculated activity for Ni-Cr-Al model alloys using JMatPro .....	100
5.6.2 Calculated activity for Ni-Cr-Al model alloys using FactSage .....	104
5.7 Conclusions .....	107
 <b>6. Elemental sublimation in Ni-Cr-Al model alloys through thermodynamic analysis and measurements of partial pressures for Ni, Al and Cr .....</b>	<b>109</b>
6.1 Sublimation induced microstructural instability in Ni-base superalloys.....	109
6.2 Principles and instrumentation of Knudsen effusion mass spectrometry .....	110
6.3 Equations for calculating partial pressure and thermodynamic activity .....	117
6.4 Experimental process of KEMS .....	124
6.5 Results of KEMS measurements .....	127
6.5.1 Sample preparation and characterisation.....	127
6.5.2 Measured ion intensities of Ni, Al and Cr in Ni-Cr-Al model alloys .....	128
6.5.3 Sublimation enthalpy and entropy of pure Ni, Al and Cr .....	130
6.5.4 Partial pressures of Ni, Al and Cr in Ni-Cr-Al model alloys .....	132
6.5.5 Thermodynamic activities of Ni, Al and Cr in Ni-Cr-Al model alloys .....	138
6.5.6 Elemental sublimation in Ni-base alloys during long-term isothermal hold at high-temperature ..	143



6.5.7 Implication of thermodynamic activity to phase field determination and optimisation of CALPHAD method.....	146
6.6 Conclusions .....	149
<b>7. Analysis of elemental sublimation during heat treatment in real superalloys .....</b>	<b>152</b>
7.1 Chemical potential for determination of atoms tendency during elemental sublimation.....	152
7.2 Implications of elemental sublimation to investment casting and solution heat treatment of Ni-base superalloys .....	153
7.3 Conclusions .....	156
<b>8. Conclusions and Future work.....</b>	<b>157</b>
8.1 Conclusions .....	157
8.2 Further work .....	158
<b>Appendix .....</b>	<b>160</b>
Outlier methods for KEMS data selection.....	160
<b>Reference .....</b>	<b>162</b>

## Figures

Fig. 2.1 Thermodynamic cycle in gas turbine (Brayton cycle) [2] .....	6
Fig. 2.2 Rolls-Royce Trent 800 cut-out showing major components in a gas turbine engine [2] .....	7
Fig. 2.3 SEM image of microstructure of Ni-base SX superalloys [30] showing large cuboidal particles $\gamma'$ enclosed with $\gamma$ phase .....	15
Fig. 2.4 The crystal structure of (a) FCC $\gamma$ phase, and (b) ordered $\text{Ni}_3\text{Al}$ $\gamma'$ phase [34] .....	16
Fig. 2.5 Microstructure of TCP phases in CMSX-10N superalloys .....	17
Fig. 2.6 (a) Conventionally cast, (b) Directionally solidified, (c) Single crystal turbine blades[2] .....	19
Fig. 2.7 Main processes of investment casting [37] .....	20
Fig. 2.8 Schematic diagram of investment casting for SX turbine blades [38] .....	22
Fig. 2.9 Microsegregation pattern in as-cast SX superalloys showing segregated elements in the inter- dendritic and dendrite core regions [45] .....	23
Fig. 2.10 Solution heat treatment cycles for SX Ni-base superalloys [49] .....	26
Fig. 2.11 Interdiffusion coefficient of alloying elements in pure Nickel [56] .....	27
Fig. 3.1 (a) As-cast SX blades showing the location of surface scale; (b) enlarged view of the scaled region on a blade, (c) different phases on scaled and un-scaled region; (d) defects in scaled region and solutionised substrate in un-scaled region during solution heat treatment. [76] .....	33
Fig. 3.2 Surface scale formation during casting of single-crystal gas turbine blades [77] .....	35
Fig. 3.3 Ir Knudsen cell used in KEMS facilities at Forschungszentrum Jülich .....	42
Fig. 3.4 Ellingham diagram [125] .....	47
Fig. 3.5 The influence of thermodynamic and kinetic on oxidation of Ni-Al alloys [123] .....	50
Fig. 3.6 Schematic diagram of linear, parabolic, sub-parabolic and logarithmic growth rates of oxides .....	50
Fig. 3.7 Oxidation mechanism of Ni-Cr-Al system (reproduced after ref.[127]) .....	52
Fig. 4.1 Schematic diagram of a time-of-flight neutron strain scanning [131] .....	57

Fig. 4.2 TOF diffraction spectrum on ENGIN-X [131].....	58
Fig. 4.3 (a) Schematic diagram of diffracted area of CMSX-10N superalloys (b) Sample configuration .....	60
Fig. 4.4 DTA heating curve of a near-solutioned sample showing limited remnant non-equilibrium eutectic and $\gamma'$ solvus temperature (heating rate of $2\text{ K min}^{-1}$ ). .....	63
Fig. 4.5 BSE image of phases at initial stage of discontinuous precipitation .....	65
Fig. 4.6 (a) Low-magnification BSE image of the entire sample cross section (b) High-magnification BSE image of detailed evolution of microstructures .....	66
Fig. 4.7 BSE images showing microstructure developing ahead of the discontinuous precipitation zone: (a) Montaged image, (b) High-magnification image showing interface with the DP zone, (c) High- magnification image in the bulk.....	68
Fig. 4.8 BSE image showing nucleation of two re-crystallised grains ahead of the DP zone after solutioning at 1633 K (1360 °C) for 1 hour.....	70
Fig. 4.9 (a) BSE image for region ahead of DP zone and position where TEM foil was extracted, (b) Dark-field STEM image showing $\gamma$ -channel and adjacent $\gamma'$ precipitates .....	71
Fig. 4.10 Spectra from two regions within the $\gamma$ -channel showing superimposing peaks of (a) Re and (b) W at corresponding keV.....	72
Fig. 4.11 Spectra from $\gamma$ -channel ahead of DP zone and within the bulk .....	74
Fig. 4.12 Measured lattice spacing for the (110) and (220) peaks during the heating stage. Different shapes of the (110) and (220) curves arise from the different thermal expansion of $\gamma$ and $\gamma'$ phases .....	75
Fig. 4.13 Variation in $\gamma'$ volume percent as a function of isothermal hold time at 1623 K (1350 °C) .....	76
Fig. 4.14 Schematic diagram showing evolution of DP zone and morphology ahead of DP zone during solution heat treatment .....	78
Fig. 5.1 Isothermal diagrams for three oxidation mechanism of Ni-Cr-Al model alloys at 1273K (reproduced after ref. [127]) .....	81

Fig. 5.2 Isothermal diagrams for three oxidation mechanism of Ni-Cr-Al model alloys at 1473K (reproduced after ref. [127]) .....	82
Fig. 5.3 Isothermal diagrams of Ni-Cr-Al model alloys at 1273K in atomic percent .....	85
Fig. 5.4 A sample of as-cast Ni <sub>2</sub> Cr <sub>5</sub> Al model alloy .....	86
Fig. 5.5 Optical image of microstructure for Ni <sub>5</sub> Cr <sub>6</sub> Al sample .....	89
Fig. 5.6 Optical image of microstructure for Ni <sub>30</sub> Cr <sub>6</sub> Al sample .....	90
Fig. 5.7 BSE image of microstructure of Ni <sub>15</sub> Cr <sub>6</sub> Al model alloy .....	91
Fig. 5.8 BSE image of microstructure of Ni <sub>15</sub> Cr <sub>6</sub> Al model alloy .....	92
Fig. 5.9 Heat/cooling cycles of DSC experiment measured in Ni <sub>5</sub> Cr <sub>7</sub> Al alloy .....	94
Fig. 5.10 DSC heating curve of as-cast Ni <sub>2</sub> Cr <sub>5</sub> Al sample .....	95
Fig. 5.11 Phase fraction of Ni <sub>2</sub> Cr <sub>5</sub> Al model alloy at 1703-1713 K .....	98
Fig. 5.12 Liquidus temperatures from DSC and JMatPro results of all samples .....	99
Fig. 5.13 Calculated Cr activities of Ni-Cr-Al mode alloys with 6 wt% Al content using JMatPro .....	100
Fig. 5.14 Calculated Ni activities for Ni-Cr-Al mode alloys with 6 wt% Al using JMatPro .....	103
Fig. 5.15 Calculated Al activities for Ni-Cr-Al mode alloys with 6 wt% Al using JMatPro .....	104
Fig. 5.16 Calculated activities of Ni in Ni-Cr-Al mode alloys with 6 wt% Al content using FactSage .....	105
Fig. 5.17 Calculated activities of Cr in Ni-Cr-Al mode alloys with 6 wt% Al content using FactSage .....	106
Fig. 5.18 Calculated activities of Al in Ni-Cr-Al mode alloys with 6 wt% Al content using FactSage .....	107
Fig. 6.1 KEMS at Forschungszentrum Jülich in Germany .....	112
Fig. 6.2 Schematic diagram for principles of static KEMS [151] .....	113
Fig. 6.3 Set-up of a magnetic sector-field Knudsen effusion mass spectrometer .....	115
Fig. 6.4 Single-cell flange used in KEMS system. Resistance heating is used with the “hairpin” element [147] .....	116
Fig. 6.5 Magnetic-sector instrument in KEMS with indications of key components [147] .....	117
Fig. 6.6 Fragments of a cross-sectional slice (Ni <sub>2</sub> Cr <sub>12</sub> Al) prepared for KEMS experiments .....	125

Fig. 6.7 Operation process of heating/cooling cycles in KEMS experiments .....	126
Fig. 6.8 Isopleth diagram of Ni-Cr-Al ternary alloys (fixed 12 at% of Al) with an increase of Cr content showing present phase region for all measured Ni-Cr-Al model alloys at 1473 K and 1573 K [144] .....	128
Fig. 6.9 Ion intensities of Ni measured at five temperatures using Ni <sub>2</sub> Cr <sub>12</sub> Al alloy determining temperature dependence of ion intensities.....	130
Fig. 6.10 Arrhenius plot of $\ln I \times T$ against $10^4/T$ from KEMS measurements of three pure substances .....	131
Fig. 6.11 Arrhenius plot of $\ln I \times T$ against $10^4/T$ for pure Ni and measured model alloys producing regression equations as thermodynamic description.....	133
Fig. 6.12 Calculated partial vapour pressure of Ni, Cr and Al in the Ni <sub>2</sub> Cr <sub>12</sub> Al alloy showing temperature dependence.....	135
Fig. 6.13 Partial vapour pressures (Pa) of (a) Ni, (b) Al, (c) Cr as a function of the inverse absolute temperature ( $1/T$ ) in all Ni-Cr-Al alloys showing composition dependence in measured alloys .....	137
Fig. 6.14 Calculated thermodynamic activities in the Ni <sub>2</sub> Cr <sub>12</sub> Al alloy showing temperature dependence of (a) Ni, (b) Al and (c) Cr.....	140
Fig. 6.15 Thermodynamic activities of all elements as a function of temperature in Ni-Cr-Al model alloys (a) Ni, (b) Al and (c) Cr showing composition dependence in measured alloys.....	141
Fig. 6.16 Thermodynamic activity and ion intensity change of (a) Ni and (b) Cr in Ni <sub>2</sub> Cr <sub>12</sub> Al alloy during isothermal experiment. ....	142
Fig. 6.17 Variation of partial vapour pressures for (a) Ni and (b) Cr in Ni <sub>2</sub> Cr <sub>12</sub> Al alloy during isothermal experiment, showing their contribution to elemental sublimation.....	144
Fig. 6.18 ion ratio change of (a) Cr/Ni and (b) Al/Ni in measured alloy during isothermal experiment, showing the loss of chromium during isothermal holding .....	145
Fig. 6.19 Ratio of ion intensity for Ni/Al from measured model alloys .....	146
Fig. 6.20 Comparison of thermodynamic activity for results of Cr/Ni ratio from KEMS and CALPHAD calculations.....	148

**Fig. 6.21 Comparison of thermodynamic activity for results of Al/Ni ratio from KEMS and CALPHAD**

**calculations.....148**

## Tables

Table 2.1 Chemical composition (wt.%) from conventional cast alloys to the 4 <sup>th</sup> generation SX superalloys..	10
Table 2.2 Crystallography of TCP phases [35] .....	17
Table 2.3 Typical solution heat treatment cycles for SX Ni-base superalloys.....	25
Table 3.1 Thermodynamic data from Ellingham diagram for oxidation of major elements in Ni-base superalloys at 1000°C .....	48
Table 4.1: Nominal compositions (wt.%) of alloying elements in CMSX-10N.....	56
Table 5.1 List of produced ternary alloy samples in weight percentage .....	83
Table 5.2 List of produced ternary alloy samples in atomic percentage .....	84
Table 5.3 Chemical analysis from EDX.....	87
Table 5.4 Chemical analysis from XRF .....	88
Table 5.5 Liquidus and Solidus temperature of tested samples.....	97
Table 5.6 Temperature range for a critical drop in calculated activity of Cr from JMatPro .....	102
Table 6.1 Compositional change (at %) of Ni-Cr-Al model alloys before and after KEMS experiments .....	127
Table 6.2 Partial pressure equation $\ln p = -A/T + B$ of measured pure Ni, Al, Cr and their enthalpy of sublimation ( $\Delta_{sub}H_{Tm} = -A \times R$ ) and entropy ( $\Delta_{sub}S_{Tm} = B \times R$ ) at mean temperature $T_m/K$ .....	132
Table 6.3 Clausius-Clapeyron equations, $\ln p_i = -A \times 10^4/T + B$ , for calculating partial vapour pressure (Pa) of Ni, Cr and Al in Ni-Cr-Al model alloys.....	134
Table 7.1 Calculated chemical potential of Ni, Al and Cr in measured Ni-Cr-Al model alloys using Equation 6.4 .....	153

# 1. Introduction

Ni-base superalloys exhibit exceptional performance for high-temperature applications. They have been widely used in producing core components of aerospace propulsion and power generators. The requirements for high efficiency and performance promote further development of superalloys properties at high temperature. Single crystal (SX) superalloys were developed to achieve this purpose thanks to the advancement of casting technique. They have superior high temperature capability since a high level of refractory elements enhances creep strength. However, the additional content in new alloys results in severe solidification segregation in the as-cast microstructure. Subsequent heat treatment is applied to dissolve the low-melting inter-dendritic phases and to homogenise chemistry of superalloys. However, it has been found that microstructural instability in Ni-base superalloys during solution heat treatment is the consequence of elemental sublimation under kinetic conditions.

This study aims to investigate a number of microstructural instabilities in Ni-base superalloys during solution heat treatment. The experiments were carried out to examine elemental behaviours on the surface of superalloys at high temperatures. With supporting evidence, phenomenological interpretations for occurrence of kinetic induced microstructural instability during heat treatment were proposed, which promote better understanding of elemental sublimation in Ni-base alloys at high temperatures and enlighten potential solutions for preventing the alloy surface from processing defects.

Chapter 2 is a literature review on chemistry and processing of superalloys used in turbine blade applications. Segregation of as-cast microstructure is also reviewed to facilitate a good understanding of existing problems in superalloys foundry.



Chapter 3 examined several types of defects caused in casting and heat treatment process, including surface scale, discontinuous precipitation (DP), and elemental vaporisation/sublimation on the surface of alloys, etc. An overview of those defects from literature and relevant mechanisms of their formation were also presented. Correlation between literature and remaining challenges in this study were discussed aiming to develop better understanding of heat treat induced defects during alloy production.

Sublimation-induced discontinuous precipitation in Ni-base superalloys during solution heat treatment was studied and the results are presented in Chapter 4. The mole-fraction of  $\gamma'$  precipitates was tracked using in situ neutron diffraction during isothermal hold. With microstructural characterisation of heat treated Ni-base superalloys at different stages of solutioning, the formation and nucleation of DP on the surface of Ni-base superalloys is induced by elemental sublimation. Hence, elemental sublimation leads to transformation from  $\gamma$  to  $\gamma'$  phase accompanied by partitioning of W, Re and Cr to the growth tip of topologically close-packed (TCP) precipitates. In addition, diffusion of Al ahead of boundary also results in  $\gamma'$  precipitation. Based on evolution of observed morphology at the surface of Ni-base superalloys, a phenomenological model was subsequently proposed that provides panoramic view of interpreting sublimation induced DP during solution heat treatment.

Ni-Cr-Al model alloys were designed to study the fundamentals of element sublimation at solution heat treatment temperatures. In Chapter 5 the measurement of thermophysical properties of the model alloys is presented and the measured solidus and liquidus temperatures was used to determine temperature window in subsequence experiments using Knudsen effusion mass spectrometry (KEMS). Calculations of thermodynamic activities in Ni-Cr-Al model alloys provide preliminary prediction of activity range for Ni, Al and Cr. The

accuracy of thermodynamic calculation using CALPHAD method can be assessed after KEMS measurements.

Chapter 6 contains important experimental results using KEMS method. It firstly introduces principles of KEMS technique for determining thermodynamic activity and partial pressure of elements in alloys at high temperatures. Details of KEMS experiments are described. Thermodynamic activities and partial pressures of Ni, Al and Cr in Ni-Cr-Al alloy were obtained from measured ion intensities in experiments. It is found that the partial pressure of Al is about two orders of magnitude lower than that of Ni, and five times lower than that of Cr, suggesting that the sublimation of Al is almost negligible compared with those of Ni and Cr at solutioning temperatures. The kinetics of Cr sublimation was measured in long term isothermal experiments at 1573 K and it is found that Cr partial vapour pressure reduces significantly during the first 20 hours and the reduction is a result of Cr segregation in as-cast condition. A considerable amount of Cr sublimates during the first 20 hours of solution heat treatment. The elemental sublimation leads to change of chemical composition and microstructural instability near the surface of the alloys during solution heat treatment of Ni-base superalloys.

Chapter 7 concludes the effect of elemental sublimation on surface of Ni-base alloys corresponding to results from DP study and KEMS experiments. Implications of this phenomenon to casting of real superalloys are discussed. Results provide experimental data for considering elemental interactions at high temperatures in terms of thermodynamic calculations, which would be a promising solutions for optimisation of heat treatment process and alloy design that avoid the formation of surface defect.

Conclusions were summarised in final chapter summarising key deductions of whole work and potential solutions of defects avoidance in Ni-base alloys production. Further work of relevant issues were also suggested.

## **2. Literature review on processing of single crystal Ni-base superalloys**

Ni-base superalloys are alloys developed for elevated temperature service. These unique high-temperature materials exhibit the most reliable and cost effective means of achieving high operating temperature and stress performance in aircraft turbine engine [1-3]. The development of superalloys has been carried out for over half-century due to their excellent resistance to mechanical and chemical degradation [3-5]. However, the increasing demands of aircraft engine lead to the requirement to improve the existing material to be more efficient and longer operating hours. The advancement of superalloys innovations is achieved by either compositional improvement or processing development.

In the last two decades the chemistry of superalloys has been significantly modified with an increase of refractory elements including Re, Ta and W in recently generations of superalloys [6-8]. The refractory element additions are used to improve the high temperature capacity with enhanced microstructure stability. However, those additions cause the formation of surface defects during casting and solution heat treatment. Surface defects, such as surface scale, surface melting and recrystallization, have become the most frequently occurring defects in SX casting foundries. The mechanism for the formation of these defects is not systematically studied to avoid the surface defect formation.

The following sections will provide an overview of the gas turbine, component requirements for turbine blade applications, the current Ni-base superalloys materials and their manufacturing processes.

## 2.1 Gas turbine engine and turbine blades

Gas turbines are a type of internal combustion engines. Their operations are based on Brayton cycle in different types of mechanical architecture to suit particular types of applications. Fig. 2.1 depicts a standard cycle for gas turbine operations, including induction, compression, combustion and exhaust. More details of gas turbines are available in numerous literatures [1-4].

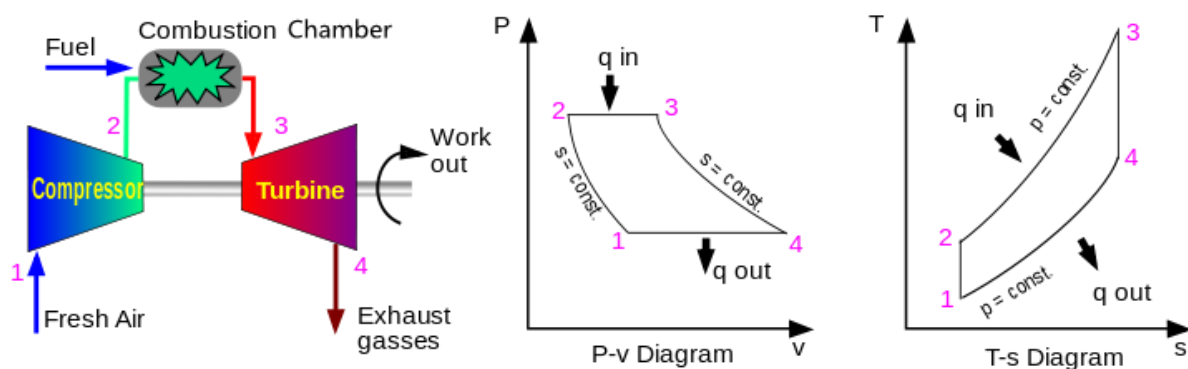


Fig. 2.1 Thermodynamic cycle in gas turbine (Brayton cycle) [2]

The jet engine is powered by gas turbine and produces a thrust which can be described by Newton 3<sup>rd</sup> law. Key components of the jet engine are presented in Fig. 2.2. The working cycle of engine starts at sucking the air into the intake fans. The air at the atmosphere pressure is then compressed and passed to combustion chamber where it is heated by burning fuel at constant pressure to increase the air volume considerably. The gas expands through turbine and jet pipe and provides a mechanical power for turbine rotation powering compressor and fan. The rest of gas is expelled at high velocity and remixed with bypass air that results in increase of the gas momentum and produce the thrust [1, 2].

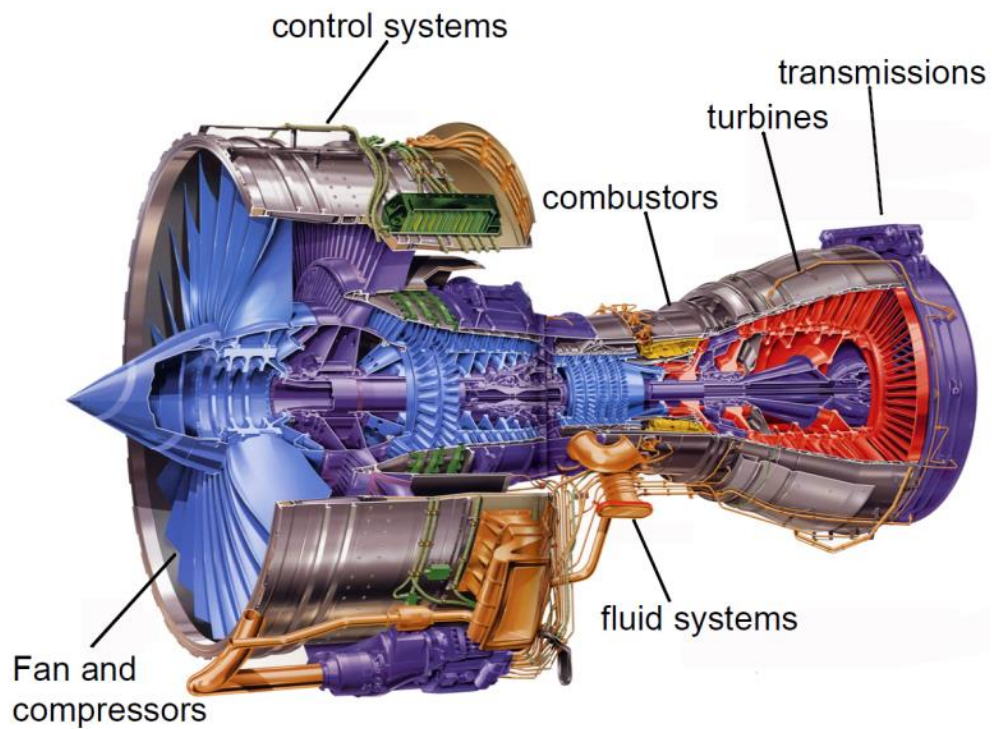


Fig. 2.2 Rolls-Royce Trent 800 cut-out showing major components in a gas turbine engine [2]

The efficiency of the gas turbine is related to thermal and propulsive efficiencies [1]. According to thermodynamic cycle, higher thermodynamic efficiency is achieved by improving the pressure ratio across the compressor or increasing the temperature at point 3 in Carnot cycle. This is defined as the turbine entry temperature (TET). High TET is not only beneficial to thermal efficiency of the engine, but also has effect on fuel consumption, since the greater difference between the cold source and TET, more useful work is generated by gases when it drives the turbine blade. By increasing the firing temperature in combustion, the material of turbine blade needs to be evolved with greater temperature capability.

Turbine blades are one of the crucial components in the aero-engine, which convert the kinetic energy of gases into useful work energy to drive the compressor. Necessities for turbine blade design are normally considering following aspects to enhance the performance

of blades. The high-pressure (HP) turbine blades operate in the most severe environment at temperature over 1873K. To impose thermal gradient and reduce temperature to around 1273K, a thermal barrier coating (TBC) and internal cooling air are introduced in blade design reducing the temperature down to 1273K [2, 3, 9]. In addition, the turbine blades are subjected to high mechanical loads because of high speed of revolution in operation. Hence, creep strength is an essential factor for alloy design.

Fatigue is another mechanical failure during operation. Low cycle fatigue (LCF) would lead to the initial and propagation of cracks when the turbine blade is under repeated process of thermal and mechanical loads [10]. Crack propagation further causes high cycle fatigue (HCF) which vibratory loading from factors such as turbulence in the combustion gases.

As the turbine blades operate in a heavily oxidising environment, the oxidation resistance of the base material is also crucial. The environment contains contaminants such as salts and fuel products, which accelerate the degradation of the blade by type I (at high temperature, generally 1073 to 1223 K) or type II (at low temperature, typically 943 to 1023 K) hot corrosion [11, 12]. To mitigate environmental attack, coating system is normally introduced for protection of turbine blades, both internally and externally.

In general, the requirements of turbine blade include high temperature creep strength, thermal stability at high temperature, surface stability and fatigue resistance, etc. The material of modern turbine blades has been optimised with the increasing addition of refractory element contents. Improvements in high temperature properties of alloy are achieved by optimisation of oxidation and corrosion resistance which contains sufficient amount of chromium and aluminium contents to form self-protective oxide scale.

## **2.2 Nickel-base superalloys for turbine blade application**

The selection of high temperature materials in aviation industry application is critical. In past several decades, superalloys met the demands arising from operating temperature and economical efficiency. A comprehensive review on Ni-base superalloys and their applications has been described by Reed [3].

Nickel acts as a matrix metal in superalloys and becomes the optimum base material in high temperature applications, because it provides a series of important properties as follows:

- High melting point (1728K) and reasonable density (8.907 g/cm<sup>3</sup>)
- Face centred cubic (FCC) structure without any phase transformations in the solid state
- A ductile FCC matrix, which is highly alloyed in both solid solution and strengthening precipitates
- Good solubility for secondary elements via direct solid-solution strengthening or indirect precipitate strengthening
- A low propensity for TCP-phase formation as third electron shell of Ni is almost filled.
- A low coefficient of thermal expansion and high thermal conductivity
- Slow diffusion rates of alloy elements offer enhanced creep performance at high temperature
- Exceptional environment resistance to oxidation and hot corrosion when combined with Cr and Al addition.

### ***2.2.1 Alloying elements***

The development of Ni-base superalloys in past decades has results in complicated alloy compositions consisting of up to 14 different elements in order to satisfy the mandatory alloy properties in applications. The compositions of a series of superalloys in commercial use are displayed in Table 2.1.



Table 2.1 Chemical composition (wt.%) from conventional cast alloys to the 4<sup>th</sup> generation SX superalloys

	Alloy	Cr	Co	Mo	W	Ta	Re	Nb	Al	Ti	Hf	C	B	Ru
Conventional Cast Alloys	Mar-M246	8.3	10.0	0.7	10.0	3.0			5.5	1.0	1.5	0.14	0.02	
	IN 100	10.0	15.0	3.0					5.5	4.7		0.18	0.01	
	Rene 80	14.0	9.5	4.0	4.0				3.0	5.0		0.17	0.02	
Directionally Solidified Alloys	IN 792	12.6	9.0	1.9	4.3	4.3			3.4	4.0	1.0	0.09	0.02	
	GTD 111	14.0	9.5	1.5	3.8	2.8			3.0	4.9		0.10	0.01	
1st generation SX Alloys	PWA 1480	10.0	5.0		4.0	12			5.0	1.5				
	Rene N4	9.8	7.5	1.5	6.0	4.8		0.5	4.2	3.5	0.15	0.05		
	CMSX-3	8.0	5.0	0.6	8.0	6.0			5.6	1.0	0.1			
2nd generation SX Alloys	PWA 1484	5.5	10.0	2.0	6.0	9.0	3.0		5.6		0.1			
	Rene N5	7.0	7.5	1.5	5.0	6.5	3.0		6.2		0.15	0.05		
	CMSX-4	6.5	9.0	0.6	6.0	6.5	3.0		5.6		0.1			
3rd generation SX Alloys	Rene N6	4.2	12.5	1.4	6.0	7.2	5.4		5.8		0.15	0.05		
	CMSX-10	2.0	3.0	0.4	5.0	8.0	6.0	0.1	5.7	0.2	0.03			
	TMS 75	3.0	12.0	2.0	5.0	6.0	5.0		6.0		0.1			
	RR2100	2.5	12		9.0	5.5	6.4		6.0		0.15			
4th generation SX Alloys	TMS 138	2.9	5.8	2.9	5.9	5.6	4.9		5.9		0.1			2.0
	RR2101	2.5	12		9.0	5.5	6.4		6.0		0.15			2.0

The effects of individual elements on alloy performance are summarised below [3-5, 13]:

Nickel (Ni): the major composition in Ni-base superalloys and acts as FCC matrix stabilizer.

FCC crystal matrix of Ni provides  $\gamma/\gamma'$  microstructure when the other elements are added.

Aluminium (Al): the principle element to generate the  $\gamma'$  phase (principal strengthening precipitates) and develops oxidation resistance of alloys, with the formation of a stable  $\text{Al}_2\text{O}_3$  alumina surface scale, to protect the alloy against further oxidation and corrosion.

Chromium (Cr): acts as a solid solution strengthening element within  $\gamma$  phase. It also plays a vital role in the hot corrosion and oxidation resistance of Ni-base superalloys as an adherent protective scale of  $\text{Cr}_2\text{O}_3$  layer is formed on the surface. Optimum oxidation resistance in Ni-Cr alloys was reported with Cr contents from 15 to 30% [4]. However, Cr content has been significantly reduced in recent generations of superalloys due to susceptibility of the formation of topologically close-packed brittle phase (TCP), which is likely to affect microstructure stability of alloys at high temperature. Other refractory elements are extensively applied as replacement of Cr in recent years.

Cobalt (Co): contributes to the strength by ordering  $\gamma'$  phase particles and distributed homogeneously in the  $\gamma$  matrix. Co has high solubility in nickel. It reduces the stacking fault energy of  $\gamma$  matrix improving creep resistance. High level of Co is beneficial to prevent the alloy from the formation of TCP precipitates and secondary reaction zone (SRZ) [14]. However, it was found that Co affects TBC compatibility and lowers the  $\gamma'$  solvus [15].

Molybdenum (Mo): is a potent solid solution strengthening element for  $\gamma/\gamma'$  phases. Additional of Mo is likely to form TCP phase. On the other hand, it has a negative influence on creep life of SX superalloys due to disruption of the continuous and uniform  $\gamma/\gamma'$  lamellae [16]. Therefore, content of Mo must be controlled.

Tungsten (W): an excellent solid solution strengthening element to improve high temperature capability. An excessive amount of W is likely to segregate strongly in the

$\gamma$  dendrites and increase the potential for TCP phase formation, nucleation and growth of grain defects. Hence, the percentage of W is strictly determined in metallurgy process.

Rhenium (Re): improves considerably high temperature capability, hot corrosion and oxidation resistance at the expense of density and microstructure stability. Re has exceptionally slow diffusivity in  $\gamma$  matrix [17] and preferential partitioning to  $\gamma$  phase, resulting in its high concentration in  $\gamma$  phase. Re played a key role in the evolution of SX superalloys.

Tantalum (Ta): a refractory metal element, which strengthens the  $\gamma'$  precipitates, particularly high-temperature strength. Ta segregates to the interdendritic region so can decrease the density inversions that will cause the nucleation of spurious grains. Ta is also beneficial for castability due to suppression on freckle defects.

Titanium (Ti): commonly applied as the  $\gamma'$  precipitates strengthener by substituting for Al in  $\gamma'$ , particularly increasing high-temperature strength. However, high levels of Ti are prone to form brittle TCP phase precipitation. The recent generation of superalloys has minor content due to its detrimental effect on oxidation resistance and thermal barrier coating (TBC).

Ruthenium (Ru): increases the stability of alloy structure and increases the strength. It suppresses the formation of TCP phase and affords the high level of strength in recent researches.

Carbon (C): improves castability of alloys due to reduction the oxides and it is also a grain boundary strengthening element. However, the carbon is no longer used in SX superalloys because it lowers the  $\gamma$  solvus and restricts the heat-treatment window.

Hafnium (Hf): contributes to alloys coatability and oxidation resistance. It prevents directionally solidified casting from cracking upon cooling. Hf also acts as grain boundary strengthener that improves creep strength, stress rupture and ductility of Ni-base superalloys [18, 19].

Yttrium (Y): improves the adherence of the  $\text{Al}_2\text{O}_3$  protective layer formed at high temperature.

Boron, zirconium, cerium, magnesium have all been used as grain boundary strengtheners to improve stress rupture. But former two elements may lower the incipient melting point of alloys.

### ***2.2.2 Chemistry development in single crystal Ni-base superalloys***

The development of Ni-base superalloys over decades is promoted by improving the thermodynamic efficiency of gas turbines in industries. For an increase of their operating temperatures, principal requirements for material used in hot sections of gas turbine are i) high melting point, ii) good oxidation resistance, iii) high temperature strength, iv) microstructural stability at high temperatures, v) low density, vi) high stiffness, vii) good fabricability, viii) acceptable cost, and ix) reproducible performance [20, 21].

The alloying elements involve a dramatic development in recent generations of SX superalloys. The first generation SX superalloys primarily used Cr, Co, Mo, W, Al, Ti and Ta with occasional addition of Nb or V. There are a high volume fraction of ordered  $\text{Ni}_3\text{Al}$   $\gamma'$  phase precipitated in the  $\gamma$  matrix providing decent strength of alloys. The first generation SX superalloys were developed as improved creep strength and thermo-mechanical fatigue with a proper balance of alloy elements [22]. The homogeneous microstructure is achieved after heat treatment eliminating almost all  $\gamma/\gamma'$  eutectic and solutioning secondary  $\gamma$  precipitates.

The Re-containing Ni-base alloys are classified as second generation of SX superalloys that improves creep strength with introduction of Re. Properties of this generation was achieved by strengthening effect of Re which reduces the  $\gamma'$  coarsening rate and leads to large negative  $\gamma/\gamma'$  misfit [23]. There are also some studies showing strengthening of  $\gamma'$  phase where about 20% of Re partitioning to  $\gamma'$  [24]. It is shown that 3 wt% Re in SX superalloys improves temperature capability of about 30 °C [25-27]. However, additional of Re was accompanied by formation of brittle TCP phases during heat treatment or service. Chemistry balance of Re-containing superalloys require careful assessment, as excess levels of Cr, Co, Mo and W will lead to supersaturation of solid solution which is associated with precipitation of Re-rich TCP phase particles. Thus, typical Cr addition in second generation Ni-base superalloys was designed as 5-7 wt%.

The third generation of SX superalloys was proceeded with an increase of Re content up to 6 wt% [28, 29]. Despite the merit of creep strength improvement in superalloys, the increase of the density and likelihood of TCP formation remain as the major challenge for third generation of SX superalloys. Due to Re preferentially partitioning to  $\gamma$  matrix, Cr content has been reduced to 2 – 4.2 wt% to avoid supersaturation of matrix and formation of TCP phases. Additions of Ru or Ir contained in third generation SX superalloys suppress the formation of TCP phases, which is benefit to partitioning ratios of elements between  $\gamma$  and  $\gamma'$  phase. With reducing the concentration of Re in  $\gamma$  matrix, it is less prone to precipitate as Re-rich TCP phases.

### ***2.2.3 Phases and microstructures of single crystal Ni-base superalloys***

The unique characteristics of Ni-base superalloys derive from the mechanical behaviour of  $\gamma'$  particles and crystallographic coherence between  $\gamma$  and  $\gamma'$  phases. The primary structure of Ni-base superalloys consists of intermetallic  $\text{Ni}_3\text{Al}$  phase ( $\gamma'$ ) embedded with  $\gamma$  phase (a FCC

Ni matrix phase). The total volume fraction and size distribution of  $\gamma'$  are determined by composition of alloy and processing, which has critical influence on its strength. The SEM image of microstructure for SX superalloys is shown in Fig. 2.3.

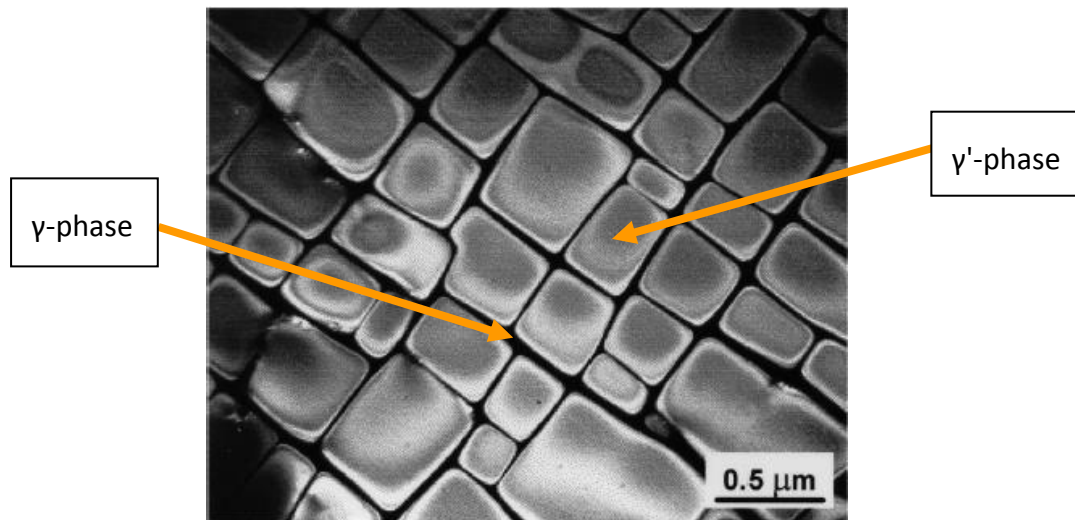


Fig. 2.3 SEM image of microstructure of Ni-base SX superalloys [30] showing large cuboidal particles  $\gamma'$  enclosed with  $\gamma$  phase

The  $\gamma$  matrix has an austenitic face-centred cubic (FCC) structure, where Ni and Al are disordered with respect to lattice sites. The FCC system consists of 12 slip systems, including 4 independent non-parallel  $\{111\}$  planes, and 3 independent  $\langle 110 \rangle$  directions in each plane, and the main slip vector in FCC lattice is the  $a/2\langle 110 \rangle$  Burgers vector [31]. The matrix is prone to deform at an increase of temperature due to dislocation on slip plane by climbing (i.e. dislocation creep).

The secondary  $\gamma'$  phase, also referred as  $L_{12}$  structure [32], is an ordered cubic precipitates that normally contains volume fraction at 70 - 80% in modern SX superalloys. Ni atoms are located at the face centres while the Al or Ti atoms position at the corners, as showed in Fig. 2.4. The  $\gamma'$  phase is coherent in  $\gamma$  matrix due to their similar lattice parameters (less than 1%). The morphology of  $\gamma'$  phase is depending upon lattice misfit, precipitate elastic modulus and

temperature. Precipitation hardening of  $\gamma'$  phase was systematically documented by Nembach and Neite [33].

The combination of  $\gamma$  and  $\gamma'$  phases contributes to the excellent material strength and creep resistance of Ni-base superalloys since the dislocation of  $\gamma'$  phase related to the  $\gamma$  matrix is in pairs of  $a/2\langle 110 \rangle$  dislocations, which removes the undesired anti-phase boundary (APB) and strengthens  $\gamma'$  particles.

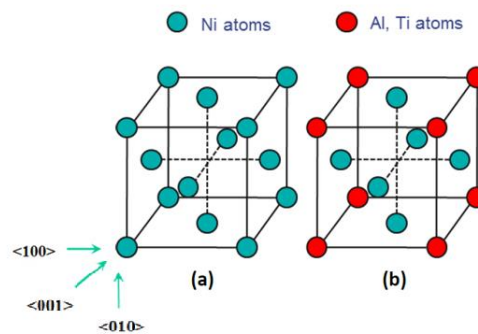


Fig. 2.4 The crystal structure of (a) FCC  $\gamma$  phase, and (b) ordered  $\text{Ni}_3\text{Al}$   $\gamma'$  phase [34]

#### **2.2.4 Topologically close-packed phases in Ni-base superalloys**

The compositions of modern SX superalloys contain 10 to 15 elements for improvement on creep resistance and solid solution strength. As a high level of refractory elements added in SX superalloys, it is susceptible to form TCP phases during heat treatment or when in service due to low solubility in the matrix. This type of instability depletes the matrix from the solution strengthening refractory elements and acts as crack initiation sites [35, 36]. Eventually, the formed TCP phases are attributed to degradation in mechanical properties of superalloys. Typical microstructure of TCP phases form in Ni-base superalloys is shown in Fig. 2.5.

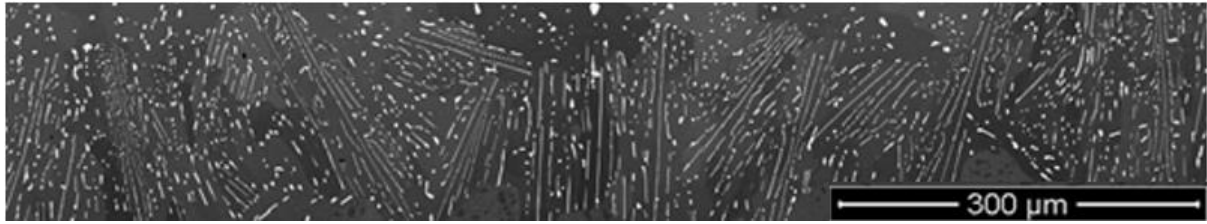


Fig. 2.5 Microstructure of TCP phases in CMSX-10N superalloys

TCP phases consist of close-packed layers of relatively small atoms, such as Ni, Cr, separated by larger atoms, such as Re, W, Ta. The most common TCP phases are  $\sigma$ ,  $\mu$ , P and R with key characteristics listed in Table 2.2.

Table 2.2 Crystallography of TCP phases [35]

TCP Phase	System	Space Group	Atoms per Unit Cell	Lattice Parameter	$\alpha$
$\sigma$	Tetragonal	136	30	$a=b=0.878\text{nm}$ , $c=4.454\text{nm}$	$90^\circ$
P	Orthorhombic	62	56	$a=1.698\text{nm}$ , $b=0.475\text{nm}$ , $c=0.907\text{nm}$	$90^\circ$
$\mu$	Rhombohedral	166	13 (hex. 39)	$a=b=c=0.904\text{nm}$ $a=b=0.904\text{nm}$ , $c=2.583\text{nm}$	$30.5^\circ$ $120^\circ$
R	Rhombohedral	148	53 (hex. 159)	$a=b=0.904\text{nm}$	$120^\circ$

In general, the close-packed layer have a high degree of coherency with  $\{111\}$  planes of  $\gamma$  and  $\gamma'$  phases, therefore it forms as plate-like morphologies parallel to four  $\{111\}$  FCC planes, which observed as needle-like microstructure in Fig. 2.5. The formation of TCP phase needs to be suppressed as depletion of strengthening elements from the matrix is detrimental to mechanical properties of superalloys.



## **2.3 Processing of single crystal alloys**

### ***2.3.1 Investment casting process***

The development of superalloys also relies on processing, which dramatically improves the performance of new alloys. The first superalloys appeared in the 1940s with application of investment casting for production of turbine blades. In 1950s, the vacuum induction casting technologies was introduced to improve the quality and cleanliness of the alloys. The further improvement was carrying out by the invention of directional solidification process (DS) which eliminates the transverse grain boundaries (around 1970s). The SX superalloys were produced base on DS process, to remove the grain boundaries completely. Hence, the fatigue life and melting point of superalloys have been improved significantly in order to satisfy the modern requirement for turbine blades [3]. The microstructure of casting turbine blades are illustrated in Fig. 2.6, showing as conventionally cast (equiaxed), directionally solidified (DS) and single crystal (SX) blades, respectively.

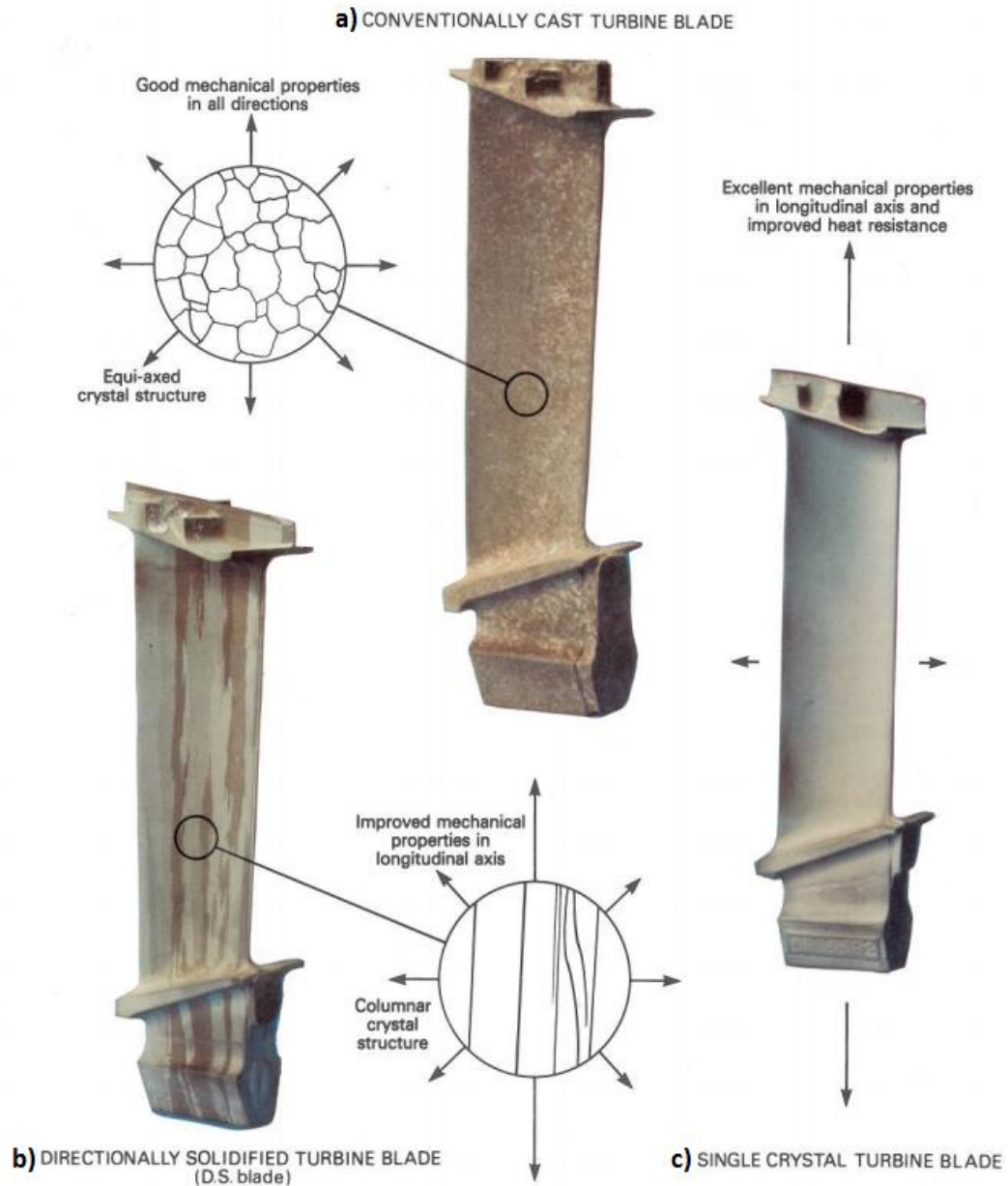


Fig. 2.6 (a) Conventionally cast, (b) Directionally solidified, (c) Single crystal turbine blades[2]

The production of DS and SX components are complex due to relatively longer and elaborated casting process. The procedure applied in current casting is also called Lost-Wax Process which is depicted in Fig. 2.7.

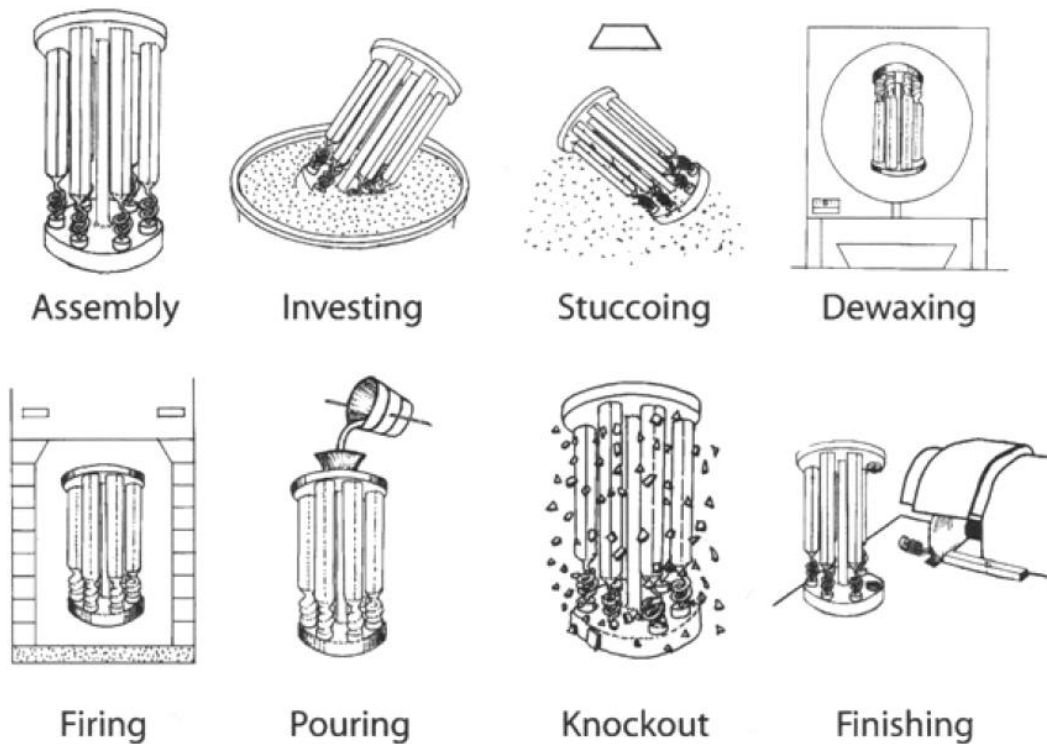


Fig. 2.7 Main processes of investment casting [37]

Wax pattern of casting component is produced from a metal die with molten wax injection, which has three critical parameters, including wax temperature, injection pressure and injection flow rate, to satisfy the requirements of wax pattern production. Intricate hollows structure, such as cooling passages in turbine blades, is manufactured by using ceramic cores. Wax pattern is assembled in clusters to improve productivity in blade casting [38, 39].

Ceramic mould is constructed from wax pattern, and is produced by coating, stuccoing and hardening. The wax assemblies are dipped into a vat containing slurry mixtures of zircon, alumina and silica, followed by stuccoing with coarse particles of similar materials to prevent further runoff of the slurry and provide bonding between individual layers. The hardening is carried out by circulating air with controlled temperature humidity in drying at room temperature. The whole process is required to be repeated several times until the strength

and thickness of mould shell is sufficient to prevent mechanical shock caused by metal pouring.

The wax is then eliminated in industrial autoclaves in which the ceramic mould is fired to high temperature to enhance its strength and the ceramic shell should be fully dried before dewaxing. Then the ceramic mould is fired between 1143K (870°C) and 1368K (1095°C) to remove moisture, residual wax and sinter the ceramics. Therefore the mould has enough strength and completely prepared for casting. The liquid filling shell is used to examine integrity of mould and identify any cracks. Casting finishing has typical sequences of knockout, cut-off, cleaning, general grinding and finishing operations to remove remnant ceramic materials after investment casting [39].

### ***2.3.2 Single crystal casting***

SX casting is typically manufactured in a Bridgman furnace in a vacuum condition to prevent reaction between molten superalloys and furnace atmosphere. Directional solidification is achieved by combination of a spiral grain selector and a prefabricated seed at the bottom. The molten alloy is poured into the mould at temperature of approximately 1773K (higher than the liquidus). A water-cooled copper chill plate is allocated to the bottom of furnace where solidification initiates. The mould is withdrawn at slow rate that leads to nucleation and growth of columnar grains in the direction of withdrawal, attributing to improve creep properties. A grain selector is applied in SX casting resulting in an entire removal of transverse grain boundaries. In consequence of this technique, only one grain with preferred orientation is able to grow at the top of the grain selector and continues in the principal part of turbine blades [39-43]. Fig. 2.8 illustrates the general view of SX turbine blade during casting process.

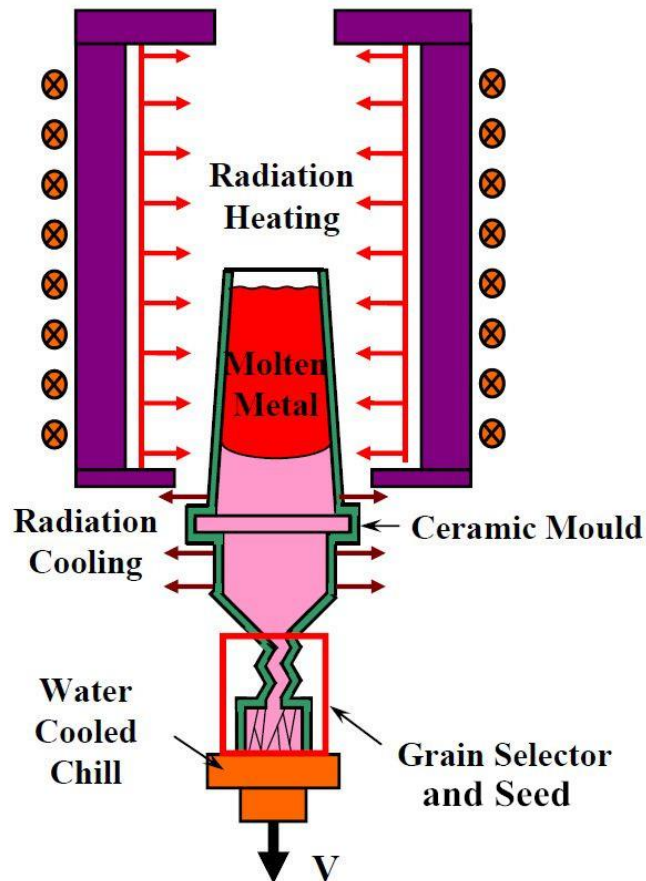


Fig. 2.8 Schematic diagram of investment casting for SX turbine blades [38]

### 2.3.3 Segregation during solidification of Nickel-base Superalloys

Microsegregation has a significant influence on superalloys material as it affects the performance of turbine blades. The typical method to reduce extent of microsegregation in as-cast microstructure is compositional design. Otherwise, optimisation of the casting conditions is required to minimise solute partitioning and remain segregation under a critical level.

Dendritic solidification in Ni-base superalloys is likely to cause segregation between the cores and interfaces of the dendrites, where non-uniform chemical distribution occurs due to the rejection of solute into liquid. Under such circumstance, the solid-liquid partitioning coefficients of alloying elements are more or less profound to severity level of segregation in

microstructures. When the solid grows, it riches in elements partitioning to the solid and rejects the solute into the liquid. Hence, this stage of solidification involves the solid dendrites and interdendritic liquid. As solid dendrites continue to grow, a localised compositional gradient is generated across the dendritic solidification, rejecting more elements into diffusive interdendritic liquid region. As a consequence, interdendritic phase formed between  $\gamma$  dendrites consists of a mixed microstructure of  $\gamma$  and  $\gamma'$  phases in last stage of solidification [44]. The interdendritic phase could results from a eutectic or peritectic + eutectic reaction.

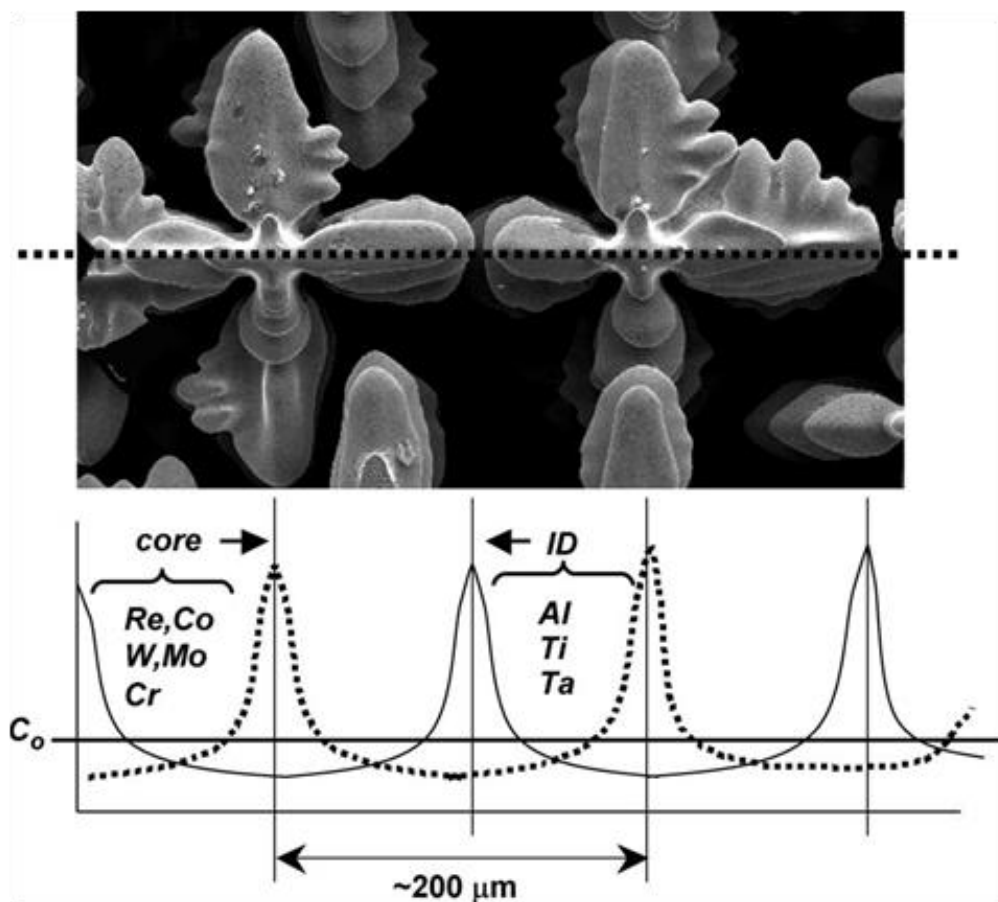


Fig. 2.9 Microsegregation pattern in as-cast SX superalloys showing segregated elements in the inter-dendritic and dendrite core regions [45]

Solute micro-segregation in Ni-base alloys has been studied revealing correlation with introduction of refractory elements, such as Re. As shown in Fig. 2.9, elements partitioning to

the solid are Re, W, Co and Cr and partitioning to liquid include Al, Ti and Ta [7, 45, 46]. It is also found that a number of elements influence the partitioning behaviour of other elements in cast microstructures. Hobbs reported that Cr and Mo reduce the degree to which Re and W partition to dendrites during solidification. Ru slightly partitions to dendrite core and reduces solid-liquid partition coefficient of Re [7]. The paper from Caldwell et al [47] concluded that Co reduces the level of segregation. Cr and Re increase the level of segregation. Mo and Ru addition have an effect on reduction of segregation of W, Re and Cr. In terms of segregation of Re in Ni-base SX superalloys, Heckl et al [48] has found that Re has the highest impact on microsegregation of Re itself as well as deterioration of segregation behaviour in other alloying elements.

#### **2.3.4 Solution heat treatment**

As-cast superalloys require applications of heat treatment to remove residual microsegregation and eutectic mixtures with enrichment of  $\gamma'$  in as-cast form, due to inhomogeneous  $\gamma'$  size and morphology caused by compositional micro-segregation after casting process [49, 50]. The microstructures at interdendritic region also contain  $\gamma/\gamma'$  interface with a range of size. To avoid incipient melting, heat treatment is performed at temperature approaching to the original solidification temperature of the alloy [51] which is called solutioning temperature.

Typical heat treatment processes applied for recent generations of Ni-base superalloys often consist of solution and ageing heat treatments [52, 53]. The former aims to homogenise the as-cast microstructure by refining  $\gamma/\gamma'$  eutectic phase at interdendritic region while the latter is to obtain optimized structure with a regular array of coherent, cuboidal  $\gamma'$  precipitates in optimum size [49, 54, 55]. Therefore, a distribution of fine  $\gamma'$  phase is grown on cooling and preceded during subsequent ageing steps.

Table 2.3 Typical solution heat treatment cycles for SX Ni-base superalloys

Alloy	W+Re+Mo+Ta (wt%)	Solution heat treatment
CMSX-3	14.6	1588K for 3h/Gas Furnace Quench (GFQ)
CMSX-4	16.4	1549K for 2h → 1560K for 2h → 1569K for 3h → 1577K for 3h → 1588K for 2h → 1594K for 2h → 1597K for 2h/GFQ
CMSX-10	20.7	1588K for 1h → 1602K for 2h → 1608K for 2h → 1613K for 2h → 1619 for 2h → 1625K for 3h → 1630 for 2h → 1633K for 5h → 1636K for 10h → 1638K for 15h /GFQ

In general, the process of heat treatment has been significantly incremental from few hours at 1588 K (1315 °C) for 1<sup>st</sup> generation SX superalloys to 45 hours solutioning up to 1638 K (1365 °C) for 3<sup>rd</sup> generation of CMSX-10. Typical commercial solution heat treatment cycles for three generations of Ni-base SX superalloys are listed in Table 2.3 presenting as an illustrative diagram in Fig. 2.10. It is showing a dramatic increase of temperature and time for solution heat treatment used in 3<sup>rd</sup> generation of SX superalloys.



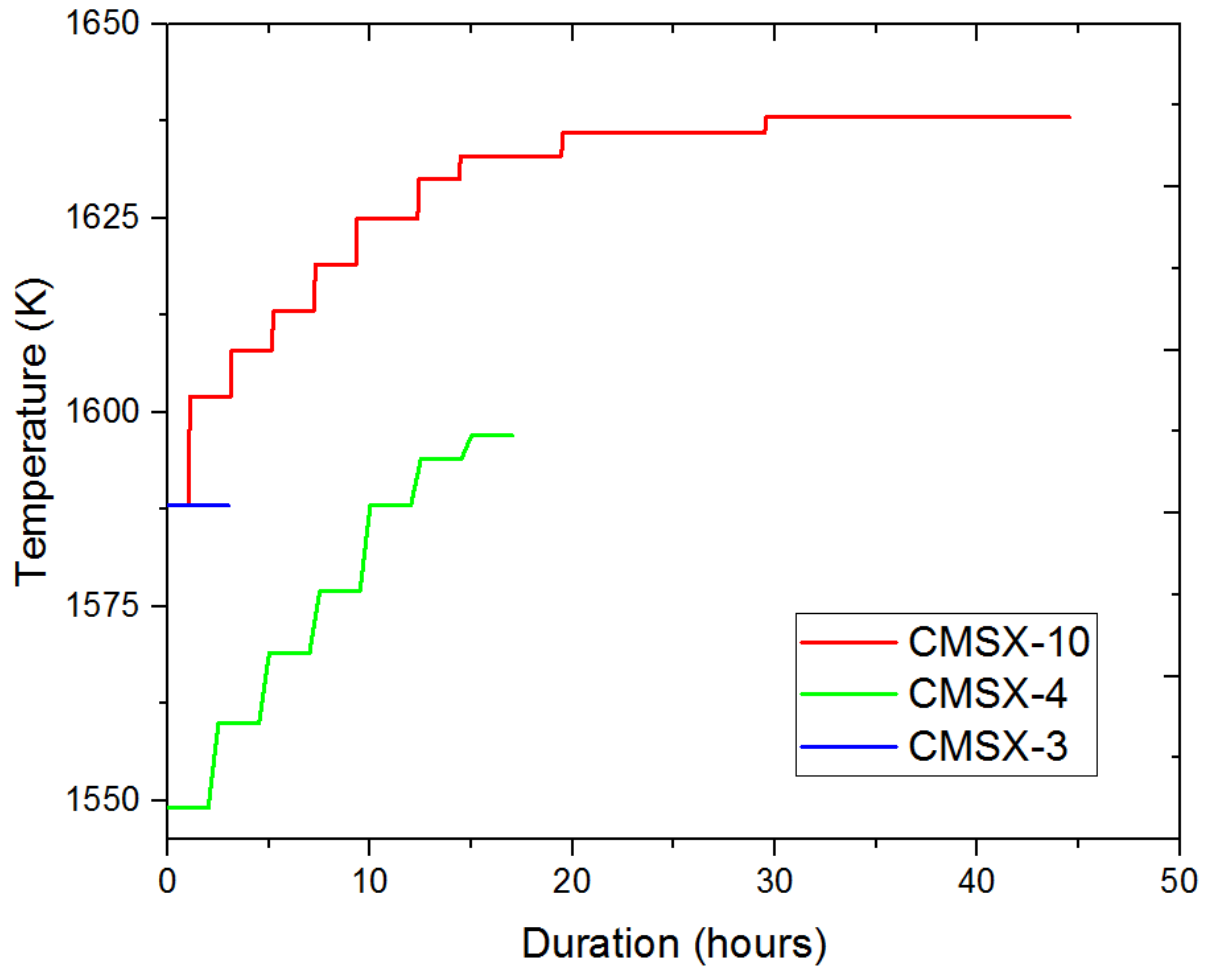


Fig. 2.10 Solution heat treatment cycles for SX Ni-base superalloys [49]

The heat treatment window, which refers to interval between the incipient melting temperature and the solvus temperature of the coarse interdendritic secondary precipitates [30], is critical for superalloys designation. The solution heat treatment is performed within the temperature range of this window that dissolves  $\gamma'$  phase into  $\gamma$  matrix solvus without incipient melting. Therefore there is a fine distribution of  $\gamma'$  precipitates to attain improved mechanical properties of production alloys after solutioning.

Diffusion rate in Ni matrix is accounted for in heat treatment process, particularly for the newer generation of superalloys that compose increased refractory elements (Mo+Re+Ta+W) which contribute to sluggish solute diffusion during solution heat treating and lead to more

highly segregated as-cast microstructures. The diffusivity diagram for elements in Ni illustrated in Fig. 2.11 shows a clear demand of increasing temperature and time in solution heat treatment.

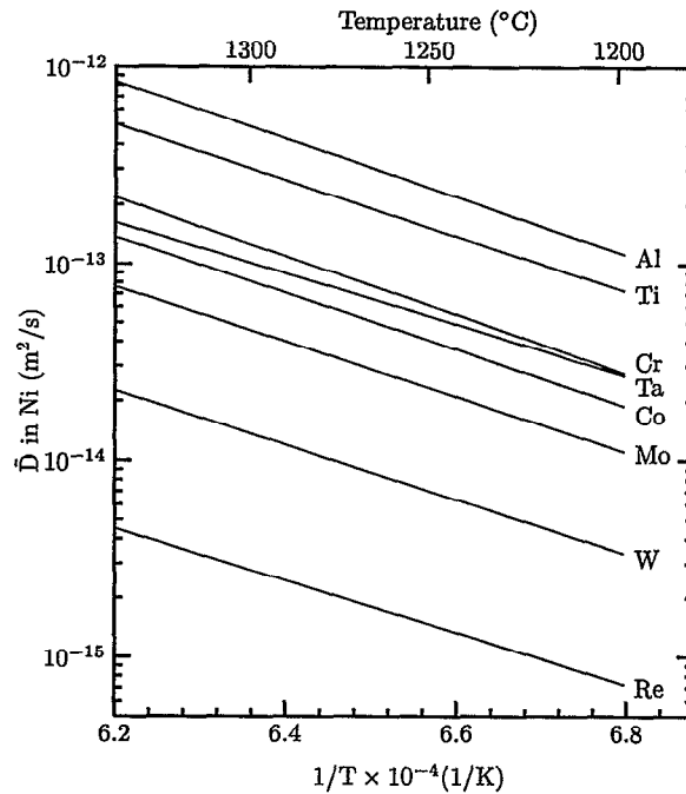


Fig. 2.11 Interdiffusion coefficient of alloying elements in pure Nickel [56]

Quenching of components with Argon gas is a typical method to complete solutioning process. The microstructure is often formed from homogenised  $\gamma'$  matrix and an irregular  $\gamma'$  precipitates during quenching. Therefore, subsequent ageing heat treatment is required to optimise  $\gamma'$  particles to enhance its mechanical properties.

For the purpose of minimising the cost and time of solutioning process, the temperature is desired to be as high as possible as the advantage of a lower time showing the same level of compositional homogeneity [57]. A quantitative characterisation of element segregation in

as-cast structure and the response of the as-cast microstructure to heat treatment are designed to optimise parameters of the solution heat treatment. The localised melting of inter-dendritic phases (IDPs) occurs when non-equilibrium solidus temperature is exceeded. Consequently, stepped ramps are applied to suppress this phenomenon by partially homogenising microstructure before the final solution temperature is reached.

To develop an efficient procedure for improving homogeneity of heavily alloyed SX superalloys after solutioning, the design of homogenization-solution heat treatments were proposed by Hedge et al [58, 59] presenting the effects of long isothermal holding at different solutioning temperature range. Recently, detailed analyse of solution heat treatment of SX Ni-base superalloys were carried out by H.T. Pang et al [55] alongside with an optimisation of heat treatment process. It showed that isothermal hold temperatures as well as length of holding time are influential factors on compositional homogeneity across the microstructure.

### ***2.3.5 Ageing heat treatment***

The ageing process is applied to achieve desired uniform  $\gamma/\gamma'$  microstructure, it consists of primary and secondary age after solution heat treatment, which holds the alloy at sub-solvus temperatures to refine  $\gamma'$  precipitates uniformly within the  $\gamma$  matrix. It is often using primary ageing at high temperature following by lower temperature secondary ageing steps [60]. The morphology of  $\gamma'$  precipitate is eventually obtained as a regular array of cuboids with a bimodal distribution of  $\gamma'$  phase in optimum size.

During primary age, the components are heat treated at temperature lower than solution heat treatment. Most of  $\gamma'$  precipitates grow and form a cuboidal  $\gamma'$  precipitate aligning with the (001) direction to minimise the elastic energy and maintain coherency at the  $\gamma/\gamma'$  interface in SX superalloys. The purpose of secondary age is to balance the  $\gamma$  and  $\gamma'$  in equilibrium at lower temperature and dissolve secondary  $\gamma'$  into the primary  $\gamma'$ .

There are two sorts of ageing process normally used in processing of Ni-base SX superalloys. The first one is called two steps ageing which initially heat treats alloy at 1413K (1140°C) for 6 hours followed by at 1143K (870°C) for 20 hours; the second method uses single step ageing at 950 °C for various time ranging from 100 to 2000 hours. The ageing used for CMSX-10 superalloys involves a primary age of 4 hours at 1413K (1140°C) followed by a secondary age of 16 hours at 1143K (870°C) [28].

### **3. Literature review on oxidation and surface defect formation during casting and heat treatment of single crystal nickel-base superalloys**

Casting of turbine blades in SX form is a challenging process to the foundry. Final products require a high level of quality, in this case, occurrence of defects, such as high-angle grain boundaries, are not tolerated. Chapter 3 reviews several types of defects formed during casting and heat treatment. And their relevant mechanisms of formation are also revised.

#### **3.1 Surface defects formation during casting and heat treatment**

Casting defects on the surface of SX superalloys has drawn more attention recently. There are various types of casting defects reported in Ni-base superalloys. Occurrence of those defects requires further rework process or dispose of scrap components after casting. Additional work on this aspect has a negative influence on economical considerations as well as productivity of turbine blades. Hence, in order to develop an effective method for reduction/elimination of surface defects, considerable research has been carried out to understand the mechanism of defects formation. Common casting and processing defects in Ni-base superalloys are introduced in follow.

Freckles are detrimental grain defects that occur during direction solidification. It is caused by thermos-solutal convection as there is difference in density of solute and bulk liquid leading to high rejection rate. As the consequence of increasing content of refractory elements in new generations of SX superalloys, severe segregation exacerbates convective instabilities at the solidification form that induced the formation of freckle defects [61, 62]. Freckles formed in solidified alloys influence their mechanical properties because the individual grains in a freckle chain are misoriented with respect to the <001> direction, as well

as differing the local composition as low melting eutectic, therefore these regions reduce the creep strength of the component at high temperatures [63].

Hot Tearing or known as hot cracking, is common type of casting defect during solidification of alloys. It occurs due to lack of liquid feeding during the final stage of solidification, which is difficulty of bridging or coalescence of dendrite arms. Detailed review of hot tearing and relevant criteria have been comprehensively reviewed by Eskin et al [64]. In scenario of casting Ni-base superalloys, the chemical composition affect hot cracking in more complex manners.

Compositional effects on susceptibility of hot tearing formation have been studied with conspicuous significance during solidification of Ni-base superalloys. The effect of Ti and Ta contents on susceptibility of hot cracking in IN792 was reported by Zhang showing the influence of Ti/Ta ratio in castability that attributes to hot tearing formation [65]. Further investigation by Zhang and Singer showed that IN792 superalloys containing Zr and B contents are susceptible to hot tearing [66]. They also studied the propensity to form cracks during directional solidification declaring change in volume fraction of liquid on crack formation during solidification [67].

Re-crystallization (RX) is the appearance of grains with random orientation, which often occurs during heat treatment or long-term service of SX superalloys. To interpret the mechanisms of recrystallization, there are extensive studies covering the formation of RX in various aspects.

Porter and Ralph [68] reviewed RX on four wrought Ni-base superalloys focusing on the effect of  $\gamma'$  distribution in motion ahead of recrystallization grain. The RX front is characterised by high diffusivity and solubility in low  $\gamma'$  fraction alloys, which results in complete dissolution of

the  $\gamma'$  ahead of the RX front followed by re-precipitation. While there is discontinuous re-precipitation of  $\gamma'$  in high  $\gamma'$  fraction alloys that occurs  $\gamma$  phase at the RX front due to the front becoming supersaturated by the dissolved  $\gamma'$  solute.

The effect of heat treatment atmosphere on surface recrystallization in directional solidified superalloys was studied by Xie et al [69] showing larger RX depth for alloys heat treatment in air. Research in latest years is showing that plastic strain induced recrystallization of Ni-base superalloys during heat treatment [69-71]. RX has an impact on degradation of creep and fatigue properties which is not tolerated in casting SX form.

Phase instability in Ni-base alloy has been often observed during heat treatment process which aims to optimise the size of  $\gamma'$  precipitates and reduce the level of segregation in dendritic microstructure. However, high content of refractory elements in Ni-base alloys limits the effect of microstructure homogenisation during heat treatment, due to long diffusion distances and inherently low diffusivity of Re and W in  $\gamma$  phase. Those refractory elements are associated with the formation of detrimental phases, including discontinuous precipitation [72, 73] and TCP phases [35, 36]. Thus spoke, phase stability tends to be a critical factor under consideration on improving performance of produced alloy at elevated temperatures. Several articles studied phase stability of Ni-base superalloys in terms of alloying elements additions and long-term exposure showing promising results for future superalloys development [52, 74, 75].

### **3.2 Formation of surface scale and its mechanism**

Surface scale is one of common defects in SX casting. It is not systematically investigated until recent years. The surface scale is associated with an oxide film formed during last stage of direction solidification of Ni-base superalloys. Its typical appearance shows as a fish-scale

layer of transient oxide,  $\text{Ni}(\text{Ti, Cr})\text{O}_x$ , with an area of discolouration. The rest of the blade is referred as “unscaled region”. Surface scale normally forms on the upper portion of the turbine blade, when the shell is removed. The mechanism for the formation of surface scale was proposed by Dong [76] as illustrated in Fig. 3.1.

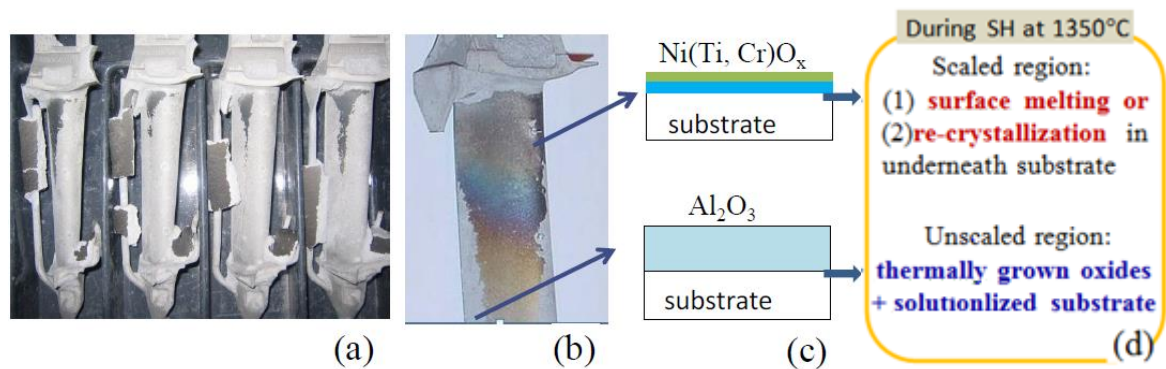


Fig. 3.1 (a) As-cast SX blades showing the location of surface scale; (b) enlarged view of the scaled region on a blade, (c) different phases on scaled and un-scaled region; (d) defects in scaled region and solutionlised substrate in un-scaled region during solution heat treatment. [76]

Solution heat treatment is a standard process applied for microstructural homogenisation of as-cast SX turbine blades. However, formation of transient oxides in scaled region replaced the protective  $\text{Al}_2\text{O}_3$  layer on the blade surface after solidification at temperature about 1373K (1100 °C). The scale region is associated with formation of defects during solution heat treatment including surface melting (changes in shape of airfoil) at 1623 K (1350 °C) and RX under the scaled area. Occurrence of surface scale results in mechanical degradation of turbine blades due to difficulties for inspecting spurious grain nucleation and microstructure instabilities under the surface of alloys. Therefore, it is acknowledged that the most effective method is to design a new pre-oxidation heat treatment forming a protective layer of  $\text{Al}_2\text{O}_3$  scale under a controlled process in the scaled surface [76, 77].



The formation of surface scale has been systematically discussed in a joint study by University of Leicester and Rolls-Royce [44, 77-81]. It is revealed that surface scale is a consequence of the mould and metal reaction in scaled region where prolonged contact with the mould was not adhered for an appreciable amount of time. Hence, mould separation occurs. The model for formation of surface scale was optimised by Simmonds as illustrated in Fig.3.2. Key stages of its formation is discussed as follow:

At the initial stage of casting after pouring, the liquid metal is in intimate contact with the mould face-coat over intact surface of the casting. The mould prime coat consists of  $\text{SiO}_2$  which is reduced by a mould-metal reaction of Al in the liquid. As a result, the formation of the  $\text{Al}_2\text{O}_3$  layer in around  $2\mu\text{m}$  thickness on the surface of casting while the amount of Si is dissolved in the liquid. The separation of metal from the mould occurs at upper sections of casting when cooling temperature is below solidus, due to differential thermal contraction. The upper, convex portion of casting eventually becomes the scaled area. The mould-metal separation is also acting as the driving force to strip  $\text{Al}_2\text{O}_3$  layer from the scaled region, where expose a “bare” surface to furnace atmosphere. The surface scale is subsequently formed by transient oxidation, consists of multi-layered oxide scale, as the casting maintains in cooling. The composition and thickness of surface scale depends on alloy composition and oxygen partial pressure/temperature within the furnace. When the mould is separated, there are small amount of remnant mould face-coat and original  $\text{Al}_2\text{O}_3$  layer retained on the unscaled region while the scaled region has no adhered mould material and exhibits a discolouration appearance [37, 77-79].

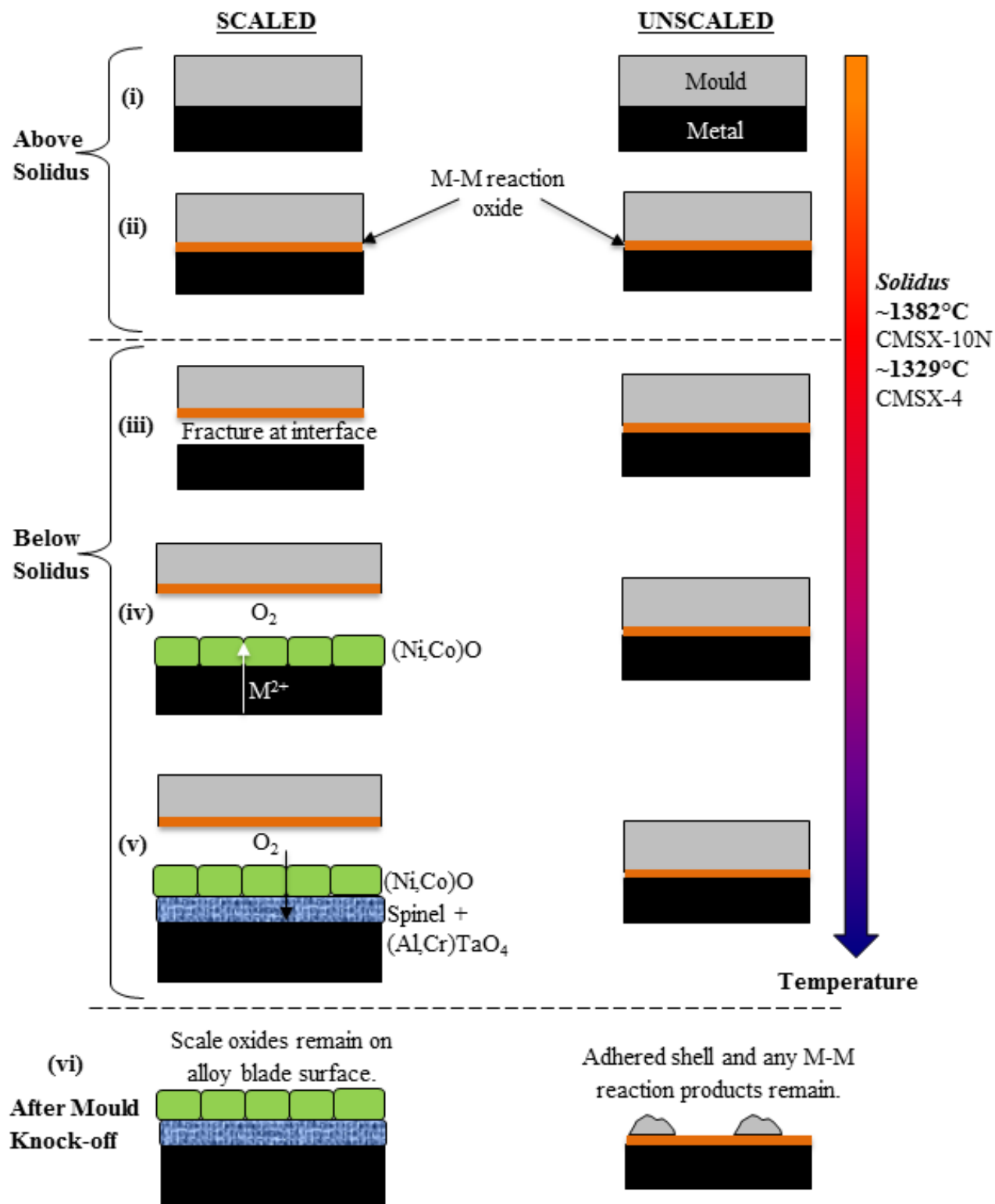


Fig. 3.2 Surface scale formation during casting of single-crystal gas turbine blades [77]

A new pre-oxidation heat treatment (OXITREAT) [37, 76, 77] was proposed to develop a method that remove or minimise the formation of the surface scale defects in SX casting. It was found that the formation of a protective layer of  $\text{Al}_2\text{O}_3$  in scaled surface is an effective way to suppress extent of casting defects in processing. However, high temperature oxidation is a sophisticated process due to 10 more compositions contained in SX Ni-base superalloys. Thermodynamic properties, such as activity of elements, in Ni-base superalloys are essential for assessment of high temperature oxidation. To simplify this problem, it was proposed to commence a fundamental research using Ni-Cr-Al model alloys to necessitate a quantitative assess of thermodynamic properties at high temperatures.

### **3.3 Elemental losses in Ni-base superalloys during solution heat treatment**

Elemental losses via evaporation/sublimation of Ni-base superalloys during solution heat treatment is a less known phenomenon in either literature or experimental studies. Although some pioneer work on elemental evaporation or sublimation of Ni-base alloys and stainless steel [82-85] has reported the effect of several elements in vaporisation/sublimation process, there is limited understanding of such phenomenon during solution heat treatment of Ni-base superalloys. In addition, compositions of those alloys studied in vaporisation experiments are essentially different with contents designed in modern commercial superalloys. Prediction of elemental losses during solution heat treatment of Ni-base superalloys relies purely on experience from alloying production and existing thermodynamic data using CALPHAD software. Therefore, in order to establish appropriate understanding of elemental loss in processing stage of superalloys, experiments aim to study thermodynamic properties of Ni-base alloys at high temperatures while relevant literature relating to sublimation in Ni-base alloys was reviewed.

More or less, the evaporation of Cr and its oxides during high temperature tends to be extensively researched [86-89]. The decomposition of  $\text{Cr}_2\text{O}_3$  at high temperature limits the formation of  $\text{Cr}_2\text{O}_3$  and degrades the oxidation resistance of substrate due to insufficient oxygen partial pressure, thus introducing the application of  $\text{Al}_2\text{O}_3$  forming superalloys at this temperature condition [34, 90].

Elemental vaporisation during solution heat treatment of superalloys was investigated by Simmonds who calculated evaporation rate of Ni, Cr and Co using Langmuir Equation [77]. By using vapour pressures from ThermoTech database, the composition of a surface layer with thickness of 20  $\mu\text{m}$  was calculated and modelled. The mass losses of 20-25% Ni, 14% Cr and 19-22% Co were determined under this circumstance. In conclusion, elemental vaporisation during solution heat treatment results in the transformation of the stable  $\gamma$  phase into  $\gamma'$  phase. Evaporative loss of  $\gamma$  phase stabilisers was identified as the cause of the melting blister defect formation and its associated microstructural instabilities in scaled region.

H. Wang et al [91, 92] reported effects of vaporisation and condensation on microstructural evolution at the surface of CMSX-10N superalloys during heat treatment. The extent of Ni and Al loss determines the final microstructure on the alloy surface. Back-scattered electron and EBSD images combined with ThermoCalc analysis have rationalised the effect of Al vaporisation, which is absent in modelling with Langmuir Law calculation. In addition, discontinuous precipitation on the surface of CMSX-10N superalloys was recently studied by Dean et al [93] further confirming the effect of Ni loss via vaporisation on  $\gamma$  phase dissolution and  $\gamma'$  phase stabilisation.

The existing understanding of elemental loss in Ni-base superalloys is based on observations of phase evaluation and simple calculations according to thermodynamic equations. In addition, their calculations were strongly dependent on reliability of database. On the other

hand, relevant experiments for determining vaporisation in Ni-base alloys are insufficient in literature. Despite recommended equations of vapour pressure given by Alcock et al [94], their method is based on data from existing publication during 1970s and 1980s [95-97]. Therefore, the re-assessment of thermodynamic properties for Ni, Al and Cr is essential. The remaining objective directs to determine thermodynamic properties in Ni-base alloys associating to evaluation of high-temperature behaviours.

In general, existing results revealed the effect of vaporisation on microstructural instability but not entirely interpreted the mechanism of elemental vaporisation during solution heat treatment of Ni-base superalloys. To solely examine interactions of Ni, Al and Cr in Ni-base alloys, Ni-Cr-Al ternary alloys were selected for investigating partial pressures and thermodynamic activities at high temperatures via KEMS method under solutioning condition.

### **3.4 Sublimation induced microstructural instability in Ni-base superalloys during solution heat treatment**

#### ***3.4.1 Discontinuous precipitation in SX Ni-base superalloys***

Discontinuous precipitation (DP) has been studied in numerous alloys system. As primary research from Scarlin [98], most DP reaction have been found with common features in terms of reaction kinetics and driving forces [99-102]. In DP reactions, the metastable parent microstructures is transformed with an abrupt change in composition and orientation in product phases. The reaction interface, commonly a grain boundary in polycrystalline material [103] or substrate beneath coating [6, 104, 105], initiates as a heterogeneous nucleation site and subsequently as a high-diffusivity mobile reaction front.

DP has been found in Ni-base superalloys with a high content of refractory elements referring to 2<sup>nd</sup> and 3<sup>rd</sup> generation of Ni-base superalloys. The reaction transforms the two-phase  $\gamma$ - $\gamma'$

parent microstructure into a three-phase cellular structure with a  $\gamma'$  matrix containing Re-rich TCP phases and agglomerated  $\gamma$  lamellae. Other study in SX Ni-base superalloys shows that DP occurs at the grain boundaries in high Re containing superalloys and is grain boundary diffusion controlled [48].

In binary system, DP initiates from the supersaturation of a matrix phase  $\alpha'$ , which converts into an equilibrium condition by the precipitation of a second phase:  $\alpha' \rightarrow \alpha + \beta$  [106]. Accordingly, the DP reaction in the two components'  $\gamma/\gamma'$  microstructure of Ni-base superalloys is summarised by Heckl et al [72] as following transformation:

$$(\gamma^{SS}_{\text{matrix}} + \gamma'_{\text{precipitates}}) = (\gamma'_{\text{matrix}} + \gamma_{\text{precipitates}}) + \text{TCP}$$

where  $\gamma^{SS}_{\text{matrix}}$  is supersaturated matrix. The supersaturation in this reaction is balanced by precipitation of TCP as the formation of a new phase. While the  $\gamma'$  precipitates form as new matrix after the discontinuous transformation with precipitation of  $\gamma$ . In Ni-base superalloys, the microstructure was observed as a transition of fine and ordered  $\gamma/\gamma'$  into a coarsened microstructure consisting of columnar  $\gamma$  and TCP phases. DP in SX Ni-base superalloys has pronounced impacts on performance of turbine blades. The presence of cellular colonies leads to a substantial reduction of creep resistance due to cracking along cell boundaries. The coarsening was reported to be detrimental to the mechanical properties [104].

Previous studies of surface defects on surface of Ni-base superalloys have been carried out at University of Leicester and Rolls-Royce showing evidence of elemental loss via sublimation on the surface of superalloys during solution heat treatment [77-81, 93]. The formation and phenomenological reasons were established and specifically discussed in many papers [78, 80, 92, 107]. It was concluded that the formation of discontinuous precipitation (DP) on the 3<sup>rd</sup> generation Ni-base superalloys, CMSX-10N is associated with vaporisation of elements with high partial pressure, such as Ni, Al and Cr. Vaporisation of certain elements from the alloy is characterised as formation of surface defect, leading to destabilisation of  $\gamma$  and  $\gamma'$

phase which is depleted in Ni and Al. With evidences from neutron diffraction technique and electrical microscopy, phenomenon of vaporisation on the surface area occurs at the high temperature and desired oxides, such as  $\alpha\text{-Al}_2\text{O}_3$ , are likely to prevent the alloy from the formation of surface defects. However, the mechanisms of vaporisation in Ni-base superalloys during solution heat treatment remains unknown. In addition, although microstructural evidence show that the formation of DP at the surface of Ni-base superalloys is induced by elemental vaporisation, there is no convincing results from thermodynamic aspect to accurately determine its effect at high temperatures. Hence, a systematic study will commence using Ni-Cr-Al ternary alloys to specifically consider effects of three elements with relative high vapour pressure at high temperature.

The following studies aim to determine thermodynamic activities in Ni-base alloys and study elemental sublimation of Ni-base alloy at high temperatures. Chemical compositions on the surface of alloy, which is associated with thermodynamic activities, are regarded as a crucial influence on phase stability of Ni-base alloys at high temperatures. Hence, in order to determine thermodynamic properties of alloying elements in Ni-base superalloys, the phenomenon of sublimation can be observed using Knudsen Effusion Mass Spectrometry (KEMS). Details of KEMS studies used in Ni-base alloys will be described in following paragraphs.

#### ***3.4.2 KEMS studies of thermodynamic properties in Ni-base system***

The first effusion method for determining vapour pressures was performed by Knudsen [108] dating back to 1909, he successfully measured vapour pressure of mercury under now called Knudsen method. With his well-known Knudsen equation (or Hertz-Knudsen equation), extrapolation of vapour pressure produced excellent agreement with results measured in other ways regarding as pioneer work for studying vaporisation of elements. Mass

spectrometry is a leading analytical method with advances that have shown the capability as the most powerful and versatile research technique for investigations of gas-solid or gas-liquid phases and their reactions at high temperatures [109-112]. Experimental data obtained by high temperatures mass spectrometry technique for individual compounds, gaseous or condensed phases, are incorporated in tabulations of dissociation energies, thermodynamic properties and of ionization potentials [96, 97, 113-115]. In general, combination of classical effusion technique and mass spectrometry were developed enabling studies of vaporisation among various materials under a reliable basis.

The mass spectrometric variant of Knudsen method, now known as Knudsen cell effusion mass spectrometry (KEMS) has been extensively used in studies of inorganic gas phase for characterisation of chemistry in high temperature vapour, since most of elements or inorganic phases sublime/evaporate at high temperature among various condensed phases in alloys. It is interest to identify the gaseous species and determine the concentration, as well as thermochemical properties, such as bond energies, which KEMS is capable of.

Typical Knudsen cell used for alloys is manufactured by the metal with high melting point and the structure of Knudsen cell used in this study is shown in Fig. 3.3. The working principle of KEMS method is based on a heated small enclosure which contains a condensed phase in equilibrium with a gas. A small orifice provides a means of measuring the vapour pressure. By counting number of ions formed from a molecular beam, partial pressures for elements contained in measured alloys are determined in high degree of accuracy in forthcoming results. Further details of KEMS method will be described in Chapter 6.

Nonetheless thermodynamics and high temperature vapours remain important in many fields, such as vapour deposited coatings, fuel cells, nuclear applications, geochemistry, and general high temperature materials. KEMS is the most versatile and reliable method for experimental



measurements of these important high temperature parameters. Hence, it is recommended that thermodynamic properties of elements in Ni-base alloys can be appropriately determined via KEMS method since there is insufficient KEMS data of Ni-base alloys at high temperatures prior to this PhD study.



Fig. 3.3 Ir Knudsen cell used in KEMS facilities at Forschungszentrum Jülich

It was successfully applying KEMS method to study vaporisation of Ni-Al and Fe-Ni-Al alloys for determining thermodynamic properties in those alloy systems by several researchers

[116-120]. Bencze et al [117] carried out experiments of evaluating chemical activities, partial enthalpies and entropies of Ni-Al alloys with acceptable accuracy. It is found that vaporisation of measured alloys in form of Ni(g) and Al(g) with no intermetallic vapour species. Arrhenius plot of logarithm of activity against reciprocal temperature depicts linearity for Ni and Al, which means partial enthalpies of formation are independent of temperature within measured range. The Gibbs-Duhem ion intensity ratio (GD-IIR) method [121] can be applied for consistency check with results from experiments which shows a good agreement in their research. Those works provide assessable method for investigating elemental vaporisation on the surface Ni-base superalloys at high temperatures. Good accuracy and sensitivity of KEMS has been proved its reliability in activity measurement directing experimental approach for fundamental study on Ni-Cr-Al model alloys. Further details of KEMS principles used in this study will be introduced in Chapter 6 from a serial of literature with well-illustrated diagrams.

### **3.5 High temperature oxidation during processing of Ni-base alloys**

Ni-base superalloys are widely used in high-temperature applications. Alloys exposed to aggressive environment at high temperatures rely on the formation of a dense and adherent oxide scale for surface protection in long-term service. Aggressive environment has prompted the development of oxidation and corrosion resistance coating since degradation of oxidation is a vital factor in determining the lifetimes of components.

Complexity of alloying chemistry in recent generations of Ni-base single-crystal turbine blades, such as CMSX-10, has been observed with formation of several defects in casting and processing. Those modern generations contain increasing contents of refractory elements including Mo, Re, Ta and W for improvement on creep strength. Meanwhile, introduction of high amount of refractory elements results in a significant reduction on Cr content due to chemistry balance. Hence, it has been reported that the oxidation resistance is likely to be

reduced due to alloying elements used. In order to establish an overview of surface behaviours in Ni-base superalloys, oxidation properties are evaluated to rationalise understanding of microstructural instability.

### **3.5.1 High temperature oxidation**

Oxidation is common reaction when metals are exposed to the environment with presence of oxygen. This phenomenon is likely to cause some detrimental effects on engineering products, including crystal defects, loss of mechanical properties, depletion of essential strengthening elements and void formation for Ni-base superalloys. Modern design of recent generations requires the formation of protective oxide layer on the surface of alloys to improve oxidation and corrosion resistance at high temperature applications. In practice, the oxidation undergoes a complicated process with presence of condensation from the vapour or impaction of particular matter. An important tool in the analysis of such problem is equilibrium thermodynamic which allows one to ascertain occurrence of potential reaction whether significant evaporation or condensation of a given species is possible.

It is a significant development on engineering the slow growing, stable and more protective oxide film at the surface of Ni-base superalloys in order to maximise lifetime of turbine blades and Thermal Barrier Coating (TBC) system. Therefore, the purpose of this section is to review thermodynamic concepts pertinent to gas-metal reaction linking to present understanding of high temperature oxidation in thermodynamics and kinetics consideration.

### **3.5.2 Thermodynamics of oxidation**

The oxidation of an alloying element M is defined by Equation 3.1 [122, 123]:



The driving force for reaction is proceeded by negative Gibbs free energy change from Equation 3.2:

$$\Delta G = \Delta G^0 + RT \ln \left( \frac{a_{MxOy}^{\frac{2}{y}}}{a_M^y a_{O_2}} \right) = \Delta G^0 - \ln(p_{O_2}) \quad \text{Equation 3.2}$$

where  $\Delta G$  is Gibbs free energy change for the reaction,  $\Delta G^0$  Gibbs free energy change at standard conditions,  $R$  is the molar gas constant,  $T$  is temperature,  $a$  is the activity of the species and  $p_{O_2}$  is partial pressure of oxygen. Therefore, the partial pressure of oxygen for oxide and metal in equilibrium can be derived as Equation 3.3 and 3.4.

$$\Delta G = 0 = \Delta G^0 - RT \ln(p_{O_2}) \quad \text{Equation 3.3}$$

$$\Delta G^0 = RT \ln(p_{O_2}) \quad \text{Equation 3.4}$$

The Gibbs free energy change of oxide formation

$$\Delta G^0 = \Delta H^0 - T \Delta S^0 \quad \text{Equation 3.5}$$

where  $\Delta H^0$  is the enthalpy change in standard conditions and  $\Delta S^0$  is the entropy change in standard conditions.

### **3.5.3 The Ellingham diagram**

The Ellingham Diagram is a useful method to represent oxides and a plot of  $\Delta G$  versus temperature where  $\Delta G$  is a measure of thermodynamic driving force when reaction occurs.

The diagram is based on calculation of thermodynamic driving force for a particular reaction to occur in a range of temperatures. The relative stabilities of different elements with respect to their oxides can also be found on the diagram, the most stable oxides sit at the lower down side of Ellingham Diagram, and the greater affinity of those metals has for oxygen [124].

Each line for an oxidation reaction is normalised for consumption of 1 mole of  $O_2$  with partial pressure of oxygen at 1 atmosphere. The majority of lines shows upward slopes because oxide are present as condensed phase for reaction between a condensed phase (the metal and oxidised compounds) and a gaseous phase (the oxidising gas), leading to a reduction in the reaction entropy.

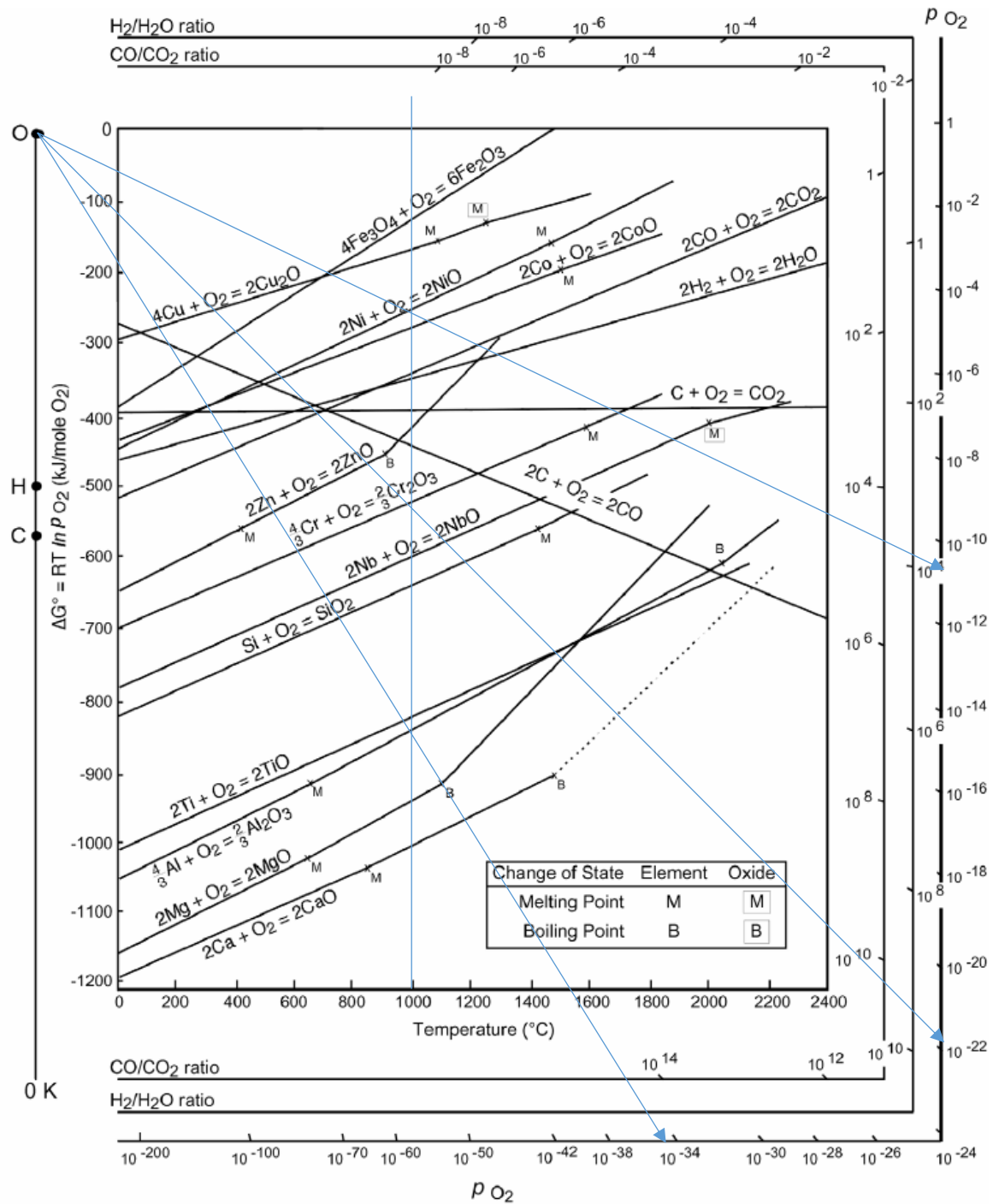


Fig. 3.4 Ellingham diagram [125]

The diagram is used to determine i) the order of oxides formation, ii) partial pressure of oxygen in equilibrium with a metal oxide and iii) ratio of CO/CO<sub>2</sub> which is able to reduce metallic oxide to pure metal.

Table 1 provides some data selected from the Ellingham diagram showing the propensity of different oxides to form at 1000°C. It is well acknowledge that alumina is the most stable and desirable oxide in engineering applications. As free energy change determines the direction in which a reaction proceeds.  $\text{Al}_2\text{O}_3$  has more negative free energy than  $\text{NiO}$ , so Al will oxidise preferentially than Ni in equilibrium. But the rate of oxidation is controlled by kinetic of process.

Table 3.1 Thermodynamic data from Ellingham diagram for oxidation of major elements in Ni-base superalloys at 1000°C

Metal	Oxide	Minimum $p_{\text{O}_2}$ required	$\Delta G^\circ$ (kJ/mol $\text{O}_2$ )
Al	$\text{Al}_2\text{O}_3$	$10^{-35}$	-850
Si	$\text{SiO}_2$	$10^{-26}$	-680
Cr	$\text{Cr}_2\text{O}_3$	$10^{-22}$	-550
Co	$\text{CoO}$	$10^{-12}$	-285
Ni	$\text{NiO}$	$10^{-11}$	-250

The equilibrium partial pressure of oxygen is the pressure at which the driving force for the reaction is zero. From equation 3.4 it states that if the partial pressure of oxygen is greater than this value, the free energy change for the reaction is negative and there is a driving force for the reaction to take place. Metal will be oxidised, and the partial pressure of oxygen will drop until it reaches equilibrium. If the partial pressure of oxygen is below the equilibrium value, oxidation is avoided. (In fact, the metal oxide will disassociate to form metal plus oxygen gas-this is because there is a driving force for the reaction to proceed backward.

### **3.5.4 Kinetics of oxidation**

Thermodynamic description of oxidation reaction only dedicates details of phase transformation versus temperature, partial pressure and thermodynamic activity if it can

occur. There is no indication of reaction rate in thermodynamics, as oxidation process depends on diffusivity of ions and electrons at interface of reaction. Hence, the kinetics shall be considered to determine occurrence of reaction in a sensible time frame as showed in Fig. 3.4.

Top part of diagram shows the Gibbs energy that is required for oxidation of Ni-Al alloy to proceed the reaction from initial to final state. While the hump of energy on the bottom diagram indicates the energy barrier to overcome at intermediate stage, which can be influenced by the formation of transient oxides, the diffusion of Al to reaction interface and transition of transient oxides to final  $\text{Al}_2\text{O}_3$  oxides etc. This energy barrier requires external energy input to advance to the final state and its magnitude is represented by the activation energy,  $\Delta G_{\text{active}}$ . In this case, thermal energy from external environment provides the activation energy to succeed oxidation process, increase of temperature would provide more thermal energy available to overcome the barrier leading to acceleration of oxidation growth [122, 123].

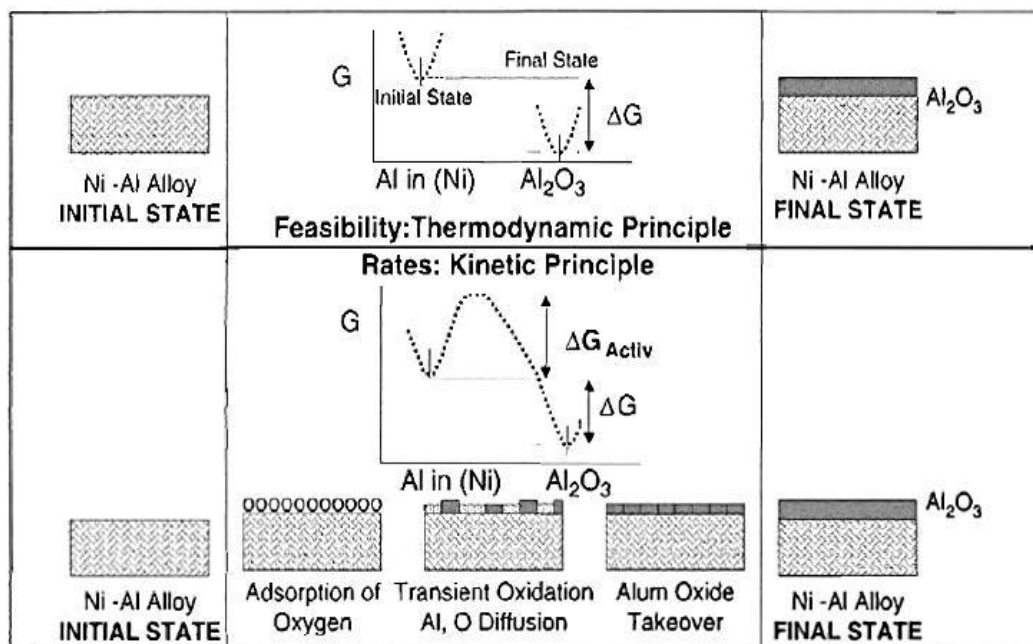




Fig. 3.5 The influence of thermodynamic and kinetic on oxidation of Ni-Al alloys [123]

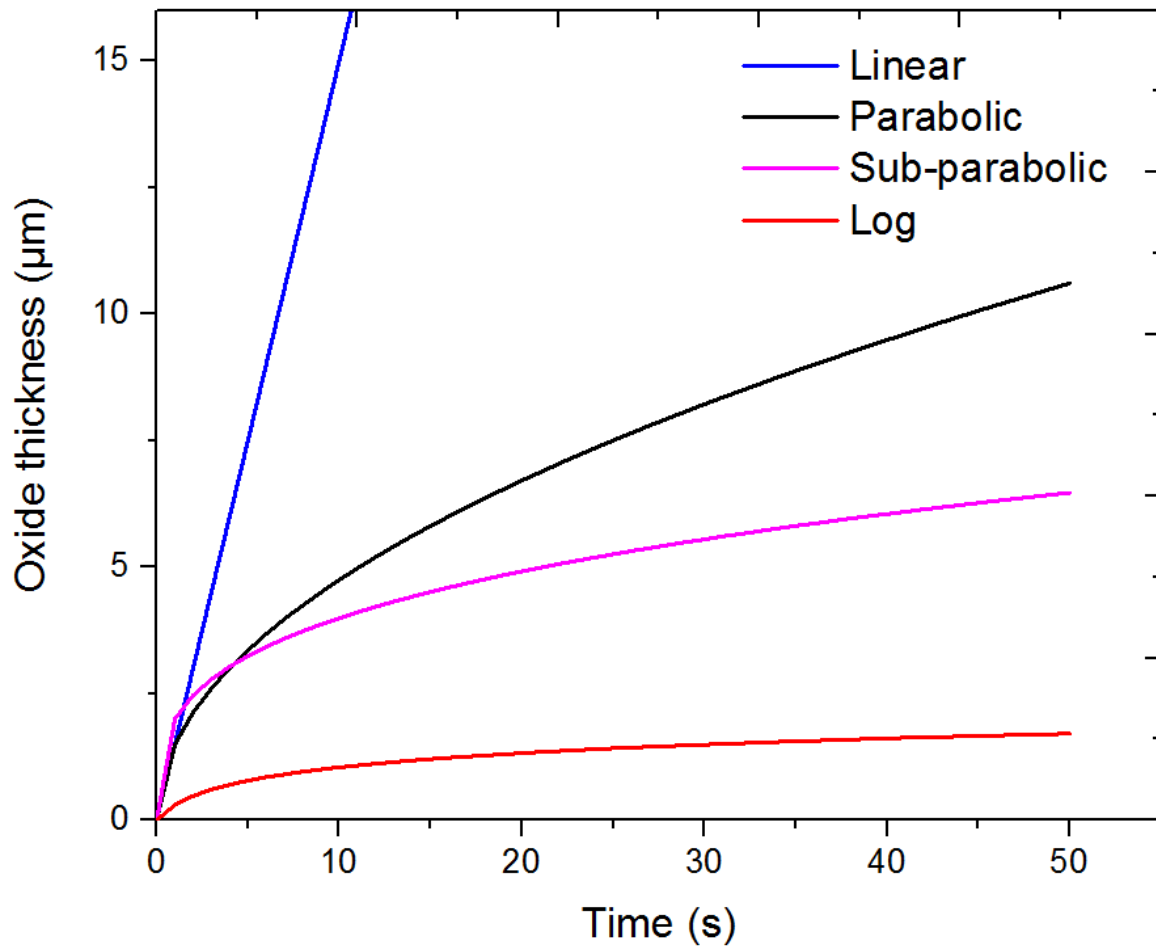


Fig. 3.6 Schematic diagram of linear, parabolic, sub-parabolic and logarithmic growth rates of oxides

The oxidation proceeds with a linear rate at initial stage, but subsequent growth follows one of four kinetic regimes when a continuous oxide film is formed for the majority of metals and alloys [122, 123]. Fig. 3.5 illustrates four kinetic regimes namely linear, parabolic, sub-parabolic and logarithmic growth. As oxidation proceeds through solid-state ionic diffusion, oxidation thickness is proportional to a certain coefficient of oxidation time,  $t$ , in each case. Parabolic and sub-parabolic growth kinetic are considered in most Ni-base superalloys studies,

and are commonly referred to Wagner's diffusion controlled parabolic oxidation law, which states that oxidation scale thickness ( $\xi$ ) is proportional to the square root of exposure time ( $t$ ) as Equation 3.6:

$$\xi^2 = K_p' t \quad \text{Equation 3.6}$$

where  $K_p'$  is parabolic scale constant which can be derived from Equation 3.7 and depends on activation Gibbs free energy  $\Delta G_{\text{active}}$ :

$$K_p' = K_0 \exp\left(\frac{\Delta G_{\text{active}}}{RT}\right) \quad \text{Equation 3.7}$$

Constant  $K_0$  is related to partial pressure of oxygen. The rate of oxidation is the rate at which the energy barrier is overcome as showed in Fig.3.5.

Whereas the sub-parabolic growth rate is determined by Equation 3.8 with a time exponent,  $1/m$ , of 0.3 in chromia growth [126]:

$$\xi = (K_p' t)^{1/m} \quad \text{Equation 3.8}$$

### **3.5.5 Oxidation mechanism of Ni-Cr-Al system**

Ni-Cr-Al system is the most significant and commonly used ternary system to study Ni-base superalloys. Earlier work on oxidation mechanism was carried out by Giggins and Pettit and it was concluded as three distinct groups on oxidation of Ni-Cr-Al system [127-129]. Fig. 3.6 represents formation of oxides on surface of ternary alloy at different stages, which is summarised as following processes:

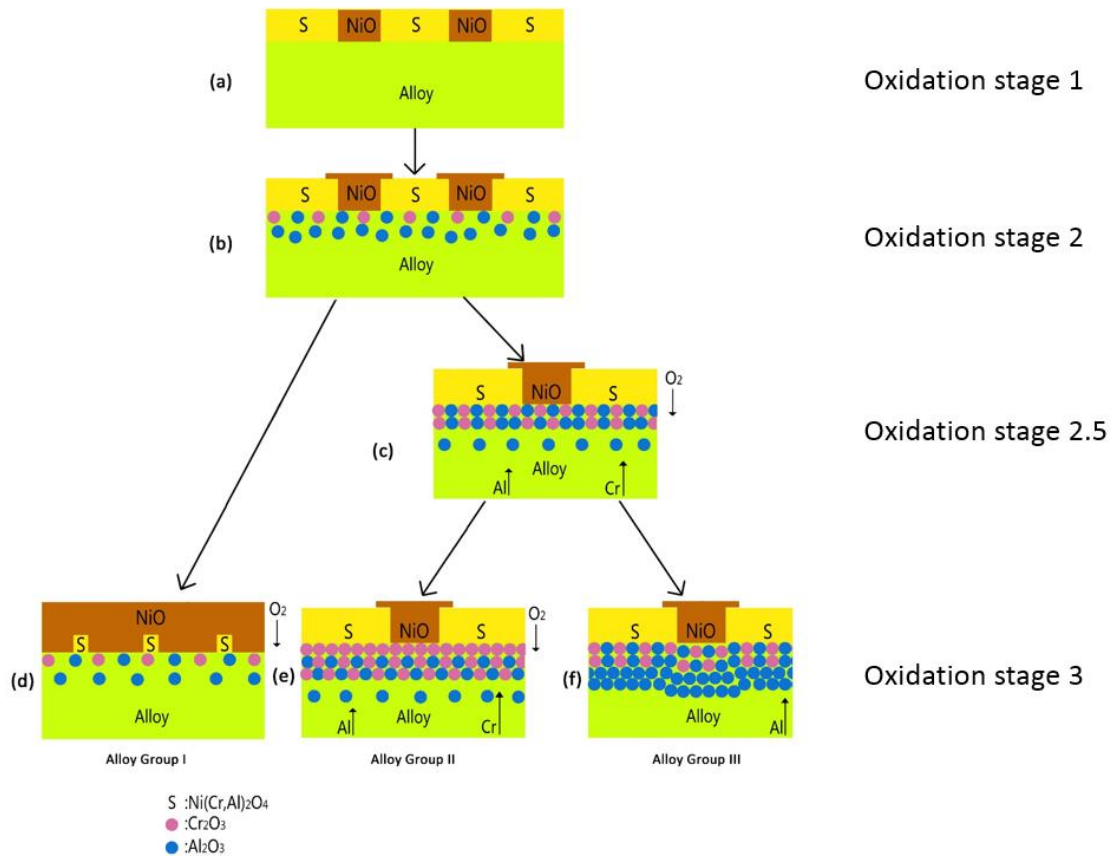


Fig. 3.7 Oxidation mechanism of Ni-Cr-Al system (reproduced after ref.[127])

Oxidation of any Ni-Cr-Al model alloys starts with conversion of surface layer to oxide due to rapid uptake of oxygen and little diffusion at this stage of reaction. Hence  $\text{Ni}(\text{Cr, Al})_2\text{O}_4$  and NiO predominant the surface layer and compositions is determined by alloy content.

As oxidation continues, diffusional process will affect reaction. Activity of oxygen required to oxidise chromium and aluminium is less than that of NiO and spinel, therefore oxygen moves into the alloy and forms  $\text{Cr}_2\text{O}_3$  and  $\text{Al}_2\text{O}_3$  precipitates beneath external NiO and spinel layers as showed in Fig. 3.6 (b). Meanwhile the activity of oxygen in aluminium oxidation is less than activity required to oxidise chromium, so particle  $\text{Al}_2\text{O}_3$  is precipitates further into the alloy.

If there is insufficient volume fraction of  $\text{Cr}_2\text{O}_3$  and  $\text{Al}_2\text{O}_3$  particles to restrict the movement of oxygen, leading to internal oxidation of chromium and aluminium in form of a

discontinuous subscale under the external layer. As fast growth of NiO layer suppresses growth of any other oxides and eventually it will completely envelopes the other phase. This case is classified as **Group I** as illustrated in Fig. 3.6 (c), the mechanism of oxidation is controlled by transport through NiO layer when a continuous NiO layer proceeds under steady-state condition.

A continuous layer of  $\text{Cr}_2\text{O}_3$  and  $\text{Al}_2\text{O}_3$  oxide will form under the external scale when there is sufficient volume fraction of precipitated  $\text{Cr}_2\text{O}_3$  and  $\text{Al}_2\text{O}_3$  particles in alloys due to diffusion of Cr, Al from interior of alloy and diffusion of oxygen through scale. The formation of a continuous, duplex oxide layer will reduce the flux of oxygen into alloy. **Group II** is characterised as a continuous  $\text{Cr}_2\text{O}_3$  layer dominant (Fig. 3.6 e) while **Group III** is dominant by a continuous  $\text{Al}_2\text{O}_3$  layer (Fig. 3.6 f). Oxidation reaction of those two groups is controlled by transport through  $\text{Cr}_2\text{O}_3$  and  $\text{Al}_2\text{O}_3$  scale, separately.

This pioneer study provides the criteria for the oxidation mechanism in Ni-base alloys, which becomes a consideration factor for designing a protective oxide layer, preferably an alumina former alloys (Group III alloys), in succeeding research of Ni-base superalloys.

In general, the effect of elemental vaporisation on surface evolution of Ni-base superalloys has drawn attention in recent researches, despite preliminary experiments showing microstructural evidence attributing to this phenomenon. There was inadequate data providing appropriate analysis under thermodynamic consideration. Hence, this work in collaboration with Forschungszentrum Jülich, Germany tends to quantify the extent of elemental losses during solution heat treatment, which will be beneficial to improve the alloying design as well as the design of thermal barrier coating for protection of alloy surface.

## **4. Sublimation-induced discontinuous precipitation in CMSX-10N superalloys during solution heat treatment**

In this chapter, the study initiates with consideration of microstructural instability in 3<sup>rd</sup> generation superalloys CMSX-10N during solution heat treatment. Using multiple approaches for investigating the formation of  $\gamma'$  surface layer and its evolution in Ni-base superalloys, the effect of elemental losses on alloy surface during solution heat treatment will be discussed.

### **4.1 Surface stability and phase evolution in Ni-base superalloys during solution heat treatment**

In order to enhance high temperature capability of Ni-base superalloys, alloys chemistry has developed by increasing the amount of refractory elementals/metals for improvement on solid solution hardening, and microstructural stability at high temperatures [3, 48, 51, 130].

Materials processing, such as production of single crystal turbine blades, enables the primary orientation of single crystal aligning along turbine blade or stress axis [23]. However, complexity of chemistry increases the challenge of controlling defects formation and microstructural stability in Ni-base superalloys during casting and subsequent heat treatment.

Microstructural stability has critical influence on high-temperature performance of Ni-base superalloys. Parameters of phase stability, including volume fraction of  $\gamma'$  phase, formation of  $\gamma'$ -phase and its phase changes, are often considered for appropriately understanding the formation of surface defects in as-cast single crystal superalloys. Otherwise, coarsening of  $\gamma'$  and formation of TCP phase are adversely affecting the stress-rupture properties which is a concern for second and third generation of SX superalloys.

DP in SX Ni-base superalloys has significant implications on performance of turbine blades. Depletion of W and Re from the bulk alloy is associated with precipitation and growth of TCP phase reducing the effect of solid-solution hardening from these alloying elements. Hence, there is a decrease in creep strength of Ni-base superalloys. Even though the evolution of  $\gamma'$  surface layer in as-cast CMSX-10N and solutioned CMSX-4 superalloys was investigated using neutron diffraction technique. However, previous experiments have not produced conclusive results to evidently examine DP at alloys surface. Therefore, a detailed analysis of DP at casting surface of solutioned CMSX-10N sample during solution heat treatment was performed. The formation of surface layer and relevant microstructural evolution in specimen were examined in more details, the neutron diffraction technique using in-situ solution heat treatment was used for progressive track solute diffusion ahead of the interface and identification of resulting phase transformation in SX CMSX-10N superalloys.

## **4.2 Experimental methods for investigation of discontinuous precipitation**

### ***4.2.1 Investment casting and heat treatment***

All test bar samples were prepared as single crystal using directional solidification which was carried out at the Precision Casting Facility, Rolls-Royce, plc, Derby, UK. Cylindrical test bars (70 mm in length with a 10 mm diameter) were cast in an industrial directional solidification furnace. The basic parameters are listed as following: furnace heater temperature was nominally 1773 K (1500 °C), vacuum level of the furnace chamber was maintained at 0.1 Pa ( $10^{-6}$  atm), and a mould withdrawal rate of around  $5 \times 10^{-5}$  m/s. The bars were chosen such that the bar axis was within 5 degree from the [001] crystal axis. Nominal Compositions of CMSX-10N sample are listed in Table 4.1.

Table 4.1: Nominal compositions (wt.%) of alloying elements in CMSX-10N

Alloy	Al	Co	Cr	Ti	Mo	Ta	W	Re	Ni
CMSX10N	5.9	3.1	1.6	0.1	0.45	8.5	5.5	6.8	Bal

A Schmetz furnace with a cuboidal working volume was used for heat treatment. Solution heat treatment cycle took place under Ar pressure of 50 Pa ( $5 \times 10^{-4}$  atm). The solution heat treatment cycle used numerous isothermal holds along the ramp cycle up to the final soak temperature of 1636 K (1363 °C). Test bars were positioned on ceramic tiles within the centre of the furnace working volume and held at 1636 K (1363 °C) for 25 hours. Following completion of the top soak phase, the bars were rapidly gas fan quenched using forced Ar flow giving an approximate cooling rate of  $240 \text{ K min}^{-1}$ . Test bars underwent primary ageing in the same furnace at 1423 K (1150 °C) for 5 hours under a vacuum level of 0.1 Pa ( $10^{-6}$  atm) and subsequently rapidly gas fan quenched using Ar.

#### ***4.2.2 Application of neutron diffraction method for determination of microstructural instability***

Neutron strain scanning (NSS) is a non-destructive technique that provides insights into strain and stress fields deep within engineering components. With two decades development of this technique, the 3<sup>rd</sup> generation ENGIN-X has been designed with improvements in performance of accurate engineering strain measurements in polycrystalline material lattice parameters at precisely determined location in an object [131].

ENGIN-X is a time-of-flight (TOF) sourced neutron diffractometer can simultaneously collected multiple diffraction peaks corresponding to the different grain families {hkl}. The schematic diagram of ENGIN-X apparatus is illustrated in Fig. 4.1, which shows a pulsed beam

of neutrons with energy emits from moderator travelling to the sample with a small fraction of beam diffracted at an angle  $2\theta_B$ .

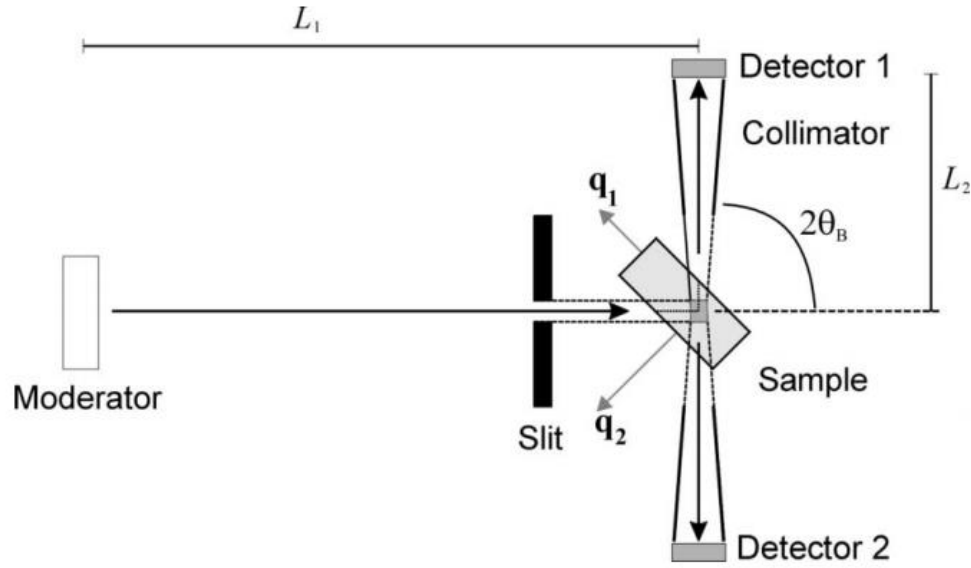


Fig. 4.1 Schematic diagram of a time-of-flight neutron strain scanning [131]

The wavelength of the detected neutrons in an elastic collision is defined as,

$$\lambda = \frac{h}{m(L_1 + L_2)} t \quad \text{Equation 4.1}$$

where  $h$  is Planck's constant,  $m$  is the neutron mass and  $L_1$  and  $L_2$  are the primary and secondary flight paths, respectively. Figure 14 is a typical diffraction spectrum from a polycrystalline material. The lattice planes in terms of  $(hkl)$  dimensions are given by Bragg's law, therefore the  $d$ -spacing corresponds to position  $t_{hkl}$  of the peak in the TOF spectrum is given by,

$$d_{hkl} = \frac{h}{2\sin\theta_B m(L_1 + L_2)} t_{hkl} \quad \text{Equation 4.2}$$

The change in the atomic interplanar distances  $d_{hkl}$  is compared with the  $d_{hkl}^0$  measured in unstressed condition to obtain elastic strain, i.e.  $\epsilon_{hkl} = (d_{hkl} - d_{hkl}^0)/d_{hkl}^0$ . The engineering strain



in TOF instruments is derived from the change in the average lattice parameters over the complete diffraction spectrum [132].

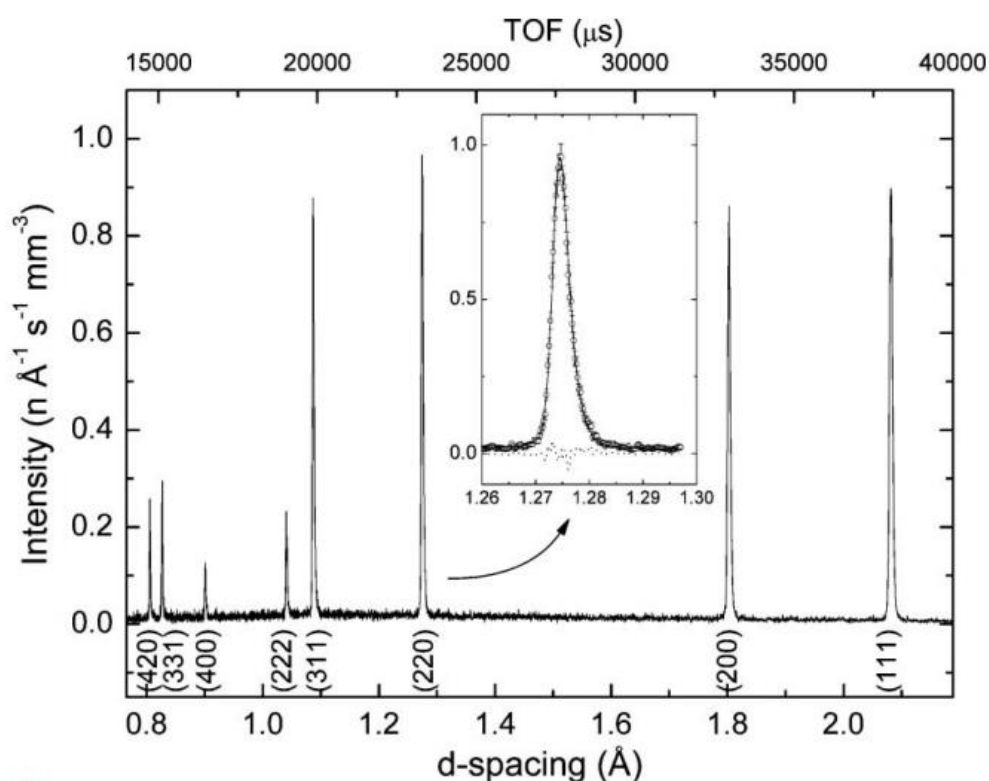


Fig. 4.2 TOF diffraction spectrum on ENGIN-X [131]

In a TOF NSS scan, the sample materials is placed in a gauge which is located in the path of incident bean intersected with sight of collimator detectors as showed in Fig. 4.2. Primary and secondary detectors are allocated at approximately  $90^\circ$  from incident beam in opposite side to ensure same volume of sample in measurements which are taken simultaneously at two perpendicular strain directions.

An in-situ heat treatment (repeat heat treatment) was carried out inside the ENGIN-X hutch using GEM furnace with Nb heating elements at ISIS, Rutherford Appleton Laboratory, UK. The pressure in the furnace pressure was maintained  $10^{-8}$  atm using an AC motor pump. An initial ramp rate of by  $10 \text{ K min}^{-1}$  was followed by an intermediate isothermal hold at 1523 K

(1250 °C) for 90 minutes to allow the furnace temperature to equilibrate. This was then followed by ramping at 5 K min<sup>-1</sup> until the final temperature was attained. A final top soak temperature of 1623 K (1350 °C) was used and this was followed by an isothermal hold for 14 hours. A schematic of the sample set up is shown in Fig. 4.3 (a).

The sample was mounted vertically on a ceramic base with additional ceramic supports to prevent movement, as observed in Fig. 4.3 (b). Specimens were secured to the furnace plunger using Ta wire with ceramic piping preventing contact between the wire, plunger and specimen. The sample was then secured using Ta wire. A dummy specimen was mounted on the other side acting as a counter balance. Type W thermocouples were positioned on the curved face of the sample to measure the temperature during the heat treatment process and to provide furnace temperature control. The outer flat target surface was aligned parallel to the incoming beam first visually then more accurately using the image detector. The holder was installed inside the furnace and the sample firmly attached on the holder to prevent any disturbance. To ensure the neutron beam targets the correct position on the sample, the flat surface of quadrant cross-section was made parallel to the emitting direction of the neutron beam. Therefore, the long edge of sample was adjusted to be in position vertically parallel to the sample holder. Detectors at 90° to the sample were used to measure the  $\gamma$  and  $\gamma/\gamma'$  peak. The obtained results on volume fraction of  $\gamma'$  phase is reported in Section 4.3.2.

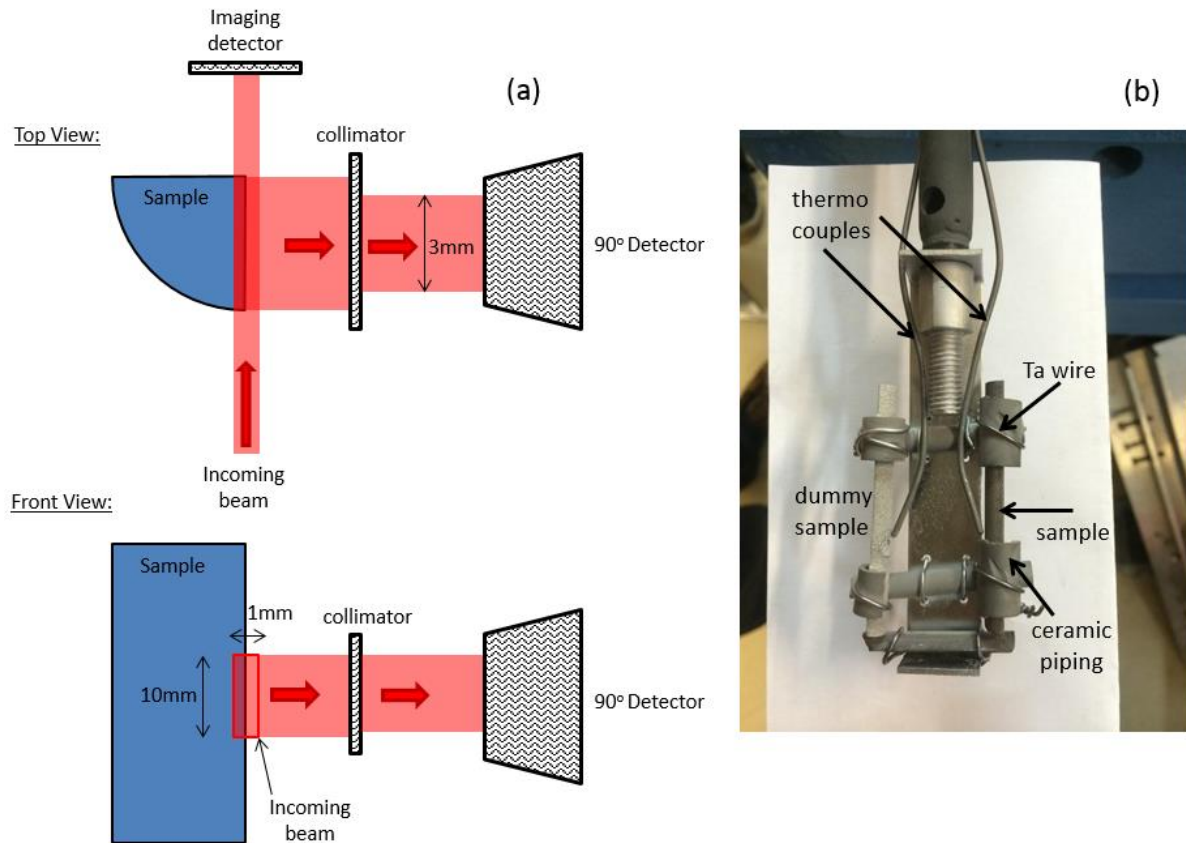


Fig. 4.3 (a) Schematic diagram of diffracted area of CMSX-10N superalloys (b) Sample configuration

#### ***4.2.3 Interrupted solutioning experiments to examine microstructures at the early stage of solution heat treatment***

Solutioning experiments using directionally solidified test bars were also conducted in a TAV vacuum furnace at University of Birmingham, UK. All solutioning experiments were conducted in an Ar atmosphere at a pressure of  $2 \times 10^{-4}$  atm (0.2 mBar). The test bars were located in alumina boats and positioned in the centre of the furnace, which was fitted with eight thermocouples at the corners and one at the centre of the load. Heating involved a series of ramps and isothermal holds until the set temperature was attained and a soak of 0.5 hour at top temperature was used. In this case, a set temperature of 1563 K (1290 °C) was used. After completion of the top soak phase quenching was done in an argon flow at approximately 90 K

min<sup>-1</sup>. In one instance, a sample was heated up to 1633 K (1360 °C), and then isothermally held for 1 hour before quenching.

#### **4.2.4 Electron microscopy**

The bars were cross-sectioned, Au sputtered and Ni electro-plated to preserve the surface in subsequent sample preparation.

Microstructure of heat treated samples was performed using Scanning electron microscopy (SEM) which has an ultra-high resolution field emission gun (FEG) examining detailed microstructures of samples. Back-scattered electron (BSE) images were collected using a retractable solid-state back-scatter detector with high electron beam (20 kV) accelerating voltage to enhance compositional contrast of microstructure on samples. Chemical analysis was undertaken in SEM at 20 kV using a PGT Spirit Energy-Dispersive X-ray Spectroscopy (EDX). Spectra were collected from three sites within an area of interest to verify for consistency. Observations of microstructures at different stages of heat treatment show evolution of discontinuous precipitation.

Further Scanning Transmission Electron Microscopy (STEM) analysis was carried out at Loughborough University. The TEM sample was extracted using an omniprobe micromanipulator and was attached to a Cu grid. The analysis was performed in a FEI Tecnai F20 operating at 200 kV. The system is equipped with an Oxford instruments XMAXN 80 TLE windowless Silicon Drift Detector (SDD) Energy Dispersive Spectroscopy (EDS) detector. Images were collected with a bright field (BF) and High Angular Annular Dark Field (HAADF) detectors in STEM. EDX spectrum maps were collected using Aztec software to assess sample compositional homogeneity. From these maps regions for collecting comparative spectra were defined and these were collected for 20 seconds live time.

#### ***4.2.5 Differential Thermal Analyses to determine solvus temperature of CMSX-10N***

A Stanton Redcroft 1640 Differential Thermal Analyses unit (DTA) was used for the cylindrical samples (diameter 4 mm, height 3 mm). All experiments were conducted using a dynamic high purity Ar atmosphere to minimise potential oxidising effects. The unit was calibrated using pure metals with melting points of 1337 K (1064 °C) for Au and 1728 K (1455 °C) for Ni. Alumina crucibles were used in all DTA experiments. The thermal resistances between different regions of the instrument were calibrated by fitting experimental data of melting pure nickel. With the calibrated thermal resistances for the instrument, the programme is able to de-convolute the measured signals and to extract accurate transition temperatures and enthalpy changes from the DTA measurements [133]. Fig. 4.4 corresponds to the heating curve of a solutioned bar with a heating rate of 2 K min<sup>-1</sup>. Limited amount of un-dissolved eutectic (~ 2.5 %) was detected showing as the minor endothermic peak. The  $\gamma'$  solvus temperature is determined as 1638 K (1365 °C) and single phase  $\gamma$  exists in the temperature range,  $1638 \text{ K} \leq T \leq 1655 \text{ K}$ .

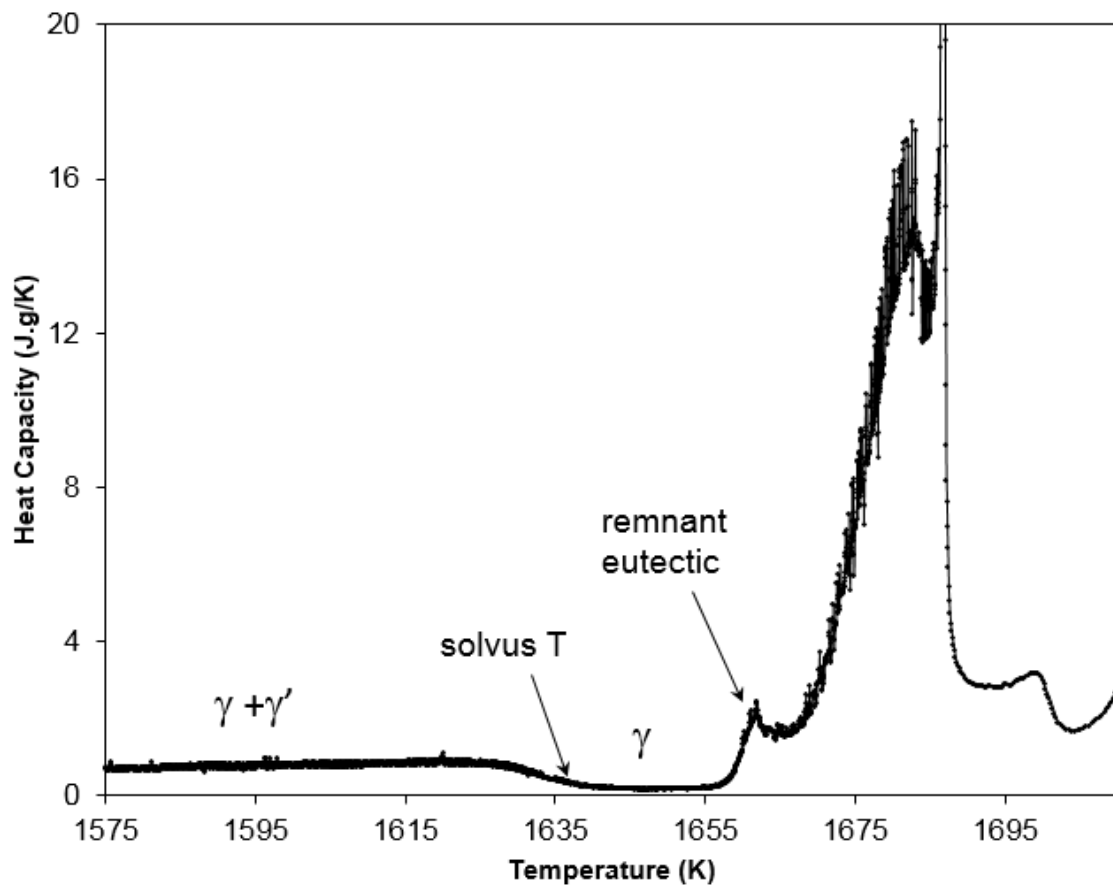


Fig. 4.4 DTA heating curve of a near-solutioned sample showing limited remnant non-equilibrium eutectic and  $\gamma'$  solvus temperature (heating rate of 2 K min<sup>-1</sup>).

### 4.3 Experimental observations of discontinuous precipitation at the surface of CMSX-10N superalloys during solution heat treatment

#### 4.3.1 Microstructural evolution of discontinuous precipitation at the surface during solution heat treatment

Occurrence of discontinuous precipitation has been found at two different solutioning temperatures, i.e. ramping stage at 1563 K (1290 °C) and below solvus temperature at 1623 K (1350 °C). Microstructural characterisation of discontinuous precipitation will be presented.

Fig. 4.5 is the back-scattered electron (BSE) image of cross section of the test bar showing the morphology of discontinuous precipitation at 1563 K (1290 °C) which has three distinct layers in surface area. To preserve the surface topography from metallographic grinding and polishing, an Au layer and electro-deposited Ni layer were sputtered on the top surface of the test bar after solution heat treatment. It is observed that the microstructural evolution is independent of processing conditions on as-cast surface, i.e. grit-blasted or grit-blasted. The role of induced surface strain is not considered in this study.

Observations of microstructures during the initial stage of solution heat treatment (1563 K) can be summarised as follow:

- The formation of a continuous  $\beta$ -island layer with thickness around 5  $\mu\text{m}$  below the surface, Ni/Al ratio measured by EDS is 58/36 indicating formed  $\beta$  phase. The precipitation of refractory-rich TCP phase also forms in the layer.
- The  $\gamma'$  layer beneath  $\beta$  layer has crisscross TCP phases with 5  $\mu\text{m}$  thickness layer. The Ni/Al ratio is 74/15 showing present of  $\gamma'$  phase.
- Discontinuous precipitation shows a morphology of a needle-like TCP phases within  $\gamma'$  matrix. The thickness of DP is 20  $\mu\text{m}$ .

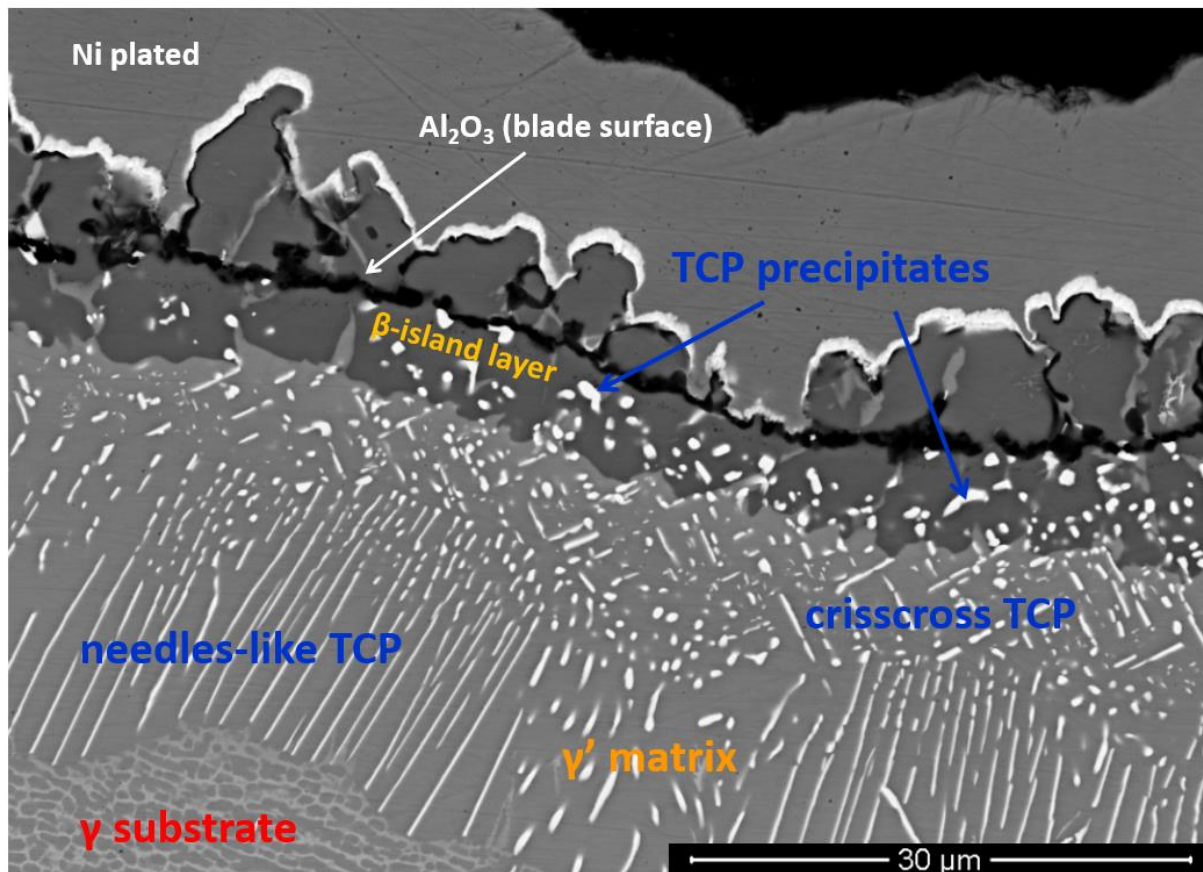


Fig. 4.5 BSE image of phases at initial stage of discontinuous precipitation

Discontinuous precipitation morphology is comprised of refractory-rich TCP phases within a  $\gamma'$  matrix. The growth of DP zone at temperature approaching its solvus was investigated and observed as microstructure showed in Fig. 4.6. Outmost layer at the surface consists of enriched refractory precipitates, unknown grey phase and DP zones, which are distinct with microstructures observed in previous study.



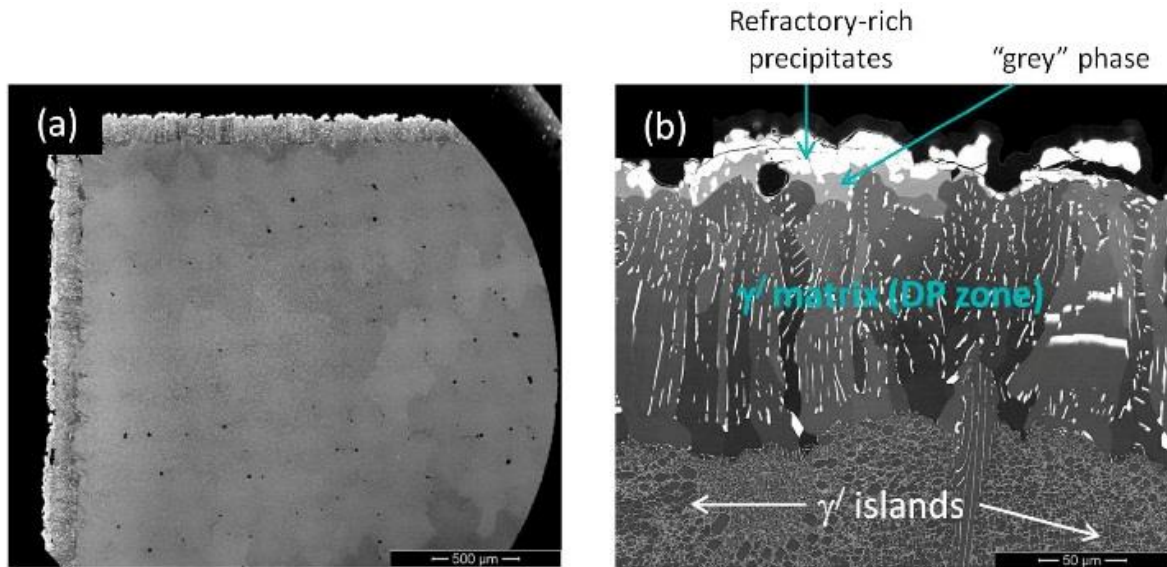


Fig. 4.6 (a) Low-magnification BSE image of the entire sample cross section (b) High-magnification BSE image of detailed evolution of microstructures

The growth of the DP cell is dependent on the inter-diffusion of solute with the substrate. Fig. 4.7 (a) is a montage image corresponding to 1623 K (1350 °C) that extends further into the substrate and the BSE image in Fig. 4.7 (b) focuses on the interface between the DP cell and the substrate, while that in Fig. 4.7 (c) corresponds to the microstructure within the bulk well ahead of the DP cell. The morphology can be summarised as follow:

- The coarse  $\gamma'$  morphology ahead of the DP zone is restricted extends to  $\sim 150 \mu\text{m}$  beyond the DP cell interface into the substrate and the  $\gamma'$  morphology is roughly globular in shape.
- The  $\gamma'$  within the bulk shows the more regular cube-type morphology. However, the  $\gamma'$  morphology between abutting globular  $\gamma'$  is much less regular in shape, albeit their relative sizes are comparable to that within the bulk.

The nucleation and growth of  $\gamma'$  is accompanied by rejection of Cr, W and Re to the surrounding  $\gamma$ -phase, since these elements have very limited solubility in  $\gamma'$  phase. As

observed in Fig. 4.6 (a), there is an irregular  $\gamma/\gamma'$  morphology in the region of interest ahead of the DP cell. Therefore, any form of composition measurement using microprobe analyses using SEM will be seriously biased owing to the “volume-averaging” effects [130]. A more appropriate method that is less susceptible to these effects would be the measurement of composition within the individual  $\gamma$ -channels themselves. Composition within  $\gamma$ -channels in the vicinity of the DP interface were compared with those in the bulk. For an accurate comparison it is imperative to have TEM foils of similar thickness. This is because thicker samples can lead to increased absorption of low energy X-rays which can skew the elemental comparison (Ni-K, Re-M and W-M peaks).

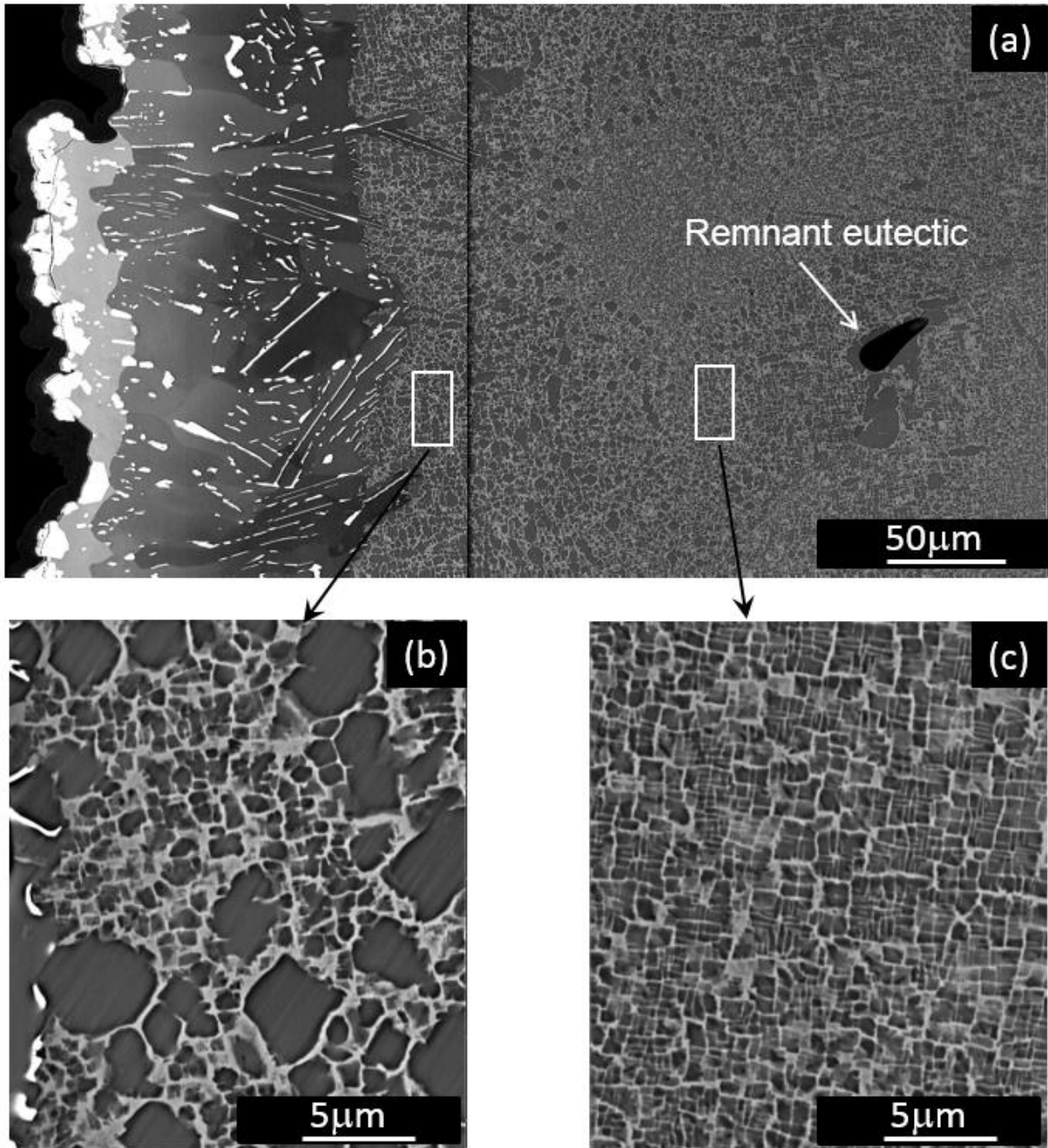


Fig. 4.7 BSE images showing microstructure developing ahead of the discontinuous precipitation zone: (a) Montaged image, (b) High-magnification image showing interface with the DP zone, (c) High-magnification image in the bulk.

Fig. 4.8 is a BSE image that shows the DP cells growing from the surface into the substrate, where the microstructure is similar to that observed in Figs. 4.4 (a) and 4.5 (b) although

there is also some evidence of  $\gamma$ -lamellae within the cells at the grain boundary. However, there exists one fundamental difference - there is the nucleation and growth of two re-crystallised grains ahead of the DP cell interface (grain boundary) and which subsequently grow into the substrate. The  $\gamma'$  morphology within these grains clearly indicates that these grains have nucleated in the single  $\gamma$  phase-field. Since there exists a grain boundary at the DP cell interface that precedes the nucleation of these grains, any remnant plastic strain that is dissipated would not require “new” nucleation. In fact, the growth of a strain-free grain would be sustained by the advancement of the DP cell boundary. However if this were the case, advancement of this boundary would be necessarily constrained by growth of the TCP needles, whose tips outline the grain boundary. Growth is then driven by solute super-saturation requiring partitioning of Cr, W and Re along the boundary to the precipitate tips. But if super-saturation is absent, the boundary will be “pinned” by the TCP needles. Therefore, dissipation of strain would then require nucleation of a “new” grain at the existing DP boundary and subsequent growth of this new grain will not be constrained by solute super-saturation, which is consistent with the observations in Fig. 4.6.

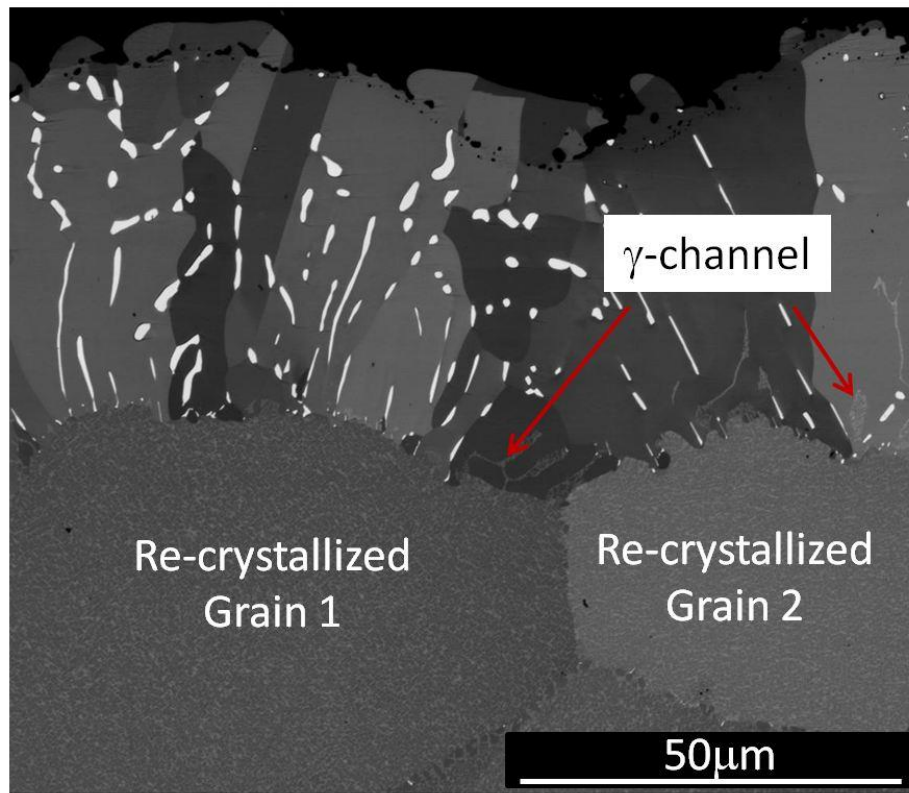


Fig. 4.8 BSE image showing nucleation of two re-crystallised grains ahead of the DP zone after solutioning at 1633 K (1360 °C) for 1 hour.

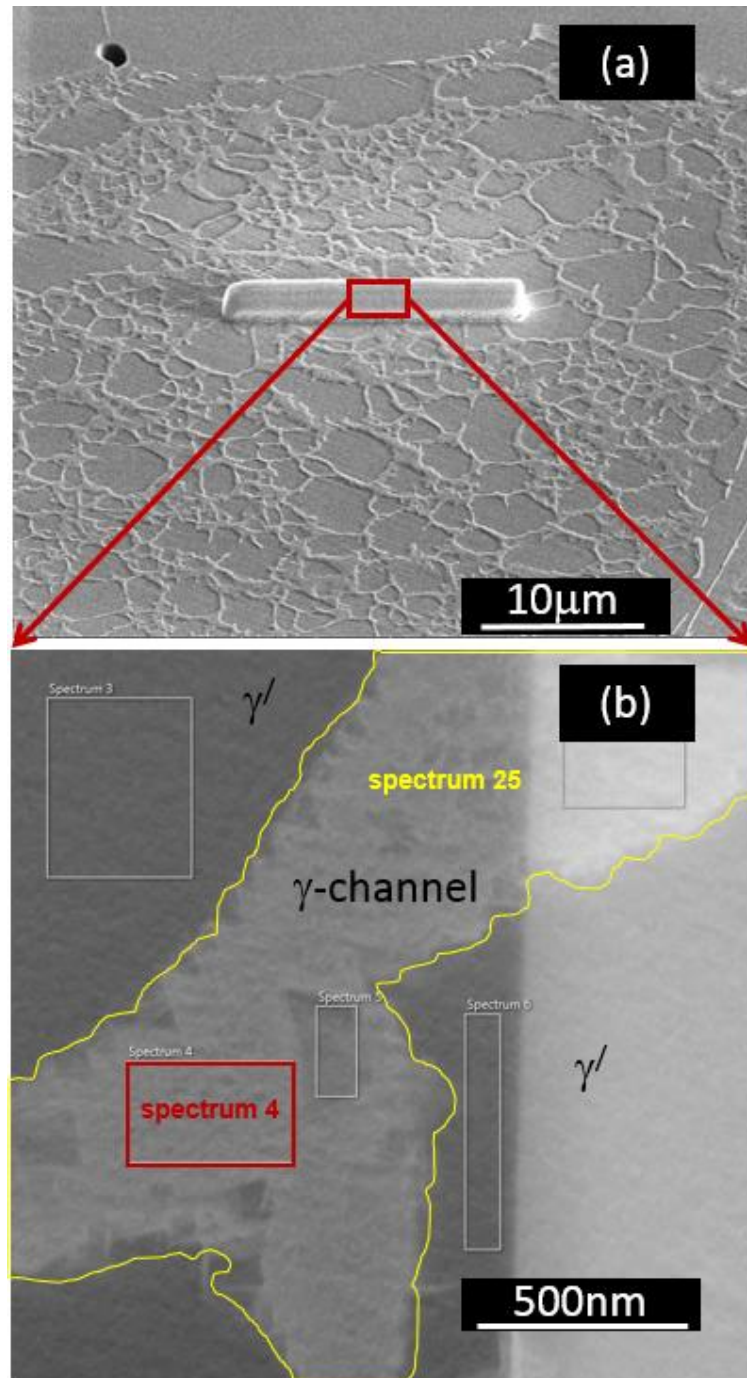


Fig. 4.9 (a) BSE image for region ahead of DP zone and position where TEM foil was extracted, (b) Dark-field STEM image showing  $\gamma$ -channel and adjacent  $\gamma'$  precipitates

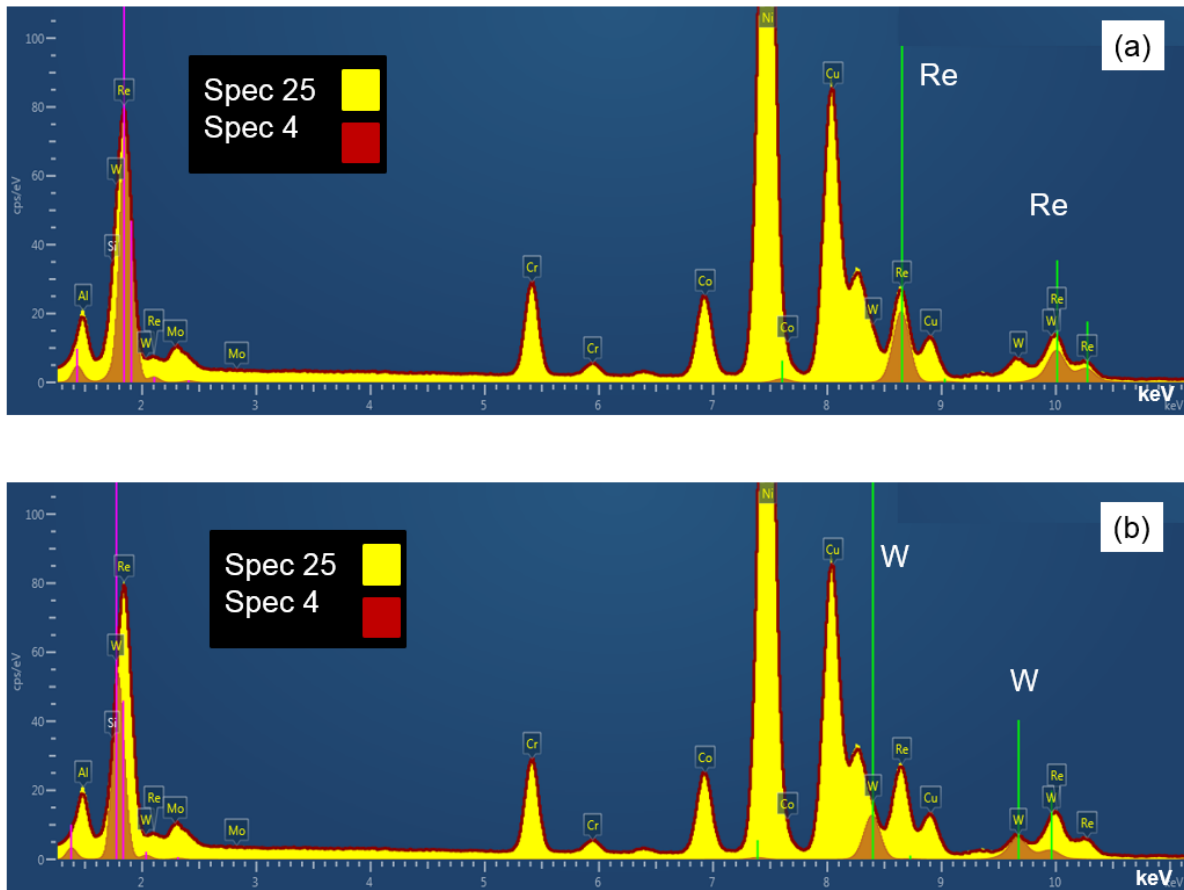


Fig. 4.10 Spectra from two regions within the  $\gamma$ -channel showing superimposing peaks of (a) Re and (b) W at corresponding keV

Fig. 4.9 (a) is a BSE image showing the region from where a TEM foil was extracted ahead of the DP interface, where the surface deposited Pt-layer is observed. Fig. 4.9 (b) is a dark-field STEM micrograph, which shows  $\gamma'$  (dark) precipitates and the  $\gamma$ -channel (bright) in between. Spectra were acquired from regions within the micrograph with indication of numbers. To ensure that the acquired spectra are not affected by the choice of regions, the spectrum 25 was acquired from the entire area of the  $\gamma$ -channel outlined in Fig. 4.9 (b). A comparison is made between spectrum 4 (red outline) and spectrum 25 (yellow outline) are presented in Figs. 4.10 (a) and 4.10 (b), where spectrum no. 4 is a subset of a region within the  $\gamma$ -channel. Also, given that Ta, W and Re energy peaks suffer significant overlap, the “true” location of a

Re and W peak (i.e. keV) is indicated in Fig. 4.10 (a) and 4.10 (b) respectively and corresponds to the region shaded in “brown”. The following observations can be made:

- There is no difference between the two spectra, i.e. the red and yellow regions overlap. Therefore, the secondary  $\gamma'$  within the  $\gamma$ -channel is not affecting the measurement.
- When the measured spectra are compared with the keV location of W and Re peaks, it is clear that the greatest contribution to the measured spectra arises from Re. This is because the keV location of the Re peak is centred close to the measured peak in the spectra, unlike W.
- The  $\gamma$ -channel is primarily segregated in Re, W, Cr and has a less extent Co and Mo compared to  $\gamma'$ . The Cu peak should be ignored as it arises from interaction with the Cu-grid used for the TEM foil.

Likewise, a similar measurement was carried out using a TEM foil extracted from within the bulk. The overlaid spectra corresponding to  $\gamma$ -channels at the surface and in the bulk is presented in Fig. 4.11. It can be summarised as follow:

- There is a similar Ni-K/Ni-L peak ratio in both cases. This indicates absence of significantly different absorption effects between the two samples and categorically emphasising the validity of the comparison of compositions in the two samples (owing to similar thickness of the two foils).
- The  $\gamma$ -channels at the surface are more segregated in Cr, W, Re and Mo compared to the channels within the bulk. Quantitative analyses of the spectra give a segregation ratio (R) for the principal elements;  $R^{Cr} = 1.6$ ,  $R^W = 1.3$ ,  $R^{Re} = 1$ , where  $R = \frac{\text{composition in } \gamma\text{-channel at surface}}{\text{composition in } \gamma\text{-channel in bulk}}$ .



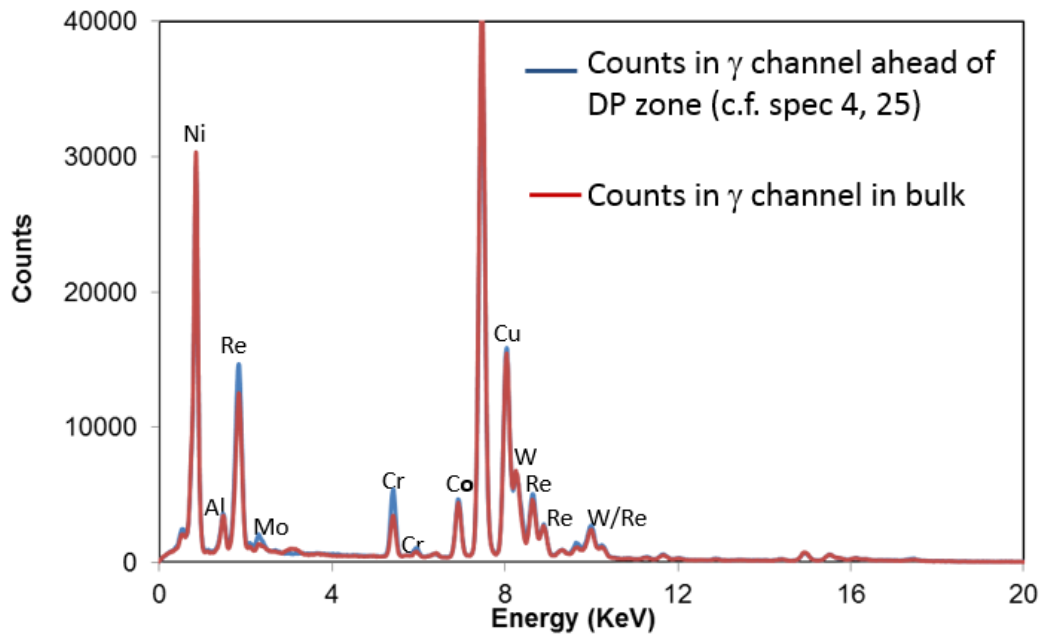


Fig. 4.11 Spectra from  $\gamma$ -channel ahead of DP zone and within the bulk

#### 4.3.2 Evolution of $\gamma'$ ahead of the discontinuous precipitation cell interface

The mole-fraction of  $\gamma'$  was measured during temperature ramps up to 1623 K (1350 °C) and during subsequent isothermal hold by measuring the diffracted intensity of the (110) peaks.

The (110) and (330) peaks arise exclusively from the super-lattice of the  $\gamma'$  phase, while the (220) peak has contributions from both  $\gamma$  and  $\gamma'$  phases. Fig. 4.12 the measured lattice spacing for the (110) and (220) peaks during the heating stage, where the different shapes of the (110) and (220) curves arise from the different thermal expansion of the individual phases. The close agreement between these curves for different heating runs confirms the absence of any significant thermal lag during heating.

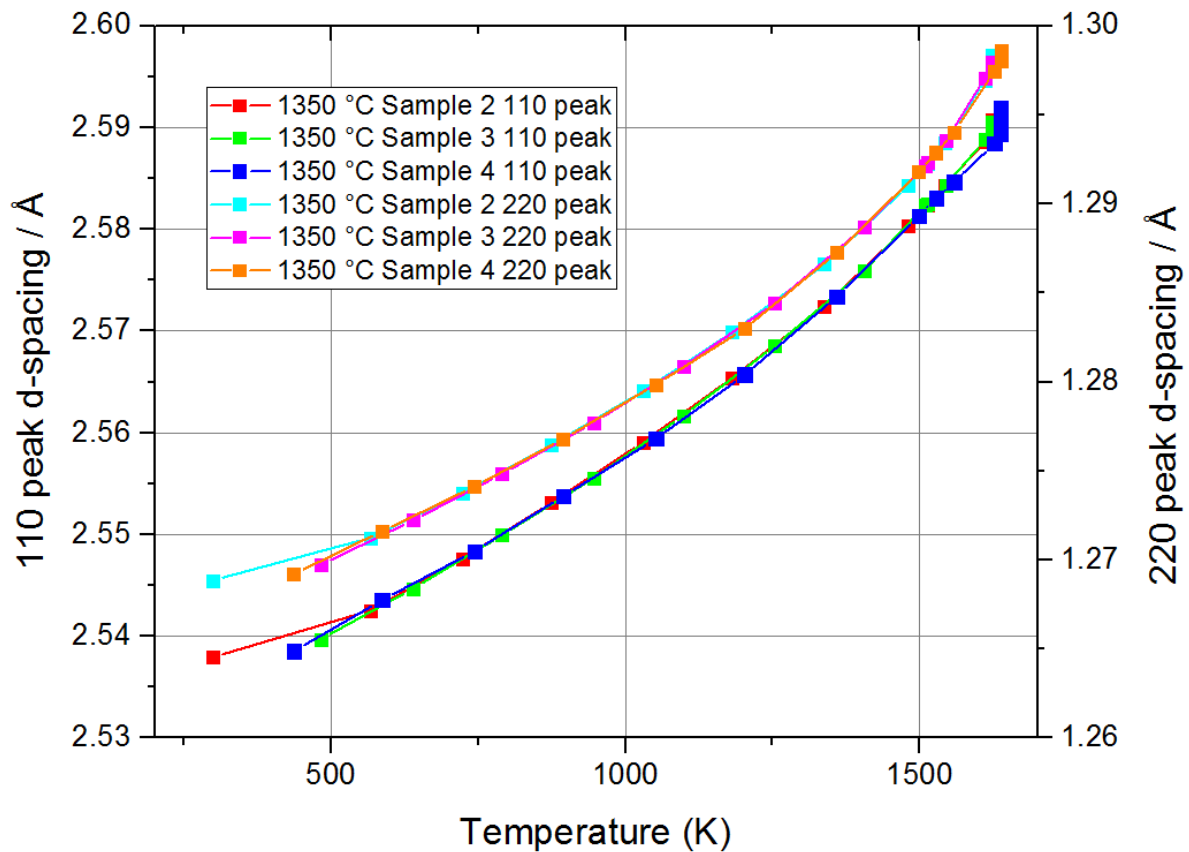


Fig. 4.12 Measured lattice spacing for the (110) and (220) peaks during the heating stage.

Different shapes of the (110) and (220) curves arise from the different thermal expansion of  $\gamma$  and  $\gamma'$  phases

Fig. 4.13 shows the calculated variation in  $\gamma'$  mole-fraction as a function of isothermal hold at the set temperature of 1623 K (1350 °C). After applying the Debye-Waller correction, the  $\gamma'$  fraction is found to remain constant until 1173 K (900 °C) and between 1273 K (1000 °C) and 1473 K (1200 °C) the decrease in  $\gamma'$  follows the thermodynamic calculation results, which again corroborates our method of analyses. On reaching the isothermal hold temperature of 1623 K (1350 °C), the quantity of  $\gamma'$  is found to increase again from 4 % to about 7.5 %. It is important to emphasise that this measurement exclusively refers to  $\gamma'$  that has the same crystallographic orientation as the substrate and thus contributing to the diffracted (110)

peak. Therefore, this only pertains to the  $\gamma'$  that has nucleated and grown ahead of the DP interface and also to the remnant  $\gamma'$  present given that the solvus temperature is 1635 K (1362 °C). It categorically precludes  $\gamma'$  within the DP zone.

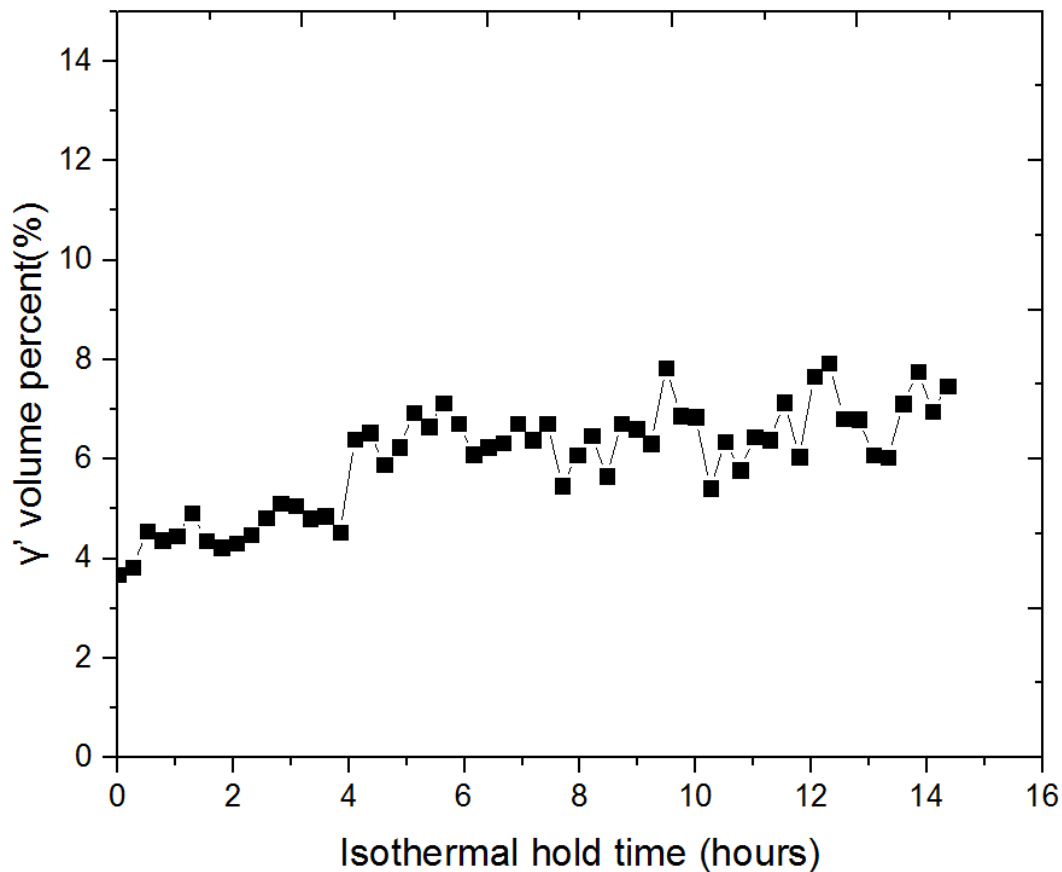


Fig. 4.13 Variation in  $\gamma'$  volume percent as a function of isothermal hold time at 1623 K (1350 °C)

#### 4.4 Phenomenological model of discontinuous precipitation evolution in Ni-base superalloys

As observed from microstructural evolution of Ni-base superalloys, the evolution of discontinuous precipitation morphology at elevated temperatures is illustrated in Fig. 4.14 with following proposal:

(a) For temperature below solvus (1473K), elemental sublimation is initiated by several elements on the surface, i.e. Ni, Co and Cr from  $\gamma$  phase and Ni from  $\gamma'$  phase due to high vapour pressures of those elements. Non-ideal solid solutions has an influence on elemental interaction at high temperatures, which affects chemical potential as well as vapour pressure in solid solution. Local condition in the vicinity of surface has also impact on sublimation which is reduced by presence of a carrier gas Ar used in solution heat treatment of Ni-base superalloys.

(b) Loss of Ni causes dissolution of  $\gamma$  phase and stabilisation of  $\gamma'$ . The excess W and Re elements are rejected from substrate matrix and precipitates as refractory-rich TCP at grain boundaries near the surface region. DP zone is formed with further growth of precipitates by short-circuit diffusion of elements.

(c) Further Ni sublimation leads to dissolution of  $\gamma$  phase and nucleation of polycrystalline  $\beta$  phase. Diffusion of Ta occurs as the result of no solubility in  $\beta$  phase. Presence of  $\beta$  phase shows evidence for sublimation of Al but its rate is significantly lower than that of Ni. The growth of DP cell is attributed to interdiffusion within the substrate. The formation of a continuous  $\beta$  phase at the surface is regarded as the end of DP evolution at the initial stages.

(d) Sublimation of Ni and Al take place from  $\beta$  phase when temperature approaches the solvus (around 1623K). The present of stable oxides, such as  $\text{Al}_2\text{O}_3$ , affects the rate of elemental sublimation showing potential solutions for preventing alloy surface from sublimation. The dissolution of  $\beta$  and  $\gamma'$  as a result of Ni and Al loss leads to growth of Re and W precipitates. Meanwhile slower sublimation of Al has an impact on volume diffusion of Al into substrate, which nucleates  $\gamma'$  in  $\gamma$  phase and eventually causes growth of  $\gamma'$ .

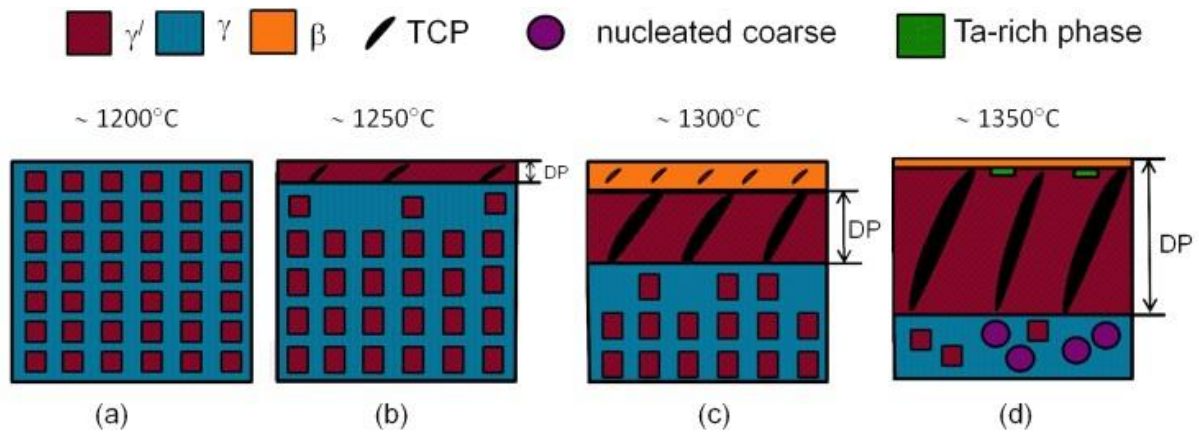


Fig. 4.14 Schematic diagram showing evolution of DP zone and morphology ahead of DP zone during solution heat treatment

Although occurrence of elemental sublimation in Ni-base superalloys has been identified during solution heat treatment as an inducement to evolution of DP at the alloy surface, mechanism of elemental sublimation was not fully understood and lack of experimental data for detailed analysis. Hence, to acquire thermodynamic data for calculating terms including chemical potential for further evaluation of sublimation process Ni-base alloys at high temperatures, thermodynamic activity and partial vapour pressure in Ni-base alloys are essential thermodynamic factors for determining elemental sublimation under such considerations. Based on functionality of high-temperature apparatus, application of KEMS technique was proposed to effectively evaluate thermodynamic activities and partial vapour pressures of Ni, Al and Cr in Ni-Cr-Al ternary system. Pertinent thermodynamic calculations will provide an overview of sublimation induced phase evolution in Ni-base alloys during solution heat treatment and determine high temperature behaviours of elements contained in Ni-base alloys.

## 4.5 Conclusions

Sublimation induced discontinuous precipitation (DP) at different stages of solution heat treatment has been studied. It was observed that DP forms at temperature approaching the solvus and diffusion in alloys near the solvus temperature is volume diffusion dominated. With increasing temperature, volume diffusion is accompanied by a loss in the driving force due to the advancement of the grain boundary. This is primarily concomitant with diffusion of Al ahead of the boundary.

With respect to microstructure observed at different stages of solution heat treatment, a phenomenological model of microstructural evolution on the surface of alloy was proposed as the consequence of elemental sublimation. Excessive amount of Ni loss leads to microstructural instability on the surface of alloy showing transformation of  $\gamma \rightarrow \gamma'$ . The growth of DP is associated with partitioning of W, Re and Cr to growing tip of TCP precipitates. However, when volume diffusion is dominant, transformation of  $\gamma \rightarrow \gamma'$  ahead of the interface is accompanied by super-saturation of Cr and W within the  $\gamma$  channels ahead of the DP cell. This arises since TCP phase nucleation is suppressed owing to the absence of heterogeneous sites and excess Cr and W are therefore accommodated within  $\gamma$ -channels.

Even though microstructural evidence revealed that microstructural instability in Ni-base SX superalloys was induced by elemental losses during solution heat treatment, sublimation process was not precisely determined from pertinent thermodynamic data with analytical manner to further explicate such phenomenon. Hence, to investigate the degree of elemental sublimation on the surface of Ni-base alloys, thermodynamic analysis, which refers to utilize KEMS method, will be carried out in subsequent experiments measuring partial vapour pressure of elements in Ni-base alloys at high temperatures.

## **5. Thermophysical properties of Ni-Cr-Al model alloys**

The elemental sublimation occurs in non-equilibrium condition during solution heat treatment of Ni-base superalloys. Complexity of alloy chemistry in CMSX-10N SX superalloys creates barrier for the accurate quantification of elemental losses when it occurs. Despite several evidences showing the effect of elemental sublimation attributing to Ni, Al, Cr and Co, insufficient researches are pertinent to surface sublimation in Ni-base alloys investigating in a comprehensive method with valid thermodynamic data. Therefore, it was proposed that ternary Ni-Cr-Al model alloys, which is one of the most important sub-system for Ni-base alloys research, are ideal materials for studying high temperature behaviours of elements contained in alloy. Prior to KEMS experiments which are able to examine thermodynamic properties of alloys at high temperature under equilibrium condition, thermophysical properties of Ni-Cr-Al model alloys are requisite for determining temperature range used in KEMS measurements and providing initial insights of thermodynamic calculations from existing software.

### **5.1 Materials and samples preparation**

Oxidation mechanism of Ni-Cr-Al model alloy proposed by Giggins and Pettit [127] has been well recognized as the criteria for determining which types of oxides form. According to their classification, majority of Ni-Cr-Al sample were designed as alumina former alloys (Group III type). Additional alloys were considered based on nickel oxide (Group I type) and chromia (Group II type) former as reference. The designed model alloys contain Al content ranging from 4-6 wt% which is nominal amount used in commercial SX Ni-base superalloys CMSX series. The Cr composition has been designed with an increase from 2 wt% up to 30 wt%. The specific contents of three elements are listed in Table 5.1. Fig. 5.1 and 5.2 show distinctive boundaries between group I, II and III in ternary phase diagram at 1273K (1000°C) and 1473K

(1200°C), respectively. All produced alloys have been marked separately on two ternary phase diagrams in order to verify classification of designed alloys based on existing oxidation mechanism. Alloy number 16-19 will be prepared over as new ternary alloys belonging to Group I and II.

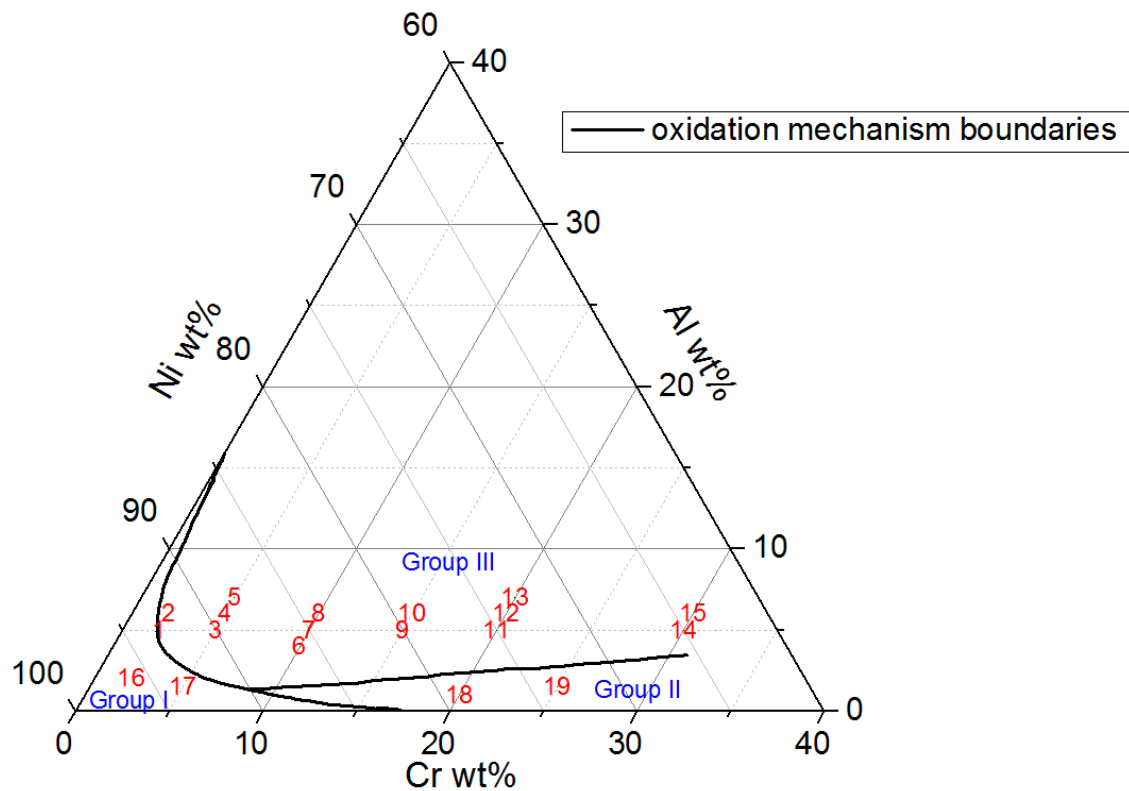


Fig. 5.1 Isothermal diagrams for three oxidation mechanism of Ni-Cr-Al model alloys at 1273K (reproduced after ref. [127])



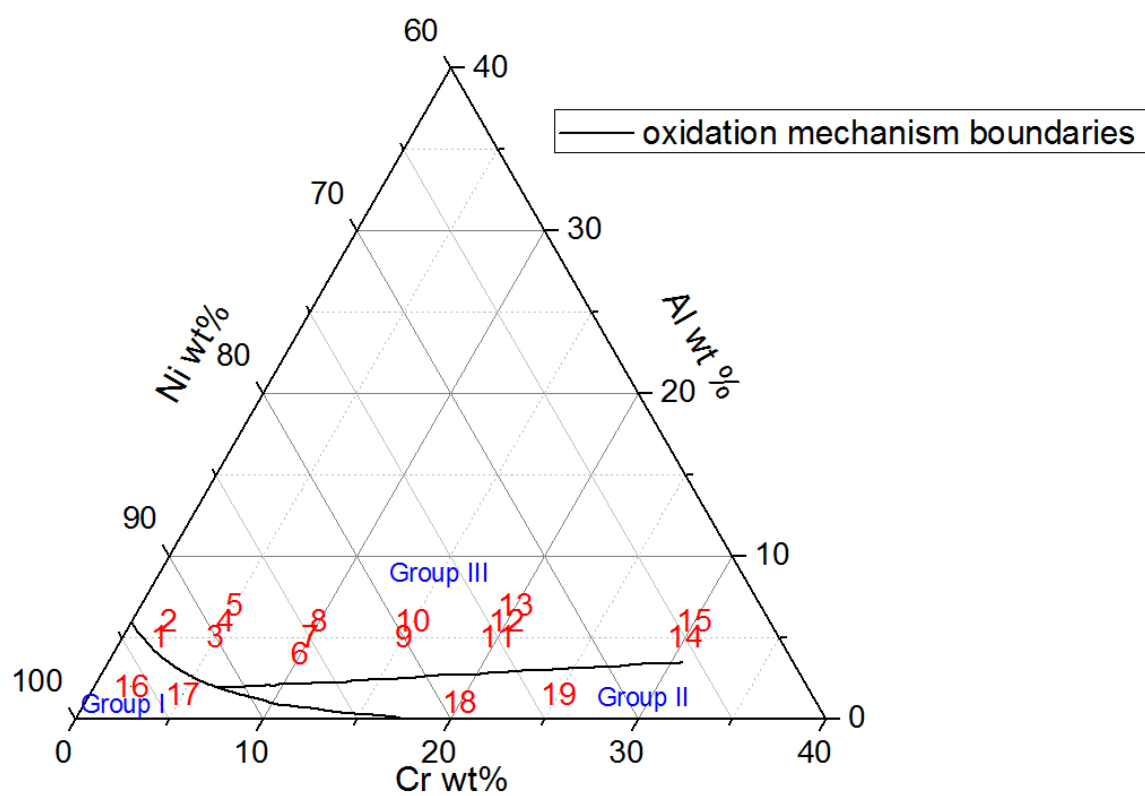


Fig. 5.2 Isothermal diagrams for three oxidation mechanism of Ni-Cr-Al model alloys at 1473K (reproduced after ref. [127])

Table 5.1 List of produced ternary alloy samples in weight percentage

Alloy number	Ni-Cr-Al Alloy	Cr weight percent	Al weight percent	Group *
1	Ni-2Cr-5Al	2.0	5.0	I
2	Ni-2Cr-6Al	2.0	6.0	III
3	Ni-5Cr-5Al	5.0	5.0	III
4	Ni-5Cr-6Al	5.0	6.0	III
5	Ni-5Cr-7Al	5.0	7.0	III
6	Ni-10Cr-4Al	10.0	4.0	III
7	Ni-10Cr-5Al	10.0	5.0	III
8	Ni-10Cr-6Al	10.0	6.0	III
9	Ni-15Cr-5Al	15.0	5.0	III
10	Ni-15Cr-6Al	15.0	6.0	III
11	Ni-20Cr-5Al	20.0	5.0	III
12	Ni-20Cr-6Al	20.0	6.0	III
13	Ni-20Cr-7Al	20.0	7.0	III
14	Ni-30Cr-5Al	30.0	5.0	III
15	Ni-30Cr-6Al	30.0	6.0	III
16	Ni-2Cr-2Al	2.0	2.0	I
17	Ni-5Cr-1.5Al	5.0	1.5	I
18	Ni-20Cr-Al	20.0	1.0	II
19	Ni-25Cr-1.5Al	25.0	1.5	II

The compositions of Ni-Cr-Al model alloy were also converted in atomic percent to show concentrations of elements corresponds to relevant atomic sizes, which are normally related to thermodynamic calculations that introduce in following sections. Comparably, the diagram of oxidation mechanism is reproduced according to atomic percent in Fig. 5.3 showing similar allocations of designed model alloys in ternary phase diagram.

Table 5.2 List of produced ternary alloy samples in atomic percentage

Alloy number	Ni-Cr-Al Alloy	Cr atomic percent	Al atomic percent	Ni atomic percent
1	Ni-2Cr-5Al	2.13%	10.25%	87.63%
2	Ni-2Cr-6Al	2.10%	12.16%	85.73%
3	Ni-5Cr-5Al	5.30%	10.21%	84.49%
4	Ni-5Cr-6Al	5.24%	12.12%	82.64%
5	Ni-5Cr-7Al	5.18%	13.99%	80.83%
6	Ni-10Cr-4Al	10.65%	8.21%	81.14%
7	Ni-10Cr-5Al	10.53%	10.15%	79.32%
8	Ni-10Cr-6Al	10.42%	12.05%	77.53%
9	Ni-15Cr-5Al	15.70%	10.09%	74.21%
10	Ni-15Cr-6Al	15.53%	11.98%	72.49%
11	Ni-20Cr-5Al	20.81%	10.03%	69.16%
12	Ni-20Cr-6Al	20.59%	11.91%	67.50%
13	Ni-20Cr-7Al	20.37%	13.74%	65.88%
14	Ni-30Cr-5Al	30.86%	9.91%	59.23%
15	Ni-30Cr-6Al	30.53%	11.77%	57.70%
16	Ni-2Cr-2Al	2.20%	4.24%	93.56%
17	Ni-5Cr-1.5Al	5.51%	3.19%	91.30%
18	Ni-20Cr-Al	21.76%	2.10%	76.15%
19	Ni-25Cr-1.5Al	26.88%	3.11%	70.01%

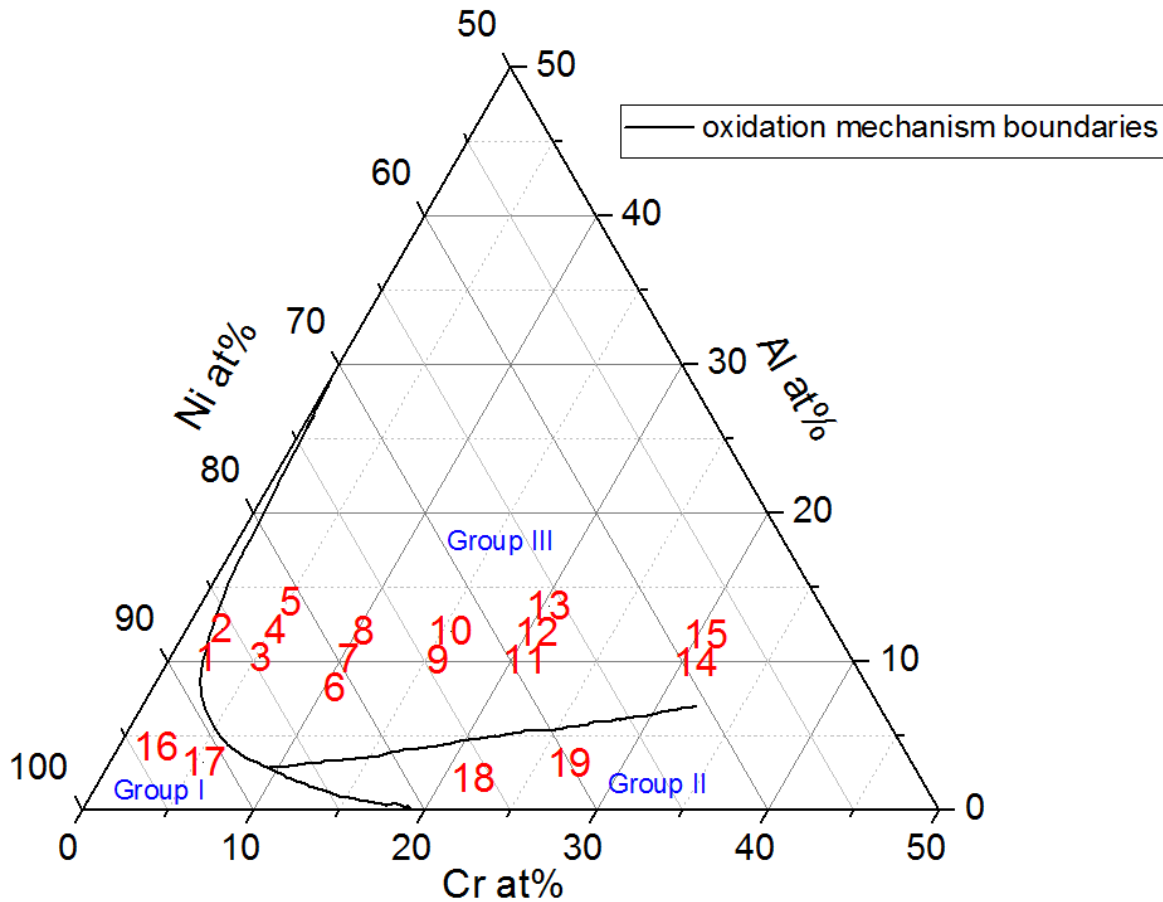


Fig. 5.3 Isothermal diagrams of Ni-Cr-Al model alloys at 1273K in atomic percent

Polycrystalline Ni-Cr-Al model alloys were prepared as test bars from high purity Ni (99.99%), Cr (99.98%) and Al (99.99%) in preparation of test bars by rapid vacuum melting. Raw materials of three elements were prepared and weighted to an accuracy of 0.001g prior to casting stage which was carried out in a vacuum induction levitation melting furnace at Taiyuan University of Technology, China. Mixture of raw material was then heated by induction to a temperature of about 1723K in the furnace while levitating in a magnetic field. The whole process operated in the condition of vacuum level at 0.1 Pa and lasted for approximately 15 minutes until the alloy was fully melted with a uniform chemistry in the furnace. The molten alloy was then pressed into a fused quartz tube at an approximate rate of 0.05 m/s to form a cylindrical bar subsequently quenching by Ar flow. Rapid solidification

prevents alloys from macrosegregation in as-cast microstructure. The quartz tube was then removed from the produced sample bar which has length of approximately 150mm and diameter of 8mm after casting.

Each test bar was eventually cut into the length of approximately 60mm as shown in Fig. 5.4. Depending on requirement for subsequent experiments, the test bar will be sectioned accordingly with more details in following contents. Additional 4 ternary alloys were produced using same method as Group I and II alloys.



Fig. 5.4 A sample of as-cast Ni<sub>2</sub>Cr<sub>5</sub>Al model alloy

## 5.2 Chemical contents of as-cast Ni-Cr-Al model alloys

Chemistry of produced Ni-Cr-Al model alloys has been measured to examine the consistency with compositions from initial design. 9 samples have been analysed using a PGT Spirit Energy-Dispersive X-ray Spectroscopy (EDX) method via the point scan in SEM. Gungor's method [134] was applied to derivate accurate measurements without bias of segregation. There is a good agreement on content of Cr and Ni with the original design of alloys. Al content has slight large discrepancy. Details of chemical analysis are listed in Table 5.3.

Table 5.3 Chemical analysis from EDX

Alloy number	Al (wt%)	Cr (wt%)	Ni (wt%)
1	4.62	1.86	93.52
4	5.87	4.79	89.34
5	6.13	4.89	88.98
8	5.59	9.41	85.00
9	4.63	14.58	80.79
10	5.57	14.60	79.83
12	5.94	19.59	74.47
14	4.47	29.26	66.27
15	5.58	29.46	64.96

Alternative method for determining chemistry of model alloys used X-ray fluorescence (XRF) which was conducted at Department of Geology, University of Leicester. 5 thin slice of cross-section samples were prepared for chemical analysis and results are summarised in Table 5.4. XRF results have shown less influence of carbon as there is limited carbon contamination during sample preparation for XRF measurements. By comparison with SEM analysis, there is a good agreement of alloys chemistry using two different methods. And the consistency of chemistry with original design of Ni-Cr-Al model alloys is acceptable for proceeding with subsequent thermal analysis and KEMS experiments.

Table 5.4 Chemical analysis from XRF

Alloy number	Al (wt%)	Cr (wt%)	Ni (wt%)
4	5.39	4.57	90.04
8	5.33	9.02	85.65
10	5.79	14.39	79.82
12	6.13	19.11	73.39
15	5.51	28.14	66.35

### 5.3 Microscopy characterisation

A thin slice of each cylindrical bar was cut for chemical analysis and microstructure characterisation to identify properties of as-cast samples. Cross-section of specimens were prepared by initial grinding using five types of SiC papers and a final polishing using 6  $\mu\text{m}$ , 3  $\mu\text{m}$  and 1  $\mu\text{m}$  diamond paste for minimum of 180 seconds at 240-300 rpm spinning speed.

SEM with an ultra-high resolution field emission gun (FEG) was applied to perform detailed observation of as-cast microstructures. Back-scattered electron (BSE) images are collected using a retractable solid-state back-scatter detector with high electron beam (20kV) accelerating voltage to enhance compositional contrast of microstructure on samples. Chemical analysis is undertaken in SEM at 20kV using a PGT Spirit EDX. Spectra were collected from three sites within an area of interest to verify for consistency.

Optical microstructures (OM) were observed using Olympus Vanox BH2 microscope. As shown in Fig. 5.5 and Fig. 5.6, OM images for microstructures of Ni<sub>2</sub>Cr<sub>6</sub>Al and Ni<sub>30</sub>Cr<sub>6</sub>Al were captured presenting observations from low Cr and high Cr containing Ni-Cr-Al model alloys. Dendrites, interdendrites and grain boundaries are labelled in OM images of two model alloys. The dendrite orients in direction of thermal gradient during solidification. It is observed that

microstructure of Ni30Cr6Al alloy sample showing more identical microstructures of dendrites and interdendrites. For Ni-Cr-Al model alloy containing high amount of Cr, there are similar microstructures observed in OM images, i.e. Ni30Cr5Al has similar microstructures to that of Ni30Cr6Al as shown in Fig. 5.6. Comparing to the alloys with lower amount of Cr, Ni2Cr5Al alloy, those alloys were cast with less interdendritic porosity and well-solidified dendrites.

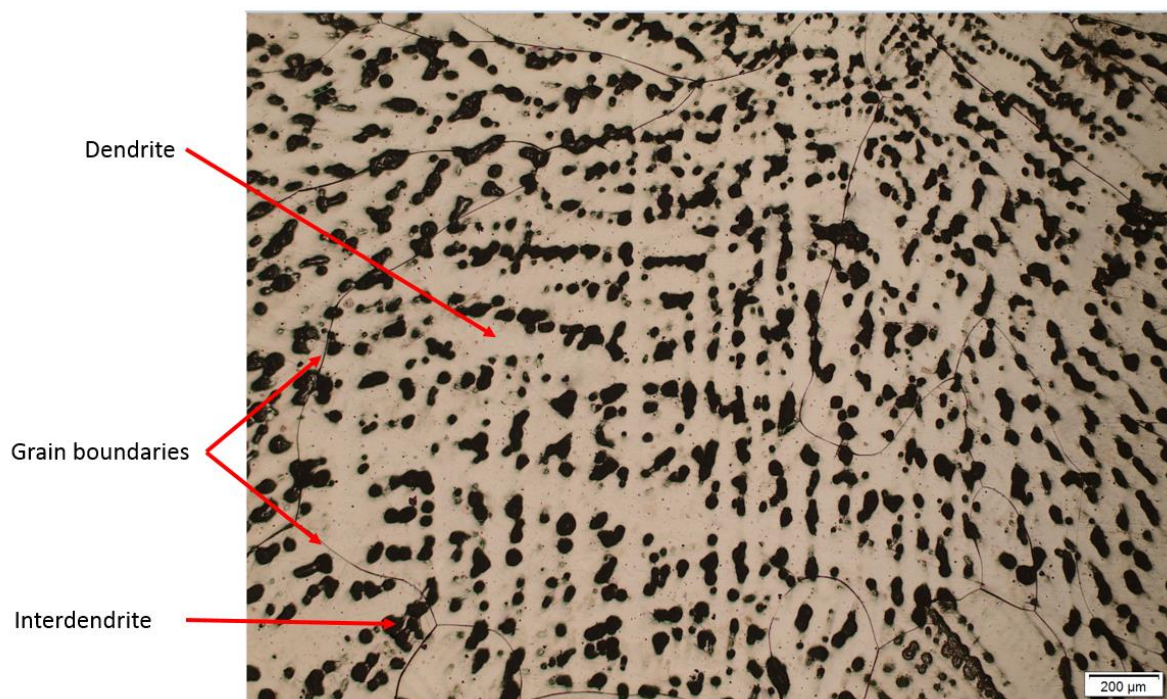


Fig. 5.5 Optical image of microstructure for Ni5Cr6Al sample



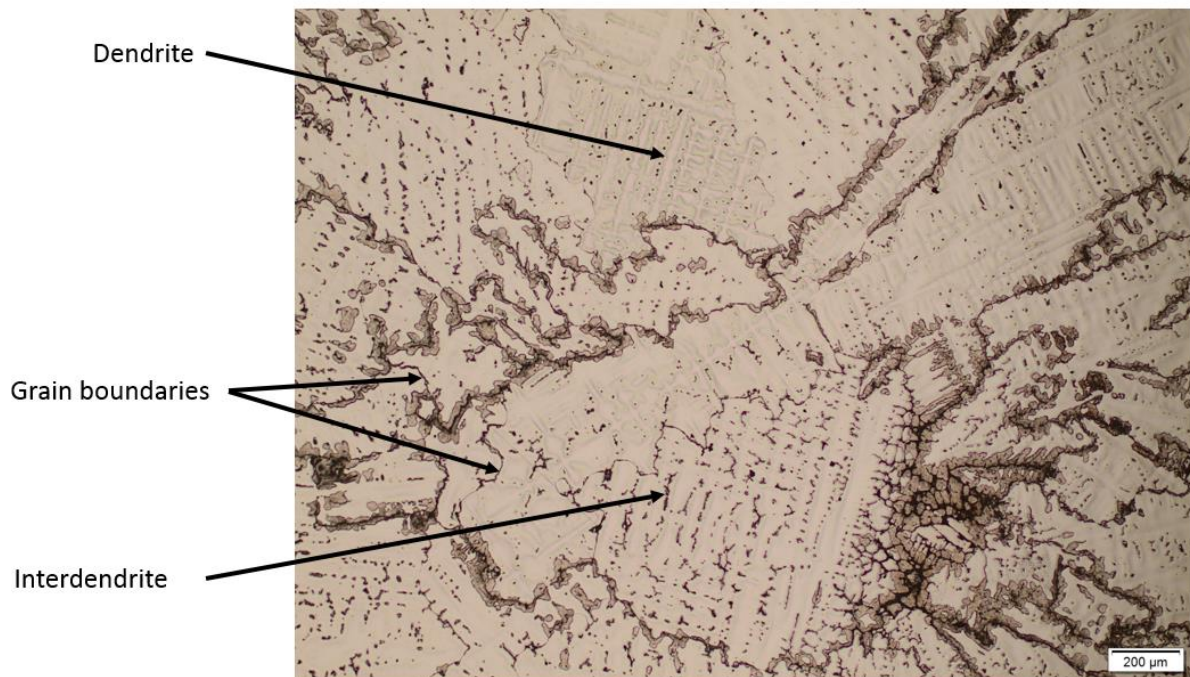


Fig. 5.6 Optical image of microstructure for Ni<sub>30</sub>Cr<sub>6</sub>Al sample

Fig. 5.7 and Fig. 5.8 are backscattered electron images (BSE) of microstructure of Ni<sub>15</sub>Cr<sub>6</sub>Al sample using different magnifications. The atomic number dependence of electron backscattering is the basis of a microanalysis technique [135] providing observation of compositional variations within a specimen. The higher atomic number of an element, lighter colour on the image showing the apparent atomic number of the specimen. Hence, observation of microstructures show a visible colour difference between dendrites and interdendrites in Ni<sub>15</sub>Cr<sub>6</sub>Al sample, which indicate that the darker area in interdendritic region is enriched of Al while dendrites confirm enrichment of Ni and Cr.

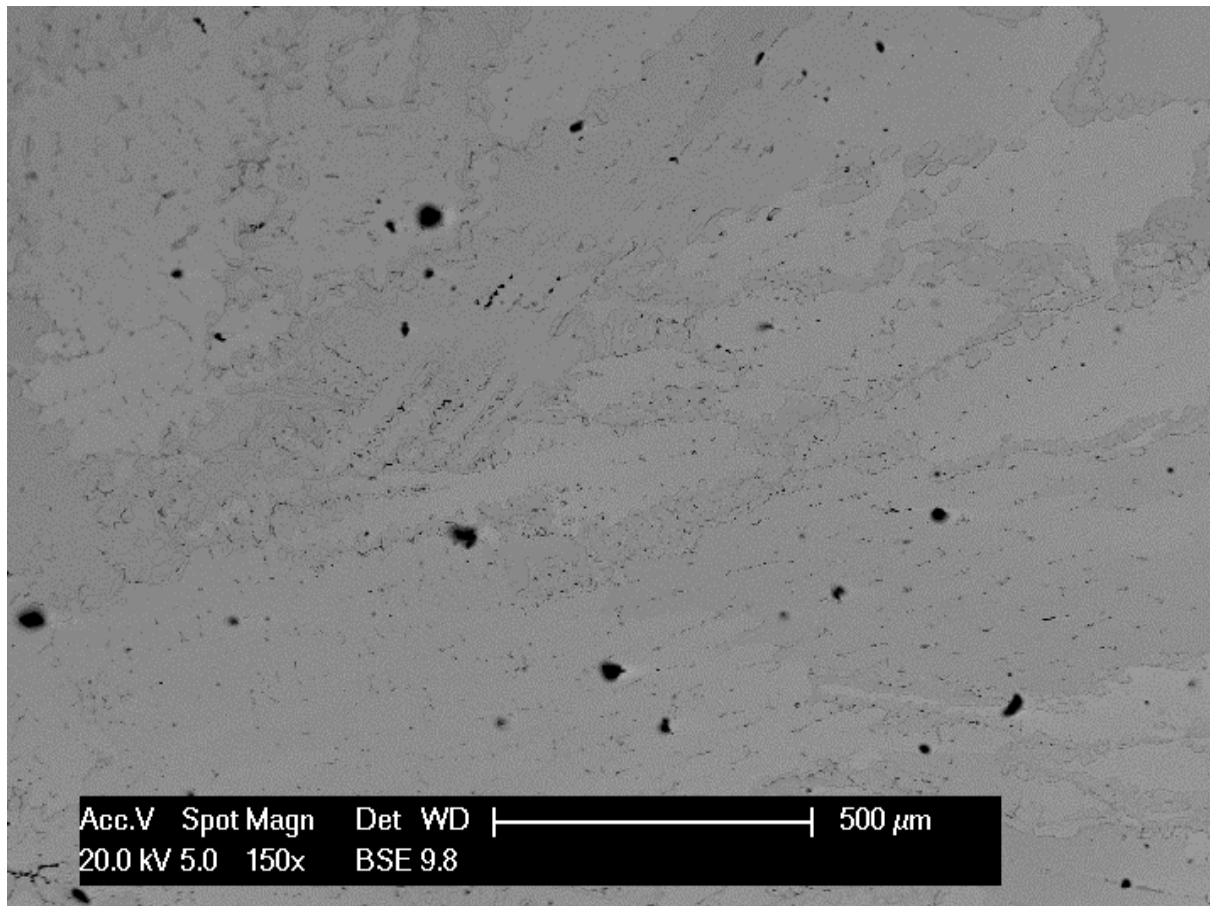


Fig. 5.7 BSE image of microstructure of Ni15Cr6Al model alloy

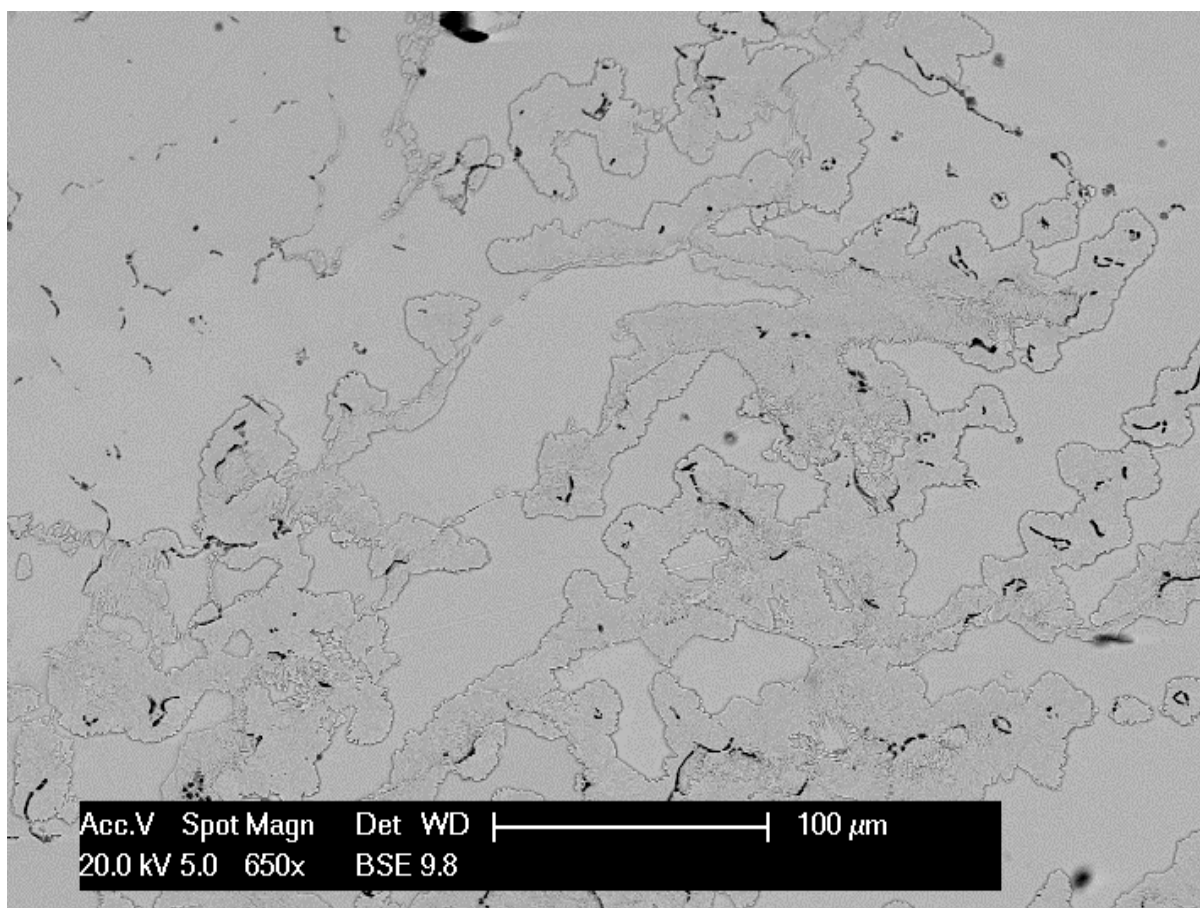


Fig. 5.8 BSE image of microstructure of Ni15Cr6Al model alloy

## 5.4 Measured liquidus and solidus temperatures of Ni-Cr-Al model alloys

### 5.4.1 DSC experiments for determination of liquidus and solidus temperature of model alloys

Differential Scanning Calorimetry is the initial step to measure the change of difference in heat flow rate in order to determine heat treatment window for solution and ageing process.

The solidus, liquidus temperatures, enthalpy changes and heat capacity of all as-cast samples were derived from a Netzsch 404 F3 Pegasus DSC instrument at University of Leicester. Temperatures are measured with S-type thermocouples (Pt10%Rh-Pt), which is calibrated against the melting temperatures of pure gold and pure nickel. Semi-circle samples of approximately 2 mm in radius with thickness of 1 mm were prepared for the DSC runs and

alumina crucibles were used in all DSC experiments. All samples have been cleaned using ultra-sonic machine to produce accurate DSC measurements. A high purity argon environment with an argon flow rate of  $50 \text{ ml min}^{-1}$  was performed during experiments in order to minimise the oxidising effects.

The heating rate corresponding to three repeated heating/cooling cycles is  $10 \text{ K min}^{-1}$ . 10 minutes isothermal hold between each heating and cooling cycle was used to equilibrate the heating flow between heating and cooling cycle. The measured heat flow during holding will be used to calibrate the heat flow during heating and cooling cycle to improve measurement accuracy of DSC signal. All samples were subjected to following heating/cooling cycles with diagram represented in Fig. 5.9:

*room temperature to 1273 K (1000 °C) → isothermal holding at 1273 K (1000 °C) for 10 minutes → heating at  $5 \text{ K min}^{-1}$  up to 1723 K (1450 °C) → isothermal holding at 1723 K (1450 °C) for 10 minutes → cooling at  $10 \text{ K min}^{-1}$  from 1723 K (1450 °C) to 1273 K (1000 °C) → isothermal holding at 1273 K (1000 °C) for 10 minutes → cooling at  $10 \text{ K min}^{-1}$  from 1723 K (1450 °C) to room temperature.*

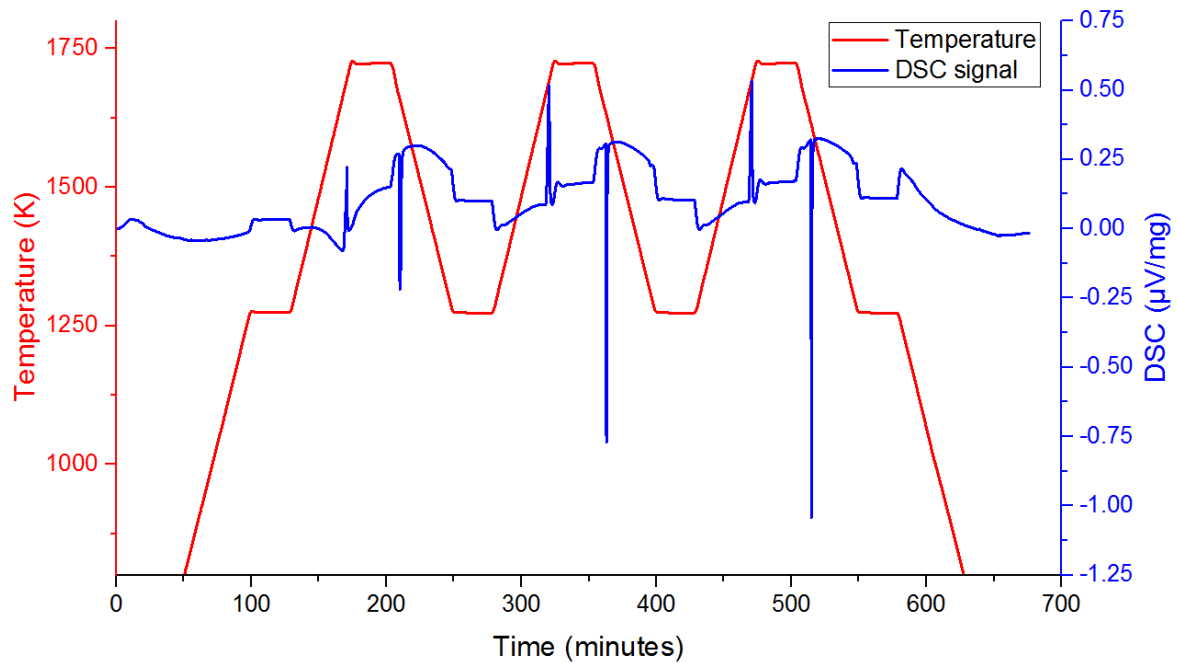


Fig. 5.9 Heat/cooling cycles of DSC experiment measured in Ni5Cr7Al alloy

The raw data from DSC was subsequently analysed by a commercial programme Netzsch Proteus Software 5.1 to evaluate thermal properties of data autonomously. In this programme, study of DSC curve is able to determine liquidus and solidus temperatures, the integral of curve provide the enthalpy change throughout the selected temperature range. Specific heat capacity in this software is obtained from three measurements, i.e. baseline without sample, calibration (using sapphire) and sample runs. All sample runs are using lids to maintain accurate thermodynamic measurements.

The raw DSC data (heating / cooling) was subsequently manipulated using a numerical programme CALCOR to calculate the enthalpy change from the DSC measurements by treating the complete process of heat flow within the DSC apparatus, details of which calibration are available from Dong et al [136-138]. With the calibrated thermal resistances for the instrument, the programme is able to de-convolute the measured signals and to extract accurate transition temperatures and enthalpy changes from the DSC measurements.

#### 5.4.2 Results of DSC experiments

Fig. 5.10 represents all peaks of DSC signal traces from repeated heating cycles measured in Ni-2Cr-5Al sample with respect to temperature. Three distinctive peaks were measured when sample is heating up to its melting points, showing the melting of the bulk of the material. The slight difference of temperature between first and the rest measurements is because the first heating segment is designed to eliminate the thermal history of the sample in order to obtain correct melt onset. Therefore, it is typically using measurements from the rest of runs to remove uncertainty of thermal record.

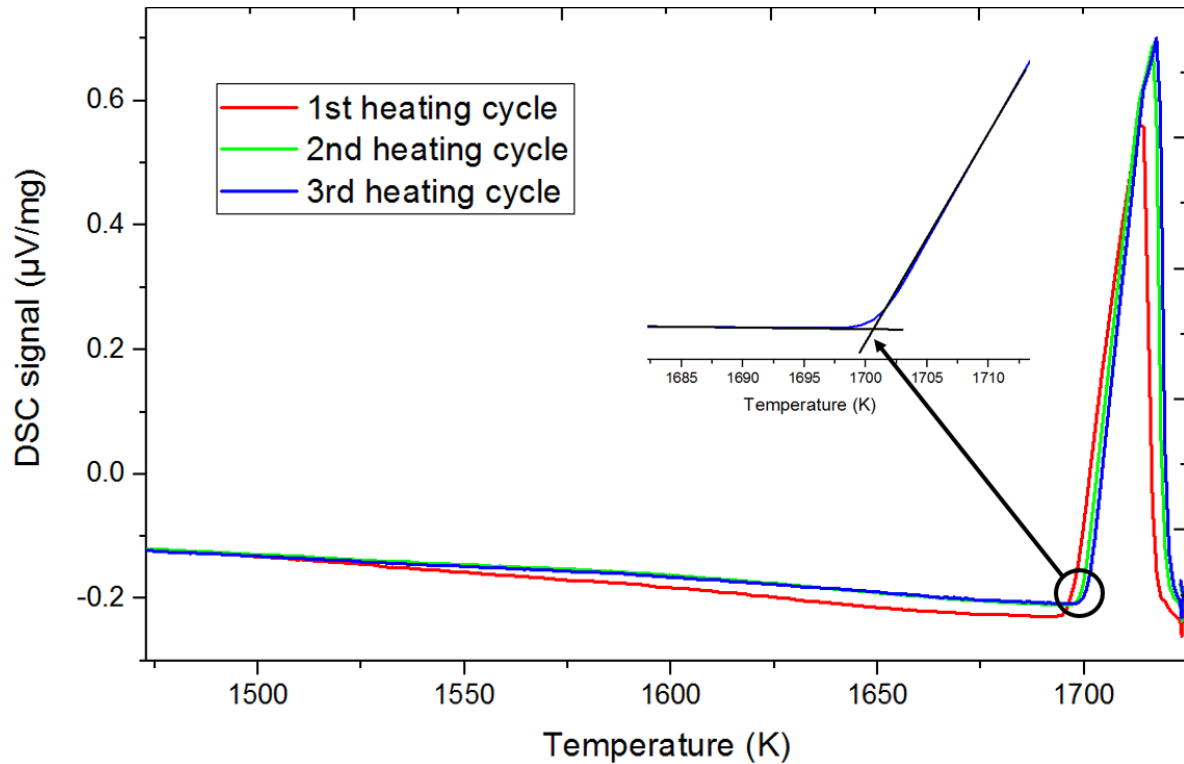


Fig. 5.10 DSC heating curve of as-cast Ni<sub>2</sub>Cr<sub>5</sub>Al sample

Liquidus and solidus temperatures are directly measured from onset of each peak at two sides. Enthalpy change of sample is derived from integral of peak curve with selected range of temperatures. Table 5.5 lists all results of measured liquidus and solidus temperatures with average values calculated in last column. Results from DSC measurements are compared with

thermodynamic calculations from JMatPro [139, 140], which is plotted in Fig. 5.13 marked with error of uncertainty to verify reliability of discrepancy. It is obvious to observe that there is small discrepancy between two lines except alloy 5. Hence, results produced reliable data for following heat treatment design and operating temperature of KEMS experiments, which are dependent on accuracy of thermodynamic results. Cooling cycles are not presented because onset values on DSC cooling curve cannot be properly determined due to the nucleation undercooling.

Table 5.5 Liquidus and Solidus temperature of tested samples

Alloy Number		1st heating cycle	2nd heating cycle	3rd heating cycle	Average
1	Liquidus (K)	1712.5	1713.7	1714.3	1713.5
	Solidus (K)	1696.4	1698.1	1699.4	1698
2	Liquidus (K)	1703.4	1707.5	1710	1707
	Solidus (K)	1691.1	1698.5	1701.5	1697
3	Liquidus (K)	1701.8	1703.3	1704.5	1703.2
	Solidus (K)	1687.2	1689.3	1691.4	1689.3
4	Liquidus (K)	1694	1696.1	1697.6	1695.9
	Solidus (K)	1678.5	1681.8	1683.9	1681.4
5	Liquidus (K)	1696.4	1696.6	1695.8	1695.8
	Solidus (K)	1678.6	1680.2	1681.9	1680.2
6	Liquidus (K)	1694.8	1697	1698.5	1696.8
	Solidus (K)	1679.5	1682.9	1685.4	1682.6
7	Liquidus (K)	1687.3	1688.7	1689.9	1688.6
	Solidus (K)	1668.2	1670.8	1672.8	1670.6
8	Liquidus (K)	1681	1681	1682.1	1681.4
	Solidus (K)	1653	1658.4	1659	1656.8
9	Liquidus (K)	1676.8	1679.5	1681.3	1679.2
	Solidus (K)	1658	1663.2	1666.1	1662.4
10	Liquidus (K)	1668.1	1669.8	1671.6	1669.8
	Solidus (K)	1640.1	1643.8	1645.8	1643.2
11	Liquidus (K)	1655.6	1659.8	1661.8	1659.1
	Solidus (K)	1635.9	1645.1	1647.2	1642.7
12	Liquidus (K)	1652	1653.7	1651.9	1652.5
	Solidus (K)	1626.6	1630.7	1626.2	1627.8
13	Liquidus (K)	1632.6	1635.5	1637.9	1635.3
	Solidus (K)	1605.6	1614.2	1617.7	1612.5
14	Liquidus (K)	1625.8	1630	1632.6	1632.5
	Solidus (K)	1604.5	1612.5	1617.4	1611.5
15	Liquidus (K)	1608.9	1613.8	1616.4	1613
	Solidus (K)	1584.9	1593.8	1597.5	1592.1



## 5.5 Thermodynamic data from CALPHAD calculations

CALPHAD [141] is an acronym for the CALculation of PHase Diagrams. The approach used is referred in scientific literature as CALPHAD method which is possible to predict the phase behaviour of complex, multi-component material based on the extrapolation of high-ordered properties from lower-order binary or ternary systems [142]. Computer programmes, such as JMatPro [139] and ThermCalc [143], are able to perform complicated calculations on a PC to predict phase equilibria in multi-component alloys to a degree that is close to experimental results.

The solidus and liquidus temperatures from JMatPro calculation were determined from phase fraction diagram in Fig. 5.11 which shows phase fraction lines for liquid and  $\gamma$  phase. The software has the function to give readings for any selected points on calculated lines, solidus and liquidus temperatures were determined as captured images in the figure.

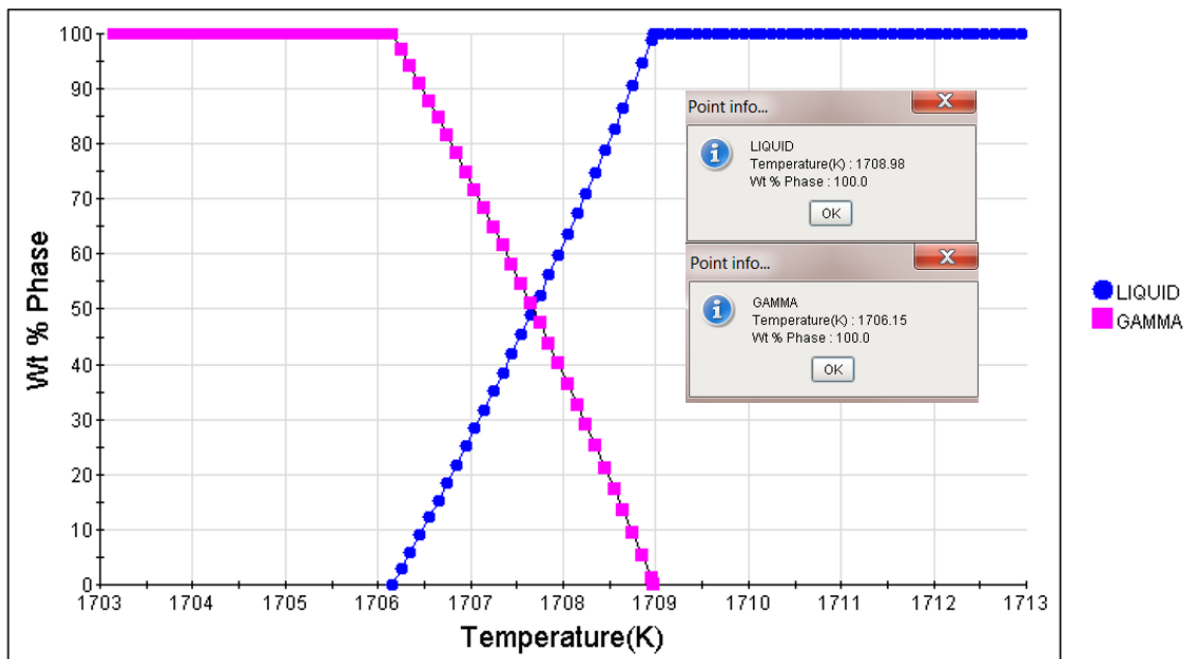


Fig. 5.11 Phase fraction of Ni<sub>2</sub>Cr<sub>5</sub>Al model alloy at 1703-1713 K

According to Table 5.5, the average liquidus temperature from DSC tests for Ni-2Cr-5Al alloy is 1713.5K which is similar to the result from JMatPro calculation. Hence, all liquidus temperatures of different Ni-Cr-Al samples from DSC measurements and JMatPro calculations have been collected and plotted in Fig. 5.12 with error bars. Two curves derived from experimental and modelling are closely attached, showing a good agreement from two methods. Therefore, thermodynamic database developed by ThermoTech Ltd provide a reliable calculation for determining solidus and liquidus temperatures, which are essential factors for subsequent KEMS experiments, in Ni-Cr-Al ternary system.

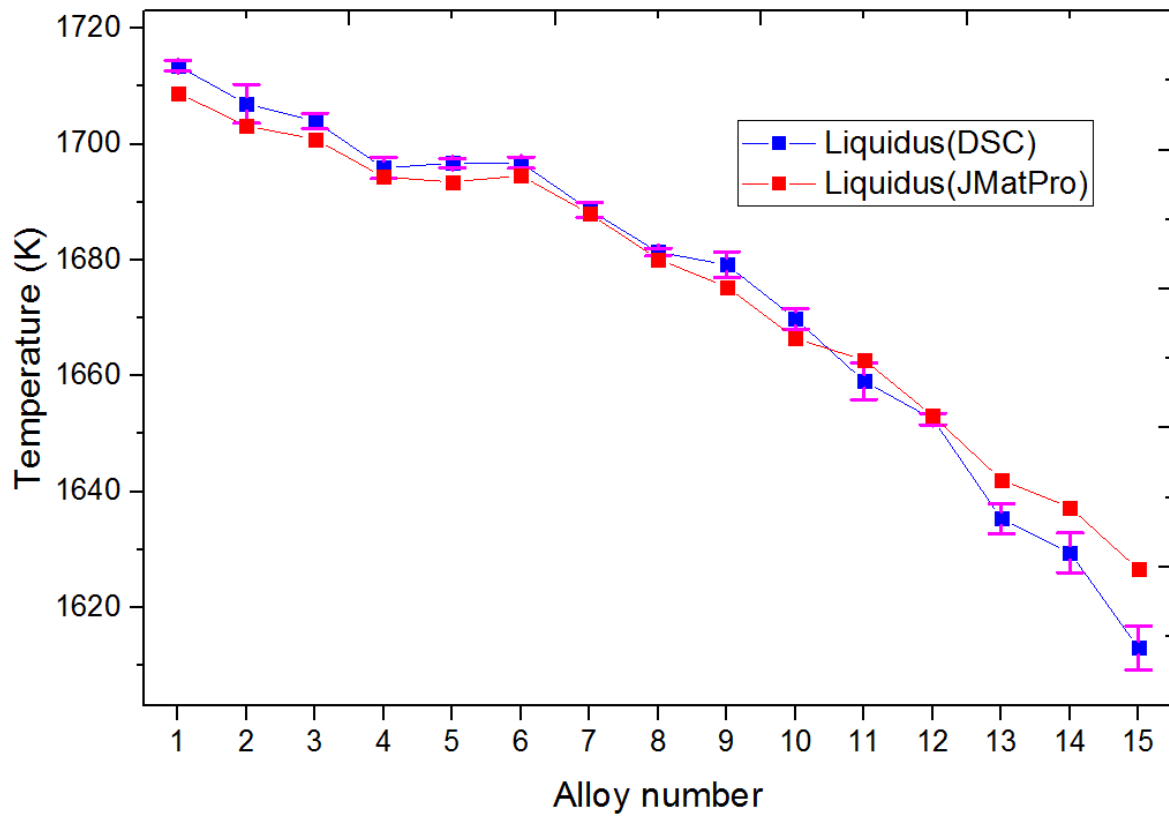


Fig. 5.12 Liquidus temperatures from DSC and JMatPro results of all samples

## 5.6 Estimated activity data for preparation of KEMS experiments

### 5.6.1 Calculated activity for Ni-Cr-Al model alloys using JMatPro

Prior to KEMS experiments, thermodynamic properties of designed Ni-Cr-Al model alloys have been analysed. The comparison between DSC results and JMatPro calculation confirms potential reliability of CALPHAD model used in calculations. In this case, thermodynamic calculation provides an initial insight of elemental interaction in Ni-Cr-Al system at high temperatures as well as predicting the range of thermodynamic activities in Ni-Cr-Al model alloys, since thermodynamic activities of Ni, Al and Cr in Ni-Cr-Al model alloys can also be calculated available in JMatPro.

In Fig. 5.13, results of calculated Cr activity in Ni-Cr-Al model alloys using JMatPro are presented for model alloys containing Al composition fixed at 6 wt%. The activity of Cr increases significantly corresponding to an increase of Cr content from 2 wt% to 30 wt%.

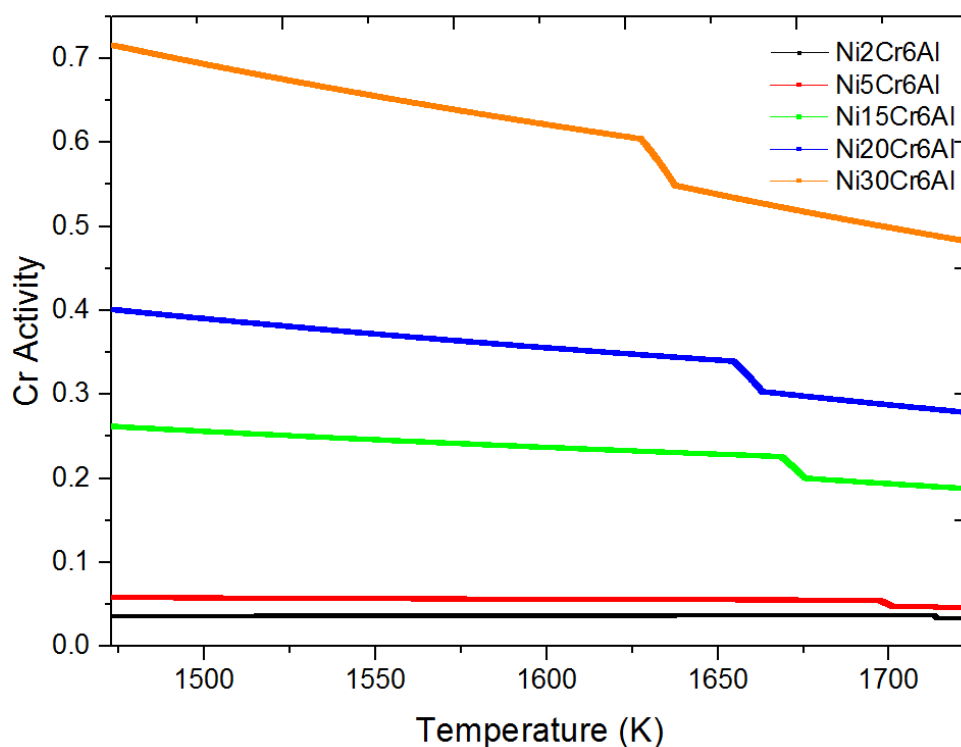


Fig. 5.13 Calculated Cr activities of Ni-Cr-Al mode alloys with 6 wt% Al content using JMatPro

For model alloys with high concentration of Cr, its activity does not strictly follow Henry's law close to ideality. It is assumed that there could be high deviation for results of Cr activity using JMatPro showing the importance of experimental measurements using KEMS technique.

It is noticed that an apparent change of Cr activity in JMatPro calculation at the temperature range from 1623 to 1703 K (1350°C-1430°C). The reason of reduction is compositional variation of concentration due to the phase transformation occurs. And temperature range of variation for each sample has been summarised in Table 5.6. Fig. 5.13 is the phase distribution diagram calculated in 0.1 K interval showing gamma phase of Ni<sub>2</sub>Cr<sub>6</sub>Al alloy transforms to liquid phase at temperature around 1707.5 K (1434.5 °C). Phase transformation at this range of temperatures leads to redistribution of alloy concentration, which reflects as temperature of activity variation of alloy as showed in Fig. 5.13 and Table 5.6.

Table 5.6 Temperature range for a critical drop in calculated activity of Cr from JMatPro

Alloy number	Temp range (K)
1	1706-1709
2	1699-1703
3	1697-1701
4	1689-1694
5	1679-1687
6	1691-1695
7	1683-1688
8	1673-1680
9	1657-1675
10	1657-1666
11	1654-1663
12	1642-1663
13	1628-1642
14	1627-1637
15	1613-1626

Similarly, thermodynamic activities of Ni and Al from JMatPro have been calculated and plotted in Fig. 5.14 and Fig. 5.15 showing predicted range of activity values.

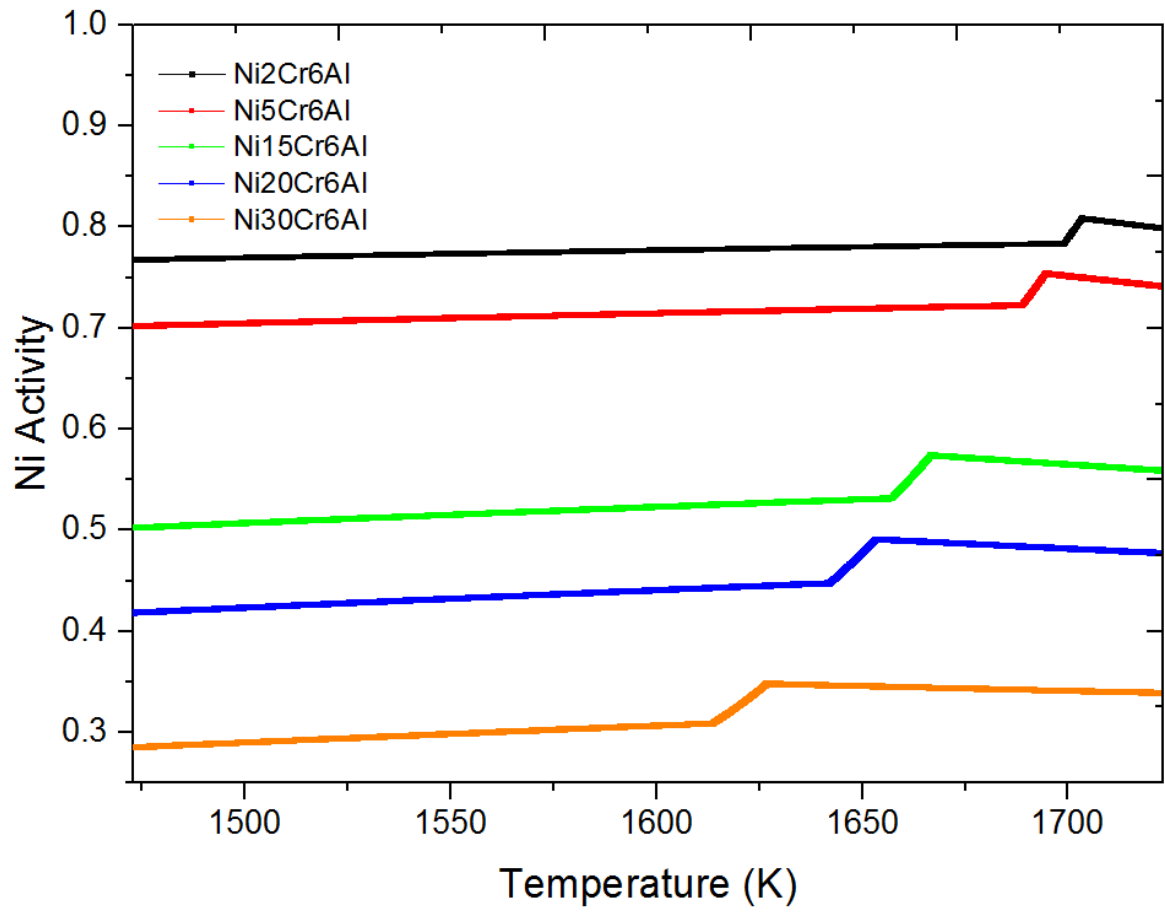


Fig. 5.14 Calculated Ni activities for Ni-Cr-Al mode alloys with 6 wt% Al using JMatPro

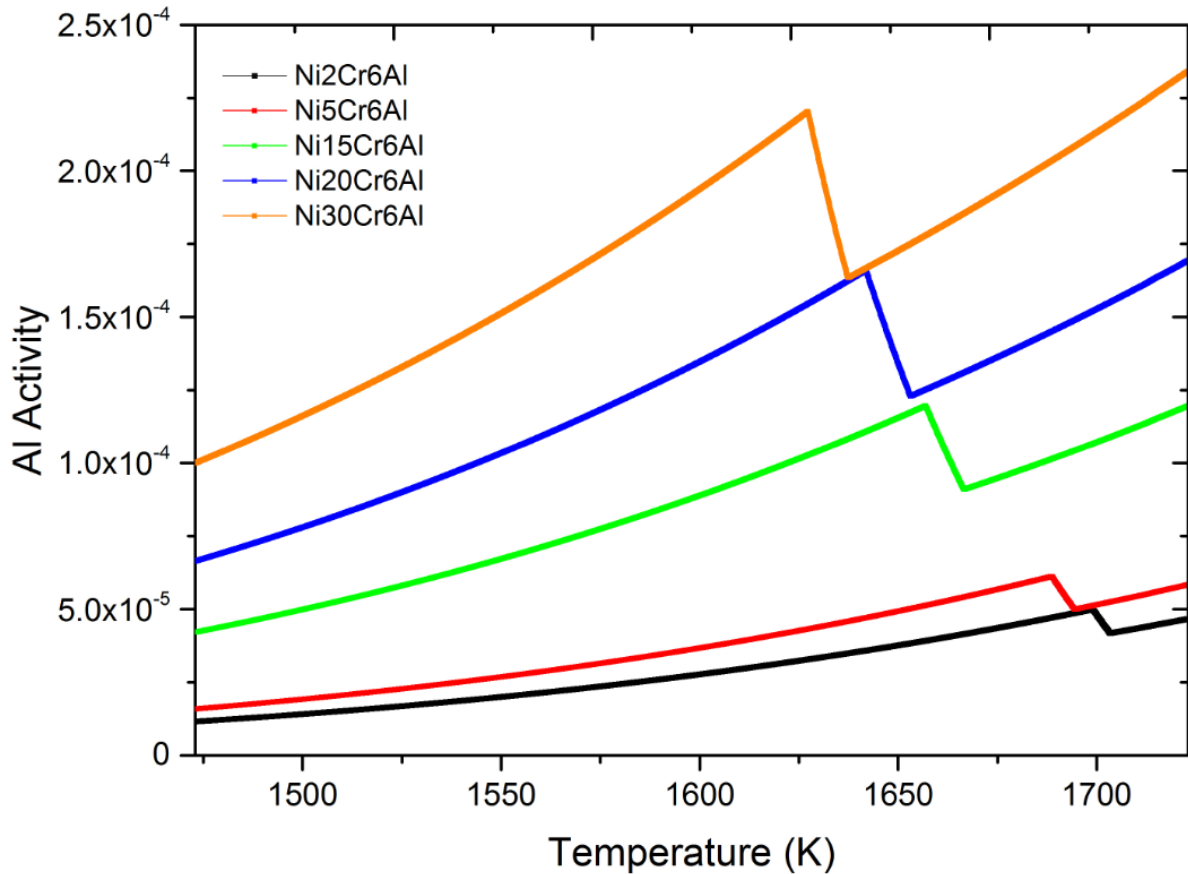


Fig. 5.15 Calculated Al activities for Ni-Cr-Al model alloys with 6 wt% Al using JMatPro

### 5.6.2 Calculated activity for Ni-Cr-Al model alloys using FactSage

The assessment on Ni-Cr-Al ternary system was also performed using the alternative thermodynamic software FactSage which is accessible in Forschungszentrum Jülich, Germany. FactSage [144-146] has a fully integrated thermochemical software and database package. Thermodynamic properties, including component activities and phase diagram, were calculated. Using thermodynamic description adopted from KEMS experiment, optimisation of Ni-Cr-Al ternary system can be achieved.

Calculated results from FactSage for dilute solutions in Ni-Cr-Al model alloys show significant differences with calculations from JMatPro. According to plots in Fig. 5.16 to Fig. 5.18, calculated activities of Ni are roughly similar to each other. The major discrepancies are

activities of dilute solution in Ni-Cr-Al model alloys calculating from two software programmes. The results derived from JMatPro are exceptionally higher than that of in FactSage. Specifically, calculated activities of Cr in FactSage for alloys contained Cr content higher than 15 wt% are at least 40% lower than that of results from JMatPro. While activities of Al calculated in FactSage is approximately half of values from JMatPro's results. Hence, in order to determine the correction of two databases, the KEMS method will provide accurate assessment for correcting thermodynamic calculation.

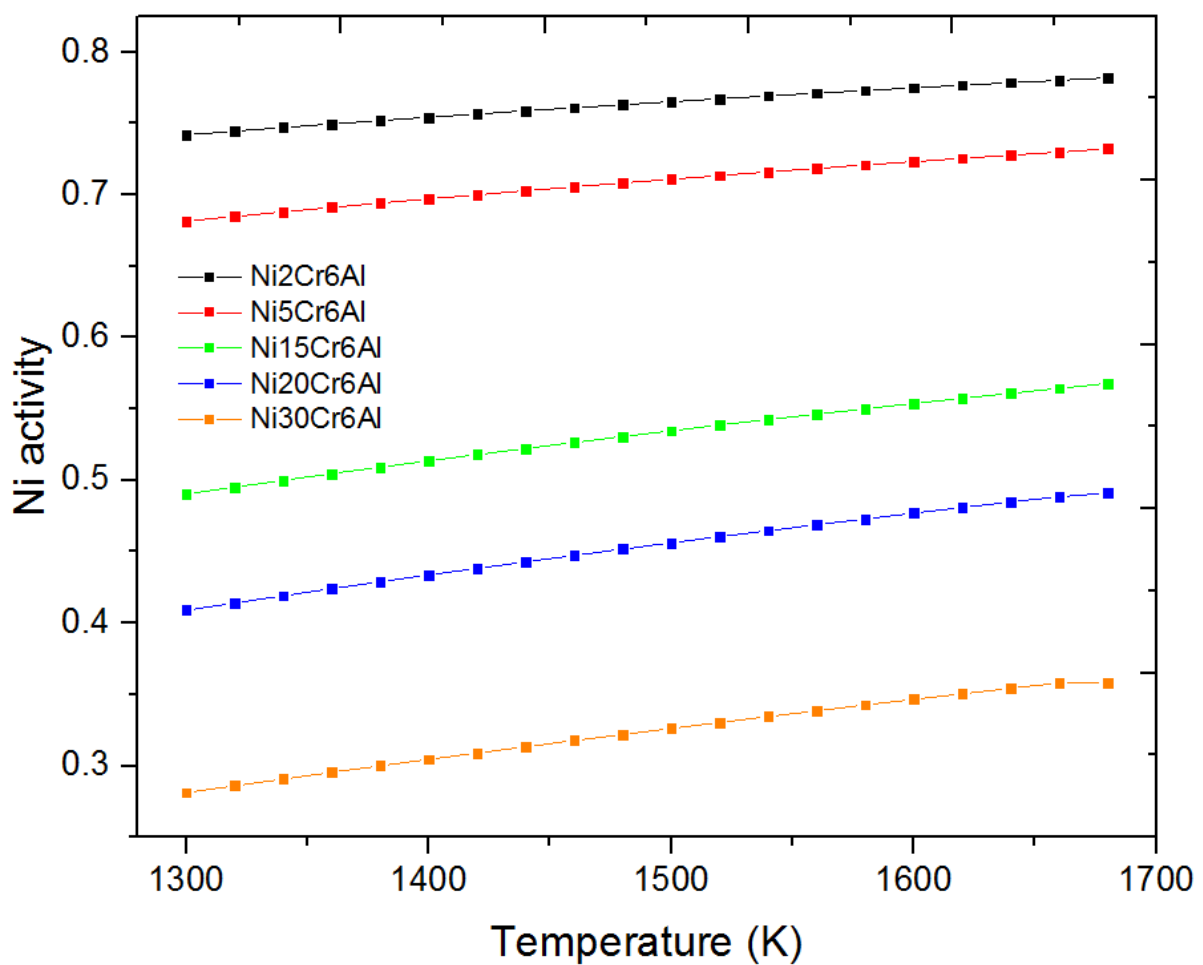


Fig. 5.16 Calculated activities of Ni in Ni-Cr-Al model alloys with 6 wt% Al content using FactSage



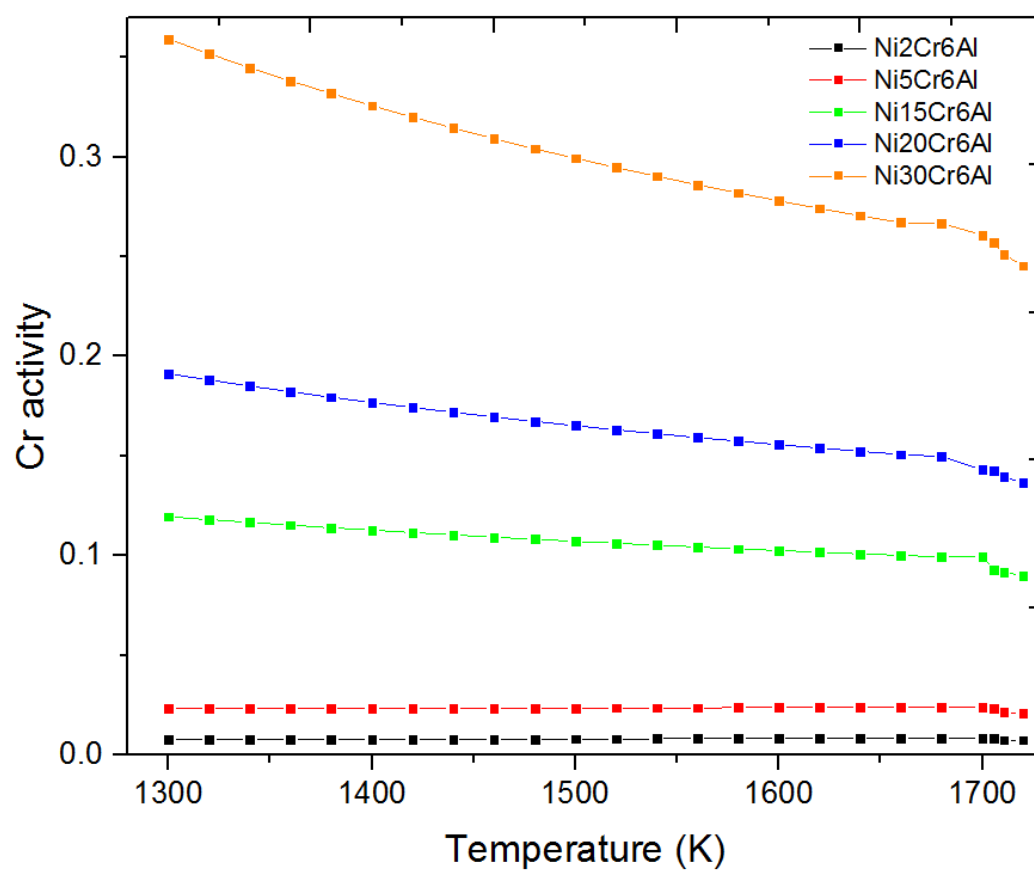


Fig. 5.17 Calculated activities of Cr in Ni-Cr-Al mode alloys with 6 wt% Al content using FactSage

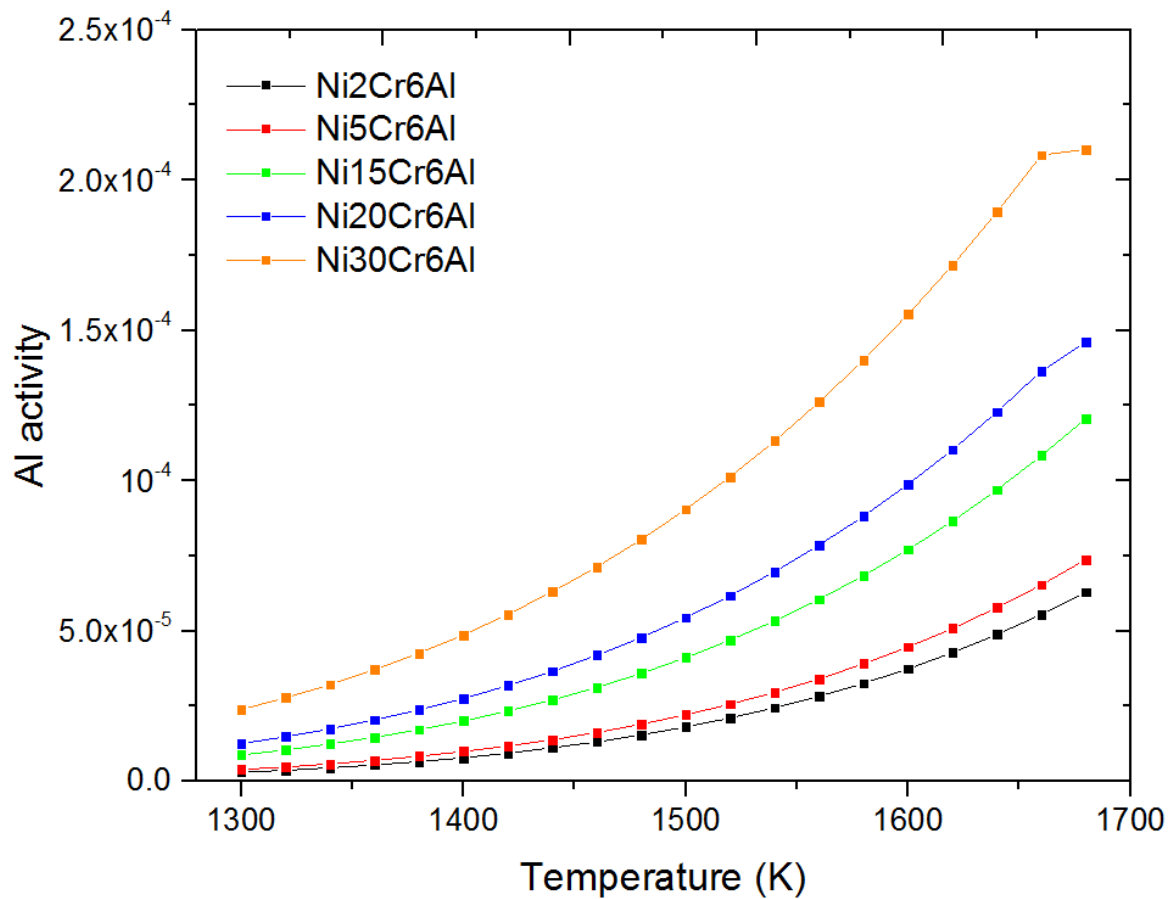


Fig. 5.18 Calculated activities of Al in Ni-Cr-Al model alloys with 6 wt% Al content using FactSage

## 5.7 Conclusions

Thermophysical properties of Ni-Cr-Al model alloys have been examined by measurements from DSC and thermodynamic calculation using JMatPro and FactSage. There is a good agreement on liquidus and solidus prediction for produced alloy. All Ni-Cr-Al model alloys have single  $\gamma$  phase field for temperature higher than 1473K (1200 °C). The measured data will be used to determine temperature range in subsequent KEMS experiments for heating/cooling cycles without reaching phase transition temperatures. According to preliminary thermodynamic data, Ni-Cr-Al model alloy require accurate assessment using KEMS method as an optimisation of existing model used in CAPHALD approach.

Microstructural characterisation of as-cast Ni-Cr-Al model alloy show potential formation of eutectic phase at grain boundaries or interface in high Cr model alloy. Hence, KEMS method also offer sufficient information in terms of thermodynamic results which can be derived from thermodynamic activity showing correlation of composition, Raoult's law and possible phase transition. More details will be discussed in following chapter.

## **6. Elemental sublimation in Ni-Cr-Al model alloys through thermodynamic analysis and measurements of partial pressures for Ni, Al and Cr**

As described in Chapter 5, the intension of KEMS study is to investigate high-temperature behaviours of elements with high partial pressure, i.e. Ni, Al and Cr, in Ni-base alloy to ascertain the effect of elemental sublimation on microstructural instability at surface. Therefore, ternary Ni-Cr-Al model alloys, as one of the most important sub-system of Ni-base superalloys, were selected for evaluation of elemental sublimation under such considerations.

### **6.1 Sublimation induced microstructural instability in Ni-base superalloys**

During the kinetic-influenced solution heat treatment of Ni-base superalloys, elements undergo the processes of sublimation and deposition. Elemental sublimation is likely to occur during solution heat treatment of Ni-base superalloys. This phenomenon results in microstructural instability at the casting surface of superalloys, which were reported in recent studies [78, 80, 91, 92, 107]. According to existing results, it was deduced that elemental losses of Ni, Al and Cr via vaporisation/sublimation and destabilisation of  $\gamma$  phase followed by redistribution of Re, Cr and W in surface region. Phase evolution on the surface of superalloys is attributed to form surface defects and degrade high temperature performance of turbine blades. Therefore, to further analyse occurrence of microstructure instability during solution heat treatment, investigation associated with thermodynamic analysis of Ni, Al and Cr on the surface area was proposed as an effective method to achieve this objective. Under this consideration, KEMS measurements is optimal technique to determine partial pressures of Ni, Al and Cr in Ni-base alloys that establishes understanding of elemental losses during solution heat treatment. Consequently, KEMS data with proper analysis will determine elemental

interaction on the surface during solution heat treatment. Relevant mechanism/principles of sublimation on the surface can be identified. Meanwhile, protective solutions of Ni-base alloys surface can also be developed as an appreciated method to suppress the extent of microstructural defects during casting and heat treatment process.

Sublimation process can be assessed by evaluating thermodynamic properties of alloys. Occurrence of microstructural instability in Ni-base superalloys confirmed the effect of sublimation on the surface of alloy during solution heat treatment. As surface behaviours of Ni-base superalloys are complicated phenomenon combined with occurrence of oxidation and diffusion at high temperatures. To precisely investigate sublimation process in Ni-base superalloys, a fundamental study is proposed to commence with thermodynamic analysis by evaluating activities and partial pressures of Ni, Al and Cr in Ni-Cr-Al model alloys. With determination of those thermodynamic profiles, other terms, such as chemical potential, can be further derived. Incorporating thermodynamic properties of Ni-base alloy, elemental behaviours at high temperatures will be qualitatively evaluated providing solutions for preventing the alloy surface from formation of defects in casting and processing of Ni-base superalloys.

## **6.2 Principles and instrumentation of Knudsen effusion mass spectrometry**

Accurate measurement of thermodynamic properties is important for understanding multiple-component solution and predicts stability of systems at different environments. The development of CALPHAD method, which is extremely useful for modelling material processing, requires measurements of thermodynamic functions as parameters to predict reaction between different circumstances.

KEMS is the technique based on measurements of an established vapour pressure [147-149], which relates to thermodynamic measurements of metals and alloys at high temperatures. It is able to effectively analyse the vapour pressures from  $10^{-11}$  Pa and temperature range between 500-2800K. The high sensitivity of a mass spectrometer permits the measurement of very low partial pressures. The unique capability of KEMS offers advantage of identifying all species present in the vapour phase in equilibrium with a condensed phase [121]. By measuring numbers of ions with high sensitivity and resolution under high vacuum conditions, the method enables precise quantification of high temperature behaviours for the individual element in a system.

The instrument is used to detect gaseous species effusing from the Knudsen cell providing qualitative and quantitative measurements of most inorganic materials. Hence, it is a direct method to ascertain the vapour species and their equilibrium pressure above the condensed phase at high temperatures [110, 150, 151]. Reviews of high temperature mass spectrometry are available from several pioneer work in literature. Drowart and Goldfinger [152] described the method of inspection of molecular beams and discussed some thermodynamic parameters, such as change of enthalpy and ionisation cross sections. Fabian [153] presented an overview on the application of mass spectrometry in the field of metallurgy and materials science. Comprehensive reviews of molecular species observed in high temperature vapours and their bond energies have been provided by Gingerich [154]. Limitation of applying mass spectrometry to high-temperature equilibrium studies was discussed by Stafford [155].

KEMS has been proven as optimum in evaluating sublimation process in past decades with determination on thermodynamic properties of condensed phases, such as thermodynamic activities, mixing properties, and Gibbs energies of formation. Fig. 6.1 shows the KEMS

facilities at Forschungszentrum Jülich, Germany [156] showing the major components of the entire system.



Fig. 6.1 KEMS at Forschungszentrum Jülich in Germany

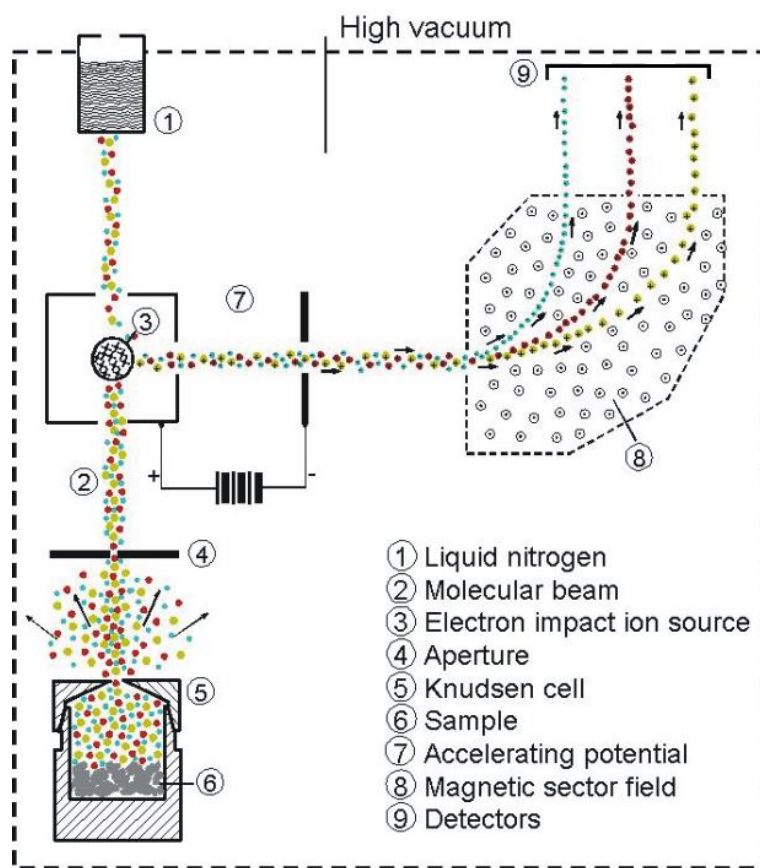


Fig. 6.2 Schematic diagram for principles of static KEMS [151]

Schematic diagram of KEMS measurements is illustrated in Fig. 6.2, the sample (6) is held in Knudsen cell (5) and heated uniformly. A molecular beam (2) of evaporated species from the Knudsen cell enters the ion source via an aperture (4). The shutter is used to separate the ion source from sample chamber to protect the ionisation chamber against contamination. The vapour species are ionised by electron impact ( $M(g) + e^- = M^+ + 2 e^-$ ) by an emission current of 0.7 mA and electron energy of 70 eV. A set of collimating lenses focuses the ion beam and, on the way to the entrance slit of the mass analyser (8), the ion kinetic energy is boosted by an accelerating potential of 8 kV. The entering kinetic energy of all ions with the same charge is nearly mono-energetic at 8 keV, but their velocities follow the law of classical mechanics, wherein the speed of a particular ion is proportional to the reciprocal to the square root of its mass. The path of an ion passing the sector field analyser is affected by a combined action of



perpendicular electric and magnetic fields described by the electromagnetic force. By dynamically changing the electrical field strength, the ions of different mass are separated according to their mass-to-charge ratio. The final place for the ions is in the detector (9). A quantity of ions is directed into a Faraday cage and the current is directly recorded as a potential drop across a high resistance ( $10^{11} \Omega$ ). At low quantity, the ions are directed to impact the first dynode of the multiplier, where they induce a secondary emission of electrons. The secondary electrons are amplified through a cascade of plates with increasing potential difference. On each plate the electron emission is multiplied and finally the number of secondary electrons ends in a shower that is about  $10^6$  times the starting number. The number of electrons is now high enough to be recorded either as a potential drop through a resistor or as a burst that is counted (ion-counting). In this study, those were generally done with ion counting in order to avoid a mass discrimination caused by the multiplier and the ion counts were converted to an intensity signal of a potential drop [157]. The schematic diagram of KEMS at Forschungszentrum Jülich has been reproduced in Fig. 6.3 showing all details of KEMS set-up.

A cryogenic pump filled with liquid nitrogen is connected for reduction of background noise in ion source. Ion getter pumps generate the ultrahigh vacuum in the mass spectrometer and a turbo molecular pump is used for evacuating the Knudsen cell chamber. The use of a Hall probe supported magnetic field controller and a mass programmer enable a fast and precise mass adjustment in measurements.

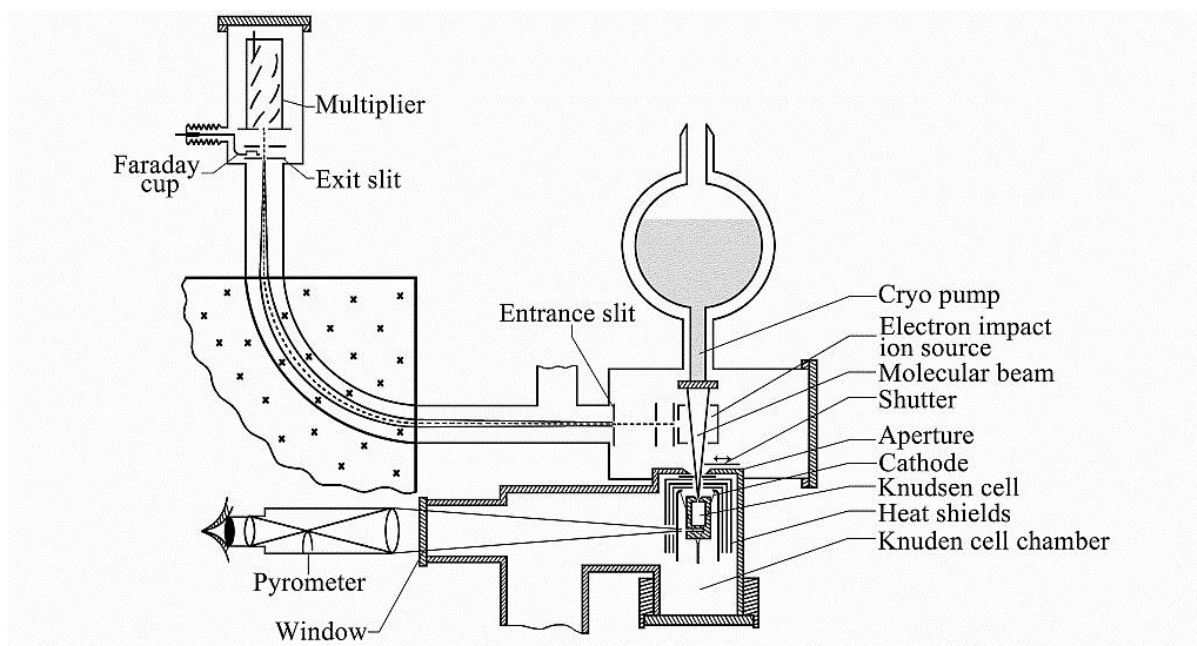


Fig. 6.3 Set-up of a magnetic sector-field Knudsen effusion mass spectrometer

Further details of KEMS principles and its instrumentation are available in several reports [110, 147]. Schematic diagrams of the major sections of equipment are shown in Fig. 6.4 and 6.5 with a good quality illustration of KEMS set-up. Images are adopted according to set-up used in Jülich.

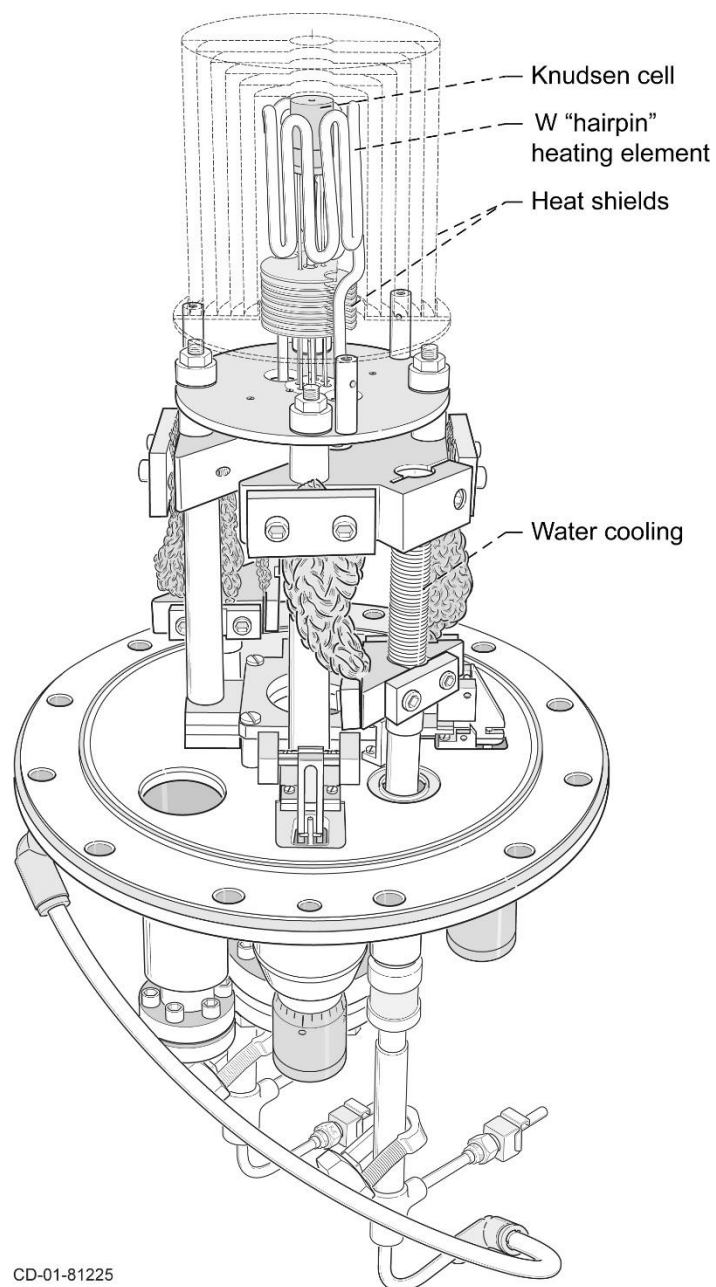


Fig. 6.4 Single-cell flange used in KEMS system. Resistance heating is used with the "hairpin" element [147]

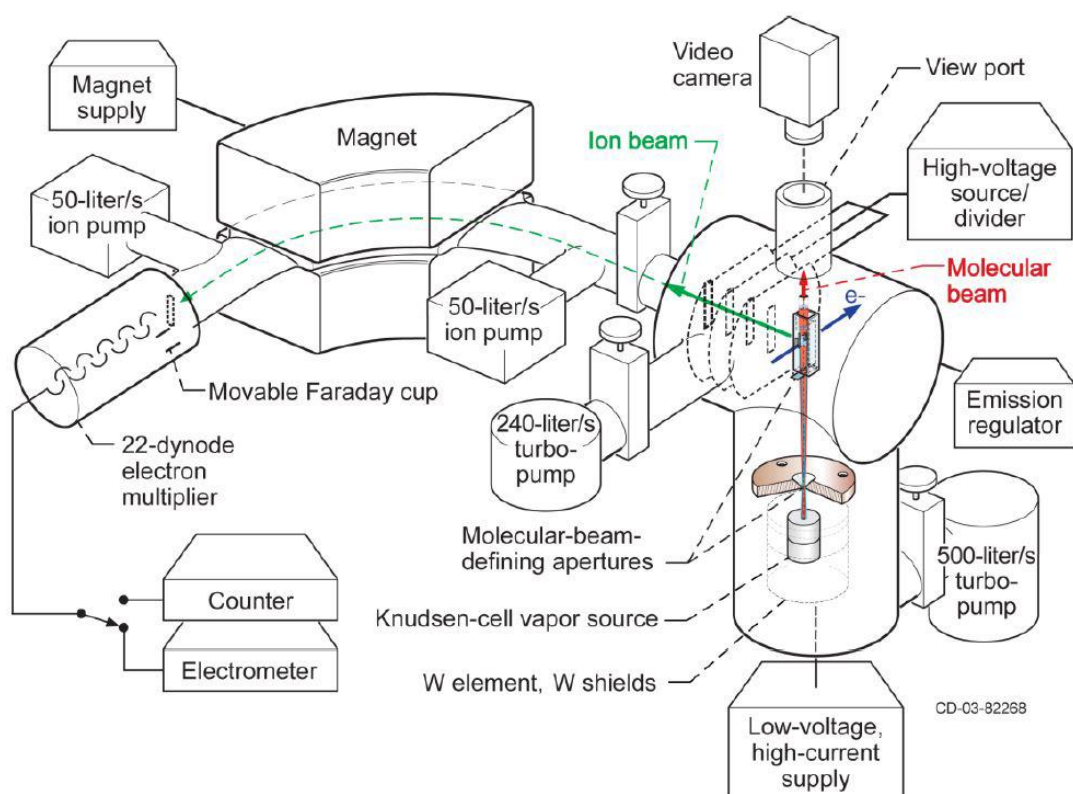


Fig. 6.5 Magnetic-sector instrument in KEMS with indications of key components [147]

### 6.3 Equations for calculating partial pressure and thermodynamic activity

Thermodynamic equilibrium is assumed in a close system during KEMS measurements while a small fraction of molecules (less than 1 mg in 24 h) effuses from a tiny orifice on top of the Knudsen cell [108, 158]. A long isothermal session is needed to effuse composition changing amounts. The sublimation of Ni, Cr and Al elements were detected by counting ions  $\text{Ni}^+$ ,  $\text{Cr}^+$  and  $\text{Al}^+$  from gaseous species  $\text{M}(\text{g})$  ( $\text{M} = \text{Ni}, \text{Cr}, \text{Al}$ ) which is originating from the Knudsen cell with a reaction equation as:  $\text{M}(\text{g}) + \text{e}^- = \text{M}^+ + 2 \text{e}^-$ .

The method for evaluating partial pressure and activity has been well described by Hilpert [150] and Kobertz et al [157]. The relevant evaluation of ion-current-ratio technique can be found from work of Neckel and Wagner [159], Belton and Fruehan [160]. Using the method

in references [150, 157], partial pressure is determined from measured ion intensities  $I_i$  of species  $i$  at temperature  $T$  using Equation 6.1:

$$p_i = k_i \frac{I_i T}{\sigma_i \gamma_i \eta_i} \quad \text{Equation 6.1}$$

where  $T$  is temperature in Kelvin,  $k_i$  is pressure calibration factor for the species  $i$ ,  $p_i$  denotes to partial pressure,  $\sigma_i$  the ionisation cross section, and  $\eta_i$  the isotopic abundance of species  $i$ .

The coefficient  $\gamma_i$  is the multiplier factor which is unity for an ion counting system.

The ionisation cross sections used for the gaseous species are  $\sigma_{Ni} = 5.48$ ,  $\sigma_{Al} = 6.18$  and  $\sigma_{Cr} = 5.1$ , which were reported by Mann [161] at ionisation energy of 70 eV. The isotopic abundance of Ni and Cr were normalised to 100% corresponding to mass of their most abundance isotopes, i.e.  $Ni^{58}$  and  $Cr^{52}$ , calculating as  $\eta_{Ni} = 0.682$ ,  $\eta_{Cr} = 0.838$ , while  $Al^{27}$  has a natural abundance of 100% giving the only isotope for Al with  $\eta_{Al} = 1$  [162-164].

The pressure calibration factor can be derived by comparing vapour pressure of pure Ni, Al and Cr calculated from KEMS measurements to that of reference from IVTANTHERMO data [165]. Therefore, by re-arranging Equation 6.3, calibration factor for Ni is given by  $2.71 \times 10^{-9}$  Pa/mV K using values of  $p_{Ni}$  (IVTANT) =  $8.44 \times 10^{-3}$  Pa,  $\eta_{Ni} = 0.682$ ,  $\sigma_{Ni} = 5.48$ ,  $I_{Ni} T = 1.15 \times 10^7$  mV K. Factors for Cr and Al can be calculated in the same manner.

After calibration of pressure factor  $k$ , partial pressures of Ni, Al and Cr are calculated from measured ion intensities of elements from Equation 6.1. According to the Clausius-Clapeyron Equation [166, 167], the relationship between variations of temperature and pressure maintaining equilibrium is given:

$$\frac{dp}{dT} = \frac{\Delta S}{\Delta V} = \frac{\Delta H}{T \Delta V} \quad \text{Equation 6.2}$$

where  $\Delta H = T\Delta S$  due to  $\Delta G = 0$  in equilibrium, as ideal gas is assumed, Equation 6.3 becomes:

$$dp = \frac{\Delta H}{\Delta V} \times \frac{dT}{T} = \frac{\Delta H \times p}{RT} \times \frac{dT}{T} \quad \text{Equation 6.3}$$

$$\frac{dp}{p} = \frac{\Delta H}{R} \times \frac{dT}{T^2} \quad \text{Equation 6.4}$$

Thus, by integrating Equation 6.5, it is derived as pressures related to temperature change,

i.e.

$$\ln\left(\frac{p_1}{p_2}\right) = -\frac{\Delta H}{R}\left(\frac{1}{T_1} - \frac{1}{T_2}\right) \quad \text{Equation 6.5}$$

where  $p_1$  is initial pressure and  $p_2$  is pressure related to temperature change from  $T_1$  and  $T_2$ .

R is gas constant. Considering partial pressure change for a pure element,  $p_p$ , when temperature changes from  $T_1$  to  $T_2$ ,

$$p_{p,T_2} = p_{p,T_1} e^{-\Delta H_p/R(T_2-T_1)} \quad \text{Equation 6.6}$$

Similarly, partial pressure in a system,  $p_s$ , is:

$$p_{s,T_2} = p_{s,T_1} e^{-\Delta H_s/R(T_2-T_1)} \quad \text{Equation 6.7}$$

By using Clausius-Clapeyron Equation, activity can be arranged as at temperature  $T_2$ :

$$a = \frac{p_{s,T_2}}{p_{s,T_1}} \times \frac{p_{p,T_1} e^{-\Delta H_s/R(T_2-T_1)}}{p_{p,T_2} e^{-\Delta H_p/R(T_2-T_1)}} = \frac{p_{s,T_2}}{p_{s,T_1}} \times \frac{p_{p,T_1}}{p_{p,T_2}} \times e^{-(\Delta H_s + \Delta H_p)/R(T_2-T_1)} \quad \text{Equation 6.8}$$

$p_{p,T_1}$  and  $p_{s,T_1}$  in Clausius-Clapeyron Equation are set to standard condition where  $T = 298\text{K}$

and  $p = 1 \text{ atm} = p^\ominus$ , hence  $p_{p,T_1} = p_{s,T_1} = p^\ominus$ . The value of activity depends on choice of

reference state, which is normally using stable defect-free phase of pure element at selected temperature.

Activity ( $a_i$ ) is defined as the ratio of a component's fugacity ( $f_i$ ) in the solution to its fugacity in standard state ( $f_i^0$ ) [168]. Thus, Equation 6.9 is given:

$$a_i = \frac{f_i}{f_i^0} \quad \text{Equation 6.9}$$

Hence the activity of an species is calculated in the partial pressure of the element compared to the standard pressure,  $p^\ominus$ , which is listed as Equation 6.9:

$$a_i = \frac{p_i}{p^\ominus} / \frac{p_i^0}{p^\ominus} = \frac{p_i}{p_i^0} \quad \text{Equation 6.10}$$

where  $p_i$  and  $p_i^0$  are equilibrium vapour pressure of  $i$  over alloy and pure substance, respectively. This is a special form where the equilibrium constant at mean temperature  $T_m$  is represented by the partial pressure of the elements under consideration.

The equilibrium constant  $K$  is defined as the product of the activities  $a_i$  of the reactants, which can be determined from partial pressures and temperature dependence [150] using Equation 6.3:

$$K_p = \Pi \left( \frac{p_i}{p^\ominus} \right) \quad \text{Equation 6.11}$$

Considering KEMS method, for a pure element, partial pressure using equation 6.1 can be arranged as Equation 6.12:

$$p_p = k \frac{I_p T}{\sigma_p \gamma_p \eta_p} \quad \text{Equation 6.12}$$

For a system, partial pressure in Equation 6.1 is shown as follows:

$$p_s = k \frac{I_s T}{\sigma_s \gamma_s \eta_s} \quad \text{Equation 6.13}$$

It is considered in a same element,  $\sigma_p = \sigma_s$ ,  $\gamma_p = \gamma_s$ ,  $\eta_p = \eta_s$ , therefore, activity can now be calculated using the following equation:

$$a = \frac{p_s}{p_p} = \frac{I_s}{I_p} \quad \text{Equation 6.14}$$

As  $\Delta G = 0$  in equilibrium, Gibbs energy is derived with respect to the equilibrium constant  $K_p$  according to its definition as:

$$\Delta G_T^0 = -RT \ln K_P = \Delta_{sub}H_i^0 - T\Delta_{sub}S_i^0 \quad \text{Equation 6.15}$$

Thus the equilibrium constant  $K_p$  is determined as an Arrhenius plot by rearranging Equation 6.15:

$$\ln K_P = -\frac{\Delta_{sub}H_i^0}{R} \frac{1}{T} + \frac{\Delta_{sub}S_i^0}{R} \quad \text{Equation 6.16}$$

$\Delta_{sub}H_i^0$  is the enthalpy of sublimation for species  $i$ ,  $\Delta_{sub}S_i^0$  is entropy of sublimation for species  $i$ .  $R$  is the gas constant. In the equation, the ratio of  $\Delta_{sub}H_i^0$  and  $\Delta_{sub}S_i^0$  to gas constant can be presented as constants  $A$  and  $B$ , therefore the linearity logarithm of partial pressure and reciprocal temperatures is obtained.

Considering reaction for element  $i$  in condensed phase and gas phase following reaction  $i(c) \rightleftharpoons i(g)$ ,  $K_p$  in pure element becomes:

$$K_P(i)_p = \frac{p_p(i(g))}{a_p(i(c))} = p_p(i(g)) \quad \text{Equation 6.17}$$

where activity for pure element is equal to 1.

And  $K_p$  in system is presented as Equation 6.18:



$$K_P(i)_s = \frac{p_s(i(g))}{a(i(c))} \quad \text{Equation 6.18}$$

Combining Equation 6.17 and 6.18, activity of element  $i$  in system is derived as:

$$a(i) = \frac{p_s(i(g))}{p_p(i(g))} \quad \text{Equation 6.19}$$

Arrhenius plot in Equation 6.16 is rearranged with respect to Equation 10 in terms of activity against reciprocal temperature as:

$$\ln \left( \frac{p_s}{p_p} \right) = \ln a_i = -\frac{\Delta_s H_i^0}{R} \frac{1}{T} + \frac{\Delta_s S_i^0}{R} = -A \times \frac{1}{T} + B \quad \text{Equation 6.20}$$

The activity equation can also be deviated in terms of the change in Gibbs free energy for a mixing/solution reaction, which provides relative chemical potentials [169, 170].

$$\mu_i = \mu_i^0 + RT \ln a_i \quad \text{Equation 6.21}$$

where  $\mu_i$  is chemical potential of species  $i$  in mixture,  $\mu_i^0$  is chemical potential of species  $i$  in mixture under standard condition which normally is chemical potential of pure compound at 298K,  $R$  is the gas constant,  $T$  is the temperature.

It is noticed that there is a profound effect of temperature on counting the number of ions in KEMS measurements. By considering temperature dependence without affecting sensitivity between different sets of data [160, 171, 172], coefficient  $s$  is applied to calibrate the sensitivity dependence of KEMS data. This method combines ion intensity data from pure Nickel and Ni-Cr-Al model alloys to eliminate possible temperature bias in ion counting. Following equations express the method corresponding to KEMS data:

$$s_{pure}(i) = \frac{I_{pure}(i)}{I_{pure}(Ni)} \quad \text{Equation 6.22}$$

$$s_{alloy}(i) = \frac{I_{alloy}(i)}{I_{alloy}(Ni)} \quad \text{Equation 6.23}$$

With combination of Equation 6.6, 6.11 and 6.12, the activity of the component  $i$  can be determined as Equation 6.13:

$$a_i = a_{Ni} \frac{s_{pure}(i)}{s_{alloy}(i)} \quad \text{Equation 6.24}$$

where  $a_{Ni}$  is equal to  $\frac{I_{alloy}(Ni)}{I_{pure}(Ni)}$ .

The consistency of measured activities can be simultaneously verified by calculations from Gibbs-Duhem integral Equation. In terms of activity coefficient, it can also be derived as Gibbs-Duhem ion intensity ratio (GD-IIR) method [171-173] which uses mixture of components in Ni-Cr-Al ternary system with following equations:

$$\ln \gamma_{Ni}(c) = \ln \gamma_{Ni}(c_{ref}) - \int_{c_{ref}}^c c_{Al} d \ln \frac{I_{Al} c_{Ni}}{I_{Ni} c_{Al}} - \int_{c_{ref}}^c c_{Cr} d \ln \frac{I_{Cr} c_{Ni}}{I_{Ni} c_{Cr}} \quad \text{Equation 6.25}$$

$$\ln \gamma_{Al}(c) = \ln \gamma_{Al}(c_{ref}) - \int_{c_{ref}}^c c_{Cr} d \ln \frac{I_{Cr} c_{Al}}{I_{Al} c_{Cr}} - \int_{c_{ref}}^c c_{Ni} d \ln \frac{I_{Ni} c_{Al}}{I_{Al} c_{Ni}} \quad \text{Equation 6.26}$$

$$\ln \gamma_{Cr}(c) = \ln \gamma_{Cr}(c_{ref}) - \int_{c_{ref}}^c c_{Ni} d \ln \frac{I_{Ni} c_{Cr}}{I_{Cr} c_{Ni}} - \int_{c_{ref}}^c c_{Al} d \ln \frac{I_{Al} c_{Cr}}{I_{Cr} c_{Al}} \quad \text{Equation 6.27}$$

where the activity coefficient  $\gamma_i$  is defined as the ratio of activity and concentration,  $a_i/c_i$ . The atomic mole fraction  $c_{Ni}$ ,  $c_{Al}$  and  $c_{Cr}$  are calculated in terms of atom number  $N$  from Equation 6.17.

$$c_{Ni} = \frac{N_{Ni}}{N_{Ni}+N_{Al}+N_{Cr}}, c_{Al} = \frac{N_{Al}}{N_{Ni}+N_{Al}+N_{Cr}}, c_{Cr} = \frac{N_{Cr}}{N_{Ni}+N_{Al}+N_{Cr}} \quad \text{Equation 6.28}$$

The integral term in GD-IIR method can be evaluated from the area of plot using concentration of component  $i$  against the ratio of ion intensity multiplying concentration.

It is worth pointing out that mole fraction were used for thermodynamic calculations in this chapter due to conventional approach. Hence, Ni-Cr-Al model alloys have been re-labelled according to atomic ratio, i.e. 6 wt% Al becomes 12 at% Al.

## 6.4 Experimental process of KEMS

The measurements of thermodynamic properties for Ni, Al and Cr in Ni-Cr-Al model alloys were conducted using Knudsen Effusion Mass Spectrometer at Forschungszentrum Jülich in Germany. A single-focusing CH5 (a Finnigan MAT 271, Bremen) 90° magnetic sector-field mass spectrometer was used for measurements at desired temperature ranges.

In the KEMS experiments, an  $\text{Al}_2\text{O}_3$  crucible inside the iridium Knudsen cell with diameter of 9mm and an orifice size of 0.3 mm was used to prevent chemical reaction with Ir. Thermal isolation of heating system and the Knudsen cell was achieved by using tantalum radiation shields during measurements. The cell was heated by electron bombardment at a potential 1200 V and a variation of the electron emission related to the temperature under consideration. The temperature at the bottom of Knudsen cell was measured by an optical pyrometer (Dr. Georg Maurer GmbH, Kohlberg, Germany) in a black body hole at the bottom of the cylindrical Knudsen cell. The pyrometer was calibrated by the melting points of Ag, Au, Cu, Ni and Pt. To distinguish the signal out of the cell from the background, a movable shutter allows to suppress the beam before the ion source. The accurate control of temperature, Knudsen cell geometry and other relevant parameters of measuring ion intensity in different experiments ensures the reliability of measured results for subsequent activity calculations.

Three ternary samples have been prepared as several circular sectors or fragments showed in Fig. 6.6. They were initially sent to Jülich for preliminary KEMS tests to examine the possibility of ion detection in Ni-Cr-Al model alloys. The results revealed an appropriate detection for number of ions in preliminary tests and Arrhenius plot using ion intensity provides correct calculation in activity. Then, arrangement of following KEMS experiments were scheduled aiming to measure at least 6 of as-cast Ni-Cr-Al alloys.



Fig. 6.6 Fragments of a cross-sectional slice (Ni<sub>2</sub>Cr<sub>12</sub>Al) prepared for KEMS experiments

In KEMS experiments, thermodynamic activities of Ni, Cr and Al in Ni-Cr-Al model alloys were measured in the temperature range determined by solidus temperatures from DSC results. Results from preliminary calculations in JMatPro is able to predict general thermodynamic properties of designed alloys, and then with comparison of DSC results, temperature used for KEMS measurement will be confirmed for each sample, it would be temperature lower than solidus of individual sample within 20 K range. Hence, it is expected that the activity measurement of each element in ternary alloys and dependence of sublimation on temperature of alloys are detected and studied as major purposes for this project.

Samples were placed inside a cylindrical crucible ( $\phi$ 5 mm, height of 3 mm) with approximate weight range from 50 to 100 mg. Each sample was weighted in accuracy of 0.1 mg. All designed alloys were initially measured using heating and cooling cycles at a desired temperature range. After reaching the set-up temperature, the programme waits until the ion signal is constant (about 8 to 10 minutes for alloys). A constant signal indicates chemical equilibrium, i.e. constant chemical potential. Once, a constant signal is confirmed, measurements of Ni, Al and Cr were recorded in shutter open and close conditions which labelled as (O) and (C) in Fig. 6.7. The closing and opening of the shutter were performed for

distinction between ions originating from the background gases and ions of the molecular beam. The time to register one ion depends on the sampling rate (about 20 s/ion). It took two minutes for a single measurement, so for a set of 6 measurements at a sequence of Ni(O), Ni(C), Cr(O), Cr(C), Al(O) and Al(C) took 12 minutes at one temperature. The time interval for temperature change was set to about 8 minutes waiting for signal constants. Samples were heated/cooled with repetition at 20 K interval between 1473 K and 1650 K depending on liquidus of alloys.

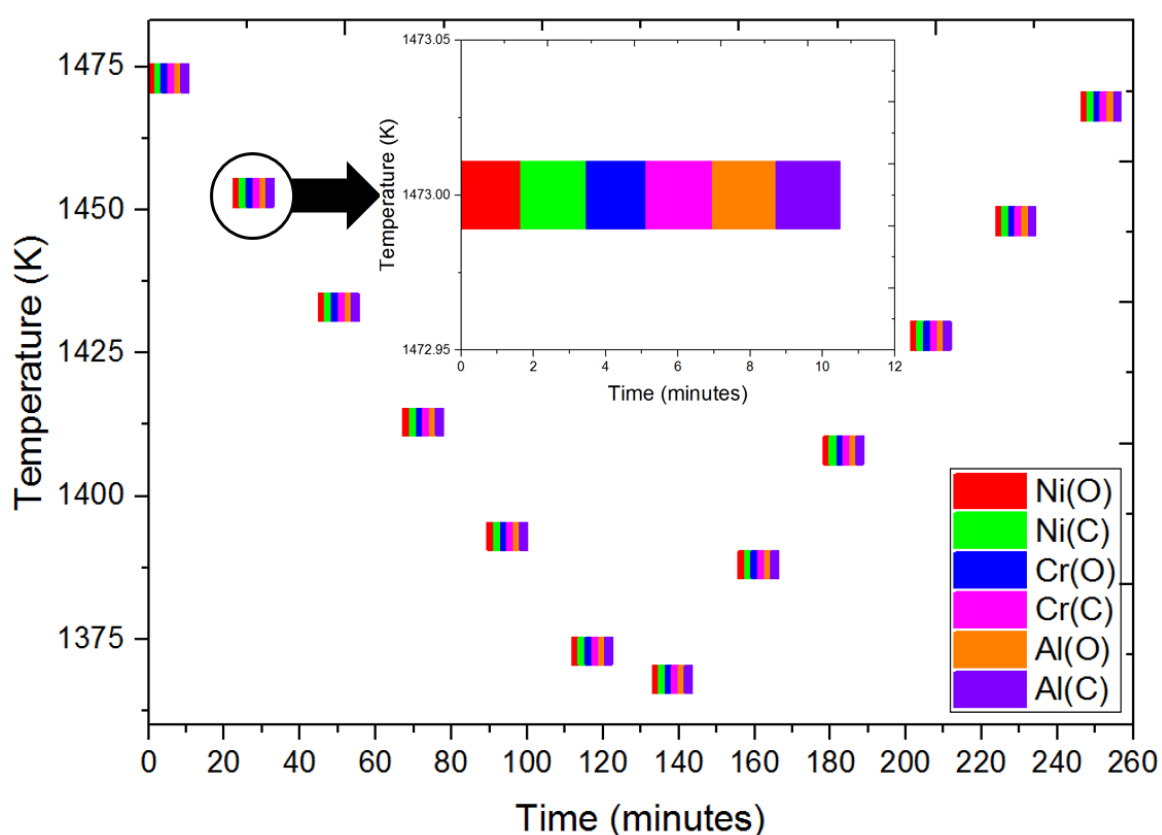


Fig. 6.7 Operation process of heating/cooling cycles in KEMS experiments

Isothermal holds (solution heat treatment) were carried out from 60 hours to 114 hours to determine the extent of elemental sublimation. For a comparison, the extent of element sublimation in these experiments were determined using both ion intensity change by KEMS.

## 6.5 Results of KEMS measurements

### 6.5.1 Sample preparation and characterisation

As mentioned previously, polycrystalline Ni-Cr-Al alloy samples were made from high purity Ni (99.99%), Cr (99.98%) and Al (99.99%) and prepared accordingly to fit the size of crucible used in the experiments. The KEMS experiments were carried out using five Ni-Cr-Al model alloys with constant Al content (12 at%) which is similar to Al content contained in commercial single crystal alloys CMSX series. Compositions of Ni-Cr-Al model alloys were measured by inductively coupled plasma mass spectrometry (ICP/MS) before and after the KEMS experiments, which are listed in Table 6.1. All alloys are consistent with nominal compositions in original design implying no significant loss by sublimation during production process.

Table 6.1 Compositional change (at %) of Ni-Cr-Al model alloys before and after KEMS experiments

Alloy Name	Ni		Cr		Al	
	before	after	before	after	before	after
Ni2Cr12Al	85.96	85.80	2.13	1.17	11.91	13.03
Ni5Cr12Al	83.36	84.60	5.10	2.53	11.54	12.86
Ni15Cr12Al	72.98	77.42	15.23	9.52	11.79	13.06
Ni20Cr12Al	68.41	70.96	20.13	17.09	11.46	11.94
Ni30Cr12Al	59.00	63.80	29.47	25.00	11.53	11.20

As a fully thermochemical software and database package integrated in FactSage SGTE 2004 database [144] (Intermetallic compounds, Alloy Solutions), the isopleth diagram of Ni-Cr-Al model alloys at constant 12 at% of Al is shown in Fig. 6.8. All model alloys used in this study are noted as marks on the figure at 1473 K and 1573 K. It also indicates that the phase of all model alloys from 1473-1573 K, the temperature range for KEMS measurements, is within  $\gamma$  phase region.

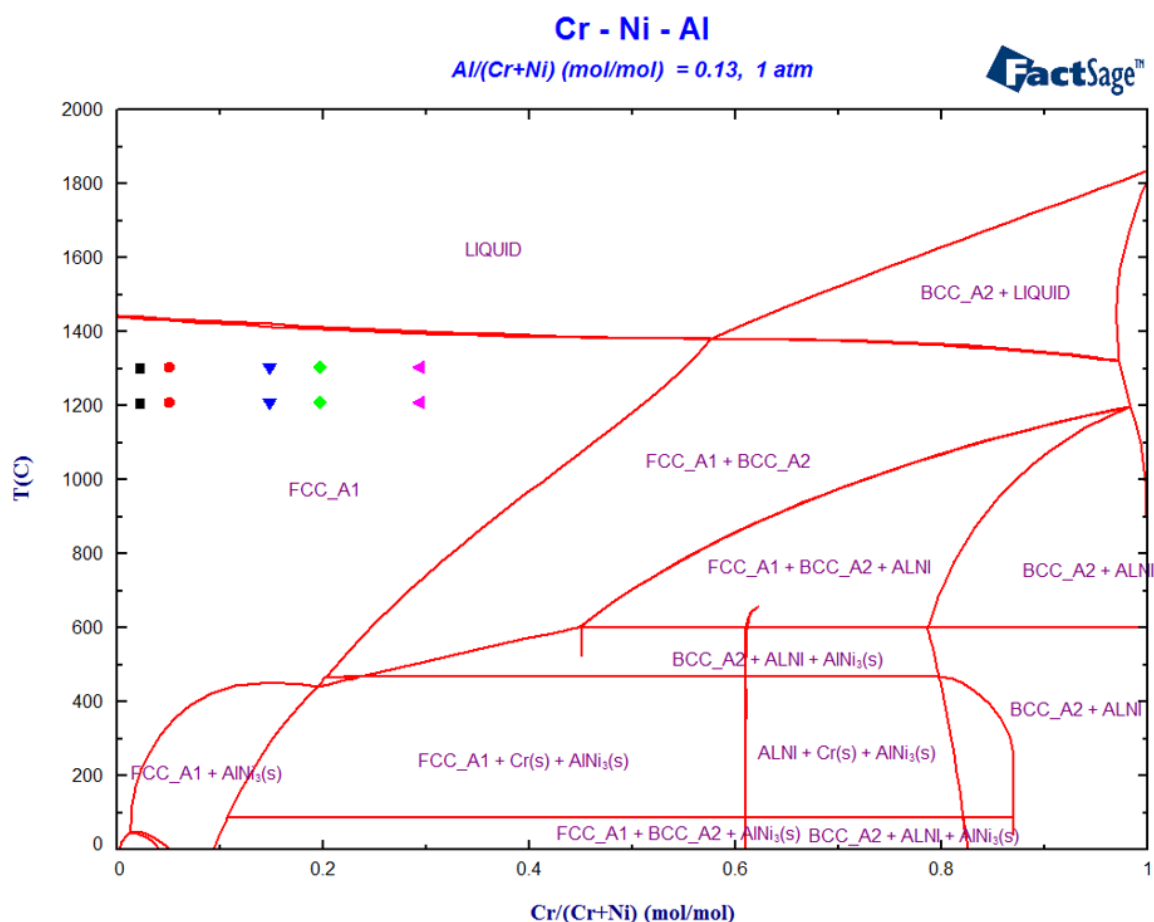


Fig. 6.8 Isopleth diagram of Ni-Cr-Al ternary alloys (fixed 12 at% of Al) with an increase of Cr content showing present phase region for all measured Ni-Cr-Al model alloys at 1473 K and 1573 K [144]

### 6.5.2 Measured ion intensities of Ni, Al and Cr in Ni-Cr-Al model alloys

Thermodynamic activities for elements in measured Ni-Cr-Al model alloys are calculated using principles as described above. Upon sublimation the alloy, ions of  $\text{Ni}^+$ ,  $\text{Al}^+$  and  $\text{Cr}^+$  were collected separately from gaseous species, and the number ions were counted by a digital impulse counter. For Ni and Cr, the ions intensity peak were measured corresponding to mass of their most abundance isotopes, i.e.  $\text{Ni}^{58}$  and  $\text{Cr}^{52}$ , while  $\text{Al}^{27}$  has a natural abundance of 100% giving the only isotope for Al [162-164].

As presented in Fig. 6.9, ion intensity corresponding to mass of the most abundance isotope of Ni has an identical peak for one measured temperature. It is observed that ion intensities for all three elements measured in Ni-Cr-Al model alloys show a proportional relationship with elevated temperatures. The magnitude of the peak from measurements is extracted as the result of ion intensity at certain temperature. Subsequently, Clausius-Clapeyron Equation is applied to produce an Arrhenius plot which show the logarithm of ion intensity multiplying by temperature against the reciprocal temperature,  $10^4/T$ . By using partial pressure calibration factor, the product of ion intensity and temperature can be converted to partial pressure which can be calculated at any desired temperatures using regression equations from Arrhenius plot. Finally, thermodynamic activity will be derived as the ratio of partial pressure in measured alloy to that of pure species. All results of partial pressures and thermodynamic activities from measured Ni-Cr-Al mode alloys will be presented in following section.



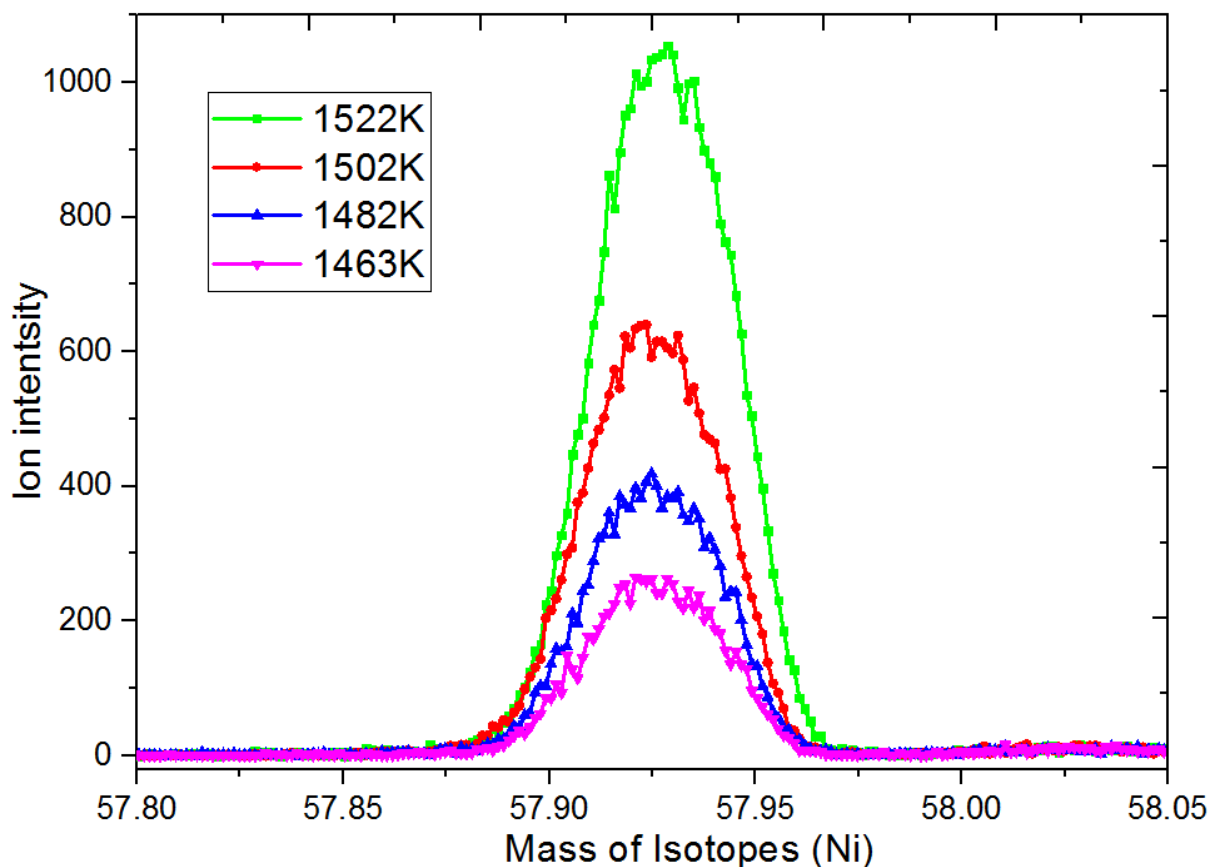


Fig. 6.9 Ion intensities of Ni measured at five temperatures using Ni2Cr12Al alloy  
determining temperature dependence of ion intensities

### 6.5.3 Sublimation enthalpy and entropy of pure Ni, Al and Cr

Fig. 6.10 depicts natural logarithm of the product of ion intensity and temperature  $\ln(I \times T)$  for pure elements of Ni, Al and Cr against reciprocal temperature that measured from KEMS. The linearity of Arrhenius lines indicates that measurements of ion intensity in our experiments were stable, and therefore a steady-state condition was satisfied during experiments.

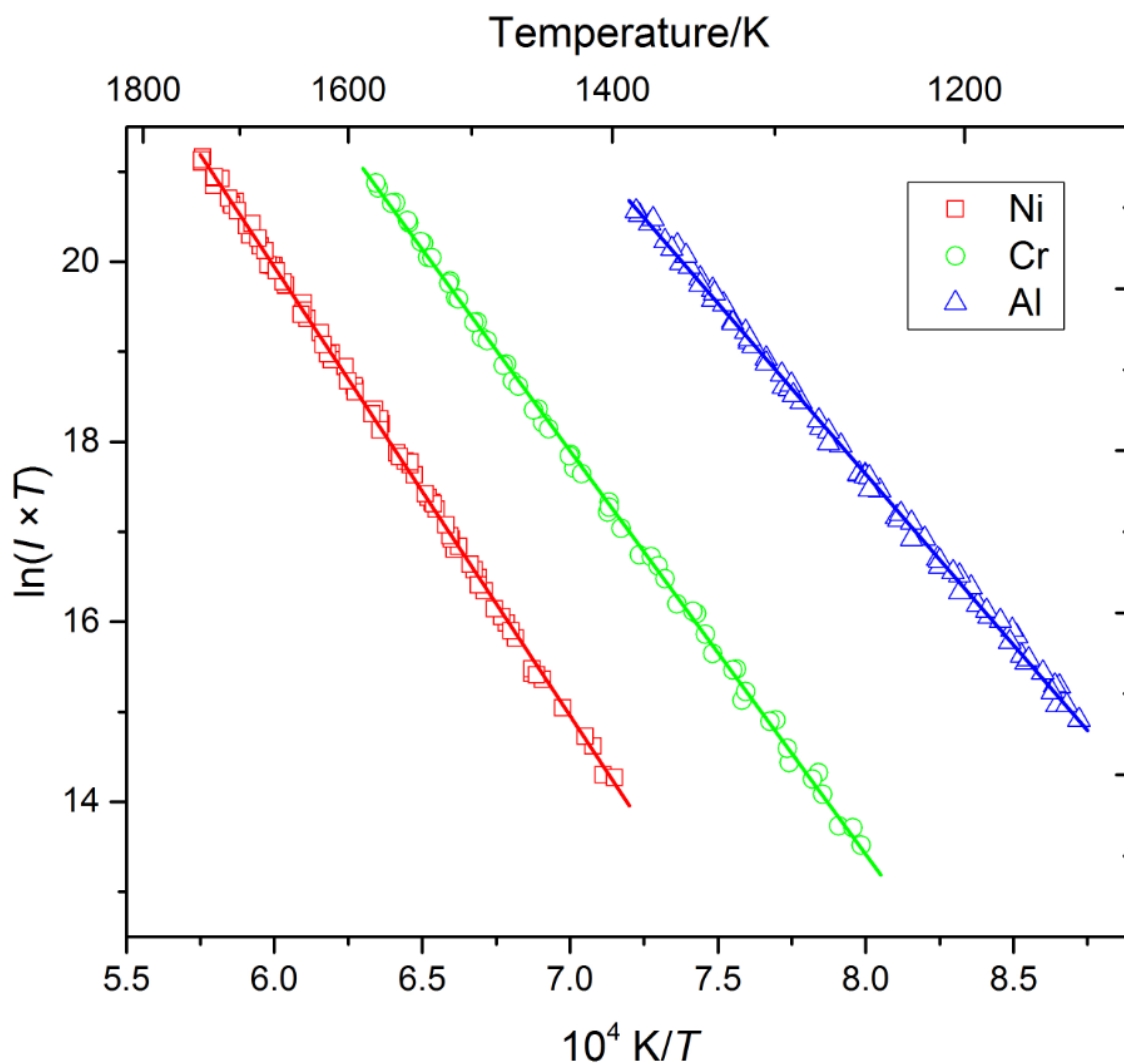


Fig. 6.10 Arrhenius plot of  $\ln (I \times T)$  against  $10^4/T$  from KEMS measurements of three pure substances

Reliability of KEMS measurements is further examined by comparing enthalpies of sublimation from our experiments with those in literature. Coefficients A and B in Clausius-Clapeyron equation,  $\ln (p) = -A/T + B$ , were used to calculate the enthalpy and entropy of sublimation as listed below:  $\Delta_i H^0 = A \times R$ .

All enthalpies and entropies of sublimation from our measurements and literature data [113, 165] are listed in Table 6.2. The enthalpy changes from our measurements at mean temperature of measured range are  $\Delta_s H_{Ni} (1577K) = 414.3$  kJ/mol,  $\Delta_s H_{Cr} (1476K) = 383.3$

kJ/mol and  $\Delta_s H_{Al}$  (1284K) = 310.3 kJ/mol, respectively. The literature data from IVTANTHERMO database [165] are:  $\Delta_s H_{Ni}$  (1500.5K) = 414.5 kJ/mol,  $\Delta_s H_{Cr}$  (1523K) = 384.3 kJ/mol,  $\Delta_s H_{Al}$  (1323K) = 310.2 kJ/mol). A good agreement is obtained between our measurements and values reported in literature.

Table 6.2 Partial pressure equation  $\ln(p) = -A/T + B$  of measured pure Ni, Al, Cr and their enthalpy of sublimation ( $\Delta_{sub} H_{T_m} = -A \times R$ ) and entropy ( $\Delta_{sub} S_{T_m} = B \times R$ ) at mean temperature  $T_m/K$

	Temperature range (K)	A	B	$\Delta H$ (kJ/mol)	$\Delta S$ (J/mol·K)	$\Delta_{ref} H[165]$ (kJ/mol)
Ni	1423-1750	-4.9851	28.451	414.26	236.43	414.45±0.2
Cr	1250-1573	-4.6122	27.872	383.27	231.62	384.34±1.0
Al	1150-1400	-3.7339	24.998	310.29	207.67	310.19±3.2

#### 6.5.4 Partial pressures of Ni, Al and Cr in Ni-Cr-Al model alloys

(a) Measured ion intensities for calculating partial vapour pressures of Ni Al and Cr in Ni-Al-Cr alloys

Fig. 6.11 shows the calculated  $\ln(I \times T)$  against  $10^4/T$  for Ni in Ni-Al-Cr alloys and pure Ni. Using Equation 1, the partial vapour pressure of Ni is determined as description of values A and B in Clausius-Clapeyron Equation,  $\ln(p_i) = -A \times \frac{10^4}{T} + B$ , which is listed in Table 6.3. Two independent runs were carried out and the regression performed on the two runs is presented as an equation with an appropriate uncertainty. The deviations of scatter plots are eliminated statistically by using Grubbs outlier method [174] which has been described with more details of its calculation principles in Appendix. With same principle applied, equations for calculating partial vapour pressure of Cr and Al in measured alloys were also listed in Table

6.3. All partial vapour pressures were calculated in Pa. Using derived regression equations, partial vapour pressures of Ni, Al and Cr in Ni-base alloys can be determined at any desired temperatures.

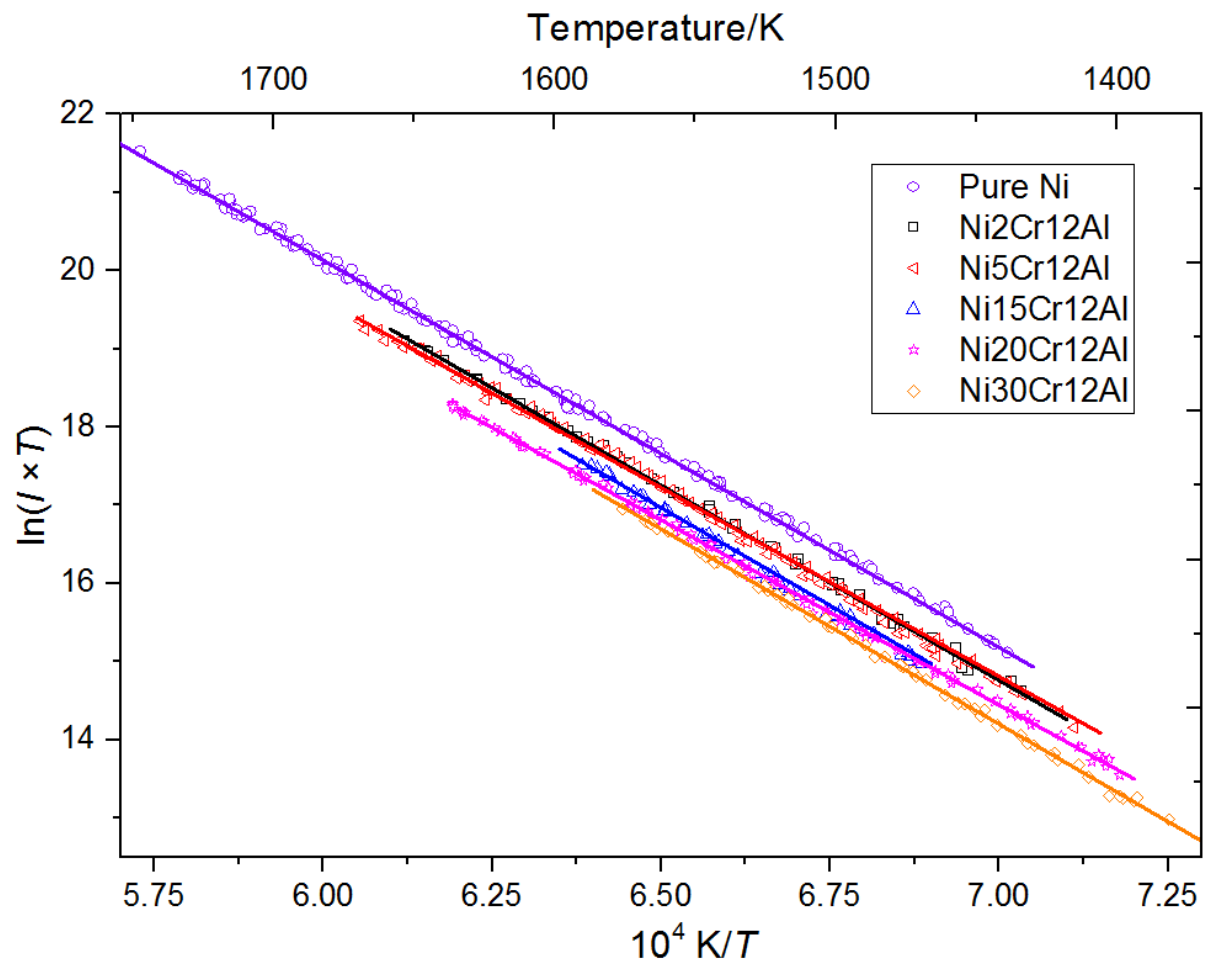


Fig. 6.11 Arrhenius plot of  $\ln(I \times T)$  against  $10^4/T$  for pure Ni and measured model alloys producing regression equations as thermodynamic description

Table 6.3 Clausius-Clapeyron equations,  $(p_i) = -A \times \frac{10^4}{T} + B$ , for calculating partial vapour pressure (Pa) of Ni, Cr and Al in Ni-Cr-Al model alloys

Alloy composition	Temperature/K	$\ln(p_i) = -A \times \frac{1}{T} + B$					
		Ni		Cr		Al	
		A/10 <sup>4</sup>	B	A/10 <sup>4</sup>	B	A/10 <sup>4</sup>	B
Ni2Cr12Al	1423-1636	Run 1	4.986±0.08	28.257±0.03	4.277±0.01	19.842±0.05	5.169±0.04
		Run 2	4.976±0.06	28.105±0.03	4.265±0.01	19.679±0.03	5.254±0.02
		regression	4.997±0.08	28.289±0.04	4.281±0.02	19.826±0.07	5.271±0.02
Ni5Cr12Al	1372-1651	Run 1	4.916±0.04	27.773±0.04	4.294±0.03	21.233±0.13	5.224±0.03
		Run 2	4.908±0.02	27.713±0.02	4.227±0.01	20.652±0.11	5.228±0.02
		regression	4.907±0.04	27.707±0.03	4.207±0.02	20.596±0.18	5.22±0.02
Ni15Cr12Al	1445-1652	Run 1	4.989±0.03	28.009±0.08	4.214±0.02	22.689±0.13	5.215±0.01
		Run 2	4.981±0.02	27.943±0.06	4.222±0.03	22.87±0.18	5.302±0.04
		regression	4.964±0.06	27.852±0.08	4.233±0.02	22.85±0.15	5.276±0.02
Ni20Cr12Al	1368-1616	Run 1	4.913±0.07	27.441±0.04	4.314±0.01	23.57±0.04	5.318±0.02
		Run 2	4.896±0.04	27.192±0.02	4.339±0.01	23.715±0.02	4.992±0.01
		regression	4.943±0.05	27.562±0.03	4.328±0.01	23.657±0.02	5.021±0.15
Ni30Cr12Al	1375-1598	Run 1	5.012±0.03	27.871±0.08	4.227±0.02	24.224±0.12	4.826±0.01
		Run 2	4.952±0.01	27.471±0.02	4.190±0.05	23.957±0.13	4.833±0.01
		regression	4.984±0.02	27.682±0.01	4.211±0.35	24.109±0.12	4.839±0.01

Fig. 6.12 shows partial vapour pressures of Ni, Al and Cr calculated from measured ion intensities in the 2Cr alloy. As can be determined, the partial vapour pressures of Ni increase from 0.0012 Pa to 0.12 Pa from 1424 K to 1636 K, and it increases slightly with temperature. While the partial vapour pressure for Al increases in a large range of magnitude at elevated temperature, rising from  $8.13 \times 10^{-6}$  Pa at 1424 K to  $9.9 \times 10^{-4}$  Pa at 1636 K (triangle dots). Similarly, partial vapour pressure of Cr plotted as circle dots also shows a dramatic increases in same temperatures range, from  $4.51 \times 10^{-5}$  Pa at 1436 K to 0.0018 Pa at 1636 K. More details

of Cr loss can be further observed in isothermal experiments showing consistent decrease of Cr/Ni ion ratio in measured alloys.

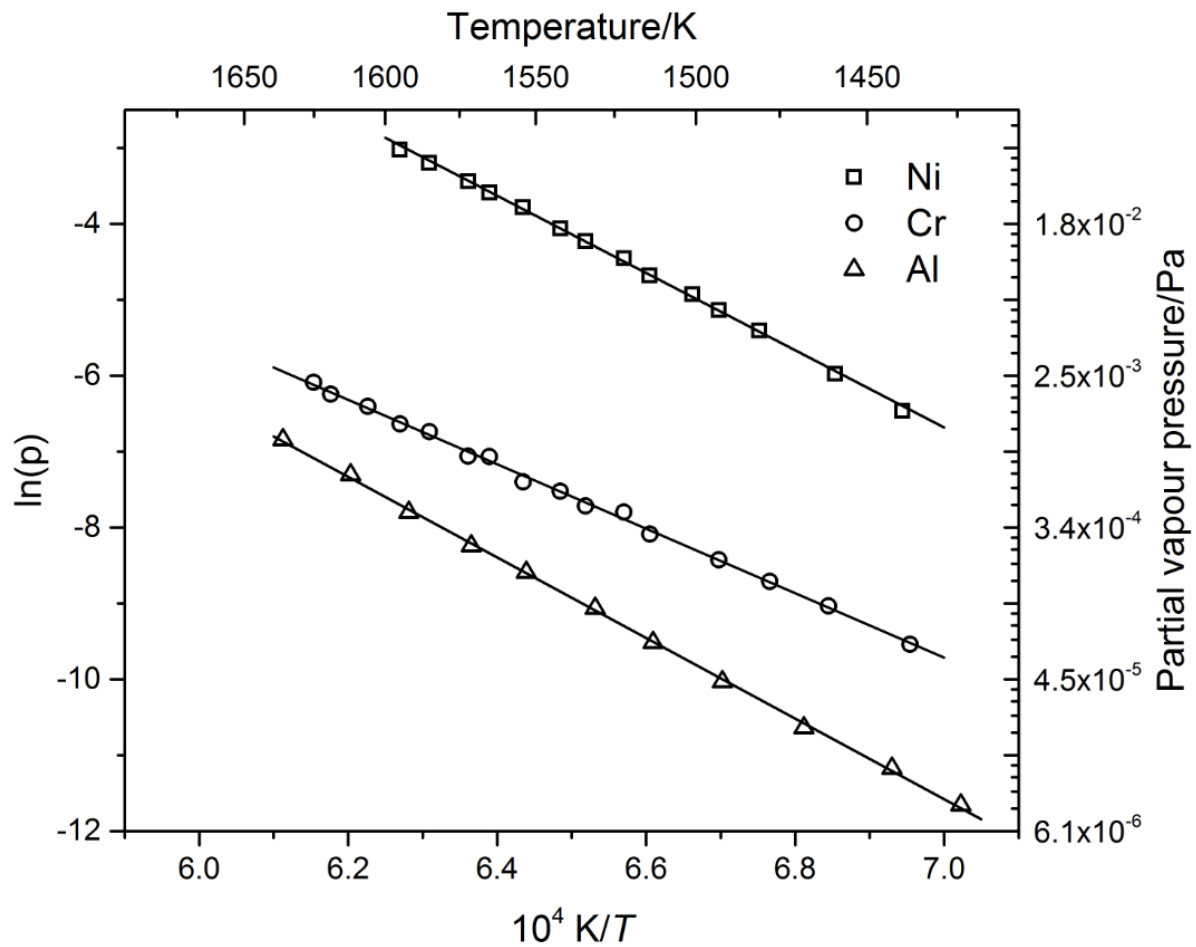


Fig. 6.12 Calculated partial vapour pressure of Ni, Cr and Al in the Ni<sub>2</sub>Cr<sub>12</sub>Al alloy showing temperature dependence.

#### (c) Composition dependence

As partial vapour pressures of Ni, Al and Cr have been measured in five Ni-Cr-Al model alloys with different compositions in our KEMS experiments, the relationship between partial vapour pressure and compositions were analysed and the results of partial vapour pressures for five alloys with different Cr concentrations are shown in Fig. 6.13. Partial vapour pressures of Ni and Al, as showed in Fig. 6.13 (a) and Fig. 6.13 (b) respectively, in Ni-Cr-Al model alloys

are directly proportion to elemental concentrations as higher content of elements in alloy contributes to an increased partial vapour pressure. Presumably, Nickel is the major element in the alloy, the partial pressure of Ni is dominant. The partial vapour pressure of Cr increases dramatically when additional amount of it was added in the alloy. As depicted in Fig. 6.13(c), the partial vapour pressure of Cr changes from  $2.86 \times 10^{-4}$  Pa for Ni<sub>2</sub>Cr<sub>12</sub>Al alloy to 0.028 Pa from Ni<sub>30</sub>Cr<sub>12</sub>Al alloy at 1523 K.

Despite a constant constitution of about 12 at% of Al in all Ni-Cr-Al model alloys, the partial vapour pressure of Al shows an increase with addition of Cr content in alloys, which changed from  $9.3 \times 10^{-5}$  Pa for Ni<sub>2</sub>Cr<sub>12</sub>Al alloys to  $6.7 \times 10^{-4}$  Pa for Ni<sub>30</sub>Cr<sub>12</sub>Al alloys at 1523 K. This can be explained by a high attractive Cr-Ni and low attractive Cr-Al forces in the alloy as compared to the Al-Ni forces, while the attractive Al-Al and Ni-Ni forces remain nearly constant. This means that the bond forces in the alloy support the substitution of Cr for Al in the  $\gamma$ -phase and with this a higher volatility of Al, and therefore it is easier for Al atoms to escape from the alloy. As a consequence the partial vapour pressure of Al increases with the increase of Cr concentration in the alloy.

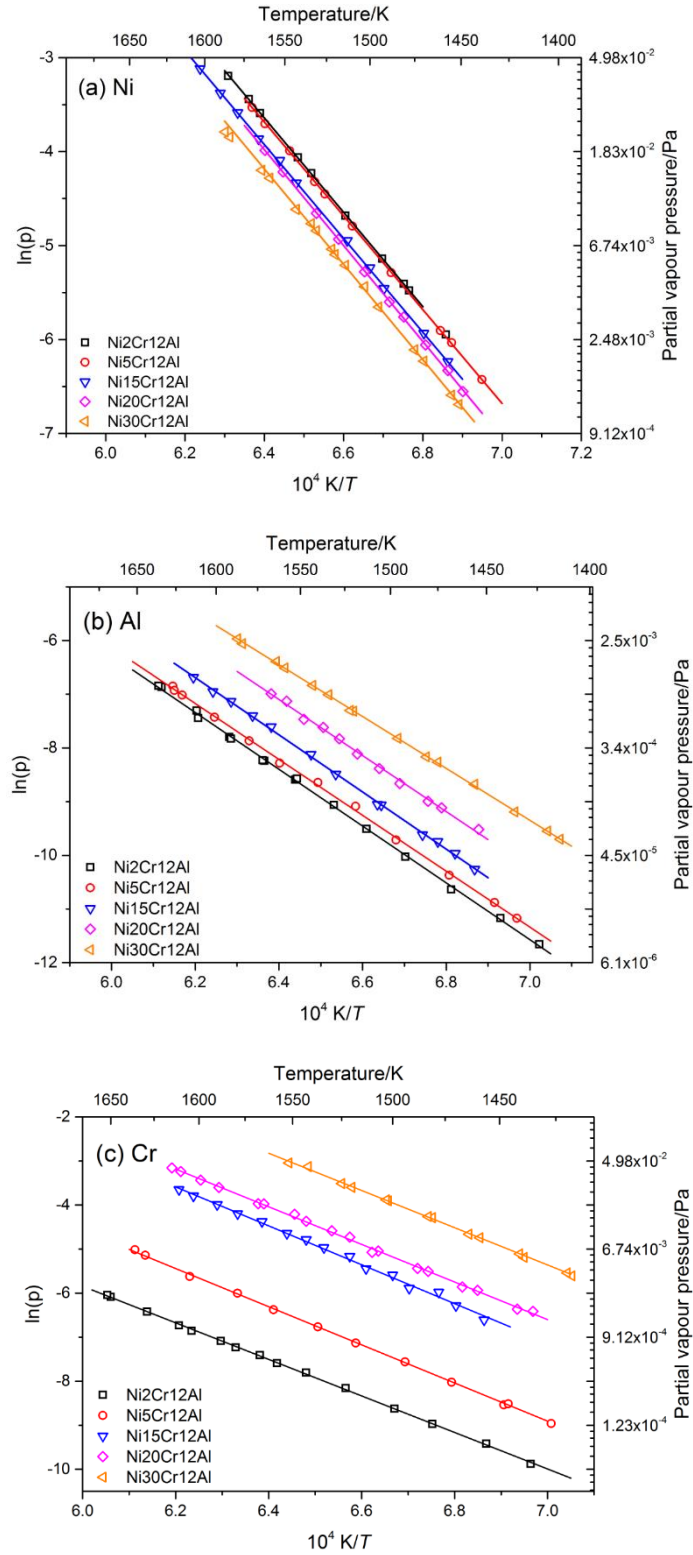


Fig. 6.13 Partial vapour pressures (Pa) of (a) Ni, (b) Al, (c) Cr as a function of the inverse absolute temperature ( $1/T$ ) in all Ni-Cr-Al alloys showing composition dependence in measured alloys



### **6.5.5 Thermodynamic activities of Ni, Al and Cr in Ni-Cr-Al model alloys**

Thermodynamic activities of Ni, Cr and Al were determined as the ratio of partial pressure in measured Ni-Cr-Al model alloys and that of in pure substances. Those results can be presented in Arrhenius plot showing as a function of temperature with derived regression equations. Temperature and composition dependence of thermodynamic activities of Ni, Al and Cr are observed with details summarised in below.

#### **(a) Temperature dependence**

Fig. 6.14 shows the calculated thermodynamic activities of Ni, Al and Cr from measured ion intensities in the 2Cr alloy. In Fig. 6.14 (a), thermodynamic activity of Ni fluctuates around magnitude of 0.8 between 1424 K to 1636 K, and it increases slightly with temperatures; thermodynamic activity for Al increases when temperature increases, rising from  $2.32 \times 10^{-5}$  at 1424 K to  $9.53 \times 10^{-5}$  at 1636 K as shown in Fig. 6.14 (b); on contrary, thermodynamic activity of Cr in Fig. 6.14 (c) gives a decreasing trend as temperature increases showing a drop from  $3.97 \times 10^{-3}$  at 1436 K to  $2.76 \times 10^{-3}$  at 1636 K. More details of Cr loss in Ni-Cr-Al model alloys at high temperature can be further observed in isothermal experiments showing a consistent decrease in thermodynamic activity of Cr in measured model alloys.

#### **(b) Composition dependence**

As thermodynamic activities of Ni, Al and Cr in Ni-Cr-Al model alloys have been measured using five different model alloys in the KEMS experiments, the relationship between thermodynamic activity and compositions were analysed and the results of thermodynamic activities for five measured alloys with different Cr concentrations are shown in Fig. 6.15.

Thermodynamic activities of Ni and Al, as showed in Fig. 6.15 (a) and Fig. 6.15 (b) respectively, in Ni-Cr-Al model alloys are directly proportion to elemental concentrations as higher content

of elements in alloy contributes to an increased thermodynamic activity. Nickel is the major element in the alloy, the activity of Ni is dominant component. It is expected to obey Raoult's law where content of Ni increases every 10% the activity rises about 0.12 exhibiting negative deviations from ideality. Thermodynamic activity of Cr increases dramatically when additional amount of it was added in the alloy. As depicted in Fig. 6.15 (c), the activity of Cr changes from  $3.54 \times 10^{-3}$  for Ni<sub>2</sub>Cr<sub>12</sub>Al alloy to 0.32 from Ni<sub>30</sub>Cr<sub>12</sub>Al alloy at 1523 K.

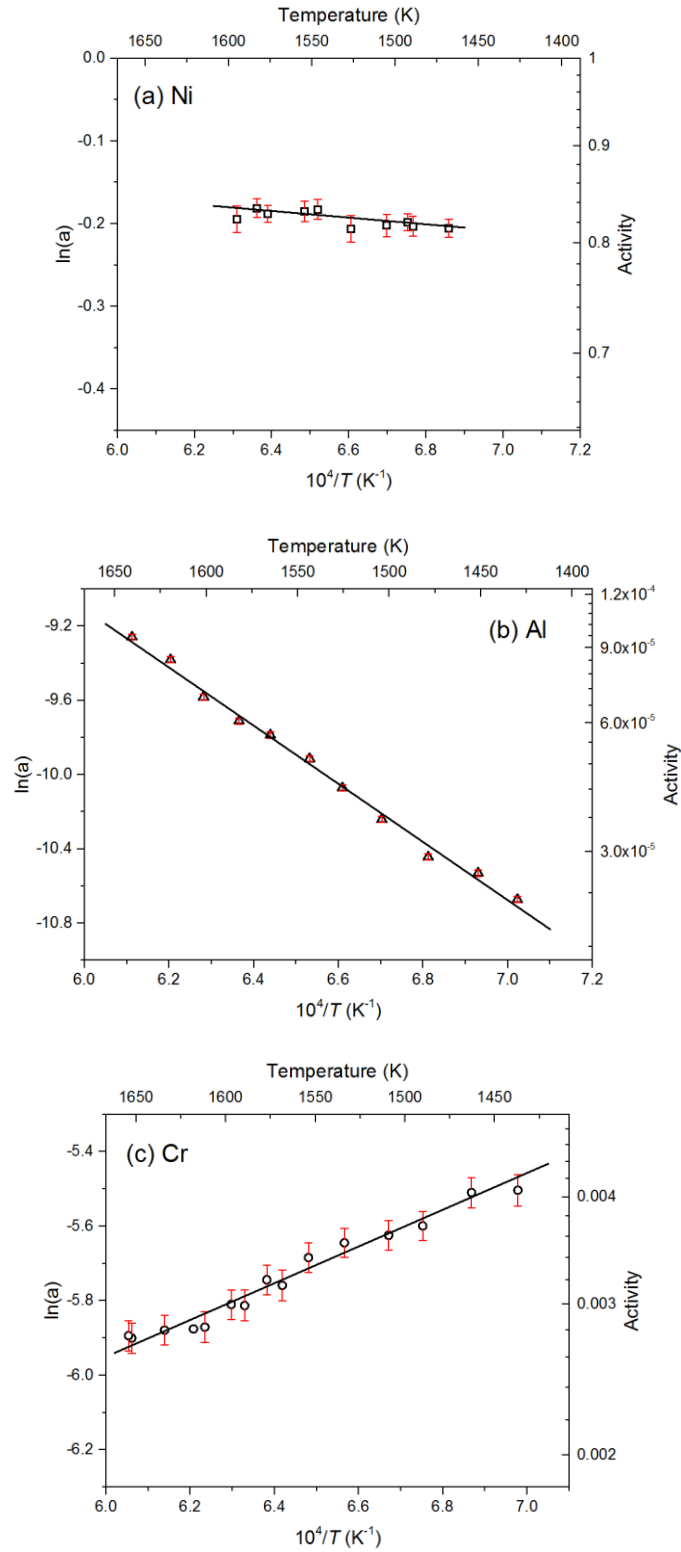


Fig. 6.14 Calculated thermodynamic activities in the Ni<sub>2</sub>Cr<sub>12</sub>Al alloy showing temperature dependence of (a) Ni, (b) Al and (c) Cr

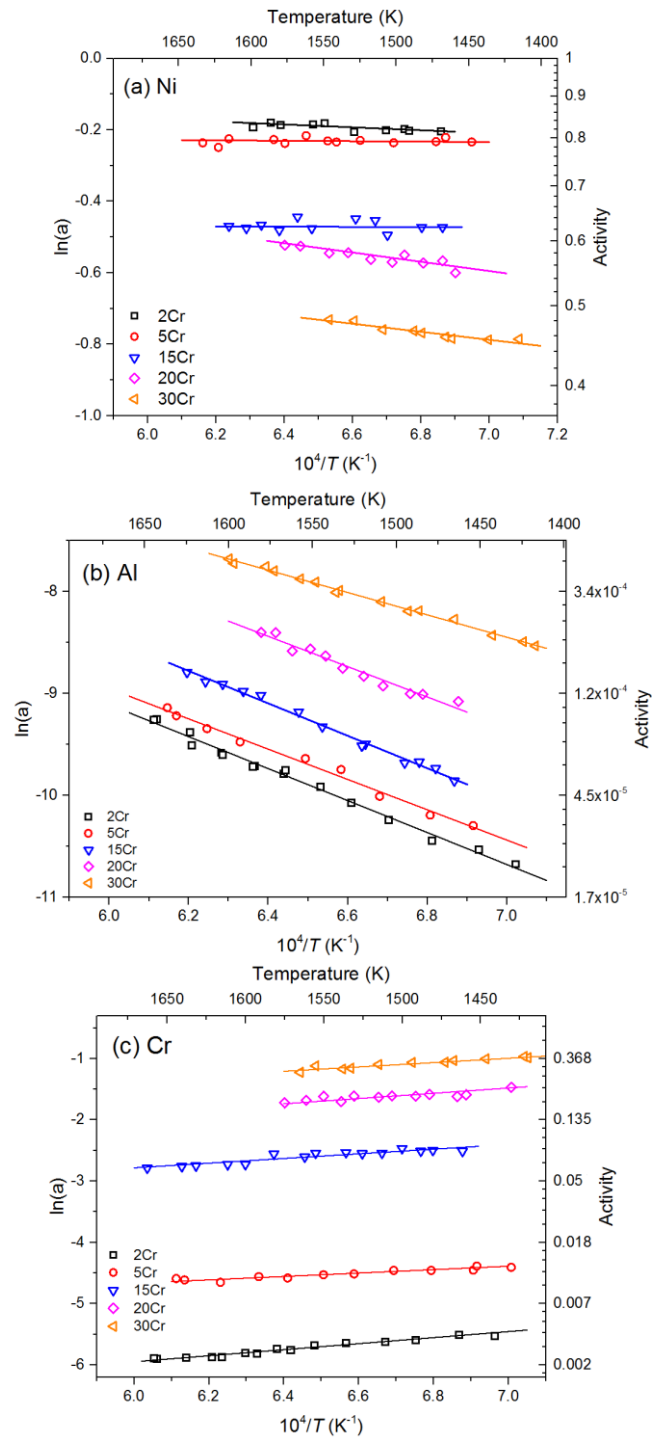


Fig. 6.15 Thermodynamic activities of all elements as a function of temperature in Ni-Cr-Al model alloys (a) Ni, (b) Al and (c) Cr showing composition dependence in measured alloys

(c) Thermodynamic activities of Ni, Al and Cr during isothermal hold

Thermodynamic activities of Ni and Cr were also calculated from KEMS data carried out in isothermal hold. As shown in Fig. 6.16, thermodynamic activity is similar to variation of ion intensity indicating change of concentration during isothermal hold. It is determined that thermodynamic activity of Ni remain around 0.7 when Ni<sub>2</sub>Cr<sub>12</sub>Al alloy is homogenised. Thermodynamic activity of Cr shows a signification decrease in first 20 hours implying an abrupt change of Cr content in Ni<sub>2</sub>Cr<sub>12</sub>Al alloy in homogenisation.

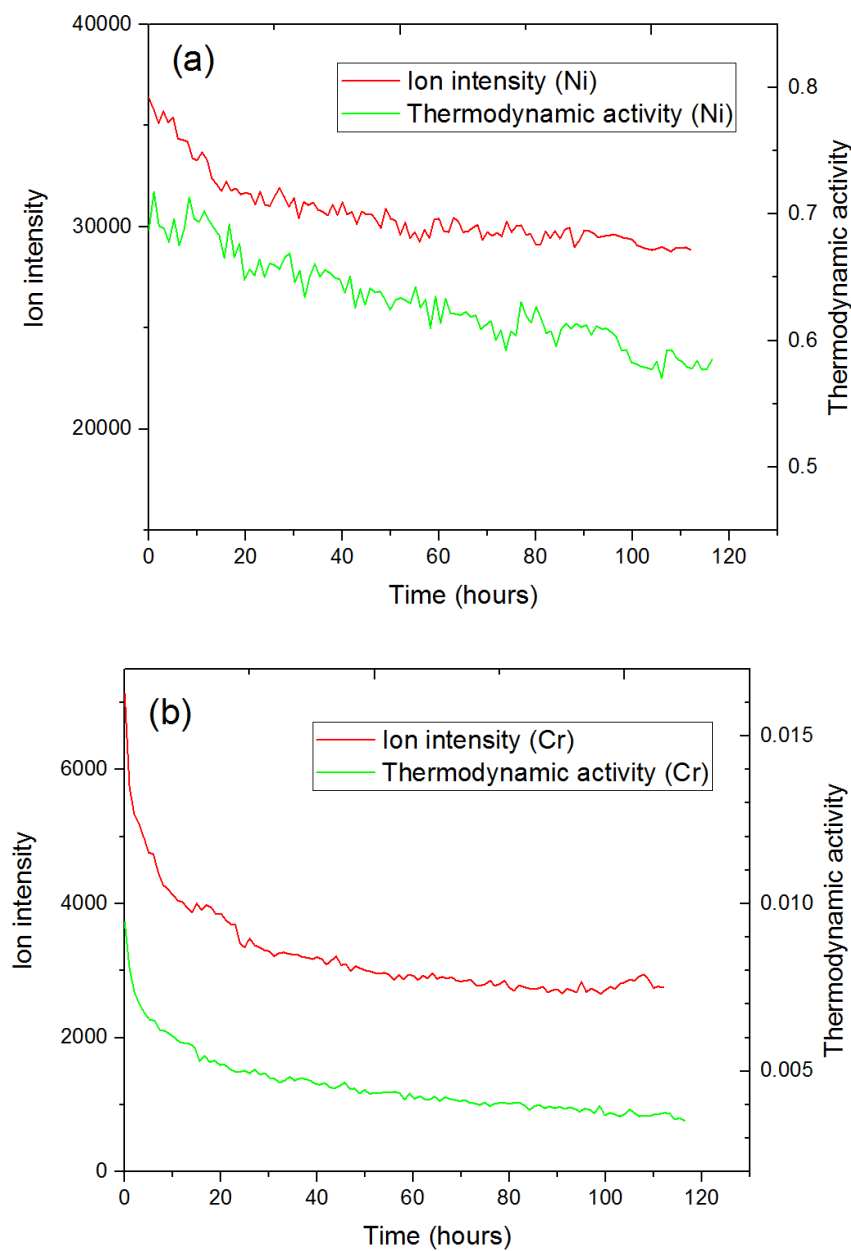


Fig. 6.16 Thermodynamic activity and ion intensity change of (a) Ni and (b) Cr in Ni<sub>2</sub>Cr<sub>12</sub>Al alloy during isothermal experiment.

#### ***6.5.6 Elemental sublimation in Ni-base alloys during long-term isothermal hold at high-temperature***

To investigate the elemental sublimation during solution heat treatment of Ni-base alloys, high temperature isothermal (1573 K) experiments were carried out from 66 hours to 114 hours for Ni<sub>2</sub>Cr<sub>12</sub>Al, Ni<sub>5</sub>Cr<sub>12</sub>Al and Ni<sub>15</sub>Cr<sub>12</sub>Al alloys. The measured ion intensity and calculated activity of Cr in the alloy Ni<sub>2</sub>Cr<sub>12</sub>Al are presented in Fig. 6.17. It is directly observed that there is an initial decline of both ion intensity and activity in the first 20 hours, the partial vapour pressure changed from  $2.57 \times 10^{-3}$  Pa at the beginning to  $1.39 \times 10^{-3}$  Pa at 20 hours, with an approximately decrease of 46% during the experiment. After the initial decline, the partial vapour pressure stabilised at a level of  $1.02 \times 10^{-3}$  Pa with small fluctuations in subsequent hours. There is similar stabilisation observed from partial vapour pressure of Ni in Ni<sub>2</sub>Cr<sub>12</sub>Al alloy, which remains around 0.035 Pa after 20 hours. In order to confirm the effect of Cr on elemental sublimation, the ratio change for Cr/Ni and Al/Ni in 3 alloys over the initial period was calculated with illustration in Fig. 6.18. In Fig. 6.18 (a), Cr/Ni ratio drops significantly in first 20 hours. In Fig. 6.18 (b), Al/Ni ratio remains stable during isothermal hold. The result of activity of Cr from isothermal hold suggests that the loss of Cr is the main reason for the ion intensity decline in the initial period.

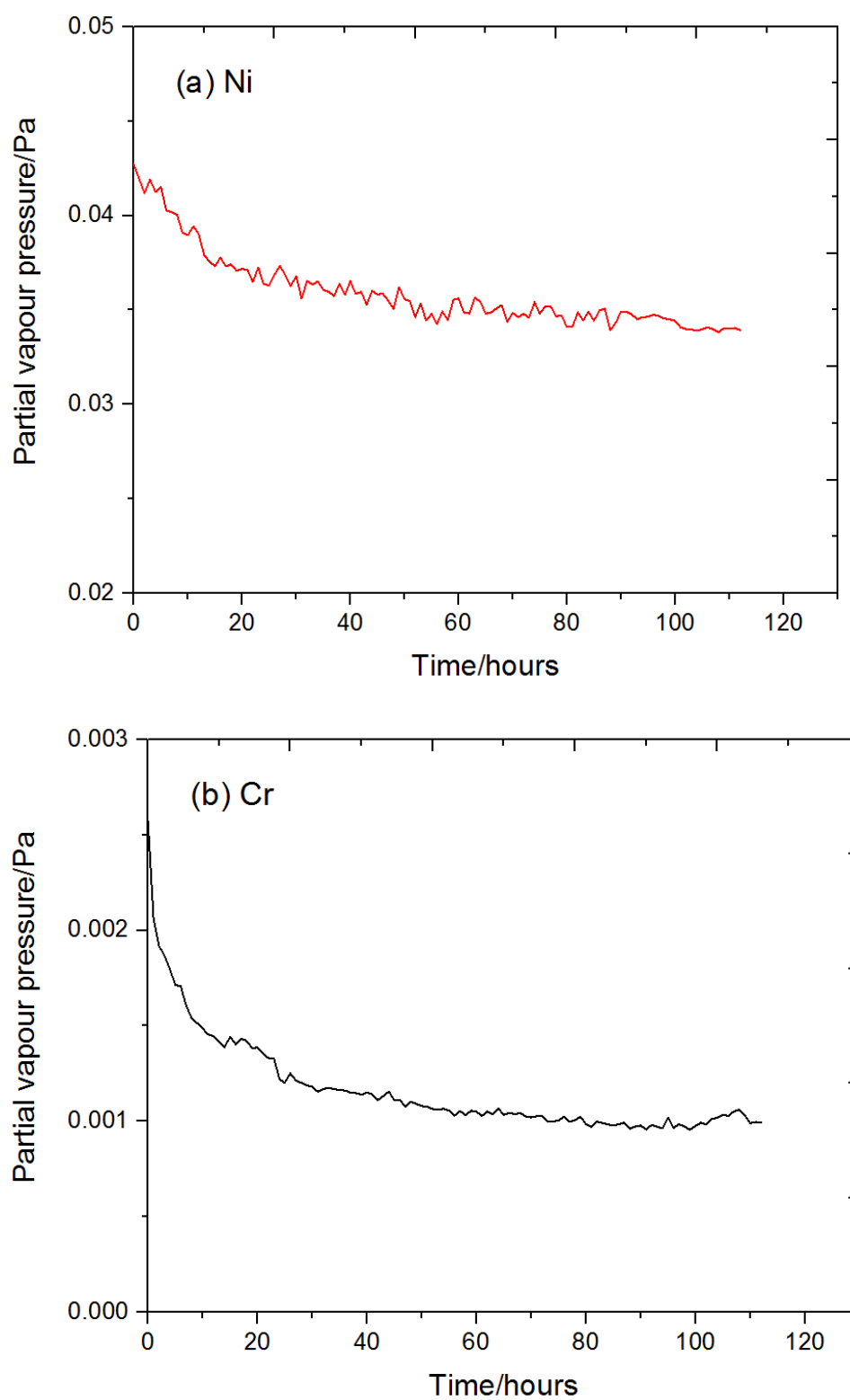


Fig. 6.17 Variation of partial vapour pressures for (a) Ni and (b) Cr in Ni<sub>2</sub>Cr<sub>12</sub>Al alloy during isothermal experiment, showing their contribution to elemental sublimation.

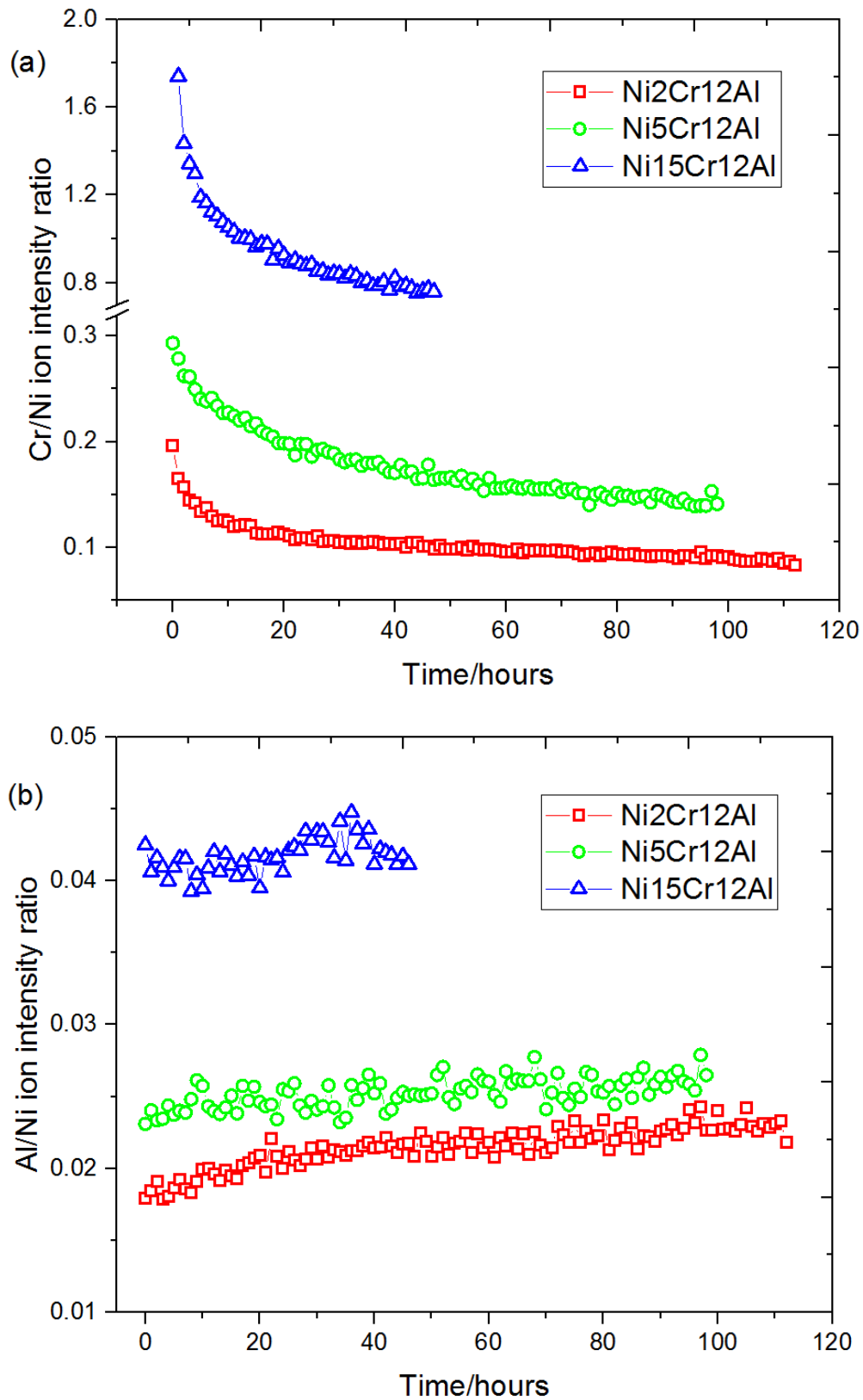


Fig. 6.18 ion ratio change of (a) Cr/Ni and (b) Al/Ni in measured alloy during isothermal experiment, showing the loss of chromium during isothermal holding



### 6.5.7 Implication of thermodynamic activity to phase field determination and optimisation of CALPHAD method

#### (a) Ni+/Al+ ion intensity ratios for phase field determination

According to the phase rule, Ni+/Al+ ion intensity ratios are independent of concentration  $x_{Ni}$ , if two phases are present in the alloy at measured temperatures [175]. The results of Ni+/Al+ ion intensity ratios in Ni-Cr-Al model alloys show a similar pattern which illustrates in Fig. 6.19. As can be observed, Ni-Cr-Al model alloys containing high concentration of Cr are prone to form  $\gamma/\gamma'$  eutectic which is shown as a constant Ni/Al ratio in the figure. In specific, Ni-Cr-Al model alloys with Cr content in the range of 20-25 at% and higher than 30 at% appear a constant Ni/Al ion ratio on the plot. According to microstructural characterisation, Ni<sub>30</sub>Cr<sub>12</sub>Al alloy actually shows presence of eutectic while Ni<sub>20</sub>Cr<sub>12</sub>Al alloy may require further confirmation for its appearance.

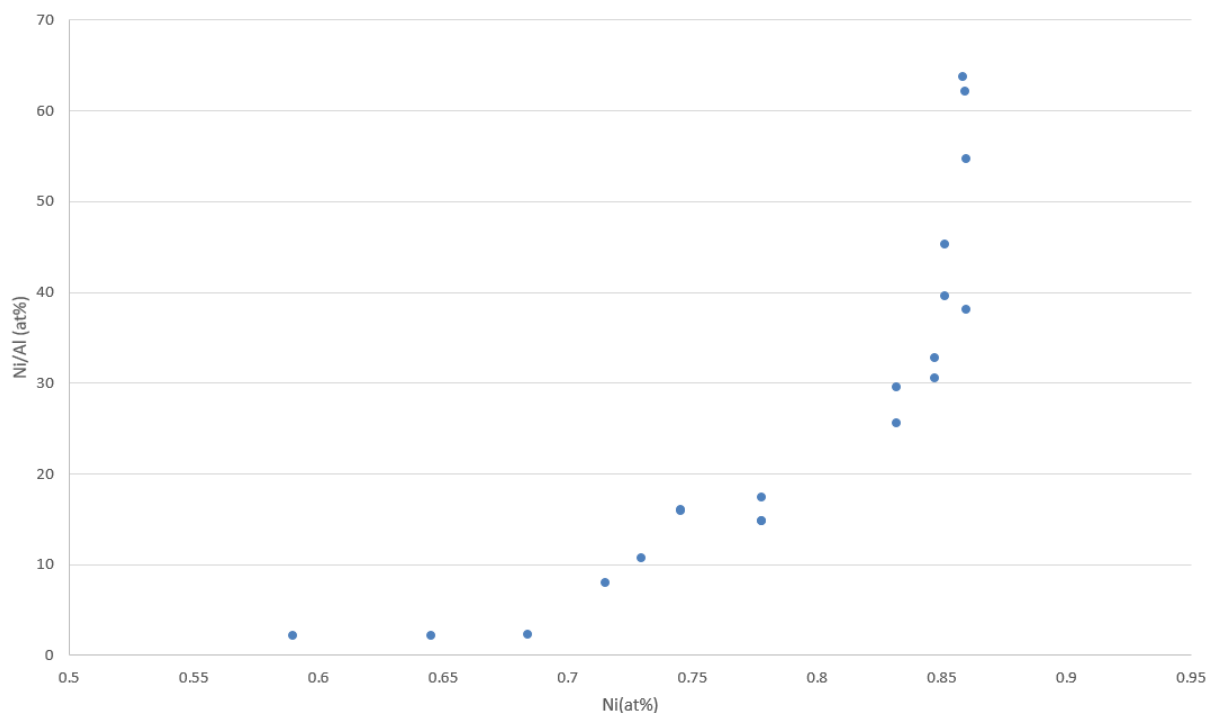


Fig. 6.19 Ratio of ion intensity for Ni/Al from measured model alloys

Under such consideration, it leads to assumption that if Cr accumulate locally forming a Cr region, the phase instability is likely to occur. As measured high Cr containing Ni-base alloys show the tendency of eutectic formation at high temperature, even though phase diagram

for ternary Ni-Cr-Al system predicts its occurrence at much lower temperature for corresponding compositions.

(b) Comparison of KEMS results and thermodynamic calculation from JMatPro and FactSage

Thermodynamic properties of Ni-base alloys can be calculated using CAPHALD method giving by some commercial software, such as JMatPro and FactSage. However, the existing model used for those calculations is based on equation fitting to measured data from existing publications. The model for calculation can be further optimised using KEMS data. To correct calculated results, thermodynamic activities of Ni, Al and Cr derived from KEMS data are compared with calculation obtained from JMatPro and FactSage.

In terms of magnitude for thermodynamic activities of Ni, Al and Cr in measured alloys, there are relatively high deviations derived from calculations and KEMS measurements. It seems that calculating the thermodynamic properties for dilute solution is vastly dependent on the model used in software which provide the results with relatively large deviations between FactSage and JMatPro.

From different points of view, if results are presented as the ratio of Cr/Ni and Al/Ni for comparison. It seems that the discrepancy of Cr and Ni have fairly acceptable agreement between calculations from FactSage and KEMS data. As shown in Fig. 6.20 and 6.21, ratios of activities for two elements in Ni-Cr-Al model alloys are compared. There is a good agreement between FactSage and KEMS results for ratio of Cr and Ni in most of measured Ni-Cr-Al model alloys. However, the ratio of Al and Ni show critical differences in both thermodynamic calculations with that of in KEMS data. It is worth pointing out that the effect of Cr contents on the increase of Al activity was observed in KEMS data. But it seems that this phenomenon is not considered in thermodynamic calculation for activity of dilute Al, which calculated in linearity manner. With respect to acceleration of Al activity, model for its activity calculation should be evaluate corresponding to Cr content for optimisation.

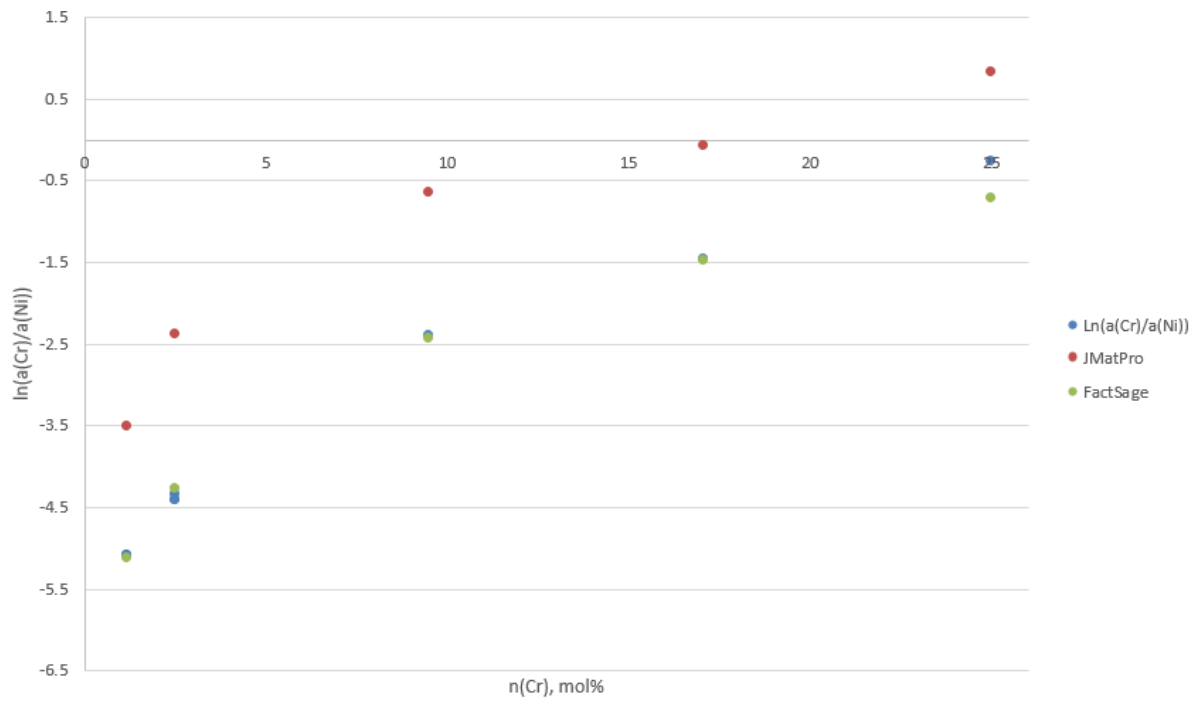


Fig. 6.20 Comparison of thermodynamic activity for results of Cr/Ni ratio from KEMS and CALPHAD calculations

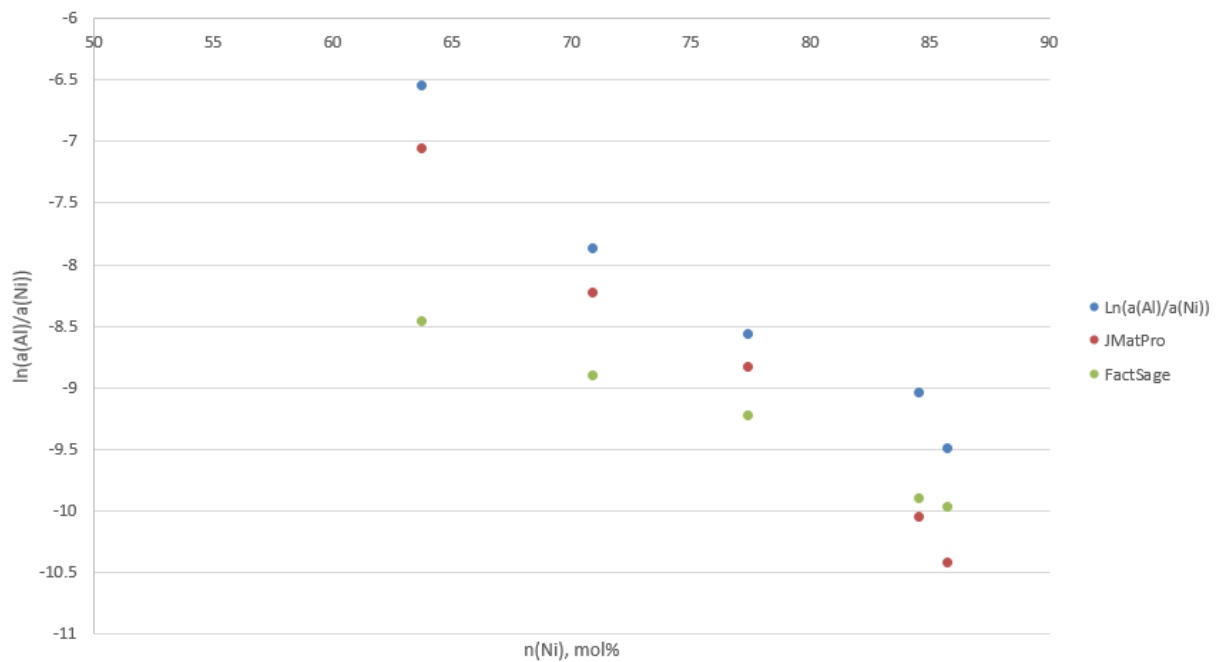


Fig. 6.21 Comparison of thermodynamic activity for results of Al/Ni ratio from KEMS and CALPHAD calculations

(c) Implications of thermodynamic data to microstructural stability in Ni-base superalloys during solution heat treatment

Reliable thermodynamic data for the analysis of elemental sublimation during solution heat treatment has been obtained using Ni-Cr-Al model alloys. As discussed in DP study, the extent of elemental sublimation is dependent on vapour pressure at high temperatures. In KEMS experiments, partial pressures of Ni, Al and Cr in measured alloys were derived from KEMS measurements revealing elemental behaviours at high temperature the surface effect via elemental sublimation in Ni-base alloys. The results of thermodynamic activities imply concentration change in bulk alloys at high temperature, which advocates moderate amount of Ni and almost negligible content of Al sublime from the casting surface of alloys. KEMS results enable accurate calculation of thermodynamic properties at high temperature showing consistence with prediction of elemental interactions in Ni-base alloys from previous studies [80, 93, 107].

A substantial decline of Cr thermodynamic activity is not expected, although the effect of Cr losses in alloy casting was reported in several studies. Lobb and Evans [85] observed evaporation of elements in stainless steel during vacuum annealing and proposing that the evaporation of Cr occurs through the grain boundary, which is potentially regarded as defects of alloys, at long annealing times. Li [176] and Gupta et al [83] reported the evaporative segregation phenomena in binary Ni-Cr and Fe-Cr alloy, suggesting solute enrichment or depletion in alloys as a result of surface evaporation. It is emphasis that elemental depletion on the surface of a dilute solid alloy has critical impacts on properties of alloy which can be a serious problem [177, 178] potentially resulting in microstructural instability of alloys. Coping KEMS observation to solution heat treatment of CMSX-10N single crystal superalloys, excessive amounts of Cr is lost via sublimation following from these observation. Hence, local depletion of Cr could affect stability of microstructures since Cr segregates to  $\gamma$  phase in Ni-base alloys [4]. With the depletion of Cr, redistribution of elements leads to the formation of gamma prime and beta phases.

## 6.6 Conclusions

Thermodynamic properties of Ni, Cr and Al in Ni-Cr-Al model alloys at high temperatures have been measured using KEMS method. The effect of partial pressures on elemental sublimation

during solution heat treatment of Ni-base alloys have been examined. Meanwhile thermodynamic activities with detailed analysis show information on homogenisation of alloys as well as provide solution for correcting thermodynamic calculation using commercial software.

On the basis of partial vapour pressure from KEMS measurements, following key points can be concluded:

1. Equations for calculating partial vapour pressures of Ni, Al and Cr in measured Ni-Cr-Al alloys as a function of temperature have been derived.
2. The partial vapour pressure of Ni and Cr is approximately two orders of magnitude higher than that of Al suggesting that the sublimation of Al is almost negligible in Ni-base alloys compared with Ni and Cr.
3. The partial pressure of Cr in Ni-Cr-Al alloys declines during the first 20 hours in KEMS measurements that shows generally an inhomogeneity of Cr in the alloy after preparation and solution heat treatment.
4. In terms of the extent of elemental sublimation, high proportional loss of Cr content at high temperatures, since the partial vapour pressure of Cr in Ni-Cr-Al alloys shows change of elemental concentration during the first 20 hours of solution heat treatment.
5. KEMS results are entirely plausible that elucidates a profound effect of elemental sublimation on phase stability of Ni-base alloys, which shows a great tendency of Ni and Cr to leave the alloy at high temperature.
6. Elemental sublimation occurs during solution heat treatment of Ni-base alloys, which leads to chemistry change and microstructural instability at the surface of Ni-base alloys.
7. Chromium has a higher resistibility being solved in the alloy structure than Ni and Al.

The preferable substitution of Al with Cr is inhibited by the low activity of Al.

8. From a detailed view of the activity at constant temperature over the range of the alloys under consideration it can be predicted that the phase boundaries in the database has to be reviewed.
9. Elemental sublimation occurs during solution heat treatment of Ni-base alloys, which leads to chemistry change of chemical composition and microstructural instability at the surface of Ni-base alloys.
10. A reliable kinetic timing in solution heat treatment and optimized homogeneous surrounding conditions in terms of temperature equilibrium can reduce unwanted casting defects.

In terms of thermodynamic activities of Ni, Al and Cr in Ni-Cr-Al model alloys at high temperatures, KEMS data shows temperature and composition dependence deriving equations for calculating thermodynamic activities of three elements as a function of temperature for different concentrations of Cr. With depletion of Ni and Cr at the surface, where the major loss of Cr content occurs, phase transformation into  $\gamma'$  and  $\beta$  is likely to occur during solution heat treatment. Considering a dramatic reduction of Cr content in SX CMSX-10N superalloys, optimisation of microstructural stability in Ni-base superalloys require re-assessment on chemistry balance, local segregation that will prevent the surface of alloys from defects formation at high temperatures.

Elemental sublimation during solution heat treatment of Ni-base alloys is associated with local chemistry change attributing to microstructural instability at the surface of Ni-base alloys. Calculations of Ni/Al ratio with respect to concentration ratio determines potential occurrence of  $\gamma/\gamma'$  eutectic for high Cr containing Ni-Cr-Al model alloys. Further examination are required for confirmation of this information derived from current study.

From a detailed view of thermodynamic activity at constant temperature over the range of the alloys under consideration it can be predicted that the phase boundaries in the database has to be reviewed.

## **7. Analysis of elemental sublimation during heat treatment in real superalloys**

Sublimation on the surface of Ni-base alloy during heat treatment is a complicated process, its occurrence depends on various reasons. In particular, it is difficult to analyse elements loss at high temperatures. Using KEMS method that analysed partial pressures of Ni, Al and Cr under equilibrium condition, it seems that quantitative equations can be derived for calculating thermodynamic terms at high temperatures. Hence, an overview of high temperature behaviours of Ni, Al and Cr is deduced providing implication for elemental sublimation in practical solution heat treatment.

### **7.1 Chemical potential for determination of atoms tendency during elemental sublimation**

In order to determine the tendency for an element to leave the system [169, 179], the chemical potential is required by using Equation 6.4 which determine its value at desired temperatures by taking account of the reference chemical potential of pure compounds at 298 K [180, 181]. Table 7.1 lists results of chemical potential showing the change of chemical potential for Ni, Al and Cr as additional Cr contained in Ni-base alloys. Chemical potential for all elements follows second law of thermodynamics. In general, the order of chemical potential in Ni-Cr-Al model alloys is  $\text{Ni} > \text{Cr} > \text{Al}$ . The concentration of elements relates to tendency towards which chemistry equilibrium that element with higher concentration tends to be released easily from Ni-Cr-Al model alloys.

It is interesting to point out that chemical potential of Cr is considerably influenced by its concentration. Variation of Cr content changes at least 10% of its chemical potential. The chemical potential of Al seems also to be affected by content of Cr, albeit that a constant Al concentration in all measured alloys.

Table 7.1 Calculated chemical potential of Ni, Al and Cr in measured Ni-Cr-Al model alloys using Equation 6.4

Alloy		Chemical potential at temperature (kJ/mol)		
		1473K	1573K	1673K
Ni2Cr12Al	Ni	-61.186	-68.551	-76.113
	Al	-190.435	-195.519	-203.892
	Cr	-116.611	-130.348	-144.384
Ni15Cr12Al	Ni	-64.579	-72.155	-79.76
	Al	-176.39	-183.13	-193.142
	Cr	-78.977	-89.6443	-101.352
Ni20Cr12Al	Ni	-65.716	-72.88	-80.239
	Al	-176.39	-183.13	-193.142
	Cr	-67.687	-78.516	-91.118
Ni30Cr12Al	Ni	-68.232	-75.44	-82.997
	Al	-158.219	-167.331	-177.845
	Cr	-61.436	-71.128	-82.018

## 7.2 Implications of elemental sublimation to investment casting and solution heat treatment of Ni-base superalloys

The occurrence of microstructural instability during solution heat treatment of Ni-base superalloys has been reported in several articles [80, 93, 107]. The morphology at the surface of alloy shows a sequence of microstructure evolution as  $\gamma \rightarrow \gamma' \text{ (Ni}_3\text{Al)} \rightarrow \beta \text{ (NiAl)}$  after solution heat treatment. It was proposed that the phase transformation is caused by vaporisation/sublimation during heat treatment since the depletion of solid solution elements destabilises the  $\gamma$  phase and facilitates the formation of new phase near the surface. However, the difficulty is associated with accurate quantification of elemental loss under non-equilibrium condition in solution heat treatment scenario. With measurements of partial vapour pressures in equilibrium, our intention is to use measured data to interpret



sublimation induced microstructural instability in Ni-base superalloys during solution heat treatment.

Thermodynamic analysis using KEMS method provides reliable data for calculating partial vapour pressures of Ni, Al and Cr in measured Ni-Cr-Al model alloys. Using those data, the elemental sublimation during solution heat treatment of Ni-base alloys can be analysed as follows:

In practice, solution heat treatment of CMSX-10N single crystal superalloys is normally carried out under a partial vapour pressure of Ar with intermittent purge cycles, therefore the sublimation of Ni and Cr occurs on the surface of alloys in non-equilibrium condition. Sublimation of Cr during processing is a common phenomenon that has also been studied in other materials. Lobb and Evans [85] observed evaporation of elements in stainless steel during vacuum annealing and proposing that the evaporation of Cr occurs through the grain boundary, which is potentially regarded as defects of alloys, at long annealing times. Li [176] and Gupta et al [83] reported the evaporative segregation phenomena in binary Ni-Cr and Fe-Cr alloy, suggesting solute enrichment or depletion in alloys as a result of surface evaporation.

Although KEMS experiments was conducted under equilibrium, the measured data can be used to interpret elemental sublimation in non-equilibrium condition. Our results show that the order of partial vapour pressures is,  $Ni > Cr > Al$ . In terms of magnitude, partial vapour pressures of Ni and Cr is at least 2 orders of magnitude higher than that of Al, indicating almost negligible amount of Al sublimed from the as-cast alloy. High partial vapour pressure of Ni is due to its high concentration in alloys. The partial vapour pressure of Cr varies in an extensive range from  $8.1 \times 10^{-5}$  to 0.047 Pa in KEMS data, which was detected as a remarkable deduction of Cr partial vapour pressure from both heating/cooling cycles and isothermal hold. It is critical phenomenon that implies excessive amounts of Cr escaped from the alloy via sublimation.

Further calculation of chemical potential determines the order of tendency for elements leaving the Ni-base alloys. It is not surprise that chemical potential of Ni is highest among three elements. Although primary elemental loss depends on Ni, from proportional point of view, significant change of Cr concentration tends to have a profound effect on phase stability at surface of Ni-base alloys as well as tendency of Cr leaving the alloy accelerates due to an

increase of Cr content. Considering that surface of alloy is the initial site for elemental sublimation, principal loss of Cr local imbalance of compositions leads to enrichment of Al at or near the surface of alloy. Moreover, Al does not sublime at high extent and remains in a stable form at measured temperatures, in this case, this indicates that Al is prone to be accumulated on the surface of alloy due to its diffusivity in  $\gamma$  phase. In addition, high concentration of Cr in the bulk tends to accelerate the Al activity [182] rejecting more Al to the surface. Eventually, this leads to potential formation of  $\gamma'$  phase on the surface.

As stated by several studies, surface depletion can be a serious problem for a dilute solid alloy [177, 178] leading to microstructural instability of alloys. As Cr segregates to  $\gamma$  phase in Ni-base alloys, the depletion of Cr is likely to cause redistribution of remaining elements within substrate. Al tends to partition to interdendrites with a formidable diffusivity. Semiatin et al [183] showed principal alloying element loss during high temperature processing of Ni-base superalloys is Cr in vacuum condition, leading to enrichment of Al at/near free surface as a consequence of heat treatment. Local imbalance of Cr concentration is likely to relate with segregation as well as affect concentration of Al which attributes to change of Al activity. According to observation from KEMS results, an increase of Al activity is accelerated by Cr addition contained in the alloys, indicating Al is prone to accumulate near the surface during vaporisation of Cr. In addition, since stabilisation of  $\gamma'$  phase is associated with increase of Ni/Al ratio or removal with principal solid solute, including Cr. Hence, the deduction rationalises the formation of  $\gamma'$  phase at the surface of Ni-base superalloys during solution heat treatment, which contributes to the formation of vaporisation induced defect. And partial pressure in Ni-Cr-Al alloys with respect to elemental concentration facilitates the improved understanding of surface evolution during heat treatment of Ni-base superalloys.

As a consequence, interaction of those elemental behaviour at high temperatures essentially results in phase evolution of microstructures in appearance as discontinuous precipitation. The loss of Cr and Ni de-stabilises  $\gamma$  and  $\gamma'$  phases during solution heat treatment, which is in consistence with experimental observation in Ni-base superalloys [80, 93, 107]. With respect to scenario of heat treatment in CMSX-10, elemental sublimation contributes to the formation of multi-phases layers, including  $\gamma$ ,  $\gamma'$  and  $\beta$  phases, on the surface of superalloys. Destabilisation of newly formed  $\gamma'$  phase occurs due to decrease of Ni/Al ratio and depletion of principle solid solute species Cr. In a nutshell, it is confirmed that a phenomenological

model describes the sequence of microstructure evolution as  $\gamma \rightarrow \gamma' \rightarrow \beta$  during solution heat treatment of the Ni-base alloys. Further work from thermodynamic consideration is required to assess overview of elemental sublimation as well as the effect of Ni condensation in cooling.

The observed kinetic orientation of ion intensity in long term homogenisation of Ni-Cr-Al alloys provide a threshold of solutioning time for dissolution of eutectic phases and segregated dendritic phases. A reliable kinetic timing in solution heat treatment and optimized homogeneous surrounding conditions in terms of temperature equilibrium have a profound effect on reducing casting defects with an effective way.

Phase transition in binary Ni-Al system studied by Hilpert et al [175] have shown transition regions of  $\beta+\gamma$  and  $\gamma+\gamma'$  for Ni content ranging from 0.7-0.72 and 0.76-0.8, respectively. Comparatively, KEMS data from Ni-Cr-Al alloys has consistent results in determining phase transition of measured alloys. From a detailed plot of thermodynamic activity in measured Ni-base alloys at constant temperature, Ni activity retains at constant when its mole fraction varies between 60 at% to 65 at% and 72 at% to 75 at%, indicating that phase transition occurs over the range of Ni compositions under consideration. Therefore it can be correlated that the phase boundaries calculated from current database, which predicted one phase region for our Ni-Cr-Al systems under the temperature range from 1473K to 1573K, has to be reviewed.

### **7.3 Conclusions**

Elemental sublimation in Ni-Cr-Al model alloys using KEMS method was analysed during solution heat treatment. The effect and implications of this phenomenon to production of commercial superalloys were discussed. Regarding to current investigation, KEMS method has been proved as an effective approach for investigating interactions of elements in Ni-base alloys at high temperatures. It also directs several further examination using commercial superalloys or the effect of protective oxides that prevent the surface from elemental losses. In general, conclusions and further work will be discussed in the last Chapter.

## 8. Conclusions and Future work

In this thesis, heat treatment related defects have been investigated during solutioning of Ni-base superalloys. It was noticed that sublimation induced microstructural instability in Ni-base superalloys during solution heat treatment. In order to precisely evaluate this phenomenon in efficient approach, the purpose of this study is to use KEMS method quantifying the extent of elemental sublimation under equilibrium, which delivers implications of sublimation effect on practical solution heat treatment devoting to solution for defects prevention. It is specifically focusing on determining partial pressures and thermodynamic activities of Ni, Al and Cr in Ni-Cr-Al model alloys generating valid equations for evaluating performance of Ni, Al and Cr in high-temperature range.

### 8.1 Conclusions

The study of discontinuous precipitation on surface of Ni-base superalloys during solution heat treatment reveal the effect of elemental loss on formation of microstructural instability. To further investigate elemental sublimation at high temperatures, KEMS method is regarded as a reliable technique for this propose. Considering contribution of elemental sublimation in Ni-base alloy, Ni-Cr-Al ternary alloys were selected for simplicity reason. The intention is to use measured KEMS data to interpret sublimation induced microstructural instability in Ni-base superalloys during solution heat treatment.

The formation of discontinuous precipitation on the surface of Ni-base superalloys was examined during solution heat treatment. The abrupt phase transformation was observed showing transition of  $\gamma$  to  $\gamma'$  phase at different stage of heat treatment. The growth of discontinuous precipitation is associated with partitioning of W, Re and Cr to growing tip of TCP precipitates.

Thermophysical properties of Ni-Cr-Al model alloys were measured. Solidus and liquidus temperatures of all measured alloys are consistent with results calculated in thermodynamic software with acceptable deviations. Thermodynamic activities of Ni, Al and Cr were also calculated in JMatPro and FactSage, which show dramatic difference in activities of Cr and Al. The assessment of results from KEMS measurements enables the optimisation of calculating thermodynamic activity in Ni-Cr-Al ternary system. Empirical results can be used for

optimisation of thermodynamic calculation in existing model. Experimental results show a good agreement with calculation from FactSage.

During the kinetic-influenced solution heat treatment of Ni-base superalloys, elements undergo processes of sublimation and deposition causing unpredictable defects. To quantitatively examine the sublimation phenomenon, partial vapour pressures of Ni, Al and Cr in Ni-base alloys were predominantly measured in the  $\gamma$  phase over the temperature range of 1473-1650 K using KEMS. Partial vapour pressures of Ni, Al and Cr in Ni-Cr-Al alloys as a function of temperature were obtained. Experimental results showed that the partial pressure of Al is about two orders of magnitude lower than that of Ni, and five times lower than that of Cr, suggesting that the sublimation of Al is almost negligible compared with those of Ni and Cr at solution heat treatment temperatures. It seemed that there is insufficient chemical potential for Al in Ni-base alloy to sublime preventing Al from escape at high temperatures.

The homogeneity of the prepared alloys was verified in long term isothermal experiments at 1573 K. It was seen that the gaseous species regarding Cr have changed by a factor of two in the first 20 hours, whereas the Ni and Al species remained nearly constant. This phenomenon is related to corresponding process of homogenisation and sublimation of unsolved Cr precipitation remained during kinetic heat treatment under as-cast condition. Elemental sublimation occurs during solution heat treatment of Ni-base alloys, which leads to chemistry change and microstructural instability at the surface of Ni-base alloys.

## **8.2 Further work**

The effect of elemental sublimation on Ni-Cr-Al mode alloys was revealed during solution heat treatment. There are several improvements can be carried out as future work to develop understanding of elemental sublimation in Ni-base superalloys in more details.

Due to availability of KEMS equipment, KEMS measurements were only carried out for model alloys containing 12 at% of Al. Despite preliminary KEMS measurements used two model alloys with 10 at% of Al, further KEMS measurements of 10 at% Al alloys are suggested for establishing the effect of Al doping on sublimation of Ni-base alloys. And the Al content can be measured up to 15 at%.

Pre-oxidation of Ni-base superalloys in casting aimed to form a protective alumina layer for preventing the surface from destabilisation prior to solution heat treatment. Despite several attempts of using pre-oxidised Ni-Cr-Al model alloy in KEMS experiments, the KEMS data doesn't show any protective effect of formed oxides on sublimation of Ni-base alloys. Hence, in order to accurately examine the effect of protective oxides, KEMS experiments need to be carefully designed using samples with well-formed oxides on the surface.

Although thermodynamic properties of commercial Ni-base superalloys can be predicted based on existing KEMS data of Ni-Cr-Al alloys, it is still worth carrying further KEMS experiments of commercial superalloys under isothermal condition, which is likely to provide sufficient data points to optimise accuracy of models due to the discrepancy of KEMS data and CALPHAD calculations. In addition, microstructural stability of Ni-base alloys is improved by additional of Ru which lowers the  $\gamma'$  solvus and reduces the volume fraction throughout temperature range. It is interesting to reveal Ru doping in Ni-Cr-Al model alloys to show its effect on elemental sublimation via KEMS method.

KEMS results have been properly compared with calculated results using Gibbs-Duhem integral Equation. The further work of this comparison would be ideal for confirming consistence between experimental measurements and theoretical calculations, which is essential for optimising model used in CALPHAD method. Hence, the optimised model will potentially calculate thermodynamic properties of Ni-base alloys to a degree closing to experimental results. Finally, it is also noticed that Ding's method [184, 185] is reasonably promising for calculating thermodynamic activities for dilute solutions in the alloys.

## Appendix

### Outlier methods for KEMS data selection

There are several statistical methods for outlier detection depending on purpose.

The Grubb's test [186] is to provide statistical rules that lead to erringly examine experimental results even outliers really exist. In this method, it is based on the assumption of normality for detection a single outlier in a univariate data. If there is more than one outlier present in data, the Tietjen-Moore test [187] or the generalized extreme studentized deviate (ESD) test [188] are recommended instead of Grubb's test.

Typical outlier method compares the difference between the suspect results to the mean of all data with the sample standard deviation, referring as  $\tau$  value. Table of criterial values for Grubbs' method have been specified in details according to number of data point, which uses Thompson  $\tau$  for deciding keep or discard outliers in a sample of a single variable. The procedure for outlier test is firstly determining sample mean  $\bar{x}$  and standard deviation  $S$  in ordinary manner, then absolute value for the deviation is calculated as  $\delta_i = |d_i| = |x_i - \bar{x}|$  for each data point. Finally, Thompson  $\tau$  can be calculated from the critical value  $t$  from following expression in a function of the number of data points  $n$ :

$$\tau_i = \frac{t \times (n - 1)}{\sqrt{n}\sqrt{n - 2 + t^2}}$$

where  $n$  is number of points,  $t$  is critical value. Therefore, a table of the modified Thompson  $\tau$  is provided below:

Table 1 modified Thompson  $\tau$  with respect to number of data point  $n$ :

n	$\tau$	n	$\tau$	n	$\tau$
3	1.1511	21	1.8891	40	1.9240
4	1.4250	22	1.8926	42	1.9257
5	1.5712	23	1.8957	44	1.9273
6	1.6563	24	1.8985	46	1.9288
7	1.7110	25	1.9011	48	1.9301
8	1.7491	26	1.9035	50	1.9314
9	1.7770	27	1.9057	55	1.9340
10	1.7984	28	1.9078	60	1.9362
11	1.8153	29	1.9096	65	1.9381
12	1.8290	30	1.9114	70	1.9397

13	1.8403	31	1.9130	80	1.9423
14	1.8498	32	1.9146	90	1.9443
15	1.8579	33	1.9160	100	1.9459
16	1.8649	34	1.9174	200	1.9530
17	1.8710	35	1.9186	500	1.9572
18	1.8764	36	1.9198	1000	1.9586
19	1.8811	37	1.9209	5000	1.9597
20	1.8853	38	1.9220	$\rightarrow \infty$	1.9600

If  $\delta_i > \tau_i S$ , there is an outlier and data point is rejected otherwise when  $\delta_i \leq \tau_i S$ , data point will be kept.

On the other hand, the generalised ESD test requires an upper bound for the suspect number of outliers, for a given upper bound  $r$ , the method is defined for the hypothesis,

For test statistic value  $R_i$

$$R_i = \frac{\max |x_i - \bar{x}|}{s}$$

where  $\bar{x}$  and  $s$  denote to the sample mean and sample standard deviation, respectively.

Corresponding to the  $r$  test statistics, critical values is computed by following equation:

$$\lambda_i = \frac{(n-i)t_{p,n-i-1}}{\sqrt{(n-i+1+t_{p,n-i-1}^2)(n-i+1)}}$$

where  $t_{p,v}$  is the percentage point from the t distrubtion with  $v$  degrees of freedom and

$$p = 1 - \frac{\alpha}{2(n-i+1)}$$

The number of outliers is determined by finding the largest  $i$  giving  $R_i > \lambda_i$ .

With assistance from Matlab and Python, the outlier method can be performed in great convenience as long as input data can be directed into the programme. Hence, the programme will automatically run the code based on principles as described above. Eventually, outliers in KEMS data were directly detected within sufficient accuracy.



## Reference

- [1] N. Cumpsty, Jet Propulsion: A Simple Guide to the Aerodynamic and Thermodynamic Design and Performance of Jet Engines, 2nd ed., Cambridge University Press, Cambridge, 2003.
- [2] Rolls-Royce, The Jet Engine, 5th ed. ed., Rolls-Royce plc1996.
- [3] R.C. Reed, The Superalloys: Fundamentals and Applications, Cambridge University Press, Cambridge, 2006.
- [4] C.T. Sims, N.S. Stoloff, W.C. Hagel, Superalloys II, Wiley-Interscience, New York, NY,1987.
- [5] S. Donachie, M.J. Donachie, Superalloys: A Technical Guide, 2nd ed., ASM International, Materials Park, United States, 2002.
- [6] C.M.F. Rae, M.S. Hook, R.C. Reed, The effect of TCP morphology on the development of aluminide coated superalloys, Materials Science and Engineering: A 396(1–2) (2005) 231-239.
- [7] R.A. Hobbs, S. Tin, C.M.F. Rae, R.W. Broomfield, C.J. Humphreys, Solidification characteristics of advanced nickel-base single crystal superalloys, Minerals, Metals & Materials Soc, Warrendale, 2004.
- [8] R.A. Hobbs, L. Zhang, C.M.F. Rae, S. Tin, Mechanisms of Topologically Close-Packed Phase Suppression in an Experimental Ruthenium-Bearing Single-Crystal Nickel-Base Superalloy at 1100 °C, Metallurgical and Materials Transactions A 39(5) (2008) 1014-1025.
- [9] R.C. Reed, C.M.F. Rae, 22 - Physical Metallurgy of the Nickel-Based Superalloys A2 - Laughlin, David E, in: K. Hono (Ed.), Physical Metallurgy (Fifth Edition), Elsevier, Oxford, 2014, pp. 2215-2290.
- [10] M. Gell, D.N. Duhl, D.K. Gupta, K.D. Sheffler, Advanced Superalloy Airfoils, JOM 39(7) (1987) 11-15.
- [11] J. Stringer, Coatings in the electricity supply industry: past, present, and opportunities for the future, Surface and Coatings Technology 108-109(Supplement C) (1998) 1-9.

- [12] G.Y. Lai, High-Temperature Corrosion and Materials Applications, ASM International, 2007.
- [13] B. Geddes, X. Huang, H. Leon, Superalloys : alloying and performance, ASM International, Materials Park, Ohio, 2010.
- [14] S. Walston, A. Cetel, R. MacKay, K. O'Hara, D. Duhi, R. Dreshfield, Joint development of a fourth generation single crystal superalloy, Minerals, Metals & Materials Soc, Warrendale, 2004.
- [15] R.W. Broomfield, D.A. Ford, J.K. Bhangu, M.C. Thomas, D.J. Frasier, P.S. Burkholder, K. Harris, G.L. Erickson, J.B. Wahl, Development and Turbine Engine Performance of Three Advanced Rhenium Containing Superalloys for Single Crystal and Directionally Solidified Blades and Vanes, Journal of Engineering for Gas Turbines and Power 120(3) (1998) 595-608.
- [16] R.A. MacKay, M.V. Nathal, D.D. Pearson, Influence of molybdenum on the creep properties of nickel-base superalloy single crystals, Metallurgical Transactions A 21(1) (1990) 381-388.
- [17] C.L. Fu, R. Reed, A. Janotti, M. Krcmar, On the diffusion of alloying elements in the nickel-base superalloys, Minerals, Metals & Materials Soc, Warrendale, 2004.
- [18] J.E. Doherty, B.H. Kea, A.F. Giamei, On the origin of the ductility enhancement in Hf-doped Mar-M200, JOM 23(11) (1971) 59-62.
- [19] D.N. Duhi, C.P. Sullivan, Some effects of hafnium additions on the mechanical properties of a columnar-grained nickel-base superalloy, JOM 23(7) (1971) 38-40.
- [20] M. McLean, Nickel-based alloys: recent developments for the aero-gas turbine, in: H.M. Flower (Ed.), High Performance Materials in Aerospace, Springer Netherlands, Dordrecht, 1995, pp. 135-154.

- [21] T.M. Pollock, S. Tin, Nickel-Based Superalloys for Advanced Turbine Engines: Chemistry, Microstructure and Properties, *Journal of Propulsion and Power* 22(2) (2006) 361-374.
- [22] C.S. Wukusick, L. Buchakjian, Property-balanced nickel-base superalloys for producing single crystal articles, Google Patents, 2000.
- [23] A.F. Giamei, D.L. Anton, Rhenium additions to a Ni-base superalloy: Effects on microstructure, *Metallurgical Transactions A* 16(11) (1985) 1997-2005.
- [24] R. Darolia, D.F. Lahrman, R.D. Field, Formation of Topologically Closed Packed Phases in Nickel Base Single Crystal Superalloys, *Minerals, Metals & Materials Soc*, Warrendale, 1988.
- [25] A.D. Celal, D.N. Duhi, Second-generation nickel-base single crystal superalloy, *Minerals, Metals & Materials Soc*, Warrendale, 1988.
- [26] K. Harris, G.L. Erickson, W.D. Brentnall, J.M. Aurrecoechea, S.L. Sikkenga, K.G. Kubarych, Development of the Rhenium Containing Superalloys CMSX-4 & CM 186 LC for Single Crystal Blade and Directionally Solidified Vane Applications in Advanced Turbine Engines, *Minerals, Metals & Materials Soc*, Warrendale, 1992.
- [27] K. Harris, G.L. Erickson, S.L. Sikkenga, W.D. Brentnall, J.M. Aurrecoechea, K.G. Kubarych, Development of two rhenium- containing superalloys for single- crystal blade and directionally solidified vane applications in advanced turbine engines, *Journal of Materials Engineering and Performance* 2(4) (1993) 481-487.
- [28] G.L. Erickson, The development and application of CMSX (R)-10, *Minerals, Metals & Materials Soc*, Warrendale, 1996.
- [29] W.S. Walston, K.S. O'Hara, E.W. Ross, T.M. Pollock, W.H. Murphy, Rene N6: Third generation single crystal superalloy, *Minerals, Metals & Materials Soc*, Warrendale, 1996.
- [30] P. Caron, T. Khan, Evolution of Ni-based superalloys for single crystal gas turbine blade applications, *Aerospace Science and Technology* 3(8) (1999) 513-523.

- [31] F.R.N. Nabarro, F. De Villiers, Physics of creep and creep-resistant alloys, CRC Press 1995.
- [32] N. Warnken, D. Ma, M. Mathes, I. Steinbach, Investigation of eutectic island formation in SX superalloys, Materials Science and Engineering: A 413 (2005) 267-271.
- [33] E. Nembach, G. Neite, Precipitation hardening of superalloys by ordered  $\gamma'$ -particles, Progress in Materials Science 29(3) (1985) 177-319.
- [34] I.M. Edmonds, The oxidation properties of uncoated and coated fourth generation nickel-based superalloys, University of Birmingham, 2009.
- [35] C.M.F. Rae, M.S.A. Karunaratne, C.J. Small, R.W. Broomfield, C.N. Jones, R.C. Reed, Topologically close packed phases in an experimental rhenium-containing single crystal superalloy, Minerals, Metals & Materials Soc, Warrendale, 2000.
- [36] C.M.F. Rae, R.C. Reed, The precipitation of topologically close-packed phases in rhenium-containing superalloys, Acta Materialia 49(19) (2001) 4113-4125.
- [37] G.J.J. Brewster, Solidification and heat-treatment related defects in single crystal nickel-base superalloys, Fitzwilliam College, University of Cambridge, 2010.
- [38] H. Dai, A Study of Solidification Structure Evolution during Investment Casting of Ni-base Superalloy for Aero-Engine Turbine Blades, University of Leicester, 2009.
- [39] H. Dong, H. Dai, 5.05 - Single-Crystal Casting/Directional Solidification A2 - Hashmi, Saleem, in: G.F. Batalha, C.J.V. Tyne, B. Yilbas (Eds.), Comprehensive Materials Processing, Elsevier, Oxford, 2014, pp. 89-108.
- [40] H.J. Dai, N. D'Souza, H.B. Dong, Grain Selection in Spiral Selectors During Investment Casting of Single-Crystal Turbine Blades: Part I. Experimental Investigation, Metallurgical and Materials Transactions A 42(11) (2011) 3430-3438.

- [41] H.J. Dai, H.B. Dong, N. D'Souza, J.-C. Gebelin, R.C. Reed, Grain Selection in Spiral Selectors During Investment Casting of Single-Crystal Components: Part II. Numerical Modeling, *Metallurgical and Materials Transactions A* 42(11) (2011) 3439-3446.
- [42] H. Dong, Grain Selection during Directional Solidification of Aero - Engine Turbine Blades, *AIP Conference Proceedings* 1045(1) (2008) 51-60.
- [43] H.B. Dong, Analysis of Grain Selection during Directional Solidification of Gas Turbine Blades, in: S.I. Ao, L. Gelman, D.W.L. Hukins, A. Hunter, A.M. Korsunsky (Eds.) *Proceedings of the World Congress on Engineering 2007*, Newswood Limited, 2007, pp. 1257-1262.
- [44] G. Brewster, H.B. Dong, N.R. Green, N. D'Souza, Surface Segregation during Directional Solidification of Ni-Base Superalloys, *Metallurgical and Materials Transactions B* 39(1) (2008) 87-93.
- [45] R.M. Kearsey, J.C. Beddoes, P. Jones, P. Au, Compositional design considerations for microsegregation in single crystal superalloy systems, *Intermetallics* 12(7) (2004) 903-910.
- [46] Q. Feng, T.K. Nandy, S. Tin, T.M. Pollock, Solidification of high-refractory ruthenium-containing superalloys, *Acta Materialia* 51(1) (2003) 269-284.
- [47] E.C. Caldwell, F.J. Fela, G.E. Fuchs, The segregation of elements in high-refractory-content single-crystal nickel-based superalloys, *JOM* 56(9) (2004) 44-48.
- [48] A. Heckl, R. Rettig, R.F. Singer, Solidification Characteristics and Segregation Behavior of Nickel-Base Superalloys in Dependence on Different Rhenium and Ruthenium Contents, *Metallurgical and Materials Transactions A* 41(1) (2009) 202.
- [49] G.E. Fuchs, Solution heat treatment response of a third generation single crystal Ni-base superalloy, *Materials Science and Engineering: A* 300(1-2) (2001) 52-60.

- [50] M. Ganesan, D. Dye, P.D. Lee, A technique for characterizing microsegregation in multicomponent alloys and its application to single-crystal superalloy castings, *Metallurgical and Materials Transactions A* 36(8) (2005) 2191-2204.
- [51] B.C. Wilson, J.A. Hickman, G.E. Fuchs, The effect of solution heat treatment on a single-crystal Ni-based superalloy, *JOM* 55(3) (2003) 35-40.
- [52] M.V. Acharya, G.E. Fuchs, The effect of long-term thermal exposures on the microstructure and properties of CMSX-10 single crystal Ni-base superalloys, *Materials Science and Engineering: A* 381(1) (2004) 143-153.
- [53] A.C. Yeh, C.M.F. Rae, S. Tin, High temperature creep of Ru-bearing Ni-base single crystal superalloys, *Minerals, Metals & Materials Soc*, Warrendale, 2004.
- [54] H.T. Pang, H.B. Dong, R. Beanland, H.J. Stone, C.M.F. Rae, P.A. Midgley, G. Brewster, N. D'Souza, Microstructure and Solidification Sequence of the Interdendritic Region in a Third Generation Single-Crystal Nickel-Base Superalloy, *Metallurgical and Materials Transactions A* 40(7) (2009) 1660-1669.
- [55] H.T. Pang, N. D'Souza, H. Dong, H.J. Stone, C.M.F. Rae, Detailed Analysis of the Solution Heat Treatment of a Third-Generation Single-Crystal Nickel-Based Superalloy CMSX-10K®, *Metallurgical and Materials Transactions A* 47(2) (2016) 889-906.
- [56] M.S.A. Karunaratne, D.C. Cox, P. Carter, R.C. Reed, Modelling of the microsegregation in CMSX-4 superalloy and its homogenisation during heat treatment, *Minerals, Metals & Materials Soc*, Warrendale, 2000.
- [57] H.T. Pang, H.B. Dong, H.J. Stone, N. D'Souza, Solution Heat Treatment in Single Crystal Ni-Base Superalloys.
- [58] S.R. Hegde, R.M. Kearsey, J. Beddoes, Design of Solutionizing Heat Treatments for an Experimental Single Crystal Superalloys, *Minerals, Metals & Materials Soc*, Warrendale, 2008.

- [59] S.R. Hegde, R.M. Kearsey, J.C. Beddoes, Designing homogenization–solution heat treatments for single crystal superalloys, *Materials Science and Engineering: A* 527(21) (2010) 5528-5538.
- [60] G.S. Hillier, H.K.D.H. Bhadeshia, The Homogenisation of Single-Crystal Superalloys, in: J. Beech (Ed.) *Perspectives in metallurgical development*, Metals Society, Department of Metallurgy, University of Sheffield, 1984, pp. 183-187.
- [61] A. Wagner, B.A. Shollock, M. McLean, Grain structure development in directional solidification of nickel-base superalloys, *Materials Science and Engineering: A* 374(1) (2004) 270-279.
- [62] T.M. Pollock, W.H. Murphy, The breakdown of single-crystal solidification in high refractory nickel-base alloys, *Metallurgical and Materials Transactions A* 27(4) (1996) 1081-1094.
- [63] D. Ma, Q. Wu, A. Bührig-Polaczek, Some New Observations on Freckle Formation in Directionally Solidified Superalloy Components, *Metallurgical and Materials Transactions B* 43(2) (2012) 344-353.
- [64] D.G. Eskin, Suyitno, L. Katgerman, Mechanical properties in the semi-solid state and hot tearing of aluminium alloys, *Progress in Materials Science* 49(5) (2004) 629-711.
- [65] J. Zhang, Effect of Ti and Ta on hot cracking susceptibility of directionally solidified Ni-based superalloy IN792, *Scripta Materialia* 48(6) (2003) 677-681.
- [66] J. Zhang, R.F. Singer, Effect of Zr and B on castability of Ni-based superalloy IN792, *Metallurgical and Materials Transactions A* 35(4) (2004) 1337-1342.
- [67] J. Zhang, R.F. Singer, Hot tearing of nickel-based superalloys during directional solidification, *Acta Materialia* 50(7) (2002) 1869-1879.

- [68] A. Porter, B. Ralph, The recrystallization of nickel-base superalloys, *Journal of Materials Science* 16(3) (1981) 707-713.
- [69] G. Xie, J. Zhang, L.H. Lou, Effect of heat treatment atmosphere on surface recrystallization of a directionally solidified Ni-base superalloy, *Scripta Materialia* 59(8) (2008) 858-861.
- [70] N. Zaafarani, D. Raabe, R.N. Singh, F. Roters, S. Zaefferer, Three-dimensional investigation of the texture and microstructure below a nanoindent in a Cu single crystal using 3D EBSD and crystal plasticity finite element simulations, *Acta Materialia* 54(7) (2006) 1863-1876.
- [71] B. Eidel, Crystal plasticity finite-element analysis versus experimental results of pyramidal indentation into (001) fcc single crystal, *Acta Materialia* 59(4) (2011) 1761-1771.
- [72] A. Heckl, S. Cenanovic, M. Göken, R.F. Singer, Discontinuous Precipitation and Phase Stability In Re- and Ru-Containing Nickel-Base Superalloys, *Metallurgical and Materials Transactions A* 43(1) (2012) 10-19.
- [73] J.D. Nystrom, T.M. Pollock, W.H. Murphy, A. Garg, Discontinuous cellular precipitation in a high-refractory nickel-base superalloy, *Metallurgical and Materials Transactions A* 28(12) (1997) 2443-2452.
- [74] A.-C. Yeh, A. Sato, T. Kobayashi, H. Harada, On the creep and phase stability of advanced Ni-base single crystal superalloys, *Materials Science and Engineering: A* 490(1) (2008) 445-451.
- [75] S. Tin, T.M. Pollock, Phase instabilities and carbon additions in single-crystal nickel-base superalloys, *Materials Science and Engineering: A* 348(1) (2003) 111-121.
- [76] H.B. Dong, Oxidation Treatment for Reducing Surface Scale Defects of Single Crystal Turbine Blade Proposal, University of Leicester, 2013.
- [77] S. Simmonds, Formation and Avoidance of Surface Defects during Casting and Heat-treatment of Single-Crystal Nickel-Base Superalloys, University of Leicester, 2014.



- [78] G. Brewster, N. D'Souza, K.S. Ryder, S. Simmonds, H.B. Dong, Mechanism for Formation of Surface Scale during Directional Solidification of Ni-Base Superalloys, *Metallurgical and Materials Transactions A* 43(4) (2012) 1288-1302.
- [79] S. Simmonds, N.D. Souza, K.S. Ryder, H. Dong, Analysis of surface scale on the Ni-based superalloy CMSX-10N and proposed mechanism of formation, *IOP Conference Series: Materials Science and Engineering* 27(1) (2012) 012038.
- [80] N. D'Souza, S. Simmonds, G.D. West, H.B. Dong, Role of Elemental Sublimation during Solution Heat Treatment of Ni-Based Superalloys, *Metallurgical and Materials Transactions A* 44(10) (2013) 4764-4773.
- [81] N. D' Souza, D. Welton, J. Kelleher, G.D. West, Z.H. Dong, G. Brewster, H.B. Dong, Microstructure Instability of Ni-Base Single Crystal Superalloys During Solution Heat Treatment, *Superalloys 2016*, John Wiley & Sons, Inc. 2016, pp. 267-277.
- [82] R.A. Swift, B.A. Noval, K.M. Merz, Fractionation of Ni–Cr–Cu–Al Alloys during Vacuum Evaporation, *Journal of Vacuum Science and Technology* 5(3) (1968) 79-83.
- [83] K.P. Gupta, J.L. Mukherjee, C.H. Li, Evaporative segregation in 80% Ni–20% Cr and 60% Fe–40% Ni alloys, *Journal of Vacuum Science and Technology* 11(5) (1974) 896-898.
- [84] A.F. Smith, R. Hales, Chromium depletion from stainless steels during vacuum annealing, *Materials and Corrosion* 28(6) (1977) 405-409.
- [85] R.C. Lobb, H.E. Evans, Evaporation of elements from 20Cr-25Ni-Nb stainless steel during vacuum annealing, *Metal Science* 15(1) (1981) 14-20.
- [86] D. Caplan, M.J. Graham, M. Cohen, Effect of Cold Work on the Oxidation of Nickel at High Temperature, *J. Electrochem. Soc.* 119(9) (1972) 1205-1215.

- [87] H. Asteman, J.-E. Svensson, L.-G. Johansson, Evidence for Chromium Evaporation Influencing the Oxidation of 304L: The Effect of Temperature and Flow Rate, *Oxidation of Metals* 57(3) (2002) 193-216.
- [88] R.T. Grimley, R.P. Burns, M.G. Inghram, Thermodynamics of the Vaporization of  $\text{Cr}_2\text{O}_3$ : Dissociation Energies of  $\text{CrO}$ ,  $\text{CrO}_2$ , and  $\text{CrO}_3$ , *The Journal of Chemical Physics* 34(2) (1961) 664-667.
- [89] C.S. Tedmon, The Effect of Oxide Volatilization on the Oxidation Kinetics of Cr and Fe - Cr Alloys, *J. Electrochem. Soc.* 113(8) (1966) 766-768.
- [90] P.F. Tortorelli, M.P. Brady, 1.21 - Design of High Temperature Alloys A2 - Cottis, Bob, in: M. Graham, R. Lindsay, S. Lyon, T. Richardson, D. Scantlebury, H. Stott (Eds.), *Shreir's Corrosion*, Elsevier, Oxford, 2010, pp. 541-557.
- [91] H. Wang, N. D'Souza, S. Zhao, D. Welton, N. Warnken, R.C. Reed, Effects of elemental vaporization and condensation during heat treatment of single crystal superalloys, *Scripta Materialia* 78–79 (2014) 45-48.
- [92] N. D'Souza, D. Welton, H. Wang, Implications of solute super-saturation in growth of vapourisation-induced recrystallised grains during heat treatment in Ni-base superalloys, *International Journal of Materials Research* 106(3) (2015) 288-295.
- [93] D. Welton, N. D'Souza, J. Kelleher, S. Gardner, Z.H. Dong, G.D. West, H. Dong, Discontinuous Precipitation in Ni-Base Superalloys During Solution Heat Treatment, *Metallurgical and Materials Transactions A* 46(9) (2015) 4298-4315.
- [94] C.B. Alcock, V.P. Itkin, M.K. Horrigan, Vapour Pressure Equations for the Metallic Elements: 298–2500K, *Canadian Metallurgical Quarterly* 23(3) (1984) 309-313.

- [95] CODATA recommended key values for thermodynamics, 1977 Report of the CODATA Task Group on key values for thermodynamics, 1977, The Journal of Chemical Thermodynamics 10(10) (1978) 903-906.
- [96] M.W. Chase, J.L. Curnutt, R.A. McDonald, A.N. Syverud, JANAF thermochemical tables, 1978 supplement, Journal of Physical and Chemical Reference Data 7(3) (1978) 793-940.
- [97] A.V. Gurvich, G.A. Khachkuruzov, V.A. Medvedev, I.V. Veits, G.A. Bergman, Termodinamicheskie Svoistva Individual'nykh Veshchestv (Thermodynamic Properties of Individual Substances), Izdatel'stvo Akademli Nauk, Moscow, 1962.
- [98] R.B. Scarlin, Discontinuous precipitation in a directionally-solidified nickel-base alloy, Scripta Metallurgica 10(8) (1976) 711-715.
- [99] D. Turnbull, Theory of cellular precipitation, Acta Metallurgica 3(1) (1955) 55-63.
- [100] K.N. Tu, D. Turnbull, Morphology of cellular precipitation of tin from lead-tin bicrystals-ii, Acta Metallurgica 15(8) (1967) 1317-1323.
- [101] J.W. Cahn, The kinetics of cellular segregation reactions, Acta Metallurgica 7(1) (1959) 18-28.
- [102] D.B. Williams, E.P. Butler, Grain boundary discontinuous precipitation reactions, International Metals Reviews 26(1) (1981) 153-183.
- [103] E. Hornbogen, Systematics of the cellular precipitation reactions, Metallurgical Transactions 3(11) (1972) 2717-2727.
- [104] W.S. Walston, J.C. Schaeffer, W.H. Murphy, A new type of microstructural instability in superalloys - SRZ, Minerals, Metals & Materials Soc, Warrendale, 1996.
- [105] A. Suzuki, C.M.F. Rae, M. Yoshida, Y. Matsubara, H. Murakami, Secondary Reaction Zones in coated 4th generation Ni-based blade alloys, Minerals, Metals & Materials Soc, Warrendale, 2008.

- [106] I. Manna, S.K. Pabi, W. Gust, Discontinuous reactions in solids, *International Materials Reviews* 46(2) (2001) 53-91.
- [107] N. D'Souza, D. Welton, G.D. West, I.M. Edmonds, H. Wang, On the Roles of Oxidation and Vaporization in Surface Micro-structural Instability during Solution Heat Treatment of Ni-base Superalloys, *Metallurgical and Materials Transactions A* 45(13) (2014) 5968-5981.
- [108] M. Knudsen, Die Molekularströmung der Gase durch Öffnungen und die Effusion, *Annalen der Physik* 333(5) (1909) 999-1016.
- [109] J. Drowart, P. Goldfinger, Investigation of Inorganic Systems at High Temperature by Mass Spectrometry, *Angewandte Chemie International Edition in English* 6(7) (1967) 581-596.
- [110] J. Drowart, C. Chatillon, J. Hastie, D. Bonnell, High-temperature mass spectrometry: Instrumental techniques, ionization cross-sections, pressure measurements, and thermodynamic data - (IUPAC technical report), *Pure and Applied Chemistry* 77(4) (2005) 683-737.
- [111] R.T. Grimley, Mass Spectrometry, in: J.L. Margrave (Ed.), *The Characterization of High Temperature Vapors*, John Wiley & Sons, New York 1967, pp. 195-243.
- [112] P. Goldfinger, Mass Spectrometric Investigation of High Temperature Equilibria, in: R.I. Reed (Ed.), *Mass Spectroscopy*, Academic, New York 1965, pp. 265-281.
- [113] L.V. Gurvich, I. Veyts, *Thermodynamic Properties of Individual Substances: Elements and compounds*, Taylor & Francis, 1990.
- [114] R. Hultgren, P.D. Desai, D.T. Hawkins, M. Gleiser, K.K. Kelley, *Selected Values of the Thermodynamic Properties of the Elements*, American Society of Metals, Metals Park, OH, 1973.

- [115] R.A. Dobbins, K. Mohammed, D.A. Sullivan, Pressure and Density Series Equations of State for Steam as Derived from the Haar–Gallagher–Kell Formulation, *Journal of Physical and Chemical Reference Data* 17(1) (1988) 1-8.
- [116] L. Bencze, T. Markus, D. Kath, S. Dash, D.D. Raj, W.A. Oates, W. Löser, K. Hilpert, Thermodynamic properties of B2-AlFeNi Alloys. Part I: Investigation by knudsen effusion mass spectrometry, *Metallurgical and Materials Transactions A* 37(11) (2006) 3171-3181.
- [117] L. Bencze, D.D. Raj, D. Kath, L. Singheiser, K. Hilpert, W.A. Oates, Thermodynamic properties and diffusion thermodynamic factors in B2-NiAl, *Metallurgical and Materials Transactions B* 35(5) (2004) 867-876.
- [118] D. Raj, L. Bencze, D. Kath, W.A. Oates, J. Herrmann, L. Singheiser, K. Hilpert, Thermodynamic activity measurements in the B2 phases of the Fe–Al and Ni–Al systems, *Intermetallics* 11(11–12) (2003) 1119-1124.
- [119] N.C. Oforka, B.B. Argent, Thermodynamics of Ni-Cr-Al alloys, *Journal of the Less Common Metals* 114(1) (1985) 97-109.
- [120] K. Hilpert, M. Miller, Study of the Vaporization of Ni-Cr-Al and Fe-Cr-Al Base Alloys by Knudsen Effusion Mass Spectrometry, *Z. Metallk.* 83(10) (1992) 739-743.
- [121] A. Neckel, Mass-Spectrometric Determination of Thermodynamic Mixing Effects of Alloys, in: H. Brodowsky, H.J. Schaller (Eds.), *Thermochemistry of Alloys: Recent Developments of Experimental Methods*, Springer Netherlands, Dordrecht, 1989, pp. 221-246.
- [122] N. Birks, G.H. Meier, F.S. Pettit, *Introduction to the High Temperature Oxidation of Metals*, 2 ed., Cambridge University Press, Cambridge, 2006.
- [123] S. Bose, *High Temperature Coatings*, Butterworth-Heinemann, Burlington, 2007.
- [124] D.R. Gaskell, *Introduction to Metallurgical Thermodynamics*, 4th ed., Taylor & Francis, 2009.

- [125] H.J.T. Ellingham, Transactions and Communications, Journal of the Society of Chemical Industry 63(5) (1944) 125-133.
- [126] S. Cruchley, H.E. Evans, M.P. Taylor, M.C. Hardy, S. Stekovic, Chromia layer growth on a Ni-based superalloy: Sub-parabolic kinetics and the role of titanium, Corrosion Science 75(Supplement C) (2013) 58-66.
- [127] C.S. Giggins, F.S. Pettit, Oxidation of Ni - Cr - Al Alloys Between 1000° and 1200°C, J. Electrochem. Soc. 118(11) (1971) 1782-&.
- [128] F.H. Stott, G.C. Wood, The mechanism of oxidation of Ni-Cr-Al alloys at 1000°–1200°C, Corrosion Science 11(11) (1971) 799-812.
- [129] D.P. Whittle, D.J. Evans, D.B. Scully, G.C. Wood, Compositional changes in the underlying alloy during the protective oxidation of alloys, Acta Metallurgica 15(9) (1967) 1421-1430.
- [130] N. D'Souza, R. Beanland, C. Hayward, H.B. Dong, Accuracy of composition measurement using X-ray spectroscopy in precipitate-strengthened alloys: Application to Ni-base superalloys, Acta Materialia 59(3) (2011) 1003-1013.
- [131] J.R. Santisteban, M.R. Daymond, J.A. James, L. Edwards, ENGIN-X: a third-generation neutron strain scanner, Journal of Applied Crystallography 39(6) (2006) 812-825.
- [132] M.T. Hutchings, P.J. Withers, T.M. Holden, T. Lorentzen, Introduction to the characterization of residual stress by neutron diffraction, CRC press 2005.
- [133] H.B. Dong, J.D. Hunt, A Numerical Model of a Two-pan Heat Flux DSC, Journal of Thermal Analysis and Calorimetry 64(1) (2001) 167-176.
- [134] M.N. Gungor, A statistically significant experimental technique for investigating microsegregation in cast alloys, Metallurgical Transactions A 20(11) (1989) 2529-2533.
- [135] M.D. Ball, D.G. McCartney, The measurement of atomic number and composition in an SEM using backscattered detectors, Journal of Microscopy 124(1) (1981) 57-68.

- [136] H. Dong, A theoretical and experimental investigation of a novel scanning calorimeter, University of Oxford, 2000.
- [137] H.B. Dong, J.D. Hunt, A Novel Single-pan Scanning Calorimeter. Measurement of thermophysical properties of metallic alloys, *Journal of Thermal Analysis and Calorimetry* 64(1) (2001) 341-350.
- [138] B. Kantor, C. Mason, N. D'Souza, H.B. Dong, N.R. Green, Influence of Al and Nb on castability of a Ni-base superalloy, IN713LC, *International Journal of Cast Metals Research* 22(1-4) (2009) 62-65.
- [139] N. Saunders, U.K.Z. Guo, X. Li, A.P. Miodownik, J.-P. Schillé, Using JMatPro to model materials properties and behavior, *JOM* 55(12) (2003) 60-65.
- [140] Z. Guo, N. Saunders, J.P. Schillé, A.P. Miodownik, Material properties for process simulation, *Materials Science and Engineering: A* 499(1) (2009) 7-13.
- [141] L. Kaufman, H. Bernstein, *Computer Calculation of Phase Diagrams with Special Reference to Refractory Metals*, Academic Press, 1970.
- [142] N. Saunders, P. Miodownik, *CALPHAD: Calculation of Phase Diagrams — A Comprehensive Guide*, Pergamon 1998.
- [143] J.O. Andersson, T. Helander, L. Höglund, P. Shi, B. Sundman, Thermo-Calc & DICTRA, computational tools for materials science, *Calphad* 26(2) (2002) 273-312.
- [144] C.W. Bale, E. Bélisle, P. Chartrand, S.A. Decterov, G. Eriksson, A.E. Gheribi, K. Hack, I.H. Jung, Y.B. Kang, J. Melançon, A.D. Pelton, S. Petersen, C. Robelin, J. Sangster, P. Spencer, M.A. Van Ende, *FactSage thermochemical software and databases, 2010–2016*, *Calphad* 54(Supplement C) (2016) 35-53.

- [145] C.W. Bale, P. Chartrand, S.A. Degterov, G. Eriksson, K. Hack, R. Ben Mahfoud, J. Melançon, A.D. Pelton, S. Petersen, FactSage thermochemical software and databases, *Calphad* 26(2) (2002) 189-228.
- [146] C.W. Bale, E. Bélisle, P. Chartrand, S.A. Decterov, G. Eriksson, K. Hack, I.H. Jung, Y.B. Kang, J. Melançon, A.D. Pelton, C. Robelin, S. Petersen, FactSage thermochemical software and databases — recent developments, *Calphad* 33(2) (2009) 295-311.
- [147] E.H. Copland, N.S. Jacobson, *Measuring Thermodynamic Properties of Metals and Alloys with Knudsen Effusion Mass Spectrometry*, NASA, 2010, p. 54.
- [148] M. Miller, K. Armatys, Twenty years of Knudsen Effusion Mass Spectrometry: Studies Performed in the Period 1990-2010, *The Open Thermodynamics Journal* 7 (2013) 2-9.
- [149] K. Hilpert, High temperature mass spectrometry in materials research, *Rapid Communications in Mass Spectrometry* 5(4) (1991) 175-187.
- [150] K. Hilpert, *Chemistry of inorganic vapors, Noble Gas and High Temperature Chemistry*, Springer Berlin Heidelberg, Berlin, Heidelberg, 1990, pp. 97-198.
- [151] K. Hilpert, Potential of mass spectrometry for the analysis of inorganic high-temperature vapors, *Fresenius' Journal of Analytical Chemistry* 370(5) (2001) 471–478.
- [152] J. Drowart, P. Goldfinger, Die Massenspektrometrie anorganischer Systeme bei hohen Temperaturen, *Angewandte Chemie* 79(13) (1967) 589-604.
- [153] D.J. Fabian, Mass spectrometry and its applications in metallurgy and materials science, *Metallurgical Reviews* 12(1) (1967) 27-48.
- [154] K.A. Gingerich, Mass spectrometric investigation of gas phase reactions during sublimation, *Journal of Crystal Growth* 9(Supplement C) (1971) 31-45.
- [155] F.E. Stafford, Limitations in applying mass spectrometry to high-temperature equilibrium studies, *High Temp.-High Press.* 3(2) (1971) 213-224.



- [156] Forschungszentrum Jülich KEMS. [http://www.fz-juelich.de/iek/iek-2/EN/Forschung/Thermochemie/Methoden/Methoden\\_Uebersicht/KEMS/KEMS\\_node.html](http://www.fz-juelich.de/iek/iek-2/EN/Forschung/Thermochemie/Methoden/Methoden_Uebersicht/KEMS/KEMS_node.html), (accessed 30/07.2015).
- [157] D. Kobertz, M. Müller, A. Molak, Vaporization and caloric studies on lead titanate, *Calphad* 46 (2014) 62-79.
- [158] K. Hilpert, *Chemistry of Inorganic Vapors, Noble Gas and High Temperature Chemistry*, Springer-Verlag 1990, pp. 97-198.
- [159] A. Neckel, S. Wagner, Mass spectrometric determination of thermodynamic activities in ternary systems, *Monatshefte für Chemie / Chemical Monthly* 100(2) (1969) 664-670.
- [160] G.R. Belton, R.J. Fruehan, Determination of activities by mass spectrometry. I. The liquid metallic systems iron-nickel and iron- cobalt, *The Journal of Physical Chemistry* 71(5) (1967) 1403-1409.
- [161] J.B. Mann, Recent developments in mass spectroscopy : proceedings of the international conference on mass spectroscopy, Kyoto, in: K. Ogata, T. Hayakawa (Eds.) University Park Press, Baltimore, Md., 1970, pp. 814–819.
- [162] M. Berglund, M.E. Wieser, Isotopic compositions of the elements 2009 (IUPAC Technical Report), *Pure and Applied Chemistry* 83(2) (2011) 397-410.
- [163] NIST, Atomic Weights and Isotopic Compositions for All Elements. [http://physics.nist.gov/cgi-bin/Compositions/stand\\_alone.pl](http://physics.nist.gov/cgi-bin/Compositions/stand_alone.pl)  
<http://physics.nist.gov/PhysRefData/Handbook/Tables/nickeltable1.htm>.
- [164] F.A. White, T.L. Collins, F.M. Rourke, Search for Possible Naturally Occurring Isotopes of Low Abundance, *Physical Review* 101(6) (1956) 1786-1791.
- [165] G.V. Belov, V.S. Iorish, V.S. Yungman, IVTANTHERMO for Windows — database on thermodynamic properties and related software, *Calphad* 23(2) (1999) 173-180.

- [166] R. Clausius, Ueber die bewegende Kraft der Wärme und die Gesetze, welche sich daraus für die Wärmelehre selbst ableiten lassen, *Annalen der Physik* 155(4) (1850) 500-524.
- [167] É. Clapeyron, Mémoire sur la puissance motrice de la chaleur, *Journal de l'École polytechnique* 23 (1834) 153-190.
- [168] L.S. Darken, R.W. Gurry, *Physical chemistry of metals*, International student edition ed., McGraw-Hill, New York, 1953.
- [169] M. Hillert, *Phase Equilibria, Phase Diagrams and Phase Transformations: Their Thermodynamic Basis*, 2 ed., Cambridge University Press, Cambridge, 2007.
- [170] P.W. Atkins, J. De Paula, *Physical chemistry*, 10th ed., W.H. Freeman, New York, 2010.
- [171] N.S. Jacobson, G.M. Mehrotra, Thermodynamics of iron-aluminum alloys at 1573 K, *Metallurgical Transactions B* 24(3) (1993) 481-486.
- [172] G.R. Belton, R.J. Fruehan, The determination of activities by mass-spectrometry—some additional methods, *Metallurgical Transactions* 2(1) (1971) 291-296.
- [173] G.R. Belton, R.J. Fruehan, Mass-spectrometric determination of activities in Fe–Cr and Fe–Cr–Ni alloys, *Metallurgical Transactions* 1(4) (1970) 781-787.
- [174] A.N. Analytical Methods Committee, Using the Grubbs and Cochran tests to identify outliers, *Analytical Methods* (2015).
- [175] K. Hilpert, D. Kobertz, V. Venugopal, M. Miller, H. Gerads, F.J. Bremer, H. Nickel, Phase Diagram Studies on the Al– Ni System, *Z. Naturforsch. Sect. A-J. Phys. Sci.* 42(11) (1987) 1327-1332.
- [176] C.H. Li, *Normal evaporation of binary alloys*, Grumman Aerospace Corp., Bethpage, NY, United States, 1972.
- [177] P.K. Raychaudhuri, F.E. Stafford, Alloy thermodynamics by mass spectrometry: A critical review, *Materials Science and Engineering* 20 (1975) 1-18.

- [178] P.K. Raychaudhuri, Mass Spectrometric and Galvanic Cell Studies of the Thermodynamic Properties of Solid Silver-Palladium Alloys, Northwestern University, Ann Arbor, 1971, p. 236.
- [179] D.A. Porter, K.E. Easterling, Phase Transformations in Metals and Alloys, 2nd ed., Chapman & Hall 1992.
- [180] ThermoCalc Ni-based Superalloys Database. TCNI8, version 8.0. Thermo-Calc Software AB, Stockholm; 2006. [http://www.thermocalc.com/media/23650/tcni8\\_extended\\_info.pdf](http://www.thermocalc.com/media/23650/tcni8_extended_info.pdf), (accessed 01/04.2016).
- [181] A.T. Dinsdale, SGTE data for pure elements, Calphad 15(4) (1991) 317-425.
- [182] E. Godlewski, K. Godlewski, Chromaluminizing of nickel and its alloys, Oxidation of Metals 22(3) (1984) 117-131.
- [183] S.L. Semiatin, J.M. Shank, W.M. Saurber, A.L. Pilchak, D.L. Ballard, F. Zhang, B. Gleeson, Alloying-Element Loss During High-Temperature Processing of a Nickel-Base Superalloy, Metallurgical and Materials Transactions A 45(2) (2014) 962-979.
- [184] X. Ding, P. FAN, Q. Han, Models of activity and activity interaction parameter in ternary metallic melt, Acta Metall Sin 30(14) (1994) 49-60.
- [185] X. Ding, W. Wang, P. Fan, Thermodynamic calculation for alloy systems, Metallurgical and Materials Transactions B 30(2) (1999) 271-277.
- [186] F.E. Grubbs, Procedures for Detecting Outlying Observations in Samples, Technometrics 11(1) (1969) 1-21.
- [187] G.L. Tietjen, R.H. Moore, Some Grubbs-Type Statistics for the Detection of Several Outliers, Technometrics 14(3) (1972) 583-597.
- [188] B. Rosner, Percentage Points for a Generalized ESD Many-Outlier Procedure, Technometrics 25(2) (1983) 165-172.